



Università degli Studi di Salerno

FACOLTÀ DI SCIENZE MATEMATICHE, FISICHE E NATURALI

DIPARTIMENTO DI FISICA “E.R. CAIANIELLO”

Dottorato di Ricerca in Fisica

X Ciclo, II Serie

**Magneto-transport properties of thin
superconducting strips in the framework of
Time Dependent Ginzburg Landau model**

“Tesi di dottorato in Fisica”

Dottorando

Dr. Paolo Sabatino

Tutor

Dr. Giovanni Carapella

Coordinatore

Prof. Giuseppe Grella

ANNO ACCADEMICO 2010/2011

Acknowledgments

This dissertation concludes my journey of the PhD program. Along the way I am indebted to so many people in many ways. Here I can list only the most outstanding of them. The first place is certainly reserved to the my supervisor Dr. Giovanni Carapella - longtime friend and university colleague - for having guided me in these last years as a PhD student. He has been and will for sure continue to be an endless source of ideas for new interesting problems as well as even more interesting new solutions. I am grateful to Prof. Giovanni Costabile for providing me guidance, support, encouragement and freedom throughout this work. Many thanks go to Prof. Giovanni Filatrella for his moral support, being always available for discussion and advises. Special thanks to Mr. Luigi Falco for all time spent with me in the lab, helping me to solve many problems by mean of his competences. I would also like to acknowledge my colleagues - too many to mention all - at the Physics Department of Salerno for their availability to discussions, advices and friendship.

Last but not least, I would like to give special thanks to my mother 'Gemma', my wife Amalia, and my sons Emanuele, Francesca and Michela. Your tireless love, support, and encouragement both in life and throughout the entire frenzied writing process have truly been priceless.

Contents

Acknowledgments	i
Contents	iii
Introduction	1
1 Ginzburg-Landau Model	7
1.1 Introduction	7
1.2 Superconductors in a nutshell	8
1.3 The Time-Dependent Ginzburg-Landau equations	9
1.3.1 Dimensionless units	13
1.3.2 Gauge transformation	14
1.3.3 Microscopic derivations	15
1.3.4 High- κ , High-Field model	16
1.3.5 TDGL model with applied field and current	17
1.4 Numerical method	19
1.4.1 The $U - \psi$ Method	19
1.4.2 Simplified algorithm	22
1.4.3 Boundary conditions	24
1.4.4 Hardware and Software Platform	25
Bibliography	31
2 Fabrication and measurement techniques	35
2.1 Introduction	35
2.2 Electron Beam Lithography	36
2.3 Equipments	37

2.4	The Scanning Electron Microscope	38
2.5	EBL digital pattern generator	41
2.5.1	Resist layer preparation	42
2.5.2	Pattern design	43
2.5.3	Positioning and alignment	44
2.5.4	Measure beam current and focus	47
2.5.5	Exposure	48
2.5.6	Pattern transfer	51
2.6	Thin film deposition system	52
2.7	Photolithographic patterning of wiring pads	54
2.8	Images of patterned structures	55
2.8.1	Preliminary results	62
2.9	Measurement system setup	64
2.9.1	HelioxVL cryostat	64
2.9.2	Measurement electronics	65
	Bibliography	69
3	A finite geometry ferromagnet-superconductor bilayer	71
3.1	Introduction	71
3.2	Basic phenomenology and discussion	72
3.3	Numerical simulations	76
3.3.1	Micromagnetics	76
3.3.2	Vortex dynamics	79
3.4	Summary	88
	Bibliography	89
4	Nb thin films with nanometer-sized square antidots array	93
4.1	Introduction	93
4.2	Experimental results and discussion	94
4.3	Numerical simulations	98
4.4	Summary	102
	Bibliography	103
5	Curved mesoscopic superconducting strips	107
5.1	Introduction	107
5.2	Theoretical model	108
5.3	Section of a cylindrical shell: asymmetry	111
5.4	Cylindrical shell: high dynamical resistivity branches	116
5.5	Summary	120
	Bibliography	121

6	Mesoscopic superconducting cylindrical surface	123
6.1	Introduction	123
6.2	The theoretical model	124
6.3	Numerical results and discussion	128
6.4	Summary	132
	Bibliography	133
7	Niobium thin strip of plano-convex section	135
7.1	Introduction	135
7.2	Experimental results	137
7.3	Numerical results and discussion	143
	7.3.1 Full 3D model: exploration	144
	7.3.2 Simplified 2D model: numerical results	151
7.4	Summary	159
	Bibliography	161
8	Thin superconducting strip with trapezoidal profile	163
8.1	Introduction	163
8.2	Experimental results	164
8.3	Discussion	167
	8.3.1 Model	168
	8.3.2 Preferentially directed flux motion	170
	8.3.3 Geometrical force	175
8.4	Summary	177
	Bibliography	179
	Conclusions	181

Introduction

This dissertation summarizes my experimental/phenomenological research activities conducted at the laboratories of Physics Department, University of Salerno under the supervision of Dr. G. Carapella. The experimental work consisted in the fabrication of mesoscopic superconducting devices made using Electron Beam Lithography (EBL) on Niobium thin films obtained by magnetron RF sputtering deposition. The EBL technique was accessible only from the end of 2009 and I was the first to develop the new technology available at the said Department. Among the devices fabricated with success are worthy of attention thin strips (25 nm) of Niobium with a regular array of antidots in deep submicron scale (15 nm diameter holes spaced 50 nm) on which studies were performed about the matching of Abrikosov vortices lattice at high magnetic fields in collaboration with another research group headed by Prof. C. Attanasio working at the Department of Physics. Other devices successfully produced have been superconducting strips with lateral dimensions of the order of microns, but with variable thickness on the nanometer scale. On this type of devices I has conducted a study of magneto-transport properties at cryogenic (liquid helium) and deep cryogenic (300 mK) temperatures in a magnetic field both parallel and perpendicular to the substrate. The most interesting result was that these devices may exhibit a behavior of superconducting diode.

In parallel to laboratory activities were carried out investigations aimed at the theoretical and computational description/interpretation of the phenomena observed experimentally in the framework of Time-Dependent Ginzburg-Landau (TDGL) model of superconductivity. The direct numerical integration of the TDGL as well as its specialization to magneto-transport properties

of superconducting strips in finite and unconventional geometry had not tradition at the Department of Physics, and I gave a my original contribution to this research line. Results acquired in this activity that are worth mentioning are the interpretation of the asymmetry and bistability in a Abrikosov diode based on superconductor/ferromagnet strips, the interpretation of matching properties in strips with square arrays of antidots in the nanometer scale, the behavior of superconducting cylindrical shells in the presence of a magnetic field applied parallel and perpendicular to the axis, including the dynamics of a single Abrikosov vortex trapped in these shells, and finally the magneto-transport properties of superconducting strips with variable section at the nanoscale.

This dissertation is organized as follows. The Chapter 1 explains in details the theoretical background of the thesis, i.e., the TDGL model of superconductivity, which describes the superconducting state using a complex order parameter. We introduce the equations of the TDGL model using both phenomenological and microscopic approaches. The TDGL equations are also written in their dimensionless form and the characteristics of the material as well as the universal constants are included in the dimensionless variables, making them easier for analysis and computations. It is well known that the TDGL equations are gauge invariant, thus, in order to obtain the well-posedness of the problem, we describe how to impose the gauge conditions. Moreover, the TDGL model is examined in the high- κ , high magnetic field limit which simplifies the complexity of the general model. We have analyzed in detail how to employ a transport current both in the general and in the simplified model, and how to derive from both the interest physical quantities. We also introduce two methods to discretize the TDGL equations with the help of link variables and we describe how to impose the boundary conditions for finite geometries. Finally, we give a short description of the hardware and software platform used for simulating both models. Chapter 2 describes in more detail the experimental techniques used to fabricate and measure the devices under investigation in this thesis. The main instrumental aspects of EBL are described in this Chapter. First, the general characteristics of the technique are summarized. Then, direct writing EBL is presented by the description of the different elements of the system. A brief description of lithographic capabilities introduced to the SEM is included. In particular, the general procedure for exposure is generally schematized. Finally, we briefly presented the best devices obtained using the above fabrication techniques and some preliminary results of electrical transport measurement successfully performed for two fabricated samples that not been discussed in detail in following chapters of this thesis. Moreover, we describe the measurement system setup (cryostats and measurement electronics) used for the

acquisition of the I-V characteristics in magnetic field of our devices.

A previous published work has shown that Py/Nb bilayers patterned in a strip geometry can exhibit asymmetric transport properties and bistability. In Chapter 3, with the help of numerical simulations in the framework of TDGL model for superconductor and Landau-Lifshitz-Gilbert (LLG) model for ferromagnet, it is demonstrated that the asymmetric and bistable magneto-transport response of the bilayers can be accounted for by the stray fields from the patterned ferromagnetic layer [1]. Numerical simulations on vortex dynamics show that in the dissipative branch of the bilayer a peculiar spontaneous channeled flux flow regime is realized, with alternating vortex and antivortex chains moving in the opposite directions in the superconducting layer.

Chapter 4 explains how Nb thin films containing a regular square array of antidots with 17 nm diameter and 50 nm spacing have been fabricated using a relatively simple lithographic process. The critical current density $j_c(H)$ curves, obtained here by electrical transport measurements, exhibit commensurability effects with pronounced maxima just above the expected matching fields, down to temperatures as low as 2.3 K. The behavior of $j_c(H)$ as well as the position of the maxima are consistent with the ones calculated in the framework of the time dependent Ginzburg-Landau model [2].

In Chapter 5, transport properties of curved mesoscopic superconducting strips are investigated in the framework of TDGL formalism. The geometries of superconducting strips considered here are either a section of a cylindrical shell or a full cylindrical shell in which the magnetic field is applied perpendicular to the axis. The cylindrical section can exhibit considerably asymmetric transport properties, making it potentially interesting as a sub-micrometer scale superconducting current rectifier. The full cylindrical surface exhibits well developed dissipative branches in the voltage-current curves, that can be accounted for by kinematic vortex-antivortex phase slip lines [3]. Such kind of phase slip lines compels voltage oscillations in a frequency range higher than the one associated to familiar flux flow regime.

The behaviour of a single Abrikosov vortex trapped in a mesoscopic superconducting cylindrical surface with a magnetic field applied transverse to its axis has been investigated in Chapter 6. In the framework of time-dependent Ginzburg-Landau formalism is shown that, provided the transport current and the magnetic field are not large, the vortex behaves as an overdamped quasi-particle in a tilted washboard potential [4]. The cylindrical thin strip with the trapped vortex exhibits $E(J)$ curves and time-dependent electric fields very similar to the ones exhibited by a resistively shunted Josephson weak link.

In Chapter 7 it is demonstrated experimentally and numerically that in

the presence of an in-plane magnetic field the voltage-current curve of a Nb thin strip having plano-convex cross section exhibits considerable asymmetry of the critical current. The observed behavior can be accounted for by the magnetic field component normal to the top convex surface of the strip [5]. Such a component is inhomogeneous, changes sign in the middle of the strip and affects the three-dimensional vortices that in this system have sections locally perpendicular to the top convex surface, though the magnetic field is applied parallel to the bottom flat surface. These sections can be described, from the point of view of the top curved surface, as two-dimensional vortex-antivortex pairs or double kinks and, surprisingly, play the most significant role in the generation of the observed asymmetry. The double kink mechanism is addressed here with numerical simulations in the framework of time dependent Ginzburg-Landau model and a maximum asymmetry ratio of about 300% at 4.2 K is observed when the strip is in the mixed state.

Chapter 8 reports an experimental and numerical study of the vortex matter moving in a very thin type II superconducting strip with asymmetrically nanostructured profile. The asymmetric thickness profile generates a geometrical force landscape that sets a preferential direction for vortex motion, resulting in an uncommon voltage-current curve of the strip, with vanishingly small asymmetry in the positive and negative critical currents but appreciably large asymmetry in the voltages. Experimental results as well as the geometrical force affecting the moving vortex matter are discussed in the framework of time dependent Ginzburg-Landau model for superconductors with variable thickness.

References

- [1] G. Carapella, P. Sabatino, and G. Costabile, *Asymmetry, bistability, and vortex dynamics in a finite-geometry ferromagnet-superconductor bilayer structure*. Phys. Rev. B **81**, 054503 (2010).
- [2] P. Sabatino, C. Cirillo, G. Carapella, M. Trezza, and C. Attanasio, *High field vortex matching effects in superconducting Nb thin films with a nanometer-sized square array of antidots*. J. Appl. Phys. **108**, 053906 (2010).
- [3] P. Sabatino, G. Carapella, and G. Costabile, *Magneto-transport properties of curved mesoscopic superconducting strips*. Supercond. Sci. Technol. **24**, 125007 (2011).

-
- [4] G. Carapella, P. Sabatino, and G. Costabile, *A single Abrikosov vortex trapped in a mesoscopic superconducting cylindrical surface*. J. Phys.: Condens. Matter **23**, 435701 (2011).
 - [5] G. Carapella, P. Sabatino, and G. Costabile, *Considerable asymmetry of the critical current in a niobium thin strip of plano-convex section*. J. Appl. Phys. **111**, 053912 (2012).
 - [6] P. Sabatino, G. Carapella, and G. Costabile, *Preferentially directed flux motion in a very thin superconducting strip with nanostructured profile*. (submitted to Phys. Rev. B).

Ginzburg-Landau Model

1.1 Introduction

The Ginzburg-Landau (GL) theory was developed according to Landau's previously established theory of second-order phase transitions based on minimizing the Helmholtz free energy [1,2]. It was published in 1950 but was not widely accepted immediately due to its phenomenological nature. However, in 1959, Gor'kov showed that the macroscopic GL theory was equivalent to the microscopic Bardeen-Cooper-Schrieffer (BCS) theory close to the critical temperature T_c [3]. Due to this work of Gor'kov, the GL theory became widely accepted as a valid macroscopic model for superconductivity.

In the GL model, a superconductor is characterised by a complex-valued order parameter $\psi(\mathbf{r})$ to describe how deep the system is into the superconducting phase. The local density of superconducting charge carriers is represented by $n_s = |\psi(\mathbf{r})|^2$. The need for ψ to be complex is related to the macroscopic quantum nature of superconductivity. The theory postulates that close to the critical temperature T_c , the free energy density can be expanded in a series of the form [1,2,4-6]:

$$\begin{aligned} \mathcal{L}(\psi, \nabla\psi, \mathbf{A}, \nabla \times \mathbf{A}) &= \alpha |\psi|^2 + \frac{1}{2}\beta |\psi|^4 + \frac{\hbar^2}{2m_s} \left| \left(\nabla - i\frac{e_s}{\hbar} \mathbf{A} \right) \psi \right|^2 \\ &\quad + \frac{1}{2\mu_0} |\nabla \times \mathbf{A} - \mu_0 \mathbf{H}|^2 \end{aligned} \quad (1.1)$$

where α and β are phenomenological parameters that depend on external parameters such as temperature, pressure, concentration of impurities, etc., \mathbf{A} denotes the vector potential, so that $\mathbf{B} = \nabla \times \mathbf{A}$ is the magnetic induction, \mathbf{H} is an external magnetic field, $2\pi\hbar$ is Planck's constant, μ_0 is the magnetic permeability of free space, and e_s and m_s are the effective charge and the

effective mass of the superconducting electrons (Cooper pairs), which are usually taken to be twice the electron charge and mass respectively. Below the transition temperature T_c , α becomes negative, whereas $\beta > 0$ for all T . Note that has been used the natural unit $c = 1$, where c is the speed of light in vacuum. In this expression, the first two terms are the Landau expansion of the free energy in powers of $|\psi|^2$ near T_c , that corresponds to the condensation energy of the superconductor in the absence of magnetic field, the term accounting for the spatial variation of the order parameter corresponds to the Gauge invariant kinetic energy of the superconducting electrons, and the last term is the magnetic energy and the magnetic coupling.

1.2 Superconductors in a nutshell

Before we introduce the mathematical model, let us describe some of the basic properties of superconducting materials. The transition from normally conducting (normal) to superconducting is usually associated with a critical temperature T_c , below which the superconductor is able to pass an electric current without an associated electric field, that is, it exhibits *perfect conductivity*. Zero electrical resistivity or equivalently perfect conductivity is the first hallmark of superconductors.

The second hallmark of superconductivity is the *perfect diamagnetism*, i.e., not only a magnetic field is excluded from entering a superconductor, as could be explained by perfect conductivity, but also that a field penetrating a sample is expelled as the sample is cooled below T_c . This phenomenon, on the opposite to perfect conductivity which would trap the field inside, was called *Meissner effect*. There are two types of superconducting materials which are distinguished by their behavior under the influence of a magnetic field.

For type-I superconductors in sufficiently low magnetic fields the material is in the superconducting state, and the field is excluded from the interior of the sample except in thin boundary layers (Meissner effect). However, there is a *critical magnetic field* H_c , above which the material will revert to the normally conducting (normal) state, and the magnetic field will penetrate it fully [see Fig. 1.1].

In type-II superconductors this critical magnetic field splits into a *lower critical field* H_{c1} and an *upper critical field* H_{c2} . For magnetic fields below H_{c1} the material is in the superconducting state and the field is excluded from the interior, while for magnetic fields above H_{c2} the material is in the normal state and the field penetrates it fully [see Fig. 1.1]. For magnetic fields between H_{c1} and H_{c2} a third state exists, known as the “*mixed state*”, in which there is a

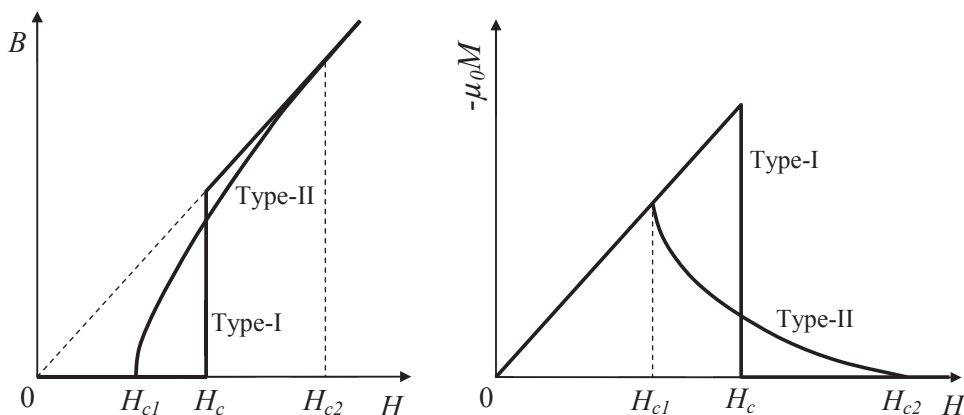


Figure 1.1: Comparison of flux penetration behavior (left) and magnetization (right) curves of type-I and type-II superconductors with the same thermodynamic critical field H_c . [6]

partial penetration of the magnetic field into the superconducting material, which occurs by means of thin filaments of non-superconducting material each carrying a quantum of magnetic flux (“flux tubes”) and circled by a *vortex* of superconducting current (hence these filaments are often referred to as *vortices*). These vortices repel each other since the current circulating around a vortex generates a repulsive Lorentz force on another vortex. If these vortex-vortex repulsive forces are dominant over other forces, then the vortices will form a hexagonal lattice called an *Abrikosov lattice*. When an electrical current is applied to the superconductor, these vortices will move due to the introduction of a Lorentz force by the applied current. The movement of these vortices dissipates energy and thus causes resistivity and destroys superconductivity.

1.3 The Time-Dependent Ginzburg-Landau equations

The state variables (ψ, \mathbf{A}) will minimize the free energy (1.1) in steady state. The minimization conditions can be written as functional derivatives:

$$\frac{\delta \mathcal{L}}{\delta \bar{\psi}} = 0 \quad \text{and} \quad \frac{\delta \mathcal{L}}{\delta \mathbf{A}} = 0$$

where $\bar{\psi}$ is the complex conjugate of ψ . These equations define the time-independent Ginzburg-Landau equations and are nothing but the equations

the Euler-Lagrange equations of the free energy functional (1.1). If we want to describe nonequilibrium systems, we can construct a *relaxational model* using the same free energy:

$$-\gamma \partial_t \psi = \frac{\delta \mathcal{L}}{\delta \bar{\psi}} \quad \text{and} \quad -\Gamma \partial_t \mathbf{A} = \frac{\delta \mathcal{L}}{\delta \mathbf{A}}$$

The leading idea of time-dependent derivations is to consider that the order parameter and the vector potential are driven out of equilibrium and that they will relax with a certain rate that depends on its deviation from equilibrium. If we compute the two functional derivatives, $\delta \mathcal{L}/\delta \bar{\psi}$ and $\delta \mathcal{L}/\delta \mathbf{A}$, we find:

$$-\gamma \partial_t \psi = \alpha \psi + \beta |\psi|^2 \psi - \frac{\hbar^2}{2m_s} \left(\nabla - i \frac{e_s}{\hbar} \mathbf{A} \right)^2 \psi \quad (1.2)$$

$$-\Gamma \partial_t \mathbf{A} = \frac{1}{\mu_0} \nabla \times (\nabla \times \mathbf{A} - \mu_0 \mathbf{H}) - \frac{\hbar e_s}{2m_s i} (\bar{\psi} \nabla \psi - \psi \nabla \bar{\psi}) + \frac{e_s^2}{m_s} |\psi|^2 \mathbf{A} \quad (1.3)$$

In the first equation, describing the motion of the order parameter, if we consider a situation where there are neither currents nor magnetic fields, we can see that in the bulk, where ψ does not vary, it will have the value $\psi_0 = \sqrt{-\alpha/\beta}$. In the second equation, we can identify the term $\nabla \times (\nabla \times \mathbf{A} - \mu_0 \mathbf{H})$ as the total current density generating the local magnetic field. If we notice that a stationary system has $\partial_t \mathbf{A} = 0$, we see the last two terms must constitute the supercurrent.

The equation (1.3) as it stands describes only supercurrent in a sample. Since we are also interested in samples with normal current, we should add an electric field somewhere. If we start from Maxwell's Equations, we know that the total current density is related to the magnetic field by:

$$\nabla \times (\nabla \times \mathbf{A} - \mu_0 \mathbf{H}) = \mu_0 \mathbf{j} = \mu_0 (\mathbf{j}_n + \mathbf{j}_s) \quad (1.4)$$

Distinguishing the current as either normal or superconducting is called the *two-fluid model*. It implies there are distinct populations of normal and superconducting electrons. Comparing Eq. (1.4) with Eq. (1.3), we see the supercurrent density is:

$$\mathbf{j}_s = \frac{\hbar e_s}{2m_s i} (\bar{\psi} \nabla \psi - \psi \nabla \bar{\psi}) - \frac{e_s^2}{m_s} |\psi|^2 \mathbf{A} \quad (1.5)$$

If we want to include a normal current in our model, we can look at replacing $\Gamma \partial_t \mathbf{A}$ with a traditional term of the form $\mathbf{j}_n = \sigma \mathbf{E}$. Maxwell's Equations tell us we can always express the electric field with a scalar potential φ of the form $\mathbf{E} = -\nabla \varphi - \partial_t \mathbf{A}$. Therefore, the normal current density satisfies the generalized Ohm's law:

$$\mathbf{j}_n = \sigma (-\nabla \varphi - \partial_t \mathbf{A}) \quad (1.6)$$

where σ is the electrical conductivity. If we substitute (1.6) into (1.3), assembling the pieces in the form $\mathbf{j} = \mathbf{j}_n + \mathbf{j}_s$, we find:

$$\frac{1}{\mu_0} \nabla \times (\nabla \times \mathbf{A} - \mu_0 \mathbf{H}) = -\sigma (\nabla \varphi - \partial_t \mathbf{A}) + \frac{\hbar e_s}{2m_s i} (\bar{\psi} \nabla \psi - \psi \nabla \bar{\psi}) - \frac{e_s^2}{m_s} |\psi|^2 \mathbf{A}$$

In addition, we have found that Maxwell's Equations determine the coefficient Γ for the relaxation equation for the vector potential.

One can find in the above equation a gauge symmetry whereby the equation is unchanged under transformations of the type

$$\psi \rightarrow \psi e^{i \frac{e_s}{\hbar} \chi} \quad \mathbf{A} \rightarrow \mathbf{A} + \nabla \chi \quad \varphi \rightarrow \varphi - \partial_t \chi$$

In order that both the equation for the magnetic potential and the order parameter be gauge invariant, we should add a gauge-invariant term for φ to Eq. (1.2) to get the *phenomenological* Time-Dependent Ginzburg-Landau (TDGL) equations:

$$\frac{\hbar^2}{2m_s D} \left(\partial_t + i \frac{e_s}{\hbar} \varphi \right) \psi = \frac{\hbar^2}{2m_s} \left(\nabla - i \frac{e_s}{\hbar} \mathbf{A} \right)^2 \psi + |\alpha| \psi - \beta |\psi|^2 \psi \quad \text{in } \Omega \quad (1.7)$$

$$\frac{1}{\mu_0} \nabla \times (\nabla \times \mathbf{A} - \mu_0 \mathbf{H}) = \mathbf{j} = \mathbf{j}_n + \mathbf{j}_s \quad \text{in } \Omega \quad (1.8)$$

with boundary conditions:

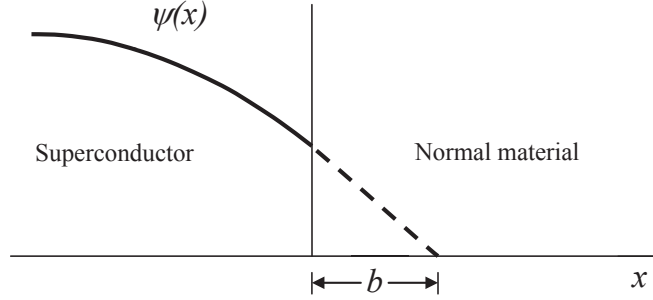
$$\left(\nabla - i \frac{e_s}{\hbar} \mathbf{A} \right) \psi \cdot \mathbf{n} = 0 \quad \text{on } \partial\Omega \quad (1.9)$$

where D is a phenomenological *diffusion constant*, $\Omega \subset \mathbb{R}^2$ or \mathbb{R}^3 denotes the superconducting sample, the boundary of the sample is denoted by $\partial\Omega$ and \mathbf{n} is the outward normal unit to $\partial\Omega$. Note that our insertion of an electric field by hand has effectively switched to proper canonical variables. Equation (1.8) is the Maxwell equation for the magnetic field without the displacement current $\epsilon_0 \dot{\mathbf{E}}$, as it only becomes significant for velocities close to the speed of light. As we will discuss in the Sec. 1.3.3, the TDGL equations derived by Gor'kov and Eliashberg from microscopic theory results only a minor modification (see parameters) of those derived from the simple relaxational dynamics above.

The total current density \mathbf{j} also obeys the continuity equation for the conservation of the charge:

$$\nabla \cdot \mathbf{j} + \frac{\partial \rho}{\partial t} = 0 \quad (1.10)$$

Figure 1.2: Schematic diagram illustrating the boundary condition (1.12) at an interface characterized by an extrapolation length b . [6]



where ρ is the charge density of electrons. As the plasma frequency is much greater than the characteristic frequency of the superconducting electrons, we can neglect the variations in the density of electrons. We obtain the electroneutrality equation:

$$\nabla \cdot \mathbf{j} = 0 \quad (1.11)$$

We use the boundary condition (1.9) for superconductor-vacuum boundaries or superconductor-insulator boundaries [6]. This automatically implies that the supercurrent perpendicular to the boundary vanishes. Indeed, on substituting (1.9) into the equation (1.5) for the supercurrent, we see that $\mathbf{j}_s|_{\partial\Omega} = 0$; that is, there is no supercurrent entering or leaving the superconductor. If we do the inverse, and impose $\mathbf{j}_s = 0$, we do not obtain (1.9), but a more general boundary condition, the so-called de Gennes boundary condition [8]:

$$\left(\nabla - i \frac{e_s}{\hbar} \mathbf{A} \right) \psi \cdot \mathbf{n} = -\frac{1}{b} \psi \quad \text{on } \partial\Omega \quad (1.12)$$

where b is a real parameter derivable from the microscopic theory. As shown in Fig. 1.2, if $\mathbf{A} \cdot \mathbf{n}|_{\partial\Omega} = 0$, b is the *extrapolation length* to the point outside the boundary at which ψ would go to zero if it maintained the slope it had at the surface. The value of b will depend on the nature of the material to which contact is made, approaching zero for a magnetic material and infinity for an insulator, with normal metals lying in between. In practice, if $b > 0$ this is the type of boundary condition encountered for a superconductor-normal metal interface, which will cause superconductivity to be weaker at the edge of the sample (suppressed surface superconductivity) and inducing weak superconductivity in the normal metal (*proximity effect*). The case $b < 0$ enhances superconductivity because it simulates the presence of a material with higher T_c in contact with the superconducting sample. Notice that if we put $b \rightarrow \infty$ in (1.12), then we recover (1.9), i.e. a superconductor-vacuum/insulator interface, which means that no superconducting currents can flow out of the superconductor. If we multiply by b both sides of (1.12) and let $b \rightarrow 0$, then the de Gennes boundary condition (1.12) implies the

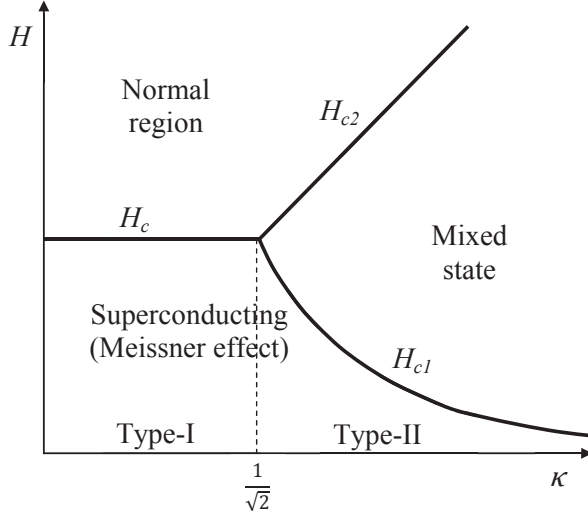


Figure 1.3: *The response of a superconducting material as a function of the applied magnetic field H and the Ginzburg-Landau parameter κ .*

Dirichlet boundary condition $\psi = 0$ on $\partial\Omega$, the case of a superconductor-ferromagnet interface or superconducting surfaces with a high density of defects.

1.3.1 Dimensionless units

We render the TDGL model dimensionless by measuring lengths in units of the *coherence length* $\xi = \hbar/\sqrt{2m_s|\alpha|}$, the characteristic length for the order parameter, time in units of a characteristic *relaxation time* $\tau = \xi^2/D$, the order parameter in $\psi_0 = \sqrt{|\alpha|/\beta}$, the vector potential in $A_0 = \sqrt{2}\kappa H_c \xi$, where $H_c = \mu_0 |\alpha|^2/\beta$ is the *thermodynamic critical field*, the electric potential in $\varphi_0 = (\xi/\tau)A_0$, and conductivity in units of the normal state conductivity $\sigma_0 = 1/\kappa^2 D \mu_0$. The so-called *Ginzburg-Landau parameter* is given by $\kappa^2 = 2m_s^2 \beta/e_s^2 \hbar^2 \mu_0$. The characteristic length scale for variations of the magnetic field is the *London penetration depth* $\lambda = \kappa \xi$, and $\nabla \times \mathbf{A}$ measures the magnetic field in units of $H_{c2} = \sqrt{2}\kappa H_c$. In scaled units the TDGL Eqs. (1.7) and (1.8) become:

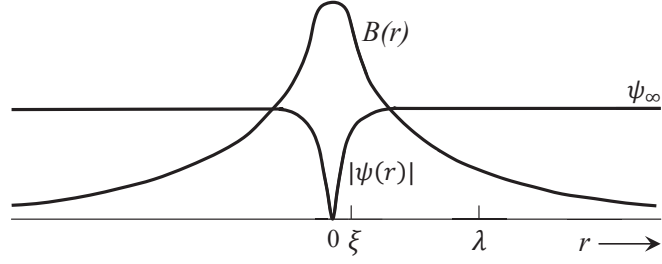
$$(\partial_t + i\varphi)\psi = (\nabla - i\mathbf{A})^2\psi + (1 - |\psi|^2)\psi \quad (1.13)$$

$$\kappa^2 \nabla \times \nabla \times \mathbf{A} = \underbrace{|\psi|^2 (\nabla \vartheta - \mathbf{A})}_{\mathbf{j}_s} + \underbrace{\sigma (-\nabla \varphi - \partial_t \mathbf{A})}_{\mathbf{j}_n} + \underbrace{\kappa^2 \nabla \times \mathbf{H}}_{\mathbf{j}_{ext}} \quad (1.14)$$

where ϑ denotes the phase of ψ , if ψ is written as $|\psi| e^{i\vartheta}$, so that

$$|\psi|^2 \nabla \vartheta = (\bar{\psi} \nabla \psi - \psi \nabla \bar{\psi})/2i. \quad (1.15)$$

Figure 1.4: *Structure of an isolated Abrikosov vortex in a material with $\kappa \approx 8$. The maximum value of $B(r)$ is approximately $2H_{c1}$. [6]*



with boundary conditions:

$$(\nabla - i\mathbf{A})\psi \cdot \mathbf{n}|_{\partial\Omega} = 0 \quad (1.16)$$

The last term in Eq. (1.14) can be used to model external fields or magnetic impurities in the material. In dimensionless units, the dynamics of the superconductor depends only on the dimensionless parameter σ and κ . For values $\kappa < 1/\sqrt{2}$ one finds a behaviour characteristic of a type-I superconductor whereas for $\kappa > 1/\sqrt{2}$ a type-II superconductor is modelled [see Fig. (1.3)].

In the case of type-II superconductor ($\kappa > 1$, $\lambda > \xi$) in the mixed state, a vortex has a “core” of the size ξ , where the order parameter varies rapidly, and the outer region of the size λ where the magnetic field decays to zero. $|\psi(r)|$ vanishes at the center and in the vicinity of the vortex axis the order parameter grows linearly with distance. Beyond distances of the order of ξ the order parameter approaches the equilibrium value at zero field. The vortex core is surrounded by persistent currents which, together with the magnetic field, decay away from the vortex core at distances of the order of λ . The overall shape of the behaviour of the order parameter and magnetic field in a vortex is presented in Fig. 1.4.

1.3.2 Gauge transformation

The TDGL equations contain the vector potential \mathbf{A} . But it is well-known that the choice of \mathbf{A} is not unique. Indeed, the dynamics of the measurable quantities \mathbf{E} , \mathbf{B} , $|\psi|^2$, and \mathbf{j} are invariant under the transformation [7]:

$$\begin{cases} \mathbf{A} \rightarrow \mathbf{A} + \nabla\Lambda \\ \psi \rightarrow \psi e^{i\Lambda} \\ \varphi \rightarrow \varphi - \partial_t\Lambda \end{cases} \quad (1.17)$$

where Λ is an arbitrary scalar field. It is clear that for the TDGL model, we must choose a suitable gauge to fix the non-uniqueness of the solution. Therefore extra constraints on the TDGL equation are needed. We choose

the *zero potential gauge* setting $\partial_t \Lambda(\mathbf{r}, t) = \varphi(\mathbf{r}, t)$, in other words from the last transformation $\varphi(\mathbf{r}) \equiv 0$ at all times. For this choice, Eqs. (1.13) and (1.14) become:

$$\partial_t \psi = (\nabla - i\mathbf{A})^2 \psi + (1 - |\psi|^2) \psi \quad (1.18)$$

$$\sigma \partial_t \mathbf{A} = |\psi|^2 (\nabla \vartheta - \mathbf{A}) - \kappa^2 \nabla \times (\nabla \times \mathbf{A} - \mathbf{H}) \quad (1.19)$$

The use of any gauge changes the problem into a well-posed problem; thus, our problem now has a unique solution which is needed in order to utilize numerical computations. Note that although the scalar potential no longer appears explicitly in the equations, a normal current still arises through the time dependence of the vector potential, as apparent from Eq. (1.6).

1.3.3 Microscopic derivations

The TDGL equations were also derived from the microscopic BCS theory [8] in the case of so-called gapless superconductors, where pair breaking interactions are so strong that the energy gap vanishes from the excitation spectrum [9], or in the case of dirty superconductors with a finite gap [10]:

$$u (\partial_t + i\varphi) \psi = (\nabla - i\mathbf{A})^2 \psi + (1 - T - |\psi|^2) \psi \quad (1.20)$$

$$\partial_t \mathbf{A} = \frac{1}{2i} (\bar{\psi} \nabla \psi - \psi \nabla \bar{\psi}) - |\psi|^2 \mathbf{A} - \kappa^2 \nabla \times (\nabla \times \mathbf{A} - \mathbf{H}) \quad (1.21)$$

Here T is the temperature and the coefficient $u = 5.79$ governs the relaxation of the order parameter ψ . All physical quantities are measured in dimensionless units: the lengths are in units of the *coherence length* $\xi(0) = \sqrt{\pi \hbar D / 8 k_B T_c}$, with T_c the *critical temperature*, k_B the Boltzmann constant and D is the *diffusion constant*. Time is measured in units of the *relaxation time* $\tau(0) = 4\pi \sigma_n \lambda(0)^2 / c^2 = \xi_0^2 / Du$ (σ_n is the *normal-state conductivity*, $\lambda(0) = \kappa \xi(0)$ the magnetic field *penetration depth*, with κ the *Ginzburg-Landau parameter*). The order parameter is in units of $\Delta(0) = 4k_B T_c \sqrt{u} / \pi$, i.e., the *superconducting gap* at $T = 0$ which follows from Gor'kov's derivation of the Ginzburg-Landau equations. The vector potential is measured in units $\Phi_0 / 2\pi \xi(0)$ ($\Phi_0 = ch/2e$ is the *quantum of magnetic flux*) and the electrostatic potential is in units of $\varphi(0) = \hbar / 2e\tau(0)$. In these units the magnetic field is scaled with $H_{c2}(0) = \Phi_0 / 2\pi \xi(0)^2$ and the current density with $j_0(0) = c\Phi_0 / 8\pi^2 \lambda(0)^2 \xi(0)$. This normalization is relative to the variables at $T = 0$. This results in the explicit inclusion of normalized temperature T in the first equation [3, 9]. Both Δ and ξ are temperature dependent. In the temperature interval close to T_c , the norm of order parameter $\Delta(T) = \Delta_0 \sqrt{1 - T/T_c}$, the coherence length $\xi_{GL}(T) = \xi_0 / \sqrt{1 - T/T_c}$ and

the penetration depth $\lambda_{GL}(T) = \lambda_0/\sqrt{1-T/T_c}$. Throughout the rest of this work we will always refer to the Eqs. (1.20) and (1.21) derived from the microscopic theory as the TDGL equations.

1.3.4 High- κ , High-Field model

Since high- T_c superconductors or type-II superconductors with some concentration of impurities are known to have large κ values ($\kappa \gg 1$), the high- κ limit of the TDGL equations has been studied in various works [6, 11–14]. Compared to type-I superconductors, larger magnetic fields can be sustained in type-II materials before the material falls back to a normal state. Thus, this high κ valued model includes both of these properties:

- models the Time-Dependent G-L Equations as $\kappa \rightarrow \infty$
- models high applied magnetic fields \mathbf{H} .

In order to model this *high kappa* behavior, the TDGL equations were simplified in the limit of large values of κ and high applied magnetic fields: the so-called High- κ High-Field (HKHF) model. Formally, one expands the variables ψ , φ , \mathbf{A} , \mathbf{H} in terms of $1/\kappa^2$ and after substituting these expansions into the non-dimensional TDGL Equations (1.20)-(1.21), the resulting leading-order system is:

$$u(\partial_t + \imath\varphi)\psi = (\nabla - \imath\mathbf{A})^2\psi + (1 - T - |\psi|^2)\psi \quad (1.22)$$

$$\partial_t\mathbf{A} + \nabla \times (\nabla \times \mathbf{A} - \mathbf{H}) = 0 \quad (1.23)$$

We note that the first Equation (1.20) remains unchanged. Instead, Equation (1.23) relaxes to $\nabla \times \mathbf{A} = \mathbf{H}$ and simply describe the magnetic potential of the normal state, i.e. where $\psi \equiv 0$. Once \mathbf{A} has been solved by using this Equation, then Equation (1.22) involving ψ can be used to solve for ψ at each time step. Thus, the leading order system resulting from the expansion in terms of $1/\kappa^2$ decouples the variables \mathbf{A} and ψ . The resulting simplified leading-order system is a nonlinear equation for ψ , that needs to be solved at each time step with the known value of \mathbf{A} which only needs to be computed at the initial time step. Both boundedness and uniqueness results are shown in [13] as well as convergence results for this high kappa model as $\kappa \rightarrow \infty$.

Therefore, when we consider extreme type-II superconductors, i.e., $\kappa \gg 1$, the demagnetization effects can be neglected and instead of solving either Eqs. (1.22) and (1.23), we solved only the first equation (1.22), supplemented with the equation for the electrostatic potential [15–19]:

$$\nabla^2\varphi = \text{div} \{ \text{Im} [\bar{\psi} (\nabla - i\mathbf{A}) \psi] \} \quad (1.24)$$

The latter is nothing else than the condition (1.11) for the conservation of the total current in the sample, i.e., $\nabla \cdot \mathbf{j} = 0$, where $\mathbf{j} = \mathbf{j}_n + \mathbf{j}_s$ with Eqs. (1.5) and (1.6). In Eqs. (1.22) and (1.24) all the physical quantities are measured in dimensionless units as mentioned in Section 1.3.3. Simplified model (1.22), (1.24) can also be used in the “mesoscopic” regime, i.e., in the limit of a thin, narrow film, when the thickness is less than the coherence length ($d \leq \xi$), and the width is less than the effective penetration depth ($W \leq 2\lambda$). If the sample size becomes comparable to superconducting penetration depth λ and/or coherence length ξ , the vortex-surface interactions (confinement forces due to the superconductor boundaries) can become comparable to the inter-vortex interaction and the local flux density becomes intrinsically dependent on sample geometry, both shape and size. Indeed, in such regime, the vortices configuration is highly affected by sample geometry, differing from the Abrikosov lattice, which is the lowest energy state for ideal macroscopic samples. The critical superconducting current density also can be largely enhanced for samples of small size comparable to the coherence length and the London penetration length. Moreover, for a very thin superconducting film of thickness less than ξ , the vortex state may be present even in a type-I superconductor. Therefore, even type-I materials will exhibit vortex configurations when they are in the form of a thin film.

1.3.5 TDGL model with applied field and current

We now see how to introduce the magnetic field and the bias current both in the general model of Sec. 1.3.3 that in the simplified one of Sec. 1.3.4. First consider the TDGL equations (1.20) and (1.21) in the *zero potential gauge* [$\varphi(\mathbf{r}) \equiv 0$ at all times]. Typically, we apply an uniform magnetic field directed along a given axis, e.g., the z -axis, $\mathbf{H} = (0, 0, H)$, and an uniform transport current along a different axis, e.g., the y -axis, $\mathbf{J} = (0, J, 0)$. For a homogeneous field is $\nabla \times \mathbf{H} = 0$ and vanishes from the second equation, therefore the applied magnetic field only appears in the boundary condition of the vector potential. This condition is chosen such that magnetic induction field $\mathbf{B} = \nabla \times \mathbf{A}$ on the boundary of the outside space region (denoted by $\partial\bar{\Omega}$) goes to the applied field \mathbf{H} , when the outer boundary is chosen reasonably far from the superconductor, meaning that screening current does not modify sensibly the applied field at large distances from the superconductor. When also a transport current is present, we add to the applied magnetic field \mathbf{H} also the field \mathbf{H}_J induced by the bias density current \mathbf{J} [4], calculated using the Biot–Savart law:

$$\mathbf{H}_J(\mathbf{r}) = \frac{1}{4\pi\kappa^2} \int_{\Omega} \mathbf{J}(\mathbf{r}') \times \frac{\mathbf{r} - \mathbf{r}'}{|\mathbf{r} - \mathbf{r}'|^3} d^3r'$$

For an uniform bias density current, \mathbf{J} can be taken out of the integral sign, whereby the above integration can be carried out just once because only depends from the system geometry (superconducting region Ω). In the mesoscopic regime, it is usually used the simpler form $H_J = JW/2k^2$. Mathematically, the complete condition is written as $(\nabla \times \mathbf{A})|_{\partial\Omega} = \mathbf{H} + \mathbf{H}_J$. The second equation (1.21) supplied by the previous boundary condition allows to calculate the time evolution of the vector potential \mathbf{A} , and from it the other related physical quantities, e.g., the magnetic induction field $\mathbf{B} = \nabla \times \mathbf{A}$ and the magnetization $\mu_0 \mathbf{M} = \mathbf{B} - \mu_0 \mathbf{H}$ (or $4\pi \mathbf{M} = \mathbf{B} - \mathbf{H}$ in Gaussian units). Their mean values are obtained by spatial and temporal integration and averaging on the whole superconducting region Ω , e.g., the mean value of the magnetic induction field, if we denote by $\overline{\mathbf{B}}$ the time average and $\langle \mathbf{B} \rangle$ the spatial average, results:

$$\langle \overline{\mathbf{B}} \rangle = \frac{1}{\Delta t \int_{\Omega} d^3r} \int_{\Delta t} \int_{\Omega} \mathbf{B}(\mathbf{r}, t) d^3r dt$$

Since in the general model the scalar potential φ is chosen equal to zero, we can calculate the electric field \mathbf{E} using the relationship $\mathbf{E} = -\partial_t \mathbf{A}$. When calculating the mean value of \mathbf{E} to build up the characteristic $E(J)$ curves, we take the spatially and time averaged of electric field inside the superconducting region, at distance of few ξ away from the current injection interface. In this way the contact resistance at the interface is not taken into account and our results simulate a four-probe measurement.

We consider now the HKHF model described by the equations (1.22) and (1.24). In this case, we consider extreme type-II superconductors ($\kappa \gg 1$), therefore, neglecting the demagnetization effects, the magnetic induction field \mathbf{B} is nearly the same as the external magnetic field \mathbf{H} . In fact, in both model equations we put the vector potential \mathbf{A} which describes the external field. For example, suppose an uniform magnetic field $\mathbf{H} = (0, 0, H)$, we can set $\mathbf{A} = H(-y/2, x/2, 0)$ or $\mathbf{A} = H(0, x, 0)$. Another example we used in this work is the vector potential of the stray fields of a continuous Py film in the stripe domain regime [see Eqs. (3.3) and (3.4)]. In Chapters 5 and 6 we also defined the vector potential of curved mesoscopic superconducting strips. Moreover, the current density not explicitly appears in the HKHF equations, therefore it can only be used in the boundary condition of the scalar potential. For an uniform bias current density \mathbf{J} , we use the condition $-\nabla\varphi = \mathbf{J}$ at the injection interface as boundary condition of the second equation (1.24). As regards the physical quantities estimated in this model, when calculating the mean value of electric field E to build up the $E(J)$ curves, we take the spatially and time averaged of the electrostatic potential

difference inside the superconducting sample, at distance of few ξ away from the boundary, as in the general model.

1.4 Numerical method

The most popular approach to the solution of the TDGL equations (1.18) and (1.19), is a gauge-invariant discretization that is second-order accurate in space and first order in time [20–24]. In addition, a number of other finite-difference and finite-element methods have been developed [12, 25–29]. For large values of κ , the magnetic field is nearly homogeneous and Eq. (1.19) can be dropped, as discussed in Section 1.3.4. This case is often referred to as the London limit. The remaining equation (1.24) has been solved by Fourier method which is second-order accurate in time. An equation very similar to Eq. (1.18), the Gross-Pitaevskii equation, is used to model vortex dynamics in dilute Bose-Einstein condensates. In the following section is described the numerical method used to find an approximate solution to previous equations.

1.4.1 The $U - \psi$ Method

The widely used $U - \psi$ method is described in detail by Gropp et al. [20]. As this method forms the basis of algorithm used in numerical simulations, we briefly review the main points here. Complex link variables U^x , U^y , and U^z are introduced to preserve the gauge-invariant properties of the discretized equations:

$$\begin{aligned} U^x(x, y, z; t) &= \exp\left(-i \int_{x_0}^x A^x(x', y, z; t) dx'\right) \\ U^y(x, y, z; t) &= \exp\left(-i \int_{y_0}^y A^y(x, y', z; t) dy'\right) \\ U^z(x, y, z; t) &= \exp\left(-i \int_{z_0}^z A^z(x, y, z'; t) dz'\right) \end{aligned} \quad (1.25)$$

where (x_0, y_0, z_0) is an arbitrary reference point. The TDGL equations can then be expressed as functions of ψ and these link variables. Both the order parameter and the link variables are discretized on a three-dimensional grid with grid spacing h_x , h_y , and h_z , respectively. The mesh points for the link variables are halfway between the mesh points for the order parameter [see Fig. 1.5]. All spatial derivatives are approximated by finite differences to second-order accuracy. Denoting the complex conjugate of U by \bar{U} , the

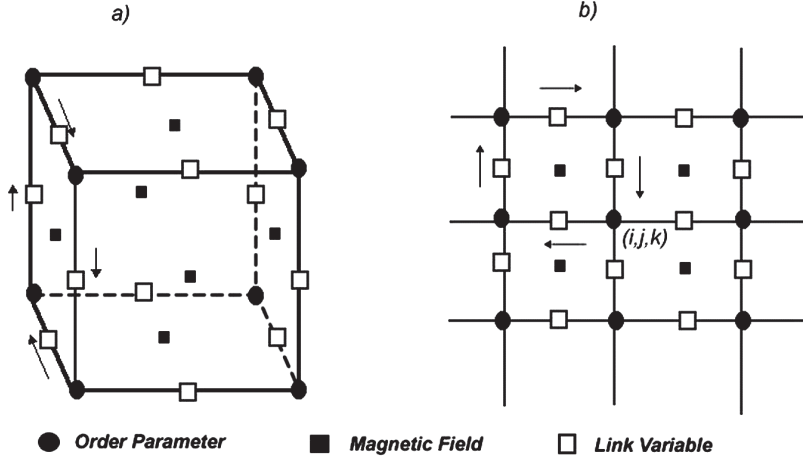


Figure 1.5: Scheme of computational cells defining the numbering of discrete variables. a) 3D scheme; b) 2D scheme. The order parameter is defined at each corner, the link variables are defined on the edges at the midpoint, and the loop variables are defined on an elementary square cell.

finite-difference representations of the TDGL equations read:

$$\begin{aligned}
\partial_t \psi_{i,j,k} &= \frac{\bar{U}_{i-1,j,k}^x \psi_{i-1,j,k} - 2\psi_{i,j,k} + U_{i,j,k}^x \psi_{i+1,j,k}}{h_x^2} \\
&+ \frac{\bar{U}_{i,j-1,k}^y \psi_{i,j-1,k} - 2\psi_{i,j,k} + U_{i,j,k}^y \psi_{i,j+1,k}}{h_y^2} \\
&+ \frac{\bar{U}_{i,j,k-1}^z \psi_{i,j,k-1} - 2\psi_{i,j,k} + U_{i,j,k}^z \psi_{i,j,k+1}}{h_z^2} \\
&+ (1 - |\psi_{i,j,k}|^2) \psi_{i,j,k}
\end{aligned} \tag{1.26}$$

$$\partial_t U_{i,j,k}^x = -i \operatorname{Im}(\mathcal{F}_{i,j,k}^x) U_{i,j,k}^x \tag{1.27}$$

where

$$\begin{aligned}
\mathcal{F}_{i,j,k}^x &= \kappa^2 \frac{\bar{U}_{i,j+1,k}^x \bar{U}_{i,j,k}^y U_{i,j,k}^x U_{i+1,j,k}^y - \bar{U}_{i,j,k}^x \bar{U}_{i,j-1,k}^y U_{i,j-1,k}^x U_{i+1,j-1,k}^y}{h_y^2} \\
&+ \kappa^2 \frac{\bar{U}_{i+1,j,k-1}^z \bar{U}_{i,j,k-1}^x U_{i,j,k-1}^z U_{i,j,k}^x - \bar{U}_{i+1,j,k}^z \bar{U}_{i,j,k}^x U_{i,j,k}^z U_{i,j,k+1}^x}{h_y^2} \\
&+ U_{i,j,k}^x \bar{\psi}_{i,j,k} \psi_{i+1,j,k}.
\end{aligned}$$

Analogous expressions for $\partial_t U_{i,j,k}^y$ and $\partial_t U_{i,j,k}^z$ can be obtained by permutating the coordinates and indices as follows:

$$(x, y, z; i, j, k) \rightarrow (y, z, x; j, k, i) \rightarrow (z, x, y; k, i, j) \rightarrow (x, y, z; i, j, k). \tag{1.28}$$

We now introduce another three auxiliary variables which are related to the magnetic field [20]:

$$\begin{aligned} W_{i,j,k}^x &= \bar{U}_{i,j,k+1}^y \bar{U}_{i,j,k}^z U_{i,j,k}^y U_{i,j+1,k}^z \\ W_{i,j,k}^y &= \bar{U}_{i+1,j,k}^z \bar{U}_{i,j,k}^x U_{i,j,k}^z U_{i,j,k+1}^x \\ W_{i,j,k}^z &= \bar{U}_{i,j+1,k}^x \bar{U}_{i,j,k}^y U_{i,j,k}^x U_{i+1,j,k}^y \end{aligned} \quad (1.29)$$

Note that these variables are the basic terms of the $\mathcal{F}_{i,j,k}^x$. From Stock's theorem, we know:

$$\begin{aligned} W_{i,j,k}^x &= \exp(-ih_y h_z B_{i,j,k}^x) \\ W_{i,j,k}^y &= \exp(-ih_x h_z B_{i,j,k}^y) \\ W_{i,j,k}^z &= \exp(-ih_x h_y B_{i,j,k}^z) \end{aligned} \quad (1.30)$$

The loop variables $W_{i,j,k}^x$, $W_{i,j,k}^y$ and $W_{i,j,k}^z$ are directly related to the magnetic field.

The our lattice structure actually involves an order parameter lattice, a magnetic field lattice with position shifted to each other [see Fig. 1.5]. The time evolution is approximated by a simple Euler step:

$$\psi_{i,j,k}(t + \Delta t) = \psi_{i,j,k}(t) + \Delta t \partial_t \psi_{i,j,k}(t) + \mathcal{O}(\Delta t^2) \quad (1.31)$$

$$U_{i,j,k}^x(t + \Delta t) = U_{i,j,k}^x(t) + \Delta t \partial_t U_{i,j,k}^x(t) + \mathcal{O}(\Delta t^2) \quad (1.32)$$

To keep $U_{i,j,k}^x$ unimodular, Eq. (1.32) is often modified to:

$$U_{i,j,k}^x(t + \Delta t) = U_{i,j,k}^x(t) \exp(-i \Delta t \text{Im} \mathcal{F}_{i,j,k}^x) + \mathcal{O}(\Delta t^2) \quad (1.33)$$

The Euler method is only first-order accurate in time, i.e., the truncation error made due to the finite-difference approximation of the time derivative is proportional to Δt^2 . However, the main problem is that the code becomes unstable if long time steps are used. The cause of this instability is the diffusionlike character of the dynamics described by Eqs. (1.26) and (1.27). Equation (1.26) can immediately be written as a diffusion equation with an additional nonlinear term:

$$\partial_t \psi_{i,j,k} = L_x \psi_{i,j,k} + L_y \psi_{i,j,k} + L_z \psi_{i,j,k} + f \quad (1.34)$$

where f stands for $(1 - |\psi_{i,j,k}|^2) \psi_{i,j,k}$ and L_x , L_y , and L_z denote the *weighted* Laplacian operators:

$$L_x \psi_{i,j,k} = \frac{a_{i-1} \psi_{i-1,j,k} - 2\psi_{i,j,k} + a_{i+1} \psi_{i+1,j,k}}{h_x^2} \quad (1.35)$$

with $|a_{i-1}| = |a_{i+1}| = 1$ in our case. The diffusion constant is 1 in dimensionless units. Equation (1.27) is also dominated by diffusive terms, as becomes

evident in the next section. Setting $\sigma = 1$, the diffusion constant for the vector potential is κ^2 . This can be seen by taking the curl of Eq. (1.19), $\dot{\mathbf{B}} = \kappa^2 \nabla^2 B + \nabla \times \mathbf{j}_s$. The one-step forward Euler method is only stable as long as the time step is shorter than the diffusion time across a cell of width h [30]. For example, using a grid spacing of $h = 0.5\xi$ and $\kappa = 5$, the theoretical limit for the time step is:

$$\Delta t < \frac{h}{2\kappa^2} = \frac{0.5^2}{2 \cdot 5^2} = 0.005 \quad (1.36)$$

In practice, a time step of $\Delta t = 0.002$ is used to ensure stability [20]. In contrast, a semi-implicit two-step algorithm is unconditionally stable for diffusive problems and enables much larger time steps to be employed [4].

1.4.2 Simplified algorithm

In this section is proposed a spatial discretization of the equations very similar to the above $U - \psi$ method. The link variables are unimodular, $|U_{i,j,k}^x| = 1$, and can be written as the exponential of a phase, $U_{i,j,k}^x = \exp(-\imath\phi_{i,j,k}^x)$. We use the real-valued variable ϕ^x instead of the complex-valued U^x . The fields ψ and ϕ are represented on a three-dimensional grid. The mesh points of the phase factors are placed between the mesh points of the order parameter [see Fig. 1.6]. For the field $\psi_{i,j,k}$, the grid point indices are $i = 1, \dots, N_x + 1$, $j = 1, \dots, N_y + 1$, and $k = 1, \dots, N_z + 1$. For $\phi_{i,j,k}^x$, the indices in the x direction are in the range $i = 1, \dots, N_x$ only, due to the relative displacement of the grids. Similarly, $j = 1, \dots, N_y$ for $\phi_{i,j,k}^y$ and $k = 1, \dots, N_z$ for $\phi_{i,j,k}^z$.

We now discretize the spatial derivatives in Eqs. (1.18) and (1.19) using the modified link variables ϕ^x , ϕ^y , and ϕ^z . For Eq. (1.18), we reuse the expansion (1.26) except that we replace $U_{i,j,k}^x$ with $\exp(-\imath\phi_{i,j,k}^x)$, and so forth:

$$\begin{aligned} \partial_t \psi_{i,j,k} &= \frac{\exp(\imath\phi_{i-1,j,k}^x)\psi_{i-1,j,k} - 2\psi_{i,j,k} + \exp(-\imath\phi_{i,j,k}^x)\psi_{i+1,j,k}}{h_x^2} \\ &+ \frac{\exp(\imath\phi_{i,j-1,k}^y)\psi_{i,j-1,k} - 2\psi_{i,j,k} + \exp(-\imath\phi_{i,j,k}^y)\psi_{i,j+1,k}}{h_y^2} \\ &+ \frac{\exp(\imath\phi_{i,j,k-1}^z)\psi_{i,j,k-1} - 2\psi_{i,j,k} + \exp(-\imath\phi_{i,j,k}^z)\psi_{i,j,k+1}}{h_z^2} \\ &+ (1 - |\psi_{i,j,k}|^2)\psi_{i,j,k} \end{aligned} \quad (1.37)$$

With the help of the relation $-\nabla \times \nabla \times \mathbf{A} = \nabla^2 \mathbf{A} - \nabla(\nabla \cdot \mathbf{A})$, the second-

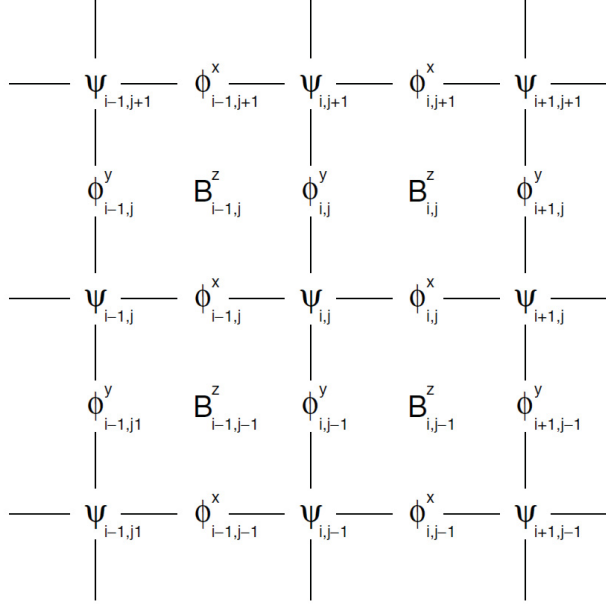


Figure 1.6: The evaluation points for the fields ψ and ϕ in the $x - y$ plane. A finite-difference approximation for the magnetic field B_z is given in (1.43).

order-accurate finite-difference representation of (1.19) is:

$$\begin{aligned}
\partial_t \phi_{i,j,k}^x &= \frac{\kappa^2}{h_y^2} (\phi_{i,j+1,k}^x - 2\phi_{i,j,k}^x + \phi_{i,j-1,k}^x) + \frac{\kappa^2}{h_z^2} (\phi_{i,j,k+1}^x - 2\phi_{i,j,k}^x + \phi_{i,j,k-1}^x) \\
&+ \frac{\kappa^2}{h_y^2} (-\phi_{i+1,j,k}^y + \phi_{i,j,k}^y + \phi_{i+1,j-1,k}^y - \phi_{i,j-1,k}^y) \\
&+ \frac{\kappa^2}{h_z^2} (-\phi_{i+1,j,k}^z + \phi_{i,j,k}^z + \phi_{i+1,j,k-1}^z - \phi_{i,j,k-1}^z) \\
&+ \text{Im}(\exp(-i\phi_{i,j,k}^x) \bar{\psi}_{i,j,k} \psi_{i+1,j,k})
\end{aligned} \tag{1.38}$$

The expressions for $\partial_t \phi_{i,j,k}^y$ and $\partial_t \phi_{i,j,k}^z$ are given by cyclic permutation (1.28).

Note that the discretized equations are still invariant under the gauge transformation:

$$\begin{cases} \psi_{i,j,k} \rightarrow \psi_{i,j,k} \exp(i\Lambda_{i,j,k}) \\ \phi_{i,j,k}^x \rightarrow \phi_{i,j,k}^x + (\Lambda_{i+1,j,k} - \Lambda_{i,j,k}) \\ \phi_{i,j,k}^y \rightarrow \phi_{i,j,k}^y + (\Lambda_{i,j+1,k} - \Lambda_{i,j,k}) \\ \phi_{i,j,k}^z \rightarrow \phi_{i,j,k}^z + (\Lambda_{i,j,k+1} - \Lambda_{i,j,k}) \end{cases} \tag{1.39}$$

Retaining the gauge invariance at the discrete level is often equivalent to preserving certain conservation laws and physical principles. It is crucial that the numerical approximation not depend on the particular choice of

gauge. If, for example, one studies the motion of a vortex lattice due to an applied electric field E_x , the measurable quantities \mathbf{B} , $|\psi|^2$, and \mathbf{j} oscillate in time [5]. The system is driven through a series of equivalent solutions and the dynamics is roughly described by $\Lambda = E_x x t$. This means that the phase gradients in the order parameter build up in time and the phase difference between two neighbouring grid points eventually exceeds 2π . This is normally a problem as the finite-difference approximation becomes invalid. However, using the link variables U or ϕ these phase gradients are exactly cancelled by the change in the vector potential.

As mentioned above, the diffusive character of Eq. (1.19) becomes apparent in the new discretization and both Eq. (1.37) and Eq. (1.38) can be written as an initial value problem of the form:

$$\partial_t g_{i,j,k} = D(L_x g_{i,j,k} + L_y g_{i,j,k} + L_z g_{i,j,k}) + f \quad (1.40)$$

where g stands for the fields ψ or ϕ^x , ϕ^y or ϕ^z , respectively, D is the diffusion constant with $D = \kappa^2$ in (1.38), and f indicates all the other terms: $(1 - |\psi_{i,j,k}|^2)\psi_{i,j,k}$ in (1.37) and the last three lines in Eq. (1.38). Note that $L_x \equiv 0$ in (1.38).

The $\phi - \psi$ method is less memory intensive than the standard $U - \psi$ method because it uses real-valued link variables rather than complex-valued ones that must be represented by two real numbers. For a grid of N^3 points, the standard $U - \psi$ method uses an equivalent of $16N^3$ real-valued variables (the complex wavefunction and the three complex link variables at two time levels; see [20]) whereas the $\phi - \psi$ method requires the storage of a total of $10N^3$ variables (the complex wavefunction and the three real link variables at two time levels).

1.4.3 Boundary conditions

The boundary conditions depend on the geometry of the problem. Suppose we choose a system with a periodic boundary condition in the y direction. At the interfaces in the x and the z directions, boundary conditions for the magnetic field and the order parameter are applied. For the order parameter $\psi_{i,j,k}$, conditions are needed for all values at the faces of the three-dimensional box. The grid representation of the periodic boundary condition reads:

$$\begin{aligned} \psi_{i,1,k} &= \psi_{i,N_y,k}, & \psi_{i,N_y+1,k} &= \psi_{i,2,k}, \\ \phi_{i,1,k}^x &= \phi_{i,N_y,k}^x, & \phi_{i,N_y+1,k}^x &= \phi_{i,2,k}^x, \\ \phi_{i,1,k}^z &= \phi_{i,N_y,k}^z, & \phi_{i,N_y+1,k}^z &= \phi_{i,2,k}^z. \end{aligned} \quad (1.41)$$

In the x and z directions we set the supercurrent across the boundary to zero [20], i.e.:

$$\begin{aligned}\psi_{1,j,k} &= \psi_{2,j,k} \exp(-i\phi_{1,j,k}^x), \\ \psi_{N_x+1,j,k} &= \psi_{N_x,j,k} \exp(i\phi_{N_x,j,k}^x), \\ \psi_{i,j,1} &= \psi_{i,j,2} \exp(-i\phi_{i,j,1}^z), \\ \psi_{i,j,N_z+1} &= \psi_{i,j,N_z} \exp(i\phi_{i,j,N_z}^z).\end{aligned}\tag{1.42}$$

Expressions for the endpoints of the link variables can be found by incorporating information about the magnetic field at the boundaries of the box. Using the Eqs. (1.29) and (1.30), the three components of the magnetic field are given by the following second-order finite-difference approximations:

$$\begin{aligned}B_{i,j,k}^x &= \frac{1}{h_y h_z} (\phi_{i,j,k}^y - \phi_{i,j,k+1}^y - \phi_{i,j,k}^z + \phi_{i,j+1,k}^z) \\ B_{i,j,k}^y &= \frac{1}{h_z h_x} (\phi_{i,j,k}^z - \phi_{i+1,j,k}^z - \phi_{i,j,k}^x + \phi_{i,j,k+1}^x) \\ B_{i,j,k}^z &= \frac{1}{h_x h_y} (\phi_{i,j,k}^x - \phi_{i,j+1,k}^x - \phi_{i,j,k}^y + \phi_{i+1,j,k}^y)\end{aligned}\tag{1.43}$$

From these expressions, appropriate boundary conditions can be obtained. For example, the field $\phi_{i,j,k}^y$ is unknown at $i = 1$ and $i = N_x$, and we use the last equation to relate the values of $\phi_{1,j,k}^y$ and $\phi_{N_x,j,k}^y$ to known values using the z -component of magnetic field:

$$\begin{aligned}\phi_{1,j,k}^y &= -B_{1,j,k}^z h_x h_y + \phi_{2,j,k}^y + \phi_{1,j,k}^x - \phi_{1,j+1,k}^x \\ \phi_{N_x+1,j,k}^y &= B_{N_x,j,k}^z h_x h_y + \phi_{N_x,j,k}^y + \phi_{N_x,j+1,k}^x - \phi_{N_x,j,k}^x\end{aligned}\tag{1.44}$$

Likewise, using the x -component of magnetic field and the first equation:

$$\begin{aligned}\phi_{i,j,1}^y &= B_{i,j,1}^x h_y h_z + \phi_{i,j,2}^y + \phi_{i,j,1}^z - \phi_{i,j+1,1}^z \\ \phi_{i,j,N_z+1}^y &= -B_{i,j,N_z}^x h_y h_z + \phi_{i,j,N_z}^y + \phi_{i,j+1,N_z}^z - \phi_{i,j,N_z}^z\end{aligned}\tag{1.45}$$

Equations (1.37) and (1.38), combined with the boundary conditions (1.41), (1.42), (1.44) and (1.45) provide all the information needed to solve a three-dimensional problem.

1.4.4 Hardware and Software Platform

The platform we have used for all numerical simulations runs the Microsoft Windows 7 Ultimate (x64) Build 7601 Operating System (OS). It uses an Intel Core i7-940 CPU running at 2.93 GHz installed on ASUS P6T DELUXE V2 motherboard, with 12 GB of DDR3-1333 system memory at 667 MHz in

Triple-Channel mode, an nVIDIA GeForce 8400 GS graphics card, which has 8 GPUs at 567 MHz with 512 MB of DDR2 global memory on board, and a 500 GB hard disk drive.

The principal software development environment we have used is Microsoft Visual Studio / Microsoft Visual C++ latest available versions (2008 and 2010). The choice of this programming language is both due to my previous work experience and its special features. C++ make possible *object-oriented programming* (OOP), which has become recognized as the almost unique successful paradigm for creating complex software. An *object* or *class* is a program structure that groups together some variables, or functions, or both, in such a way that all the included variables or functions “see” each other and can interact intimately, while most of this internal structure is hidden from other program structures and units. The key insight in OOP is that objects have *state* and *behavior*. The state of the object is described by the values stored in its member variables, while the possible behavior is determined by the member functions. We have used “objects” described in more detail in *Numerical Recipes* [30], that is a useful exemplar of a program library (or, in an OOP context, a class library) of numerical computation C++ routines, among which we have used mainly those for solving ordinary differential equations (ODE) and partial differential equations (PDE).

Another important advantage of using the C++ is the possibility of parallel programming to speed-up performances in newer multi-core PCs. The Intel processor considered here uses a native quad-core architecture, containing four separate cores on a single die. In addition, each core supports two-way multithreading, enabling the processor to support 8 separate thread contexts. In terms of software, two main options exist for parallel programming, notably Open Multi-Processing (OpenMP) and message passing solutions such as the Message Passing Interface (MPI). The latter is used with cluster computer systems, where data is transferred between nodes. While it can be used for multiple processors on a single node, the programming effort required is much higher than for OpenMP, which is designed to share memory on an individual node. For this reason, OpenMP is used here.

OpenMP is an implementation of multithreading, a method of parallelization whereby the master “thread” (a series of instructions executed consecutively) “forks” a specified number of slave threads and a task is divided among them. The threads then run concurrently, with the runtime environment allocating threads to different processors. The section of code that is meant to run in parallel is marked accordingly, with a *preprocessor directive* that will cause the threads to form before the section is executed. After the execution of the parallelized code, the threads “join” back into the master thread, which continues onward to the end of the program

or another parallel clause. The number of threads can be assigned by the runtime environment based on environment variables or in code using the function `omp_set_num_threads(n)`: if we set `n=0` all the possible threads on our CPU are used. The OpenMP functions are included in a header file labelled “omp.h” in C/C++. “Work-sharing constructs” can be used to divide a task among the threads so that each thread executes its allocated part of the code. In the our C++ software code, the preprocessor directive `#pragma omp parallel for` was placed at the start of each loop blocks, where intensive computations took place to calculate the flow variables for each grid point at each time level. In some cases it was necessary to use the preprocessor directive `#pragma omp parallel {...}`, where not a loop block but a whole parallel region indicated by the curly brackets was to be performed. The Numerical Recipes routines included in our calculation algorithms have all been upgraded with these preprocessor directives.

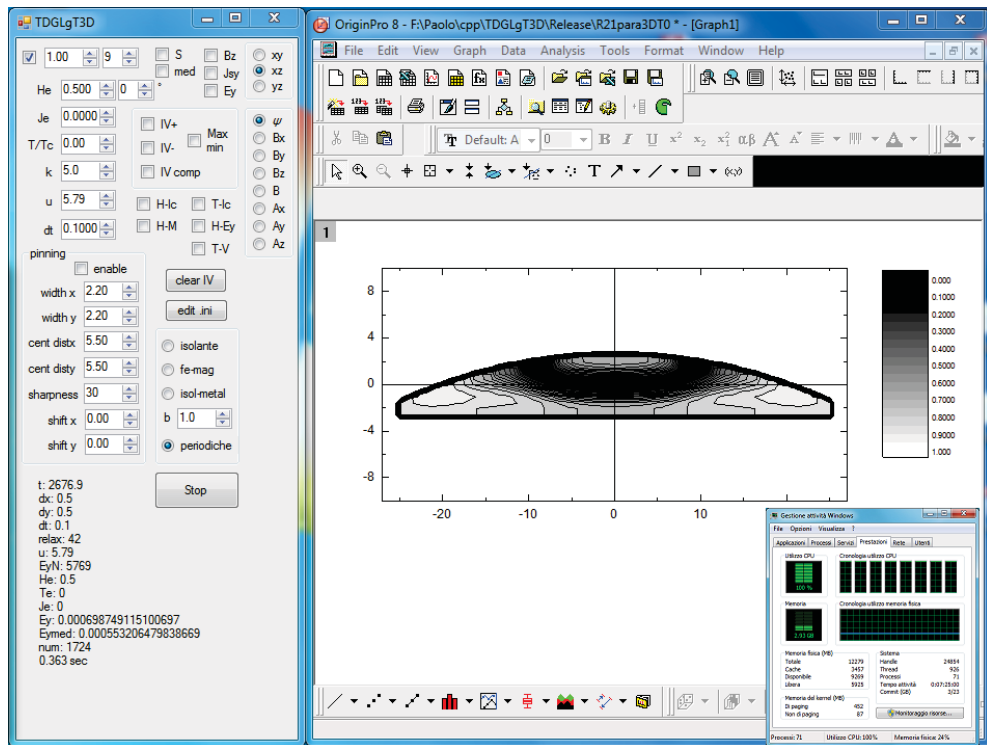


Figure 1.7: (left) *Graphical user interface screenshot of our simulation software for integrating the TDGL equations.* (right) *Screenshot of the commercial software OriginPro[®] 8 by OriginLab Corporation.*

Integrating the TDGL equations is a time-consuming process requiring considerable computing resources. However, in our simulations of vortex dy-

namics in superconductors, which were performed on the above quad-core based personal computer with an OpenMP compiler in a Windows environment, we have achieved good performances both in 2D and 3D model. The achieved speedups of the software code were such to online plot the order parameter norm and other physical quantities, e.g., magnetic field intensity and its components, magnetic vector potential components, electric scalar potential, supercurrent density components, etc. The graphical user interface (GUI) of the calculation algorithms is shown at left in Fig. 1.7, whereas at right we see the OriginPro[®] 8 by OriginLab Corporation, a commercial software application with tools for data analysis, publication-quality graphing, and programming, which we used for data plotting. Origin software can function as an *automation server* whereby other applications communicate with Origin using methods and properties exposed by Origin. Our application software, that supports Component Object Model (COM) programming, functions as the client application that connects with Origin. Thus we can exchange data back and forth with Origin and can send commands to be executed by Origin. The COM interface software is a Microsoft standard that is used to enable interprocess communication and dynamic object creation in programming languages that support COM, like the C++ programming language. This is another advanced feature that has addressed us in choosing such programming language. Finally, at the bottom right of Fig. 1.7 we can also see the task manager of the OS, which shows the overall amount of CPU usage. All 8 separate thread supported by Intel processor achieve a 100% activity when we run our application software compiled with OpenMP directives.

Our performance results confirm the parallel efficiency of our calculation algorithms and indicate that TDGL simulations on modern platforms can be greatly accelerated if parallelism is exploited. Such simulations, particularly those of 3D models, require more computational power than that which is typically available on a single desktop computer, making the efficient use of clusters an important requirement of any PDE solver. As alternative possibility, computational scientists and engineers have begun making use of *hardware accelerators* because these can provide significant gains in the overall performance of many numerical simulations at a relatively low cost. Among the most promising and inexpensive hardware accelerators, there are the Graphics Processing Units (GPUs) that integrate on a single chip a number of cores much higher (also hundreds) than the normal microprocessors. GPUs exploit parallelism to a much greater extent than conventional CPUs and they are optimized for maximizing throughput of a given computation rather than latency of an individual operation. This is achieved by massive hardware multithreading, in combination with a parallel memory subsystem.

Moreover, single such graphics boards can be assembled together in order to develop a “personal supercomputer” that delivers cluster computing like performance and upto hundreds times faster than the present day personal computers or workstations. Some GPU card manufacturers make available software libraries for their parallel programming. For example, Compute Unified Device Architecture (CUDA) is NVIDIA’s framework, an Application Programming Interface (API) extension to the C++ programming language, for general-purpose computing on its GPUs.

Because the scalability of our numerical methods is encouraging, we would like to further explore the presented methods using more GPUs installed on a desktop computer. It will be particularly interesting to see how well bandwidth limited components scale on GPU-based systems.

Bibliography

- [1] L. D. Landau, *On the Theory of Superconductivity*. Collected papers (Oxford, Pergamon Press, 1965). English translation of: V.L. Ginzburg and L.D. Landau, Zh. Eksp. Teor. Fiz. **20**, 1064 (1950).
- [2] V.L. Ginzburg, *On Superconductivity and Superfluidity*. Nobel Lecture, December 8 (2003).
- [3] L. P. Gor'kov, *Microscopic derivation of the Ginzburg-Landau equations in the theory of superconductivity*. Sov. Phys. JETP **9**, 1364 (1959).
- [4] T. Winiecki and C. S. Adams, *A Fast Semi-Implicit Finite-Difference Method for the TDGL Equations*. J. Comput. Phys. **179**, 127 (2002).
- [5] T. Winiecki and C. S. Adams, *Time-dependent Ginzburg-Landau simulations of the voltage-current characteristic of type-II superconductors with pinning*. Phys. Rev. B **65**, 104517 (2002).
- [6] M. Tinkham, *Introduction to Superconductivity*. (McGraw-Hill, New York, 1996).
- [7] V. V. Schmidt, *The Physics of Superconductors*. (SpringerVerlag, Berlin, 1997).
- [8] P. G. de Gennes, *Superconductivity in Metals and Alloys*. (Westview Press, New York, 1999).
- [9] L. P. Gor'kov and G. M. Eliashberg, *Generalization of the Ginzburg-Landau equations for non-stationary problems in the case of alloys with paramagnetic impurities*. Sov. Phys. JETP **27**, 328 (1968).

-
- [10] L. Kramer and R. J. Watts-Tobin, *Theory of Dissipative Current-Carrying States in Superconducting Filaments*. Phys. Rev. Lett. **40**, 1041 (1978).
- [11] Q. Du, M. Gunzburger and J. Peterson, *Analysis and approximation of the Ginzburg-Landau model of superconductivity*. SIAM Review **34**, 54 (1992).
- [12] S. Chapman, Q. Du, M. Gunzburger and J. Peterson, *Simplified Ginzburg-Landau models for superconductivity valid for high kappa and high fields*, Adv. Math. Sci. Appl. **5**, 193 (1995).
- [13] Q. Du and P. Gray, *High-Kappa Limits of the Time-Dependent Ginzburg-Landau Model*. SIAM J. Appl. Math. **56**, 1060 (1996).
- [14] Q. Du, J. Wei and C. Zhao, *Vortex Solutions of the High- κ High-Field Ginzburg-Landau Model with an Applied Current*. SIAM J. Math. Analysis, 2368 (2010).
- [15] D. Y. Vodolazov and F. M. Peeters, *Dynamic transitions between metastable states in a superconducting ring*. Phys. Rev. B **66**, 054537 (2002).
- [16] D. Y. Vodolazov, F. M. Peeters, S. V. Dubonos, and A. K. Geim, *Multiple flux jumps and irreversible behavior of thin Al superconducting rings*. Phys. Rev. B **67**, 054506 (2003).
- [17] S. Michotte, S. Matefi-Tempfli, L. Piraux, D. Y. Vodolazov, and F. M. Peeters, *Condition for the occurrence of phase slip centers in superconducting nanowires under applied current or voltage*. Phys. Rev. B **69**, 094512 (2004).
- [18] D. Y. Vodolazov, F. M. Peeters, I. V. Grigorieva, and A. K. Geim, *Non-local response and surface-barrier-induced rectification in Hall-shaped mesoscopic superconductors*. Phys. Rev. B **72**, 024537 (2005).
- [19] G. R. Berdiyrov, A. K. Elmurodov, F. M. Peeters, and D. Y. Vodolazov, *Finite-size effect on the resistive state in a mesoscopic type-II superconducting stripe*. Phys. Rev. B **79**, 174506 (2009).
- [20] W. D. Gropp, H. G. Kaper, G. K. Leaf, D. M. Levine, M. Palumbo and V. M. Vinokur, *Numerical Simulation of Vortex Dynamics in Type-II Superconductors*. J. Comput. Phys. **123**, 254 (1996).

-
- [21] R. Kato, Y. Enomoto, and S. Maekawa, *Computer simulations of dynamics of flux lines in type-II superconductors*. Phys. Rev. B **44**, 6916 (1991).
- [22] M. Machida and H. Kaburaki, *Direct simulation of the time-dependent Ginzburg–Landau equation for type-II superconducting thin films: Vortex dynamics and V-I characteristics*. Phys. Rev. Lett. **71**, 3206 (1993).
- [23] H. Frahm, S. Ulah, and A. T. Dorsey, *Flux dynamics and the growth of the superconducting phase*. Phys. Rev. Lett. **66**, 3067 (1991).
- [24] G. W. Crabtree, D. O. Gunter, H. G. Kaper, A. E. Koshelev, G. K. Leaf, and V. M. Vinokur, *Numerical simulations of driven vortex systems*. Phys. Rev. B **61**, 1446 (2000).
- [25] Y. Enomoto and R. Kato, *Computer simulation of a two-dimensional type-II superconductor in a magnetic field*. J. Phys.: Condens. Matter **3**, 375 (1991).
- [26] Q. Du, *Finite element method for the time dependent GL model of superconductivity*. Comp. Math. Appl. **27**, 119 (1994).
- [27] E. Coskun and M. K. Kwong, *Simulating vortex motion in superconducting films with the time-dependent Ginzburg–Landau equations*. Nonlinearity **10**, 579 (1997).
- [28] Z. Chen, *Mixed finite element methods for a dynamical Ginzburg–Landau model in superconductivity*. Numer. Math. **76**, 323 (1997).
- [29] Q. Du, *Numerical approximations of the Ginzburg–Landau models for superconductivity*. J. Math. Phys. **46**, 095109 (2005).
- [30] W. H. Press, S. A. Teukolsky, W. T. Vetterling, and B. P. Flannery, *Numerical recipes: the art of scientific computing*. (Cambridge University Press, 2007), 3rd ed.

Fabrication and measurement techniques

2.1 Introduction

This chapter will emphasize one of the most important parts of the thesis, which is fabrication processes of mesoscopic superconducting devices. Almost a quarter of the time has been dedicated to tuning the fabrication processes, in order to build the devices to be characterized. This chapter contains a description of the equipments used, the pattern transfer process (including electron beam lithography and photolithography techniques), deposition techniques and electrical characterization of the device structures.

The advancement in nanofabrication technology opens fascinating opportunities for engineering superconducting devices with smaller size than the current state-of-the-art devices. Amongst a variety of nanofabrication techniques, Electron Beam Lithography (EBL) is widely used since the late 60s for high resolution submicron scale patterning of micro/nanostructures. This lithographic technique comprises a number of steps including resist spinning, pattern exposure, metallization, removal of resist from the sample surface and lift off of the residual materials. It is important to consider that these should not be realized independently and the final resolution is conditioned for the accumulative effect of each individual step of the process. A great number of parameters, conditions and factors within the different subsystems are involved in the process and contribute to the EBL operation and result.

The major advantages of EBL compared to its counterpart conventional optical lithography technique is the high resolution and versatility (multi-level capability) of pattern formation. Unlike photolithography, the ability to create any pattern without the need to fabricate expensive mask plates makes e-beam a highly flexible tool. However, the EBL technique is a collective term for several closely related processes and the time scale of this technique is

some days. The processing steps of the EBL technique will be described in the following sections.

In the case of nanoscale patterning, for writing complex patterns EBL technique may be problematic to some extent. This is due to the variation of the amount of doses required for writing each patterns. Besides, the resolution limit in EBL is determined by the electron interaction with the molecules in the resist that can be divided into forward and backward scattering. A combination of high electron energy and small film thickness may reduce the influence of forward scattered electrons. But electrons penetrating through the resist and into the bulk substrate underneath will be partly backscattered into the resist and will also contribute to the resist exposure. These backscattered electrons are responsible for what's called the proximity effect: the dose at any point depends on the density of the pattern around this point.

2.2 Electron Beam Lithography

Electron beam lithography technology consists of the electron irradiation of a surface covered with a resist sensitive to a focused electron beam [1]. This technology uses a direct write system, in contrast with projection systems that require the use of masks to define the patterns, avoiding in that way the effect of diffraction. The employ of the narrow electron beam, the same used also for the Scanning Electron Microscope (SEM) allows high resolution images (up to 1000k magnification) and in the same way high resolution patterns. The SEM is the core of the apparatus and includes: the electron source, the focusing system and the support for the sample substrate; in simple words the EBL is an electronic interface attached to the SEM in order to control the deflection, interruption and the energy of the beam plus a software to transfer the designed geometry. The energetic absorption in the resist causes chemical phenomena that define the features in the polymeric layer. This lithographic process comprises three principal steps: deposition of a thin resist layer (by spin coating), exposure of the sensitive polymeric material, development by an appropriated solvent to obtain pattern transfer. A great number of parameters, conditions and factors within the different subsystems (i.e. substrate, material, thickness of the resist, pattern dimension) are involved in the process and contribute to the EBL operation and result. The energy absorbed during the exposure process creates a latent image that comes out during chemical development. For positive resists, the development eliminates the patterned area, instead for negative resists, the inverse occurs.

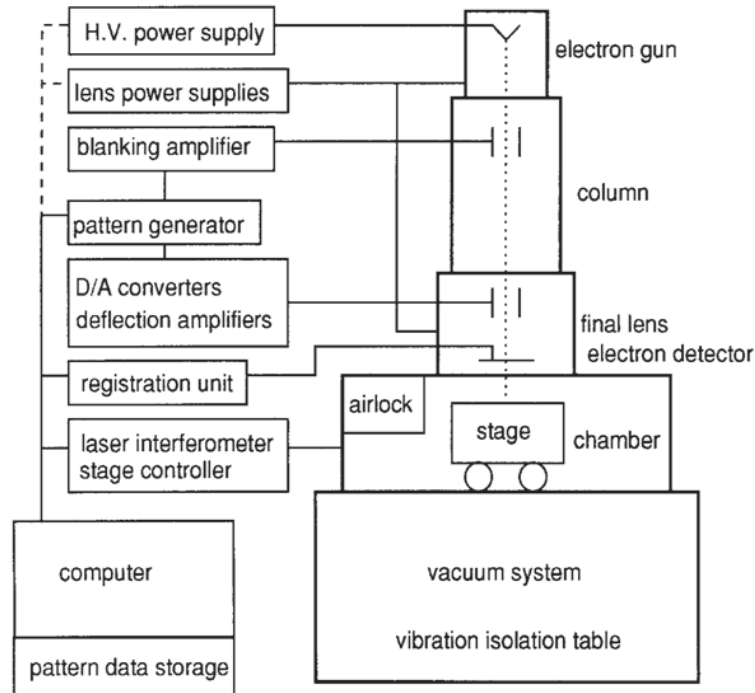


Figure 2.1: *Block diagram showing the major components of a typical electron beam lithography system [2].*

The Fig. 2.1 shows the different parts that are integrated in the EBL system. The SEM provides a beam with emission stability, perfectly circular and minimal diameter. This is accomplished working at Ultra High Vacuum (UHV) level conditions. The control of beam deflection keeps beam integrity and, at the same time, precise enough operation to define the design exactly, dimensionally calibrated and accurately positioned on the sample. In addition to this, the beam blanking should be fast enough to avoid imprecisions and the mounting stage might allow exact positioning by a laser interferometer. All these aspects require a computer based system control that is capable of managing all subsystems, fast and simultaneously.

2.3 Equipments

The EBL Laboratory at Physics Department, University of Salerno is equipped with a SEM from FEI company, model InspectTM F [see Fig. 2.2 (left)], with ELPHY Plus by Raith GmbH beam controller electronics [see Fig. 2.2 (right)]. The SEM is based on a Thermal field emitter ZrO/W filament



Figure 2.2: (left) FEG-SEM Inspect-F by FEI Company. (right) ELPHY Plus by Raith GmbH beam controller electronics.

(Schottky), hence the name Field Emission Gun - Scanning Electron Microscopy (FEG-SEM). The microscope nominal resolution is 3.0 nm at 1 kV and 1.0 nm at 30 kV, acceleration voltage is tunable from 200 V to 30 kV and beam current is ≤ 20 nA. Magnification varies from 14x to 1000kx, five apertures are available, 10, 20, 30, 40, 50 μm in diameter, one detector Everhardt-Thornley SED (secondary electron detector) is used. 6" wafers can be introduced in the chamber and stage movements are motorized in XYZ and rotation. It is also possible a manual tilt. The computer interface works under Microsoft Windows XP™.

Lithographic capabilities comprise external beam blanker and beam deflection system provided by Raith GmbH. The beam blanker abruptly deflects the beam by the application of a voltage of 200 V. The maximal frequency of switch on and off is around 2.6 MHz with transitory time of 10 ns. The control over the beam during exposure is accomplished by Elphy Plus program. It integrates the beam deflection system, the hardware for design, calibration and control of exposure conditions. The program is graphics oriented and enables different configurations adapted to each user preferences and for each lithographic task. All the works based on EBL included in this thesis have been performed with the equipments described above.

2.4 The Scanning Electron Microscope

The FEI Inspect F Scanning Electron Microscope (SEM) produces enlarged images of a variety of specimens, achieving magnifications of over 1000000x

providing high resolution imaging in a digital format. This important and widely used analytical tool provides exceptional field of view and minimal specimen preparation.

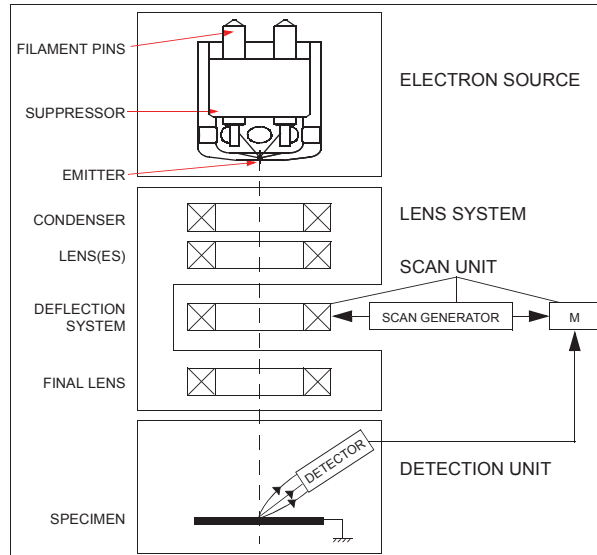


Figure 2.3: Block diagram showing the major components of FEI Inspect-F column [3].

There are four main components of the microscope (see Fig. 2.3):

- [1] Electron source: the electron beam is emitted within a small spatial volume with a small angular spread and selectable energy.
- [2] Lens system: the beam enters the lens system consisting of several electromagnetic lenses and exits to hit the specimen surface.
- [3] Scan unit: the scan generator signal, fed to the deflection systems, moves the beam in a raster pattern over the specimen area. The electrical voltage changes as it rasters, which provides serial information of the specimen surface. This signal, modulated by the detection system signal, produces the onscreen image.
- [4] Detection unit: electrons striking the specimen react with its surface producing three basic types of signal: backscatter electrons, secondary electrons and X-rays. The detection system picks up these signals, converts them into an amplified electrical signal which is sent to the control PC and displayed on the monitor.

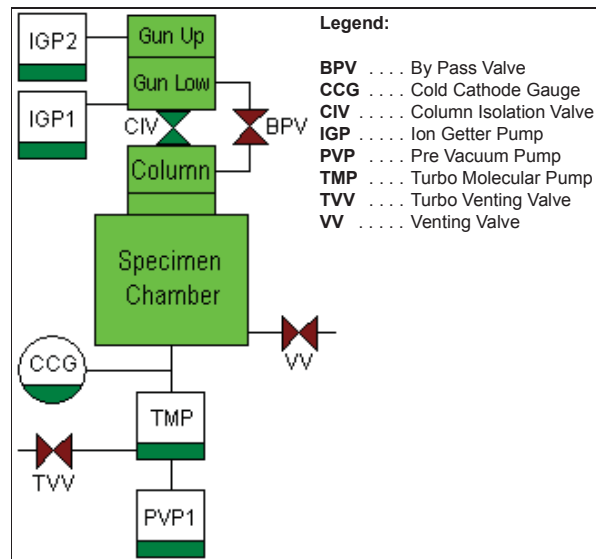


Figure 2.4: Block diagram showing the basic SEM vacuum system [3].

The entire electron path from gun to specimen must be under vacuum so that the electrons do not collide with air molecules. The beam performance and resolution is strongly conditioned by the performance of the vacuum system. Various levels of vacuum are necessary (see Fig. 2.4), so a Turbo Molecular Pump (TMP) backed by a rotary pre-vacuum pump (PVP), obtains the necessary electron source space and column/specimen chamber pressure (lower than 10^{-5} mBar). Inside the electron source (gun), two ionic pump (IGP) are used to reach the UHV (in the order or lower than 10^{-9} mBar) required for the beam operation. The SEM includes a valve (CIV) that isolates the column when chamber is vented to load samples, opening the venting valve (VV). Specimen exchanges take place through a chamber door which exposes the specimen stage when opened. Exchange time takes a few minutes. Software and interlocks protect the system against the damage and users against the injury.

The lithographic process is performed in the SEM chamber where the samples can be loaded. The specimen is attached to a specimen stub using a suitable SEM vacuum-quality adhesive, preferably carbon paint (graphite sticky tabs) [see Fig. 2.5 (left)], and housed in a multi sample holder disc [see Fig. 2.5 (right)]. These provide also to get a good electric contact in conductive samples to neutralize the charge received from the beam through the stage and the sample holder. The capabilities of the system benefit from

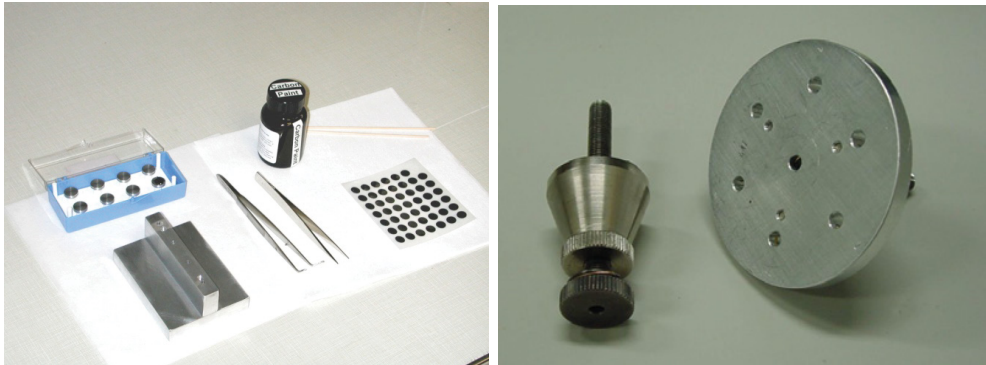


Figure 2.5: (left) *Preparation tools for loading the samples into the SEM chamber.* (right) *7-stub holding disc with a spring clip fitting.*

precise and motorized controlled displacements. Another important aspect related to the chamber is the presence of vibrations and electromagnetic noise that can distort the beam. Support is isolated from mechanical vibrations, which is even more critical for high resolution EBL than it is for conventional lithography. At the same time, computer monitors, transformers and vacuum pumps are kept separate and shielding is used to avoid interferences.

2.5 EBL digital pattern generator

The support package for SEM based lithography at Salerno is Elphy Plus from Raith GmbH. It is a PC based controller including software and hardware. It allows the creation of the designs, the remote control of electron beam system, the automation of some actions and, optional, the proximity effect correction or metrology. The specifications of the lithographic capabilities include a DAC of 16 bits, data transmission at 2.6 MHz, control of exposure time for each pixel lower than 10 ns, digital acquisition of images, alignment and mark recognition, automation of different tasks through macros, etc. The software works in Windows NTTM, graphically oriented and it integrates all the modules in a single package.

The procedure for the exposure comprises several steps: resist preparation, design of the pattern and determination of exposure coordinates, definition of reference systems (SR) for positioning and alignment, determination of actual beam current to establish the exposure conditions, optimization of focus and irradiation (exposure).

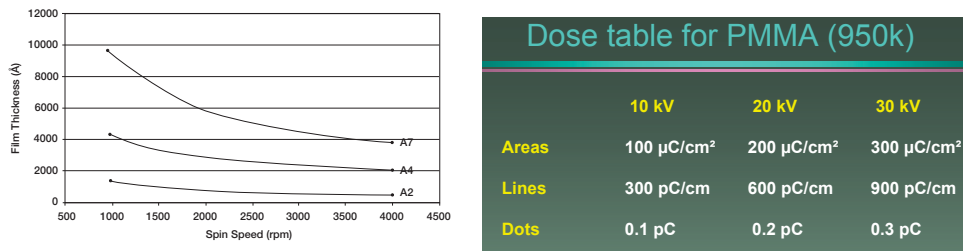


Figure 2.6: (left) *Thickness PMMA 950k layers as function of rotational speed for several solutions (2, 4, and 7%) in Anisole.* (right) *Typical doses for resist PMMA 950k.* [4]

2.5.1 Resist layer preparation

A requirement for almost any lithography technique is the ability of preparing resists layers of uniform and well-specified thickness with high reproducibility. This is commonly accomplished using spin-coating techniques, in which a drop of resist/solvent solution is applied onto the substrate and immediately distributed by rotating the substrate at high speeds. Most of the solvent is expelled from the substrate and the resulting resist layer is highly uniform and its thickness is exclusively determined by the solution composition and the rotational speed. Immediately after spin-coating most of the resist layers must be baked in an oven or in a hot plate to outgas the residual solvent and to enable the relaxation of the strain within the resist layer.

Polymethyl Methacrylate (PMMA) was used in the exposures. PMMA was one of the first materials developed for e-beam lithography. It is an organic polymer with molecules typically composed of 10000 monomers, which solid form is commonly referred as acrylic glass. When the electron beam impinges onto a PMMA layer, the extreme long molecules are broken and in consequence the exposed regions become soluble in an appropriate developer, such as methyl isobutyl ketone (MIBK). Therefore, for moderate doses, PMMA resist is positive. PMMA in two molecular weight forms (950k or 495k) dissolved in Anisole or Chlorobenzene were used. Since MIBK turns out to be a too strong developer, a mixture of it with isopropyl alcohol (IPA) is more commonly used. 1:3 MIBK:IPA solution produces a very high contrast, which is very appropriate for high resolution patterning. Temperature control is very important during the development since a variation of a few degrees destroys the reproducibility of the process. PMMA layers were always developed with solutions at 23°C.

Thicknesses of the resulting PMMA layers for a given solution and spinning speed are usually determined experimentally. Curves shown in Fig. 2.6

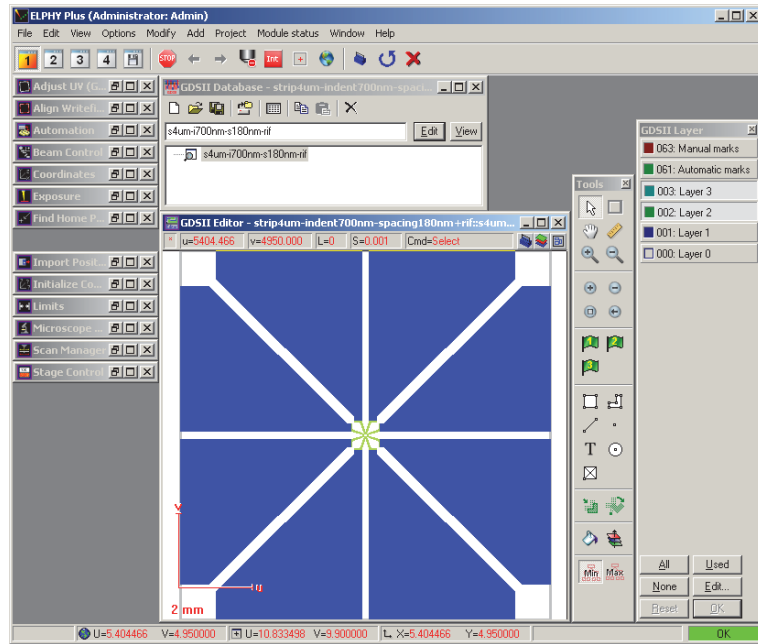


Figure 2.7: GDSII design page of ELPHY Plus software.

(left) give the thickness 950PMMA layers as function of rotational speed for several solutions in Anisole. PMMA spin coated samples were usually baked at 170°C in a convection oven for 30 min. Typical doses for e-beam radiation as a function of beam accelerations and types of structure to expose are shown in Fig. 2.6 (right).

2.5.2 Pattern design

The design files are organized by hierarchical structures in databases of extended GDSII format [5]. This format enables to determine dose information and includes special structures, such as single pixel lines (SPL), text or bitmaps. The visualization and editing is completely graphic and it allows flexible and fast data manipulation. In particular, the program allows to draw as basic structures, rectangles, polygons, circles, ellipsoids, lines, dots, etc in separated layers for multilevel exposure. Text can be included, together with practical information for documentation (date and time of exposure). It includes a generator of mathematical functions to create curves matrices or many actions to modify the basic structures: translation, scaling, iteration, deleting, merging, etc (Figure 2.7).

2.5.3 Positioning and alignment

After the PMMA is coated on the substrates, the samples are placed on the stage which is then loaded into the SEM. The loading process is automatic, so we will not discuss this in great detail. Once the stage with the samples is loaded in the machine, the stage is brought to the correct working distance (WD) of 10 mm, which is close to the correct focal distance for the e-beam. We set the right acceleration voltage and aperture: the most common setting is an aperture of 20 microns and an acceleration voltage of 10 kV. Upon setting these parameters, the SEM also brings up the last values for astigmatism, magnification, and aperture alignment configurations which can reduce the time it takes for startup each time.

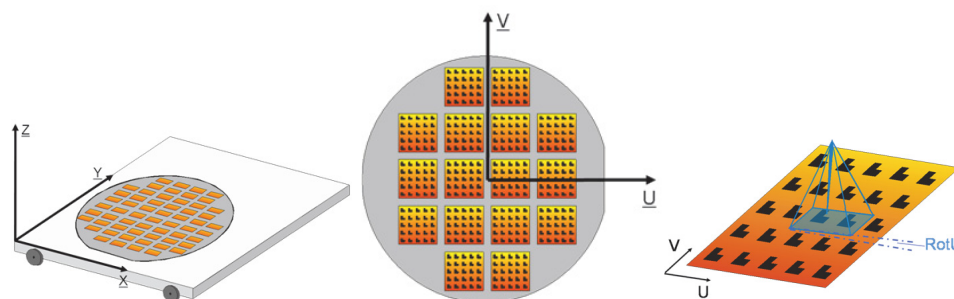


Figure 2.8: (left) *Sketch of stage coordinates (X, Y, Z).* (middle) *The sample coordinates (U, V) defined on a wafer.* (right) *Sketch of the design pattern system (u, v) with respect to the sample.* [5]

It is typical for nearly all application tasks to find a specific location on a sample and then for example to expose at this location a GDSII structure. To find this location it is very convenient to apply a coordinate system to the sample. Finding this location is then in general simply a drive command within this coordinate system. Within the Raith software are defined three coordinate systems [5] (see Fig. 2.8):

- [1] stage coordinates (X, Y, Z) - SEM coordinate system;
- [2] sample coordinates (U, V, W) - global coordinate system;
- [3] design pattern coordinates (u, v, w) - local coordinate system.

In the most cases these two coordinate systems are not identical. The two coordinate systems may have different origins, causing an offset vector. Additionally, the U, V, W system may be rotated against the X, Y, Z system and the systems may have different scales. In conclusion, a coordinate transformation has to be calculated, so that it is possible to drive to a specific

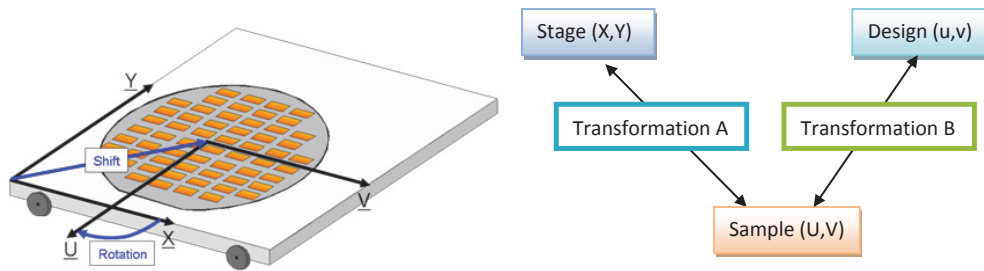


Figure 2.9: (left) *Sketch of stage-sample coordinates transformation.* (right) *Block diagram of coordinates transformations stage-sample (A) and sample-pattern (B).* [5]

location on a sample. How this transformation fits into the scheme of coordinate systems is shown in Fig. 2.9.

In our case often no pattern exists on the sample which can serve as a reference and the sample itself is not a complete wafer (only a fraction of it) with at least one straight edge. In this case the adjustment consists of two tasks. One task is to assign a certain point on the sample specific coordinates (origin correction) whereas the other task is to define the U-direction on the sample (angle correction). The sequence between these two tasks does not matter.

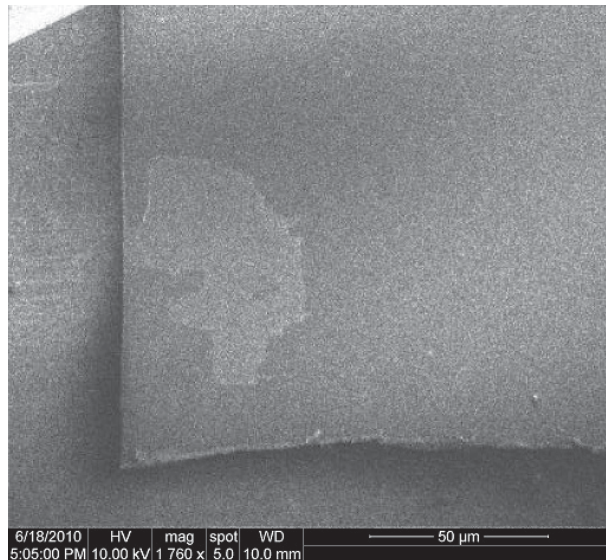


Figure 2.10: SEM *image of lower left corner of the sample.*

Now we are ready to locate a reference structure on the sample such as

the lower left corner of the sample (see Fig. 2.10). In order to do this we use the appropriate controls of SEM software to place this reference structure in the center of the field of view. Then we press Reset button in Raith software to make sure that the scaling factors as well as all other parameters set to the identity transformation, and switch to global transformation before pressing Adjust button to calculate the shift for that transformation [see Fig. 2.11 (left)]. This gives a place to start and we can always return back.

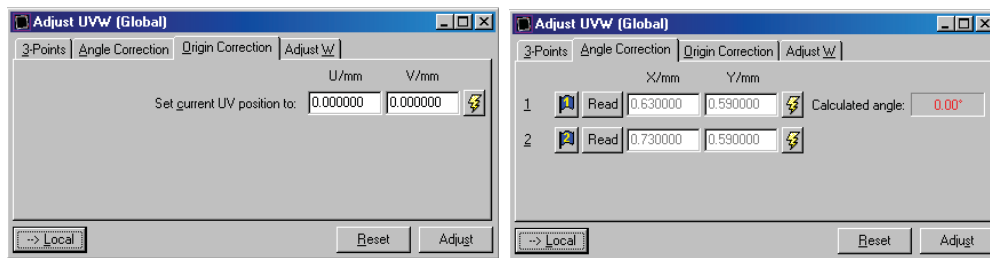


Figure 2.11: (left) *The Origin Correction tab serves to determine the shift vector between the origin of the (X, Y) system and the origin of the (U, V) system.* (right) *The Angle Correction tab offers the capability to adjust the angle between X axis and U axis.*

To calculate the angle of this transformation it is necessary to read in the X and Y of two different points along the U-axis of the sample. Naturally, the degree of accuracy of the angle is related to the accuracy of the positioning as well as the distance between these two points. If the distance is larger, it is more accurate. For simplicity the first point that we choose is the lower left corner where already we are. By pressing the read button [see Fig. 2.11 (right)], the software will take a reading of the x and y coordinates of the stage. Once that is done we can now move to the corner on the bottom right hand side of the chip. Find a spot with particular features and then press the second Read button on the angle correction window. Once the second position is read, the Adjust button on the bottom can be pressed again. This will turn the red angle calculated angle to a green light. Because we are human, and usually imperfect in the scales which we are working at, the chip is not always loaded into the stage perfectly straight. This slight angle in the sample can cause problems when trying to write a structure. By setting the global coordinates, not only we reset the corner of the chip to the origin, but we also correct for the angle which the chip usually has when placed into the sample holder. Thus a transformation of coordinate system is set.

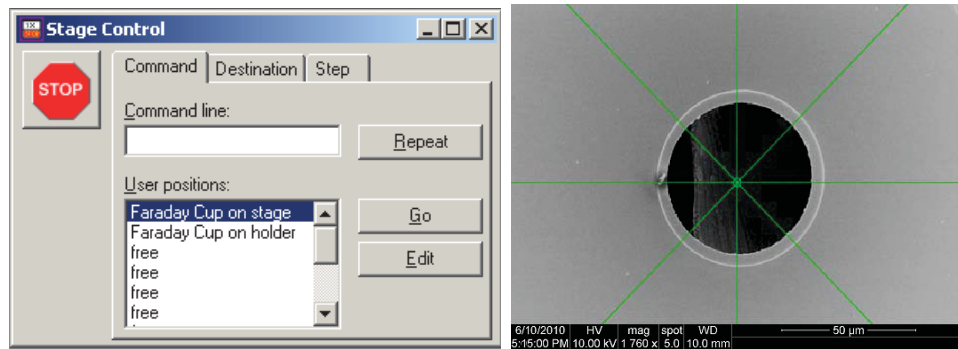


Figure 2.12: (left) *Stage control window with preset positions.* (right) *Aperture of the Faraday cup aligned with the electron beam axis direction.*

2.5.4 Measure beam current and focus

Now that the coordinates have been set, we usually measure the beam current. This is done by moving the stage until the beam is in a Faraday cup which can measure the current. We can move to the Faraday cup by pressing the button on the preset stage position found in the stage control window [see Fig. 2.12 (left)]. Once the button for the Faraday cup on holder is pressed, the stage will reposition over the cup [see Fig. 2.12 (right)]. All we have to do is to remember to turn the beam off before to choose this option, so that we not expose the sample. Once over the cup, we should start to burn

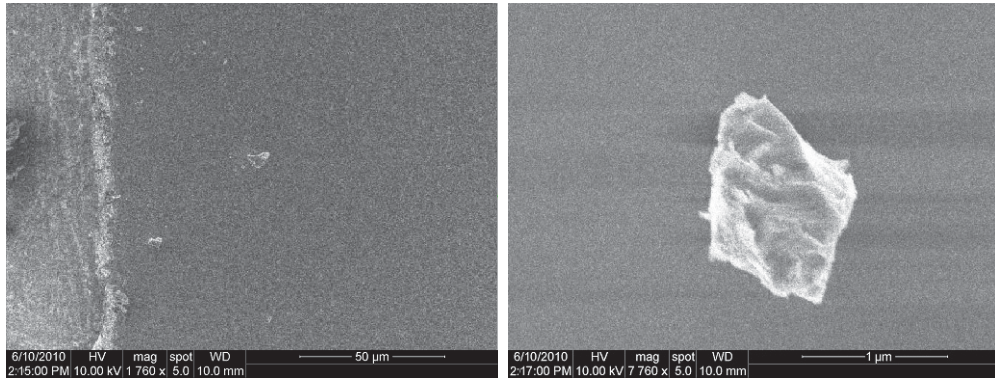


Figure 2.13: (left) *SEM picture when we first move onto the chip.* (right) *Zoomed in picture of dust used for the focus.*

a beam spot using the SEM software. By burning beam spot, we turn the beam on and have a continuous flow of electrons. Now we can measure the beam current using an external picoampere meter. A typical current for an aperture set at 20 microns and a 10 kV acceleration voltage is 200 pA. Once

the current is measured, we can return to the corner of the sample by directly entering the coordinates using the destination tab in the stage control window.

Now we can move onto the chip in order to focus the e-beam by looking for some dust [see Fig. 2.13 (left)]. As we can see from this picture, there is a lot of dust on the chip. We are also at a very low magnification. We can increase the magnification on the dust so that we can start to get a good focus. By zooming in, the dust then looks like Fig. 2.13 (right).

2.5.5 Exposure

Once the focus correction is completed, we are ready for the GDSII design file to be written on resist. First of all, we have to choose the Magnification and Write field size using the Microscope Control window (see Fig. 2.14). We can use the dropdown list to select the required write field of pattern structure. Entries in this list are blue if corresponding alignment values in database, previously stored following the procedure of Write field alignment (not described in this thesis) [5]. In order to perform a write, we must open

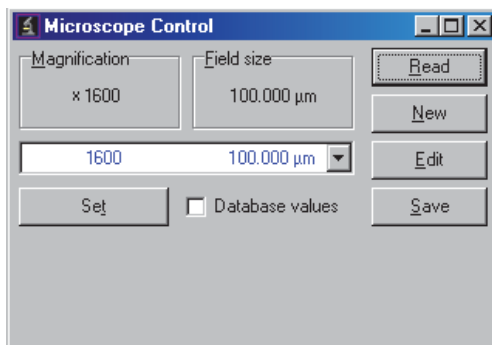


Figure 2.14: *Microscope control window where we set Magnification and Write Field size.*

up a blank position list. Once the position list is open, we can simply click on the file from the GDSII program and drag the program to the position list [see Fig. 2.15 (left)]. Once the file is in the position list, we must change the properties of the program. When we are changing the properties, we will set which layer we want to write, where the writing will occur, and the exposure settings needed for the beam. Once the file is in the position list, we can right click on the highlighted file and pull up the properties window [see Fig. 2.15 (right)]. Here we must first choose the layers which we want to expose. When we click on the button on the right of the exposure layer, a list of all the layers will pop up. From this window, we are able to choose one layer, all the layers, or any combination of the layers. Once the layers are chosen, we can enter the initial position from which the writing will occur.

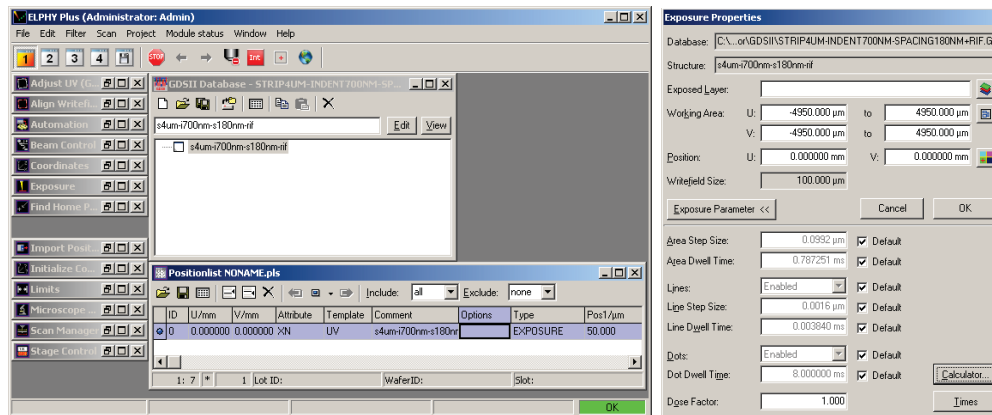


Figure 2.15: (left) Image of the position list with the GDSII database above. (right) Image of the properties of the position list file.

The final information which we need to select is the exposure parameters [see Fig. 2.16 (left)]. Here we can set up all the settings needed for the beam writing to occur. Depending on the design which we are trying to write, we might only need one of the settings. There are three choices for the writing process depending on pattern design. The design can have an area exposure, a line scan, and or single dots. A line scan will turn the beam on and write in a single line. A dot exposure will take the smallest dot which the Raith can make and turn the dot on and off, and the area exposure will raster scan to expose wide areas at a time. Careful selection in these exposure types will speed up the writing process. Because of the designs which we are going to expose are all area scans, we do not need to set up the line or dot settings. Thus we can just turn them off. The calculator will make the necessary calculations of the beam speed and dwell time using the step size and dose we selected. Here is where the beam current is needed. The beam current is entered once the current has been measured as previously described. Once

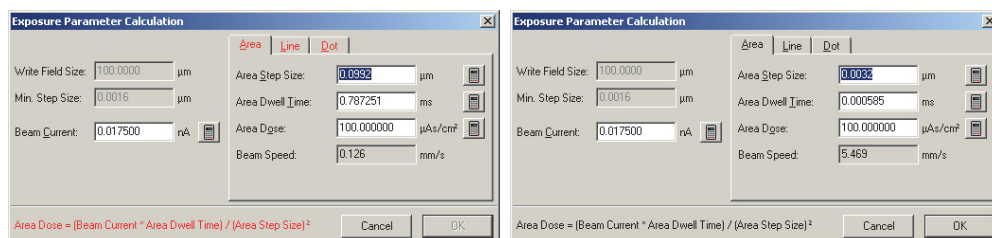


Figure 2.16: (left) Image of the calculations which need to be made. (right) Image after calculating the dwell time.

we enter the values for dose and step size (distance between exposure points) [see Fig. 2.6 (right)], we can press the calculator on the right hand side for the dwell time [see Fig. 2.16 (right)]. The dwell time is the time which the beam is sitting over one area to expose the resist. The parameters for area, line and dot exposures fulfill the following equations [5]:

$$\text{Area Dose} = \frac{\text{Beam Current} \cdot \text{Area Dwell Time}}{(\text{Area Step Size})^2}$$

$$\text{Line Dose} = \frac{\text{Beam Current} \cdot \text{Line Dwell Time}}{\text{Line Step Size}}$$

$$\text{Dot Dose} = \text{Beam Current} \cdot \text{Dot Dwell Time}$$

We can change the parameters to anything we want, but the most optimal setting is to have the beam speed between 4 and 12 mm/s. This will ensure a good write with the most control over the beam. If the beam speed is too fast, the structures will turn out blurry. If the beam speed is too slow, some times the machine will over expose, and the exposure will take a very long time. Once we have figured out the base dosage, the main setting which we will play with is the step size which the machine will take. Once these settings have been entered, we can then click on the Time button. The Raith software will then run through a simulated write of the chip and return an estimated length of time which the machine will need to write. We can then go back and change some of the settings to try to improve the time it takes to write until we find the fastest settings.

After setting the parameters, we are finally ready to expose the GDSII file in the position list. So we can do one exposure or more exposures all at the same time. Once the position list is ready, the OK command can be given [see Fig. 2.15 (right)]. Now all we have to do is sit back and let the machine run its course. The program will automatically run down the position list until it runs out of things to do. Then it will simply stop. We know that the machine is still working because a window will appear with the structure which is being written. The structures will have a highlighted block so that we can watch the progress of the machine. Once the machine has finished with one write field, the exposed area will remain in color. Once the whole structure is exposed, the window will close, and the next structure to be written will open. This process continues until the entire position list is exposed. Then we can write in another area of the chip, or simply remove and develop.

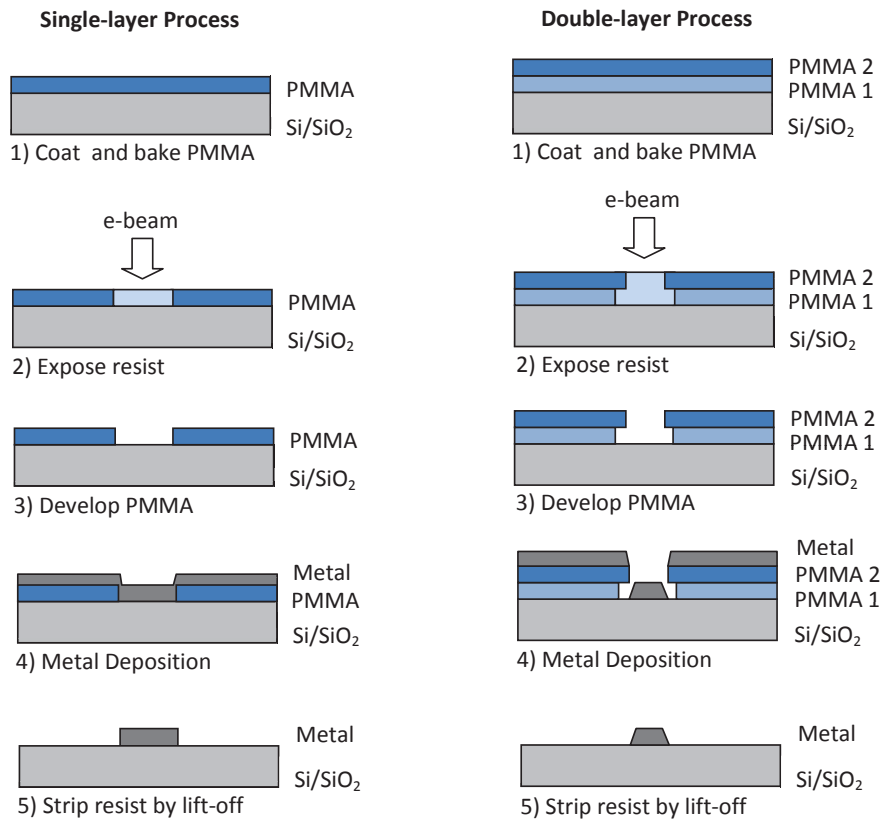


Figure 2.17: Schematic of EBL lift-off process using single and double-layer PMMA resist.

2.5.6 Pattern transfer

Metal lift-off is a common pattern transfer method for EBL applications. Either single-layer or multi-layer resists can be used for lift-off. Figure 2.17 illustrates a lift-off process using single-layer and double-layer PMMA. A single-layer resist is good for lift-off of very thin metal films, even without well defined undercut to prevent sidewall connections. The process starts with deposition by spin coating and baking of the PMMA resist on the Si/SiO₂ substrate, the second step is the electron beam exposure and third the resist development. The sample is developed in 3:1 MIBK:IPA solution for 30 sec., rinsed in IPA, and dried with N₂ blow. After this, we have defined the mask for the metal deposition that takes place in the fourth step. The end of the process, fifth and last step, is the release of the structure by under-etching of the sacrificial layer in acetone (lift-off), which transfers the pattern to the Si/SiO₂ substrate.



Figure 2.18: *Picture of the sputtering system used to fabricate the samples.*

The double-layer resist is fabricated first spinning and baking the first layer PMMA 1 on the Si/SiO₂ substrate, and then spinning and baking the second layer PMMA 2 on the first resist layer. We noticed that this double step deposition produced an appreciably different sensitivity in the two resist layers. After electron beam exposure and resist development, the bottom layer of resist forms a wider mask than the top layer: this structure acts as a “shadow mask” in the next step of the metal deposition. Due to the isotropy of the sputter process, the metal is smeared under the window formed by the top layer of resist PMMA 2, resulting in a trapezoidal profile for the metal deposited on the Si/SiO₂ substrate (see Chapter 8).

2.6 Thin film deposition system

The sputtering system used to fabricate the samples is an RF Sputtering Magnetron MRC 8602 (see Fig. 2.18), three targets can be fitted to the system. The substrates are placed onto a rotating stage, kept at room temperature thanks to a water cooling system. The system allow both real sputtering processes and etching processes; the last ones allow surfaces cleaning operations making use of negative voltages which direct the bombarding ions towards the substrate [6]. During the samples fabrication process, after a sputter etching of the sample, a pre-sputtering is done to clean the target

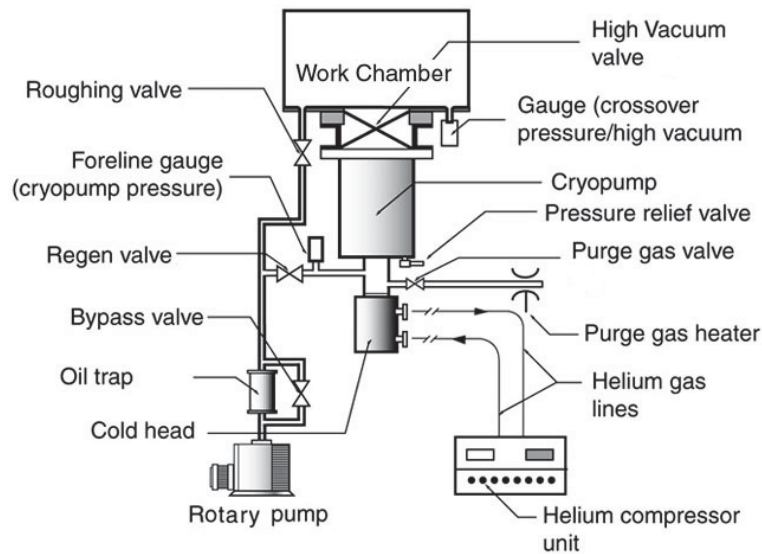


Figure 2.19: Schematic for cryopump-based vacuum system.

before deposition. Only after the pre-sputtering process the metal depositions have been done (sputtering). The deposition of the materials is done for a time depending on the thickness we intend to deposit. The system has two vacuum chambers separated by a gate valve. In the main chamber both sputtering and pre-sputtering take place, whilst in the other one, the Load-Lock, loading and unloading of the samples and substrates oxidation take place. A rotary vane mechanical pump, followed by a high vacuum cryopump, are used to evacuate the main chamber, as we see from Fig. 2.19 which depicts a schematic of the work chamber vacuum system. A turbomolecular pump backed with a rotary vane mechanical pump was used instead for pumping the Load-Lock chamber.

The fabrication process starts pumping the Load-Lock in which the pressure reaches a value of about 10^{-5} Torr, while the pressure in the main chamber is about 10^{-7} Torr. At this point we open the gate of the Load-Lock and the substrate are placed in the main chamber. Before depositing the film, to increase the adhesion properties on the substrate, we etch it for 3 min introducing an Argon gas in the main chamber at 3.1×10^{-3} Torr and using a 400 V self bias voltage at power 30W, which corresponding to an etching rate of 2 nm/min. After finished the pre-sputtering it follows the sputtering. The Nb films are deposited on 10×10 mm² Si covered with thermal oxide layer SiO₂(100) substrates. We use 99.98% pure Nb and the whole deposition process takes place in a high-vacuum with a base pressure of 5.2×10^{-8} Torr in 99.999% pure Ar at 3.3×10^{-3} Torr and power 500W,

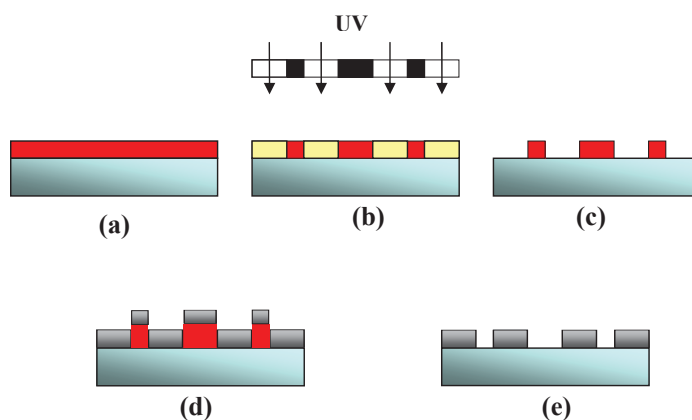


Figure 2.20: *Definition of contact pads steps.* (a) *Photoresist (red) spun on sample.* (b) *Exposure with UV light.* (c) *After develop.* (d) *Deposition of Nb layer (gray).* (e) *Schematic after the lift-off.*

which corresponding to a rate of 2.2 nm/s.

2.7 Photolithographic patterning of wiring pads

To define the external electrical contact pads of the sputter deposited mesoscopic structures the photolithographic technique has been used. Optical lithography was done making use of a Mask Aligner placed in Lithography Laboratory at Physics Department, University of Salerno. The patterning is described in the following steps [7] (see Fig. 2.20):

- After cleaning with acetone, the sample was transferred to a resist spinner, 3-4 drops of positive resist AZ1500 series are pipetted onto it and spinned at 4000 rpm. Finally, it is placed in a convection oven for about 20 minutes at 80 °C in order to cure the resist. [Fig. 2.20(a)].
- UV exposure, for 40 seconds, [Fig. 2.20(b)] and develop, for 60 sec, [Fig. 2.20(c)] of the geometry using the mask shown in Fig. 2.21 (left).
- Light Ar sputter cleaning and deposition of the Nb layer [Fig. 2.20(d)].
- Lift-off with acetone to remove the undesired film [Fig. 2.20(e)].

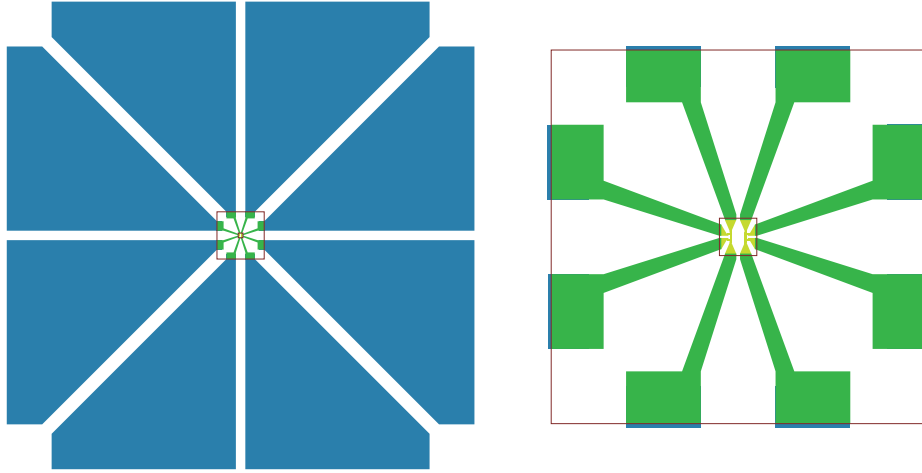


Figure 2.21: (left) *Schematic of the mask $10 \times 10 \text{ mm}^2$ used to define the contact pads of the mesoscopic structures (shown at center) by optical lithography.* (right) *EBL mask used to define the mesoscopic structure in two WF size: $1 \times 1 \text{ mm}^2$ and $100 \times 100 \mu\text{m}^2$.*

2.8 Images of patterned structures

A set of irradiation tests using the “Raith Demo Pattern” [5] is performed on Si/SiO₂ substrates under the exposure conditions shown in Table 2.1, to determine resolution and the effect of complex geometries for our exposure/development/deposition process.

Working distance:	WD = 10 mm
Write field size:	WF=100 × 100 μm ²
High voltage:	EHT = 10 kV
Aperture:	10 μm
Current:	150 pA
Area step size:	20 nm
SPL step size:	10 nm
Resist:	PMMA 950 K, thickness 100 nm, Prebake 30 min @ 170°C
Dose:	area dose: 100 μC/cm ² , SPL dose: 300 pC/cm, dot dose: 0.1 pC

Table 2.1: *Typical exposure parameters for Raith Demo Pattern.*

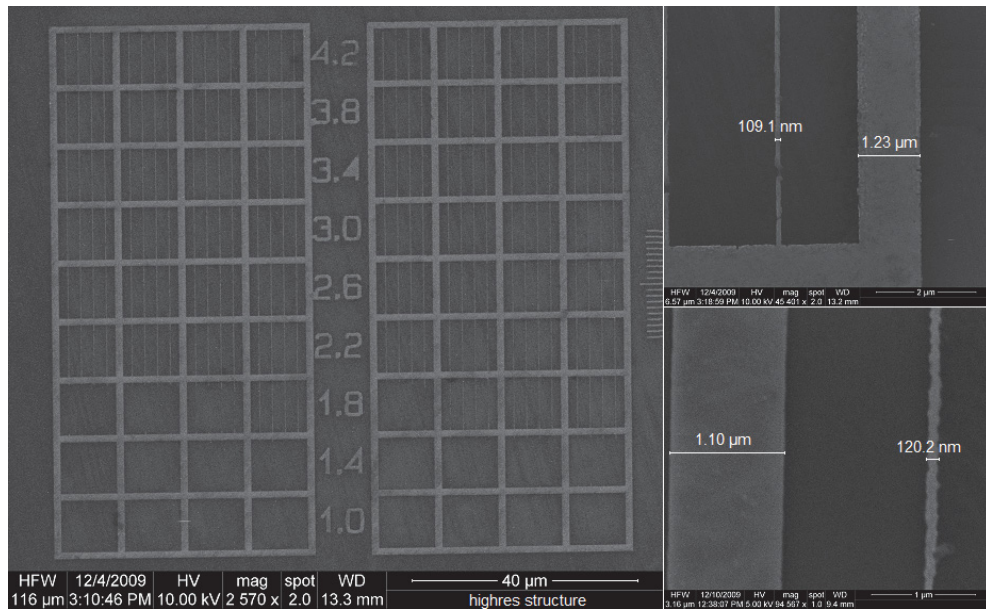


Figure 2.22: SEM micrograph of “high resolution” test (left) and two close-ups of Single Pixel Lines (right).

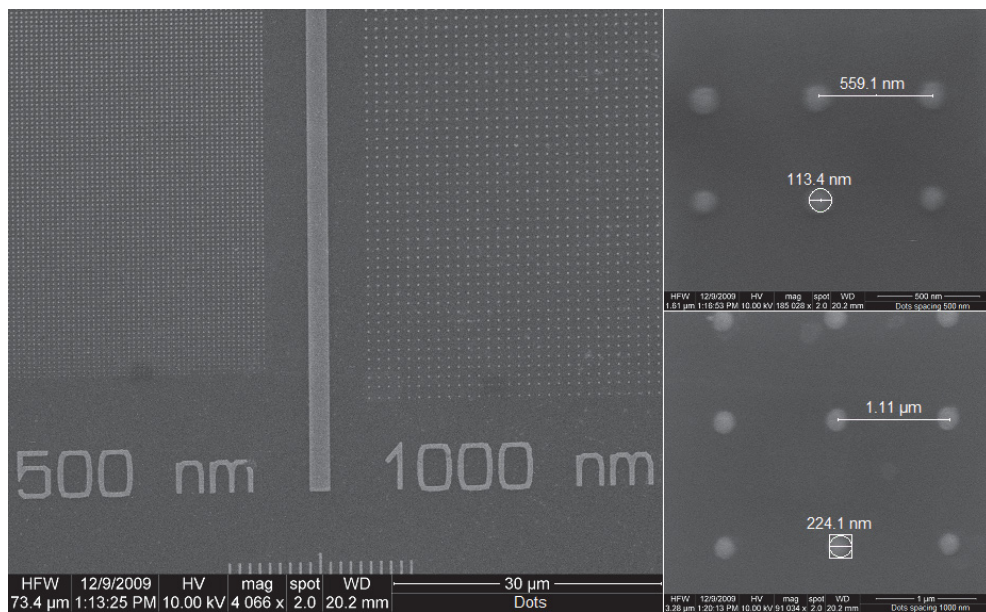


Figure 2.23: SEM micrograph of “periodic dots array” test (left) and two close-ups of dots (right).

The first result is shown in Fig. 2.22, the test pattern for high resolution

of SPL (dose factor 1.0-4.5 @ step 0.1). We note that isolated SPL (distance $> 1 \mu\text{m}$) require a higher dose (dose scaling within the pattern) by a factor greater than 2. However, we obtain well-defined niobium SPL of about 100 nm.

In Fig. 2.23 we show a periodic dots array (period 500 nm and 1000 nm) achieved with dose scaling to obtain circles with different diameters (dose factor 0.02-2.8 @ step 0.02, and 1-8 @ step 0.1). The shown Nb single dots have diameters of the order of about 100 and 200 nm.

Figure 2.24 shows the exposure result of bitmaps and of mathematically defined structures, which use areas and SPLs, including a Fresnel lens. We obtain well-defined Nb SPL ranging from 50 to 70 nm.

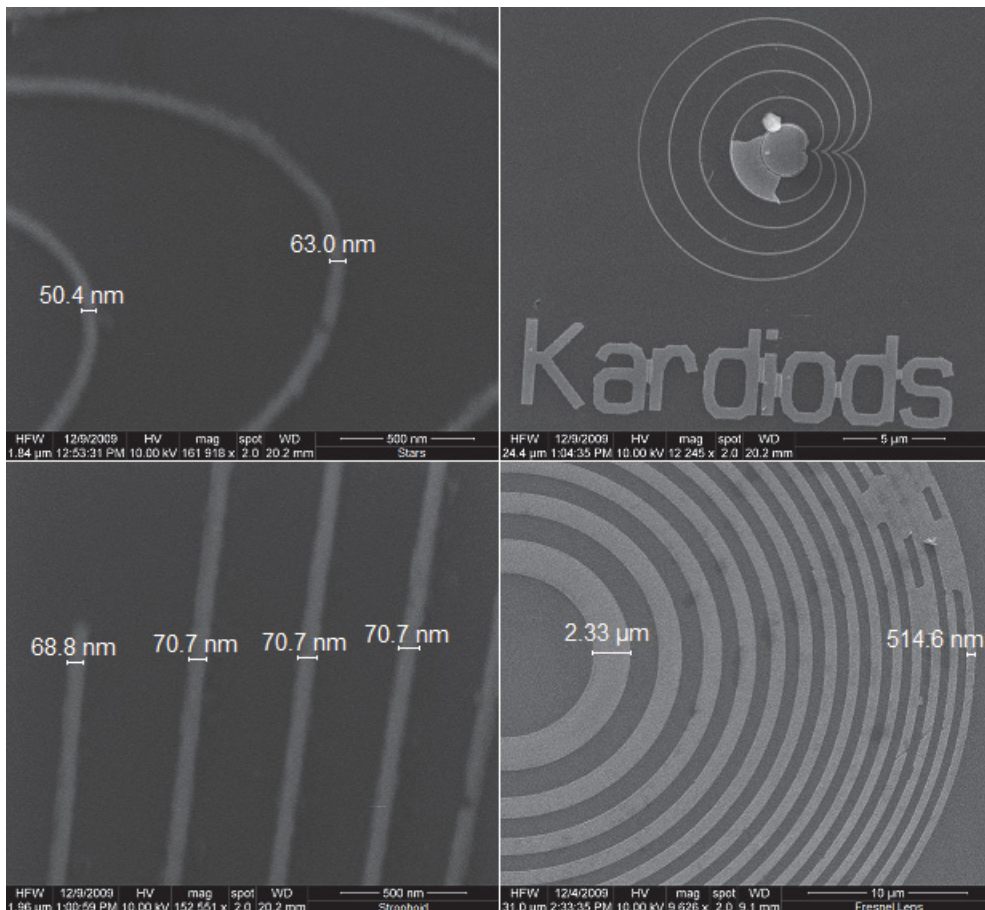


Figure 2.24: SEM micrograph of four close-ups respectively of Stars, Kardiods, Strophoid and Fresnel lens of “geometric structures” test.

After extensive patterning trials and optimization of the fabrication procedure, the production of mesoscopic superconducting devices, subject of this work, has shown good results only on a specific number of sample geometries. Some of the fabricated structures are presented in Fig. 2.25 to 2.28 on the following pages.

For devices requiring a four terminal measurement, we have used the EBL mask shown in Fig. 2.21 (right): one can see the central region of the mask that contains two devices with four terminal. The two write-fields are matched, so that the large leads, exposed with write field size $1 \times 1 \text{ mm}^2$, pass into the small leads at the border of the $100 \times 100 \text{ }\mu\text{m}^2$ central write-field. Figure 2.25 shows the SEM micrograph of a typical device produced using this EBL mask. As we see at the bottom right, in this specific device the Nb thin strip is patterned with a nanometer-sized square array of antidots. The particular exposure technique used for the central write-field which defines the array is described in detail in the Chapter 4.

Figure 2.26 shows the SEM image of a Nb thin strip with a trapezoidal profile obtained through a double-layer resist shadow mask [see Fig. 2.17 (right)]. The sample was then contacted with two macroscopic continuous Nb banks not shown in figure (bridge geometry), realized using standard optical lithography, with the current and voltage contacts $30 \text{ }\mu\text{m}$ apart. This device is described in detail in the Chapter 8.

In Fig. 2.27 is shown another device fabricated using the EBL pattern for devices with four terminal [Fig. 2.21 (right)], where one of the two central strips is modified with sideward comb-shaped structure, the other strip is retained as a reference. We designed the $100 \times 100 \text{ }\mu\text{m}^2$ central write-field of our EBL mask so that fingers of the comb-like pattern were single pixel lines 700 nm long with a spacing of 180 nm on a strip $4 \text{ }\mu\text{m}$ wide. As we see at the top right, the fingers of the fabricated structure are just over 300 nm long with a space between them is reduced up to 30 nm .

Figure 2.28 is the SEM micrograph of two single Nb superconducting nanostripline contacted in bridge geometry. This sample was realized using an EBL mask with two write field, $100 \times 100 \text{ }\mu\text{m}^2$ for the SPL used to define the nanostripline and $1 \times 1 \text{ mm}^2$ for the pads, then contacted with macroscopic Nb banks not shown in figure, realized with the mask in Fig. 2.21 (left), using standard optical lithography. The two nanostripline are wide respectively 80 and 110 nm .

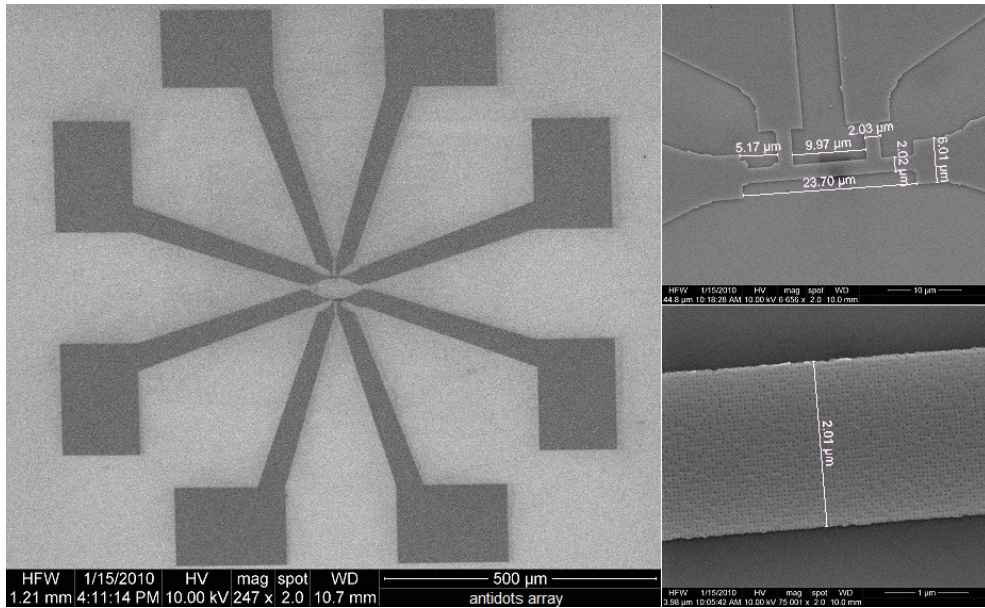


Figure 2.25: SEM micrograph of superconducting Nb thin film with a nanometer-sized square array of antidots.

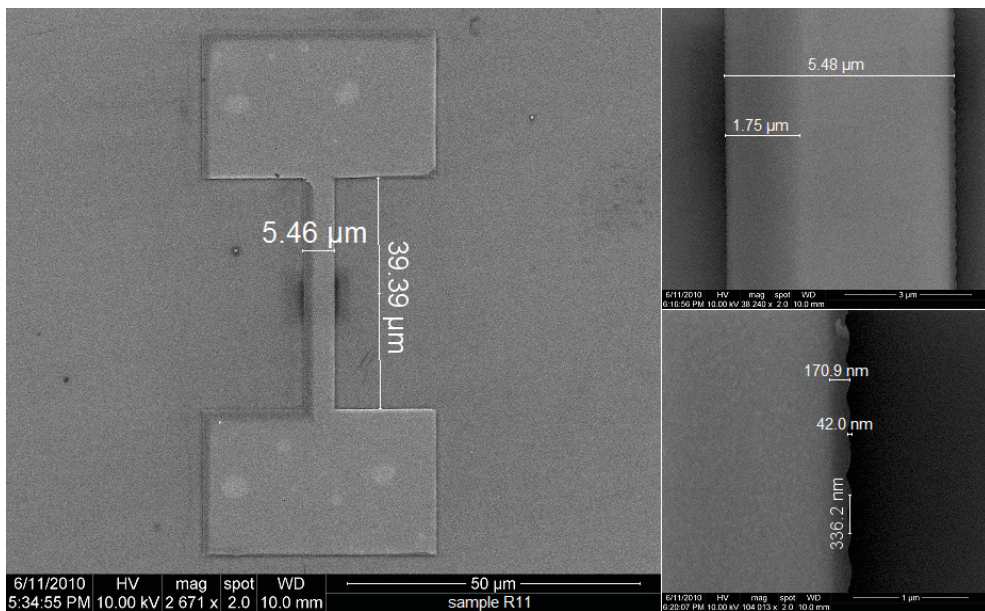


Figure 2.26: SEM micrograph of Nb thin superconducting strip with trapezoidal cross-section.

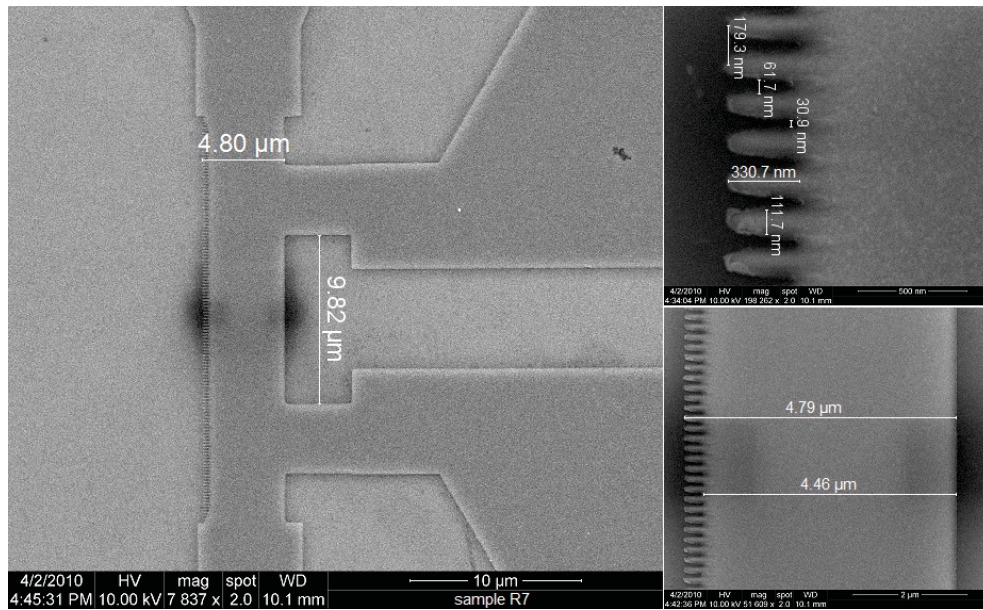


Figure 2.27: SEM micrograph of superconducting Nb thin film with sideward comb-shaped structure.

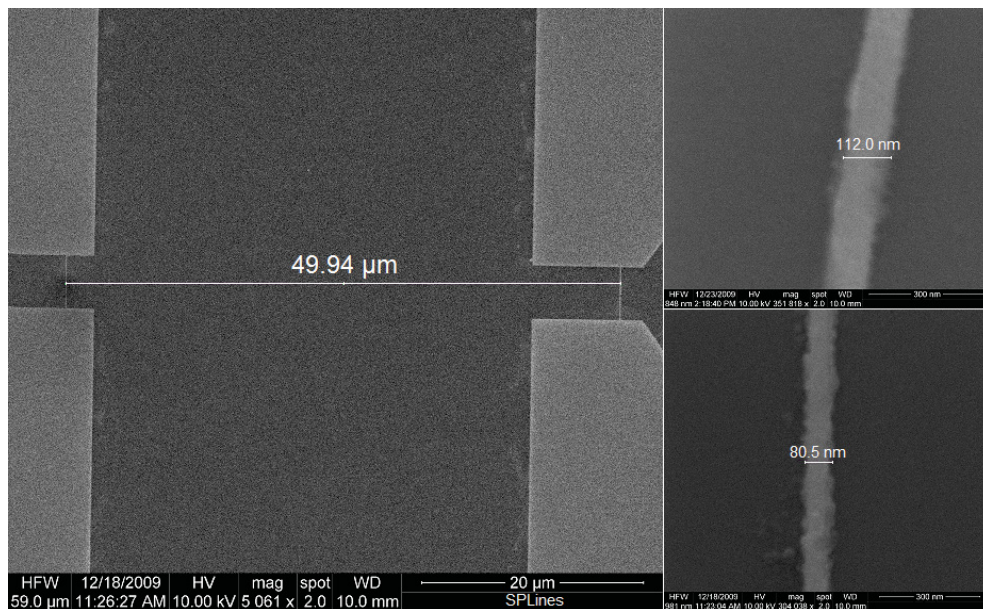


Figure 2.28: SEM micrograph of two single Nb superconducting nanotriple lines contacted in bridge geometry.

Finally, we have used EBL patterning to place working electrical contacts on to graphene monolayers (courtesy of Dr. A. Di Bartolomeo). This technique was shown to be a successful method, even though other methods can be attempted (photolithography). Because of the relatively large size of graphene flakes, movement error is not as much of a problem as with smaller nanostructures. But, graphene has the problem of rolling up and changing positions during spinning of photoresist. To limit this, we can anneal the flakes on the substrate prior to spinning and also ramp up very slowly while spinning. Also, it is incredibly difficult to see the graphene when mapping out the chip with the SEM prior to the EBL write. This makes positioning difficult. Beyond this, graphene is usually deposited on a Si substrate by mechanical exfoliation. Such deposited graphene flakes are randomly distributed on a chip. The probability of obtaining monolayer graphene in this process is very small. For this reason, patterning graphene requires deposition of graphene on a prepatterned substrate containing a coordinate system (usually defined by a matrix of marks). The coordinate system is used to precisely locate graphene on a chip allowing design of lithographic patterns. Figure 2.29 shows graphene monolayers on Si/SiO₂ substrate with contacts placed by EBL.

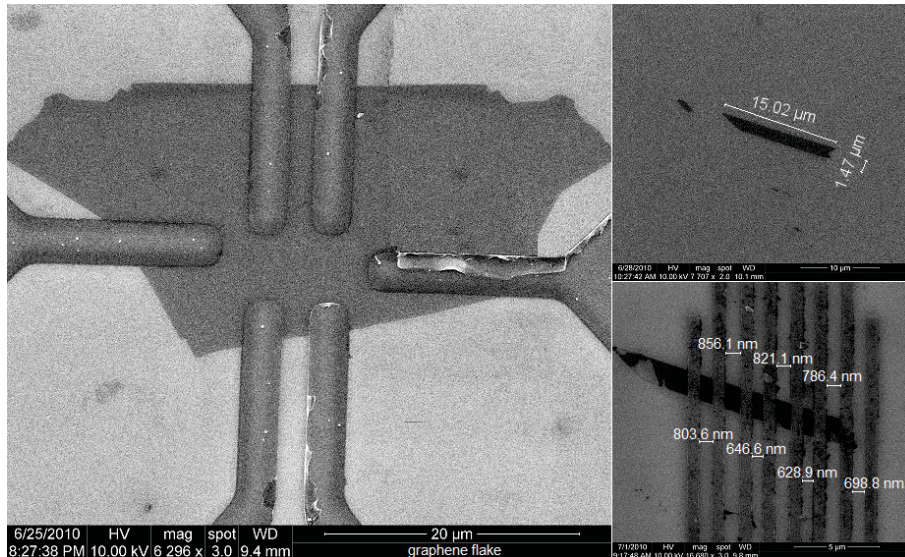


Figure 2.29: *Graphene flake contacted in a Hall-geometry (left) and in multi-contact structure (right).*

2.8.1 Preliminary results

The two devices shown above in Fig. 2.27 and Fig. 2.28 not been discussed in detail in following chapters of this work. Nonetheless, transport measurement for both samples have been successfully performed and here briefly show some results. In Fig. 2.30 we show the current-voltage (I-V) characteristics of the sideward comb-shaped strip recorded at $T = 4.2$ K for several magnetic fields applied perpendicular to substrate and to bias current. The effect of a surface defects on magnetic characteristics of type-II superconductors is an issue of considerable interest and is closely related to the problem of the onset of a magnetic flux (vortices) in superconducting samples. It is well known that vortices start penetrating in bulk type-II superconductors at some critical field H_s (nearly the value of thermodynamical field H_c) which is larger than H_{c1} (the first critical field), due to the Bean-Livingston barrier (attraction of a vortex to its “mirror image” near the surface). Obviously, surface defects will decrease field H_{en} for the first vortex entry in a superconductor: $H_{en} < H_s$ [8]. Therefore we can see a clear asymmetry in the critical currents.

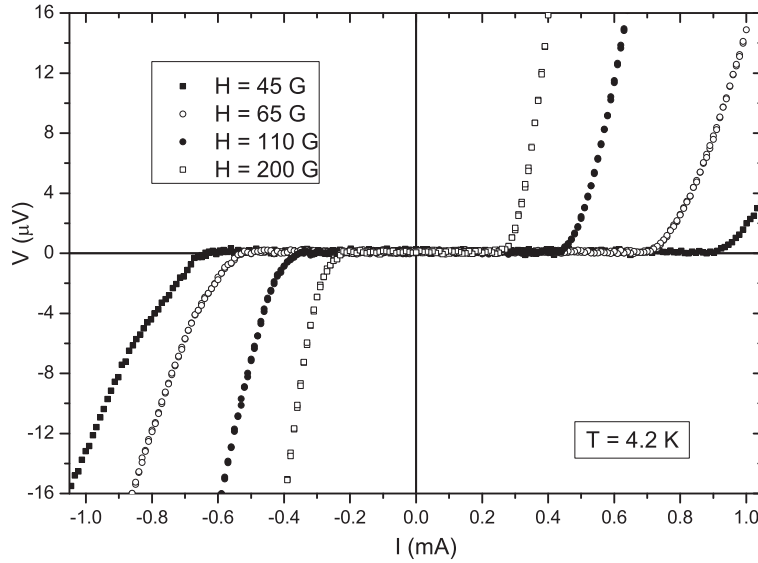


Figure 2.30: I-V characteristics of the sideward comb-shaped strip recorded at $T = 4.2$ K for several magnetic fields applied perpendicular to substrate and to bias current.

Figure 2.31 show the current-voltage characteristic of the nanostripline sample and the formation of so called phase slip lines (PSL) under the external current. One-dimensional superconductors have been expected to be the most simple system one can imagine for the investigation of the current-

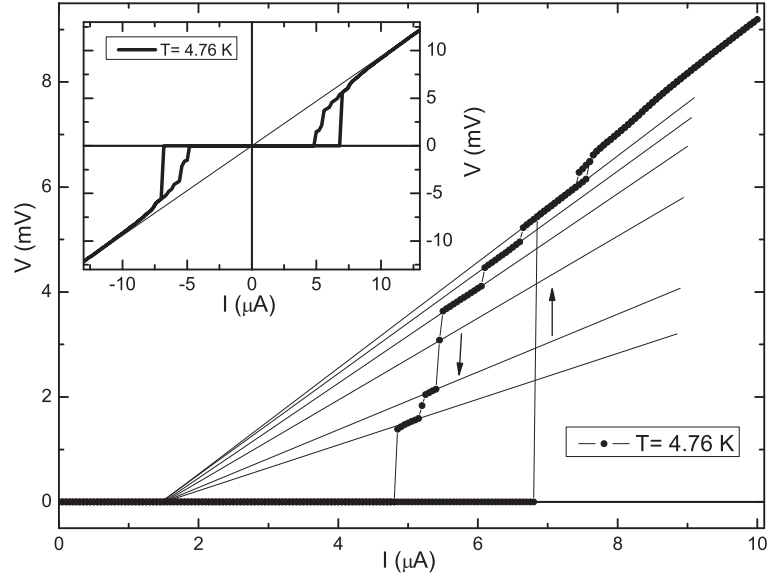


Figure 2.31: I-V characteristic of nanostructure at $T = 4.76$ K. A clear hysteresis is found with increasing and decreasing the applied current (indicated by arrows) with finite jumps in the I-V curve. In the inset, I-V characteristic in the full voltage range at $T = 4.76$ K.

induced breakdown of superconductivity. However, measurements of voltage-current characteristics at fixed temperature T of microbridges at the critical current j_c do not show the direct transition into the fully normal conducting state. Instead, as we see in Fig. 2.31, a large transition width from the first onset of voltage to the complete normal state can be usually obtained. In this transition region the voltage increases in a series of regular voltage jumps. Moreover, electromagnetic radiation can be detected in such samples resembling the Josephson effect. These facts indicated to nonequilibrium and nonstationary nature of the formation of resistive state in such small samples. A resistive state without a complete destruction of the superconducting state by temperature, magnetic field or current can be at first confusing because the first hallmark of superconductivity is violated, but it becomes clearer once one studies the responsible fluctuations in details. To summarize, applying a sufficient current to a superconducting wire can place it into a resistive state where superconductivity is not completely lost but where thermal fluctuations allow the presence of a voltage within the wire.

2.9 Measurement system setup

The measurements presented in this work has been performed using an home-made immersion-type cryostat, i.e. the insert is immersed directly into liquid helium at 4.2 K inside a dewar, and an Oxford HelioxVL helium three cryostat supplied from Oxford Instruments. The cryostat was interfaced with a dedicated electronic setup to allow low noise measurements of I-V characteristic. Here I give a brief description of both the HelioxVL cryostat and the electronic setup used to acquire the I-V characteristics in magnetic field.

2.9.1 HelioxVL cryostat

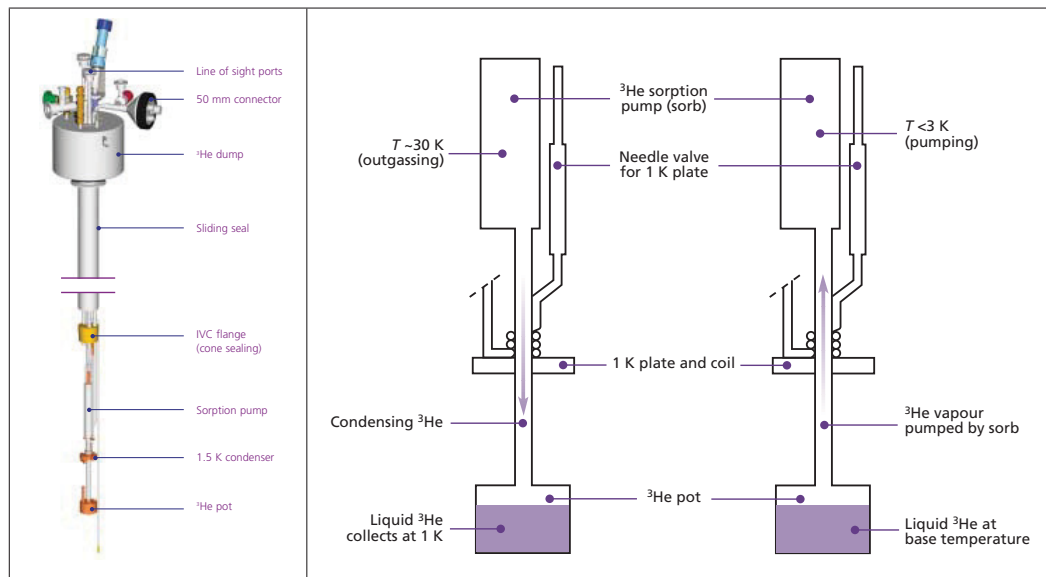


Figure 2.32: (left) *Schematic diagram of the HelioxVL system.* (right) *Operating principle of the HelioxVL.* [9]

For very low temperature measurements with larger magnetic fields the ^3He Oxford Instruments HelioxVL was used. This system has a base temperature of 0.3 K with a superconducting coil producing a maximum field of 2 T. This probe fits into a 50 mm diameter liquid helium dewar neck. The insert is described in Fig. 2.32 (left). The principle of operation of the ^3He system is shown in Fig. 2.32 (right). The sample sits in a vacuum, thermally connected to the 1 K pot and ^3He pot. ^4He is drawn up through a capillary from the dewar into the 1 K pot, which is pumped on by a rotary pump. This achieves a ~ 1.5 K temperature. With the sorption pump at ~ 30 K, ^3He is then condensed into the ^3He pot. The sorption pump is then allowed

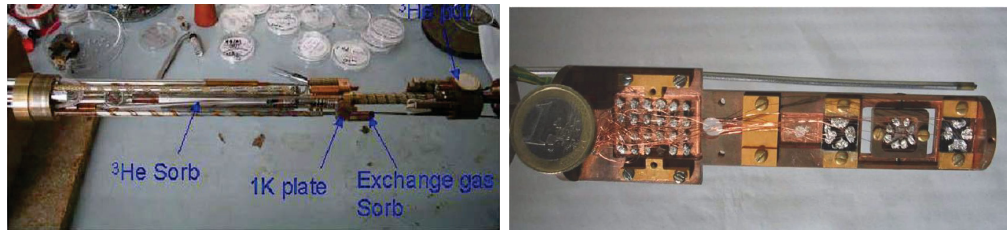


Figure 2.33: (left) *Picture of the inner IVC chamber.* (right) *Picture of the sample holder.*

to cool and pump on the condensed ^3He , reducing the temperature to 0.3 K. Base temperature could be maintained for several hours before the cycle had to be restarted.

Both the sample and the sorption pump temperature are controlled by a ITC503 Temperature Controller (Oxford Instruments). The ITC system can be configured to control the whole system and it is possible to configure computer interface using a software called Object-Bench driven by a RS232, thus we can control the insert operation in automatic mode just using the software. A picture showing the last stage of the Inner Vacuum Chamber (IVC) of the cryostat is given in Fig. 2.33 (left), in which we can clearly distinguish the ^3He Sorb, 1 K Plate, ^3He Pot and the Exchange gas Sorb, while in Fig. 2.33 (right) is shown the sample holder used to interface with a dedicated external electronic setup. The sample is loaded onto a dedicated Cu-holder and attached to the ^3He Pot, in this way the whole holder is at the ^3He temperature of the Pot and the sample is cooled by conduction.

2.9.2 Measurement electronics

For the acquisition of the I-V curves in magnetic field the electrical setup depicted in Fig. 2.34 has been used.

For measurements in liquid He, we used a superconductive solenoid that allows to sweep the field up to 8000 G. The sample is positioned into the coil bore by mean of the HelioxVL insert with electric access at head of the insert itself. The solenoid is supplied by a current generator Kepco BOP 50-20MG. It supplies 20 A with a voltage compliance of 50 V. The Kepco generator is programmable in current by mean of a voltage signal and the current supplied is detected through a monitor (voltage signal). Normally, we use a DC power supply Agilent E3631A to program the Kepco generator. Optionally, a waveform generator Agilent 33120A is used to program the current while the monitor signal (proportional to the current trough the solenoid) is read by a Agilent 34401A multimeter. Since the solenoid has not

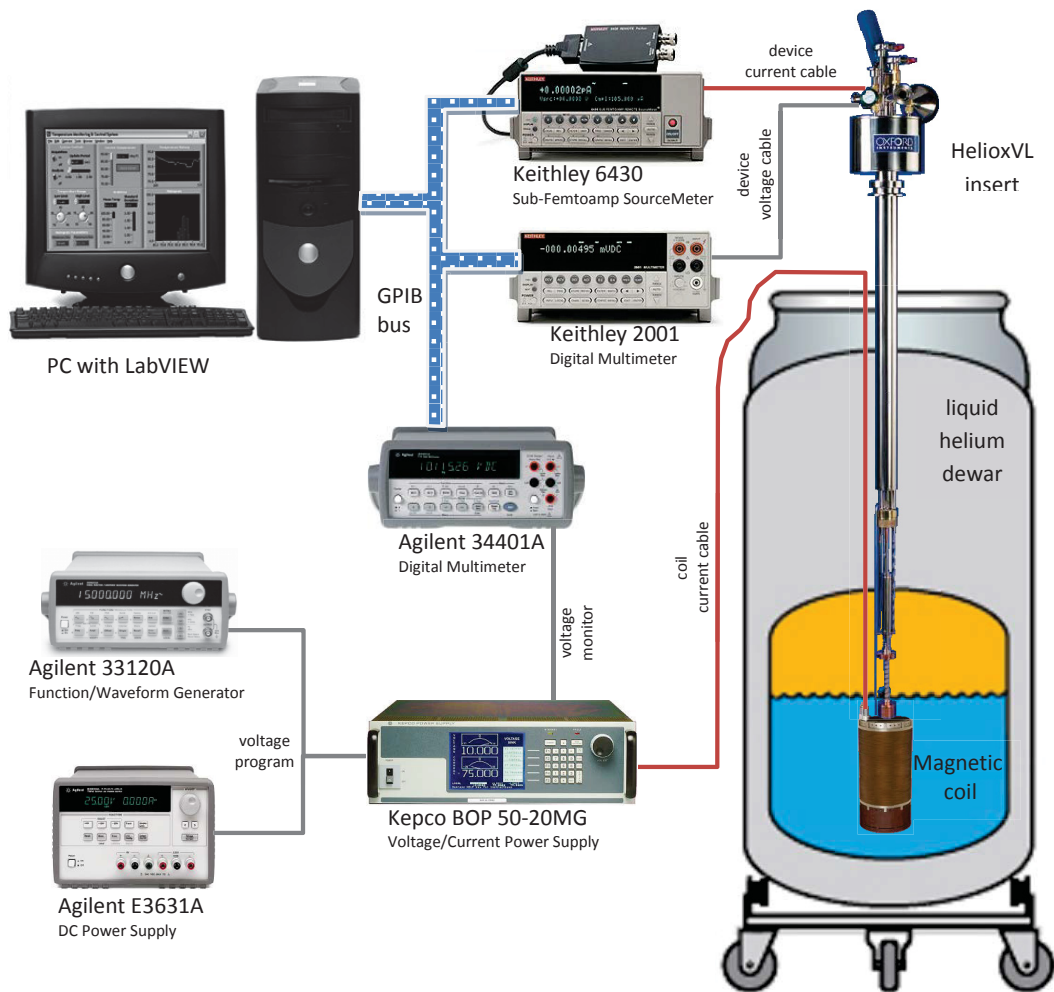


Figure 2.34: Schematic of the electrical setup used for the acquisition of the I-V curves.

hysteresis, knowing the current that passes through it and the conversion factor we are able to know the generated magnetic field. The Agilent 34401A multimeter is interfaced to LabVIEW by a GPIB board. Usually a triangular waveform is used to sweep the field with typical sweeping frequencies of the order of some mHz. With sweeping frequencies in the mHz range the field resolution is usually better than 1 G.

For measuring the I-V characteristics we use two different multimeters. The Keithley 6430 is utilized to supply the sample and to measure small currents; in fact it measures very low currents, with a current resolution of the order of the femtoampere and voltage resolution of the μV order.

The digital multimeter Keithley 2001 (sometimes also used together with a Keithley 1801 nanovolts pre-amplifier) is used to measure the voltage signal of the device. Both the multimeters are interfaced to LabVIEW by a GPIB card placed in the Measurement PC.

Bibliography

- [1] A. A. Tseng, K. Chen, C. D. Chen, and K. J. Ma, *Electron beam lithography in nanoscale fabrication: recent development*. Electronics Packaging Manufacturing, IEEE Transactions on **26**, 141-149 (2003).
- [2] M. A. McCord and M. J. Rooks, *Handbook of Microlithography, Micromachining, and Microfabrication*, edited by P. Rai-Choudhury (SPIE and The Institution of Electrical Engineers, Bellingham, Washington, 1997), Vol. 1, Chap. 2, pp. 139–249.
- [3] *The Inspect F User Operation Manual*. (FEI Company, 3rd ed., 2007).
- [4] *PMMA and Copolymer Data Sheets*. (MicroChem Corp., 2001).
- [5] *ELPHY Plus: Software Operation Manual*. (Raith GmbH, ver. 4.0, 2005).
- [6] V. Granata, *Experimental Study of ferromagnetic and ferromagnetic/superconductor heterostructures*. Ph.D. Thesis, University of Salerno (2009).
- [7] F. Russo, *Spin-dependent transport in magnetic layered heterostructures*. Ph.D. Thesis, University of Salerno (2007).
- [8] D. Yu. Vodolazov, *Effect of surface defects on the first field for vortex entry in type-II superconductors*. Phys. Rev. B **62**, 8691 (2000).
- [9] *HelioxVL Insert Manual*. (Oxford Instruments, rev. 3, 2006).

Asymmetry, bistability, and vortex dynamics in a finite geometry ferromagnet-superconductor bilayer structure

3.1 Introduction

In the past years the Ferromagnet/Superconductor (FS) hybrids [1–3] based both on oxide and metallic thin film have attracted a lot of interest, also due to the possibility to control superconductivity by the exchange field [1, 4, 5], spin imbalance [6–9], or by the stray fields generated by the ferromagnet [10–16]. Recently, FS heterostructures have also been proposed [17–20] for the realization of superconducting rectifiers [21–29] less technologically demanding and with enhanced power handling capability. Ferromagnetic materials where stripe domain magnetic structure is achieved have been demonstrated to be very effective to control superconductivity [30–32] at sub-micron scale. Very recently Permalloy-based FS hybrids with Permalloy in the weak stripe domain regime [33] have been demonstrated to induce *anisotropic* transport properties [34, 35] and to act as guiding channels [36] for Abrikosov vortices in the superconducting layer.

Recently, we have demonstrated [29] that a Py/Nb bilayer, patterned in a Hall geometry and with Py in the stripe domain regime, can exhibit strongly asymmetric and bistable transport properties, i.e., it can behave as a bistable superconducting diode. Here we discuss some additional relevant experimental data and, with the help of numerical simulations, we discuss in detail and more quantitatively the main physical mechanism involved in the bistable diode. Numerical simulations substantially confirm the hypothesis [29] that the observed bistable diode behavior can be accounted for by the stray fields from the patterned ferromagnetic layer. Moreover, using the two

dimensional time dependent Ginzburg Landau equation, in this Chapter we also numerically address in detail the vortex dynamics involved in a superconducting film embedded in the inhomogeneous magnetic field generated by a finite geometry ferromagnetic bar in the stripe domain regime. The main result of vortex dynamic simulations is that, at zero externally applied magnetic field and with current applied perpendicular to the magnetic stripes, a peculiar channeled flux flow regime is achieved, with alternating vortex and antivortex chains moving in the opposite directions in the superconducting layer. Such a regime reminds the one reported in recent works [37, 38] done in other FS heterostructures, where a periodic array of micrometer size ferromagnetic bars was used to create two channels of opposite polarity for vortex-antivortex chains. In our case, these channels are naturally created by the stray fields of the continuous Py film in the stripe domain regime. When current is applied along the magnetic stripes, another dissipative mechanism is realized, consisting of creation of vortex-antivortex pairs in the channels followed by a Lorentz force-assisted vortex-antivortex pairs annihilation.

The Chapter is organized as follow. In Section 3.2, after a very brief summary of the main experimental results [29], we present and discuss some supplementary results useful to gain insight in the physics involved in the system. In Section 3.3, we first analyze numerically the distribution of stray fields from the finite geometry ferromagnetic layer and then study the transport properties of the thin superconducting layer embedded in the inhomogeneous magnetic field generated by the ferromagnetic layer. Micromagnetic simulation are performed assuming the Landau Lifshitz Gilbert model for ferromagnet and the transport properties of the superconductor are simulated using the two dimensional time dependent Ginzburg Landau equation. A summary of the main results is given in Section 3.4.

3.2 Basic phenomenology and discussion

The focus of this Chapter is on numerical study of working mechanisms of the bistable vortex diode. Here we only recall two relevant experimental facts already published in our recent work and we add some new experiments that help us to discuss the physics involved in the diode. For further experimental results and details we refer the reader at Ref. [29].

In Fig. 3.1(a) we show the $V(I)$ curve of a Py(640 nm)/Nb(60 nm) bilayer [29] in the full voltage range, recorded at 4.6 K (superconducting state) and at 6.0 K (normal state). The critical currents (I_{CP} , and I_{CN} , the current values at which the transition to the fully normal state is achieved) are found to differ slightly, around 20%. In the bottom frame of Fig. 3.1(a)

we show a blow up of the low voltage region of the $V(I)$ curve at 4.6 K. Two rather different depinning currents (I_{DP} , and I_{DN} , the current values corresponding to the transition $V = 0 \rightarrow V \neq 0$) are exhibited. Due to two substantially different depinning currents, the bilayer exhibits infinite or finite conductance depending of the sign of the bias current, so that it behaves like a superconducting diode (the dual of a semiconducting diode).

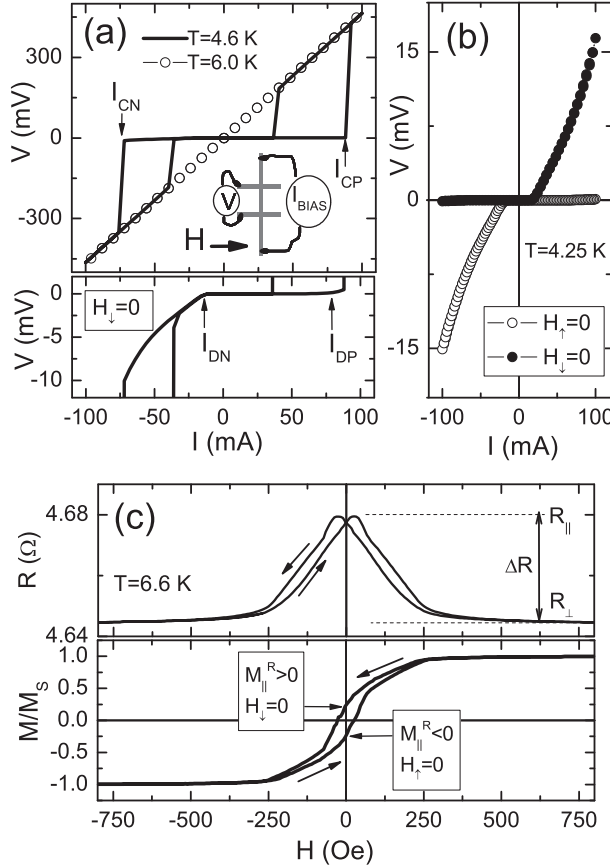


Figure 3.1: (a) The $V(I)$ curve of the Py/Nb bilayer in the full voltage range, at 4.6 K (superconducting state) and at 6.0 K (normal state). The geometry of the bilayer is shown in the insets. The $V(I)$ curve at 4.6 K with amplified low voltage range exhibits two quite different depinning currents, as shown in the bottom panel. (b) $V(I)$ curve of the device recorded in the two possible stable states at $H = 0$. (c) The AMR of the device at temperature slightly larger than the critical temperature of the Nb. The normalized hysteresis loop of the bilayer calculated from the above AMR signal is shown in the bottom panel.

The $V(I)$ curve in Fig. 3.1(a) was recorded after a preparing magnetic field was applied in the plane of the device, as shown in the inset, and was decreased from a relatively large positive value ($H=1000$ Oe) toward $H = 0$, at which value the curve was recorded. Here and in the following we shall use $H_{\uparrow} = 0$ to mean that the in-plane magnetic field was started from large negative values, and $H_{\downarrow} = 0$ to mean that the field was started from large positive values. The $V(I)$ curves of the device recorded at $H_{\uparrow} = 0$ and $H_{\downarrow} = 0$ are plotted [29] in Fig. 3.1(b). We emphasize that the $V(I)$ curve in the magnetic state at $H_{\uparrow} = 0$ is mirrored with respect to the origin in the

other stable magnetic state at $H_{\downarrow} = 0$, *i.e.*, the $V(I)$ of the FS bilayer is not only asymmetric but also bistable. With respect to the full hysteresis loop of the Py, these two states correspond to the two possible in-plane remanent magnetizations, $M_{\parallel}^R > 0$ at $H_{\downarrow} = 0$, and $M_{\parallel}^R < 0$ at $H_{\uparrow} = 0$, as it is better seen in Fig. 3.1(c), where we show the normalized hysteresis loop of the Py at 6.6 K (bottom panel) calculated [39] from the anisotropic magneto-resistance (AMR) signal (top panel) of the bilayer. The hysteresis loop $M(H)$ was extracted from the $R(H)$ measured for magnetic field applied perpendicular to the current by means of relation $M/M_S = \pm \sqrt{[R_{\parallel} - R(H)]/\Delta R}$, where the symbols are the ones shown in Fig. 3.1(c). This relation is obtained from AMR relation [39] $R(\theta) = R_{\perp} + \Delta R \cos^2(\theta)$, where θ is the angle between magnetization and current density, that, for polycrystalline materials as it is our sputtered Py, can also be recast in the form $R(H) = R_{\parallel} - \Delta R (M/M_S)^2$, with M the component of magnetization along the magnetic field direction.

In Fig. 3.2 we report some other experimental results that can be useful to gain insight into the origin of the observed asymmetric and bistable behavior of the bilayer. In Fig. 3.2(a) we compare the $V(I)$ curves of the Py(640 nm)/Nb(60 nm) bilayer recorded at 4.95 K with the preparing magnetic field applied either along or perpendicular to the bias current. Apparently, the asymmetry of depinning currents does not occur when the preparing field is parallel to the bias current. For magnetic field perpendicular to the bias current, the asymmetry was found to be strongly reduced if the Py and Nb layers were spaced by a 50 nm thick SiO_2 , as shown in Fig. 3.2(b). A substantial reduction of asymmetry was also observed when in the bilayer the width of the bottom Py layer was made larger than the width of the top Nb layer. This is seen in Fig. 3.2(c), where we compare the $V(I)$ curves of a bilayer with same width for Py and Nb (both $100\mu\text{m}$ wide) versus a bilayer with $200\mu\text{m}$ wide Py and $100\mu\text{m}$ wide Nb.

As discussed in Ref. [29], we observed asymmetry in samples with 480 nm or 640 nm thick Py, but not in a sample with 180 nm thick Py. This suggests that in the thicker samples the Py might be in the stripe domains regime [33, 36]. From magnetic measurements performed with a VSM we estimated [29] a perpendicular anisotropy constant $K_u = 9 \times 10^4 \text{erg/cm}^3$, and a critical thickness for stripe domains [33, 36] $t_c \simeq 210$ nm for our Py at $T=10$ K. This agrees with the hypothesis that a stripe domain structure builds up in the thicker samples, but not in the 180 nm-thick Py sample. The stripe width can be estimated [36] from above data as $d \approx 240$ nm. The critical thickness of our Py is similar to the one reported [33, 36] in recent works, where it has been demonstrated that a well developed stripe domain regime is in fact achieved beyond the above estimated critical thickness.

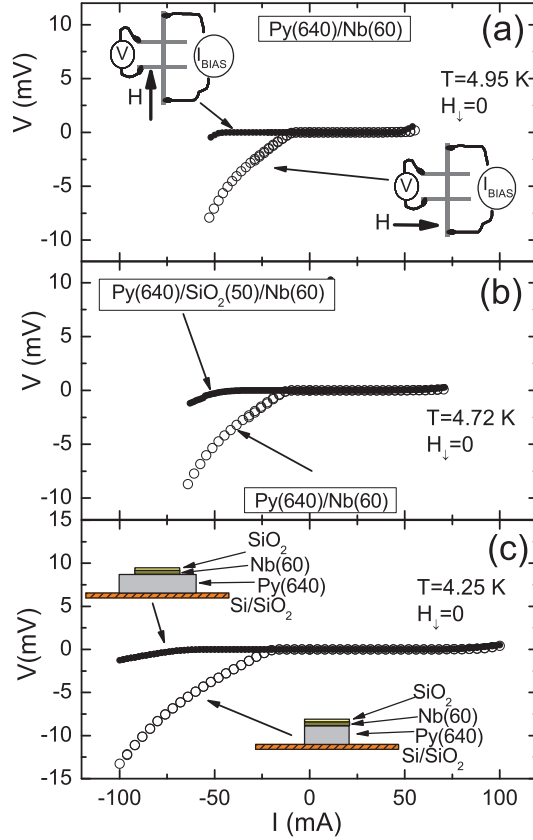


Figure 3.2: (a) Comparison of $V(I)$ curves of the Py(640)/Nb(60) bilayer recorded at 4.95 K with preparing magnetic field applied along or perpendicular to the bias current, as shown in the insets. (b) $V(I)$ curves of a Py(640)/Nb(60) and a Py(640)/SiO₂(50)/Nb(60) bilayer at 4.72 K. Bias current is perpendicular to the preparing field. (c) $V(I)$ curves at 4.25 K for two Py(640)/Nb(60) bilayers having the Py of same width as (see lower inset) or larger width than (see top inset) the Nb layer.

Magnetic data suggest that the mechanism accounting for the bistable diode behavior could involve the stray fields from the patterned Py layer in the stripe domain. Before we proceed further, we shall comment other two known mechanisms that also generate asymmetric $V(I)$ curves. The simple mechanism [19] based on fringe fields at edges of the FS bilayers that add to the self fields of transport current cannot account for all of our experimental results. If such a mechanism were the most relevant, the asymmetry should increase with magnetic field [17], as the fringe fields are stronger in the fully in plane magnetically saturated state. Inspection of Fig. 1(d) of our previous work [29] suggests that this is not our case. Moreover, an asymmetry should be observed also for the 180 nm thick Py sample. This, again, is not our case. We also think that our results are not accounted for by the mechanism of asymmetric surface barrier [21,22]. Though here we have asymmetric boundary conditions for Nb, we should admit that the in plane magnetic field generates vortices with flux lines in the plane of the Nb film so that Lorentz force pushes them out of the film, along its thickness, to experience the surface barriers. This is very unlikely in our case because the Nb film is thinner

than the London penetration length, as opposite to the experiments [21, 22] where Pb/Pb_{0.95}Tl_{0.5} ribbons much thicker than London penetration length in those materials were used. However, if present, this mechanism should be effective [21, 22] only for in plane magnetic field $H_{c1}^{\parallel} < H < H_{c2}^{\parallel}$. In our Nb film these critical fields are estimated to be equal to several thousand Oe. Instead, we observe strong asymmetry also without any externally applied magnetic field. Moreover, we should observe asymmetry even if the Py layer were made thinner than the critical thickness for nucleation of a stripe domain regime, or if its width were larger than the width of the Nb strip. As said above, this was not our case.

In our Py layers the strength of stray fields from weak stripe domain is estimated [40] to be lower than the critical field $H_{c1} \approx 300$ Oe of our Nb at 4.2 K. Thus, these stray fields can act only as a periodic potential that can channel the Abrikosov vortices or anti-vortices however generated in the Nb. The channeling effect [36] of the stripes in the Py can be expected, because the estimated stripe width is larger than the size of the vortices, *i.e.* $d \geq 2\lambda_L$, as London penetration depth of our Nb was estimated to be $\lambda_L \simeq 100$ nm at 4.25 K. In the above reported experimental data, the direction of channels was set [36] by the preparing field applied perpendicular to the transport current. But, what generates Abrikosov vortices, with flux lines perpendicular to the Nb film, that the Lorentz force associated to a transport current can move along the plane of the film in the channels so generating a voltage? A source of such vortices can be the perpendicular component of stray fields at edges of the patterned ferromagnetic strip that adds to the stray fields from stripe domains.

3.3 Numerical simulations

To make more clear the above picture, we numerically studied the distribution of stray fields from a patterned ferromagnetic layer and the response of a thin superconducting layer to the inhomogeneous magnetic field generated by the ferromagnetic layer.

3.3.1 Micromagnetics

Micromagnetic simulations were performed using the 3D OOMMF micromagnetic simulation package [41], based on Landau-Lifshitz-Gilbert equation for ferromagnets. A Py slab of width $W = 1960$ nm, length $L = 1460$ nm, and thickness $d = 480$ nm was chosen. Lateral physical dimensions was chosen to retain relevant information within capabilities of our computer

(an Intel I7 940 quad core processor with 4 GB RAM). The cell size was $\Delta x = 20$ nm, $\Delta y = 10$ nm, and $\Delta z = 10$ nm. The perpendicular anisotropy was $K_u = 3 \times 10^5$ erg/cm³, slightly larger than, though comparable to, the experimental one. The magnetic field was applied in the plane of the slab, along the x direction, and the states $H_{x\downarrow} = 0$ and $H_{x\uparrow} = 0$ were studied, with emphasis on the distribution of the out of the plane (i.e., along z direction) component of the stray fields. In Fig. 3.3(a) we show the calculated distribution of the perpendicular component of the magnetization in the remanent state (achieved at $H_{x\downarrow} = 0$) of the Py slab with anisotropy along z axis. The stripe domain regime with alternating up (brighter regions) and down (darker regions) magnetization occurs with the used parameters. In Fig. 3.3(b) we show the vectorial distribution of the total magnetic field in a cross section in the $z - y$ plane centered in the middle (i.e., at $x = W/2$) of the Py slab. Stray fields on the top of the slab appear to be periodic

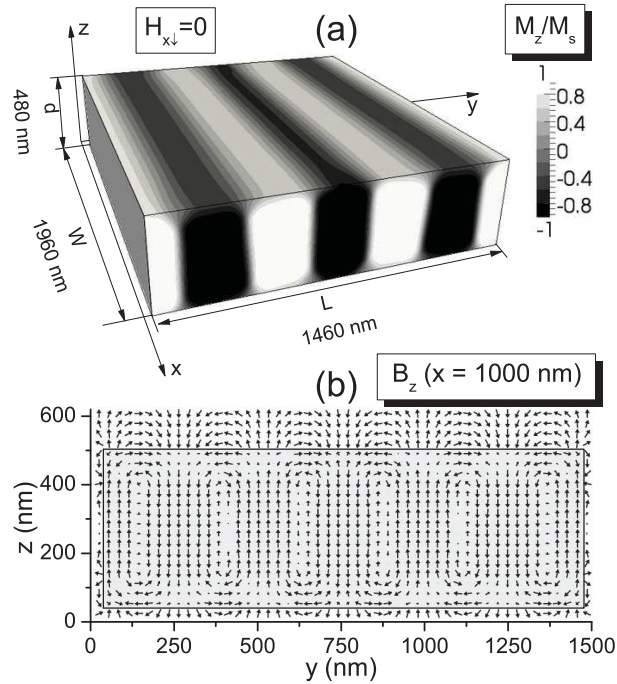


Figure 3.3: (a) Calculated distribution of the perpendicular component of the magnetization in the remanent state (achieved at $H_{x\downarrow} = 0$) of a Py slab with anisotropy along z axis showing stripes domains. (b) Calculated vectorial distribution of total magnetic field in a slice in the $z - y$ plane centered in the middle of the Py slab. Both the field in Py (shaded region) and the field out of Py (stray field) are shown.

along the length (y direction) of the slab with a spatial period 2ℓ , where $\ell \simeq 250$ nm is the stripe width.

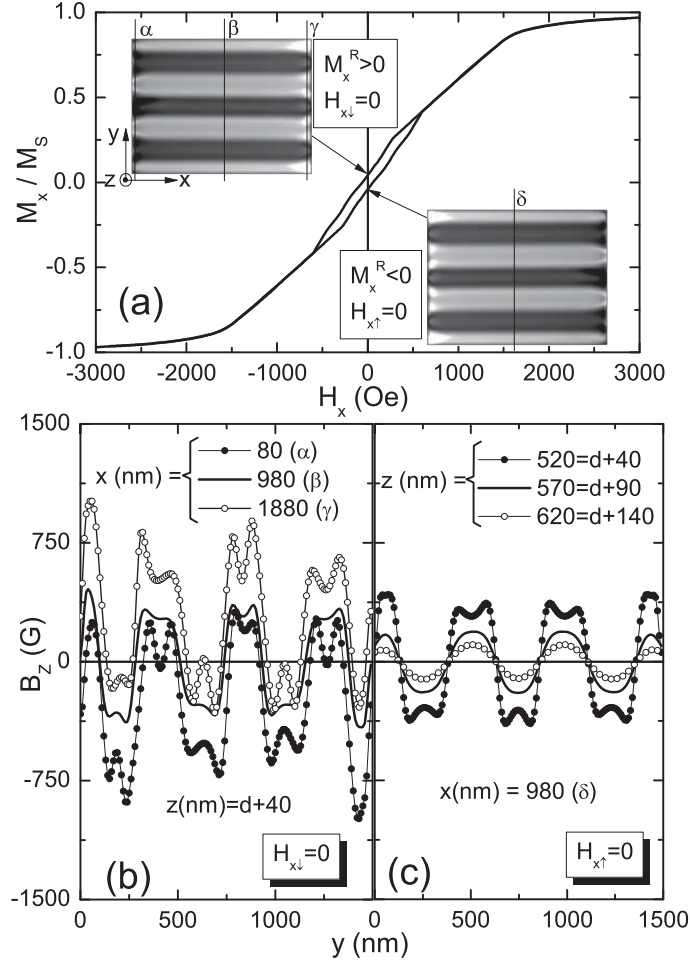


Figure 3.4: (a) Calculated in plane hysteresis loop of Py slab. In the insets, the distribution of out of plane component (z component) of stray fields on the top face of the slab for the two remanent states. (b) Out of plane component of stray field just above the slab scanned along the three different lines labeled as α , β , and γ in the upper inset in (a). (c) Out of plane component of stray field above the 480 nm thick slab scanned along the line labeled δ in (a) and three different z levels are shown.

Further details about the stray fields on the top of the slab, that are the fields affecting the Nb layer, are given in Fig. 3.4. In Fig. 3.4(a) we report the calculated in plane hysteresis loop of the Py slab and the spatial distribution of the out of plane component (z component) of stray fields on

the top face of the slab for the two remanent states. In the bright (dark) regions the field points to the positive (negative) z -direction. At the edges of the slab the intensity of the stray field is larger than at the center, with role of edges inverted in the two remanent states. In Fig. 3.4(b) we plot the out of plane component of the stray field 40 nm above the slab, scanned along the three different lines labeled as α , β , and γ in the upper inset in Fig. 3.4(a). The intensity of stray fields is about 270 G at the center of the slab but peaks to about 600 G at the right edge and -600 G at the left edge. In other words, to the stray field at the center of the slab, a field B_{0z} is added near the right edge and a field $-B_{0z}$ is added near the left edge. This modulation of stray fields along the x direction (i.e., the direction of stripes we set with applied field H_x) is accounted for by the Bloch domain walls separating the up and down stripe domains we can envisage in Fig. 3.3. At the domain walls a magnetization M_x along x direction is always present, and such a component generates magnetic charges (of opposite sign) at left and right edges. These magnetic charges, in a way similar to a ferromagnet without perpendicular anisotropy, produce an additional stray field with a maximum z component $\pm B_{0z}$ at edges of the slab that adds to the stray field from stripes. In a particular stripe domain, as one can see in Fig. 3.4(b) for a constant value of y , the total stray fields are stronger at one side while at the other side of the stripe the total stray fields are even a bit reduced. One could suspect that this kind of asymmetry in the magnetic field profile between the left and right edge of the sample breaks reflection symmetry and creates a vortex ratchet potential. But, as it will be more clear below, in our system we have not a ratchet potential [20,24], though the different intensity of stray fields at edges accounts for an asymmetric onset of vortex motion. Finally, in Fig. 3.4(c) we plot the stray field at center as a function of the separation from the top face of the 480 nm thick slab. The scanning is along the line labeled δ in Fig. 3.4(a) and three different z levels are considered. These levels correspond to 40 nm, 90 nm, and 140 nm above the surface of the slab. Apparently, beside the expected amplitude reduction, the functional form of stray fields approximates a square wave near the slab and a sinusoid far from the slab, in agreement with recent analytical results [42].

3.3.2 Vortex dynamics

To study numerically the transport properties of our thin superconducting Nb layer embedded in the stray fields of the ferromagnetic Py, we integrated the two-dimensional time-dependent Ginzburg-Landau equation supplemented

with the equation for the electrostatic potential [43, 44]

$$u \left(\frac{\partial}{\partial t} + i\varphi \right) \psi = (1 - |\psi|^2) \psi - (i\nabla + \mathbf{A})^2 \psi, \quad (3.1)$$

$$\nabla^2 \varphi = \text{div} \{ \text{Im} [\psi^* (\nabla - i\mathbf{A}) \psi] \}, \quad (3.2)$$

where $\psi = |\psi| e^{i\phi}$ is the complex order parameter, \mathbf{A} is the vector potential, φ is the electrostatic potential and the coefficient $u = 5.79$ accounts for the relaxation of the order parameter [45]. All the physical quantities are measured in dimensionless units. The spatial coordinates are in units of the coherence length $\xi_0 = \sqrt{8k_B T_c / \pi \hbar D}$ (T_c is the critical temperature, D is the diffusion constant) and time is scaled in units of the Ginzburg-Landau relaxation time $\tau_0 = 4\pi\sigma_n \lambda_L^2 / c^2$ (σ_n is the normal-state conductivity, λ_L the magnetic field penetration depth). The order parameter is in units of $\Delta_0 = 4k_B T_c \sqrt{u}$ (the superconducting gap at $T = 0$ which follows from Gor'kov's derivation of the Ginzburg-Landau equations), the vector potential is scaled in units $\Phi_0 / 2\pi\xi_0$ (Φ_0 is the quantum of magnetic flux) and the electrostatic potential is in units of $\varphi_0 = c\Phi_0 / 8\pi^2 \xi_0 \lambda_L \sigma_n$. In these units the magnetic field is scaled with $H_{c2} = \Phi_0 / 2\pi\xi_0^2$ and the current density with $J_0 = \sigma_n \hbar / 2e\tau_0 \xi_0$.

For the sake of simplicity, we neglect intrinsic pinning effects and we assume $T = 0$. Self fields associated to the bias current and the screening effects are also neglected, otherwise an equation for the vector potential \mathbf{A} should be integrated in the above model. This simplification has been often used in the so-called high κ limit [46] and it is reasonable also for our sputtered Nb. In fact, in our Nb the coherence length is estimated $\xi \simeq 13$ nm and the penetration depth $\lambda_L \simeq 100$ nm at 4.2 K giving $\kappa \simeq 8$. The condition $(i\nabla + \mathbf{A}) \psi|_{\mathbf{n}} = 0$ is assumed for the order parameter at boundary, where \mathbf{n} is the unit vector normal to the contour of the superconductor. In order to inject an uniform bias current density J in our system we used conditions $-\nabla\varphi = (0, J)$ at the boundaries.

The effect of the ferromagnet on the superconductor enters through the vector potential \mathbf{A} in Eqs.(3.1) and (3.2). For the stray fields from stripe domains of fixed width ℓ aligned along x axis, a good approximation for the vector potential [42] is

$$A_x(y) = 2h_s \ln \frac{\cosh \frac{\pi a}{\ell} + \cos \frac{\pi y}{\ell}}{\cosh \frac{\pi a}{\ell} - \cos \frac{\pi y}{\ell}}, \quad (3.3)$$

where a is the distance from the upper face of the ferromagnet. The origin of the $x - y$ reference frame is assumed here and in the following in the center

of the $L \times W$ superconducting film [see Fig. 3.5]. To describe the modulation of stray fields at edges of the slab we assume the vector potential

$$A_y(x) = \frac{h_o}{h_r} \left\{ \text{atan} [h_r (x + W/2)] - \text{atan} [h_r (x - W/2)] - 2\text{atan} (h_r W/2) \right\}. \quad (3.4)$$

According to Eqs.(3.3) and (3.4), the magnetic induction (describing stray fields) $\mathbf{B} = \nabla \times \mathbf{A}$ is vanishing but for the perpendicular component, given by

$$B_z(x, y) = h_o / [h_r^2 (x + W/2)^2 + 1] - h_o / [h_r^2 (x - W/2)^2 + 1] - \frac{4\pi h_s \cosh \frac{\pi a}{\ell}}{\ell} \frac{\sin \frac{\pi y}{\ell}}{\sin^2 \frac{\pi y}{\ell} + \sinh^2 \frac{\pi a}{\ell}}. \quad (3.5)$$

To integrate the system Eqs.(3.1) and (3.2) we make use of a finite-difference representation for the order parameter, vector potential, and electrostatic potential on a uniform Cartesian 129×129 space grid (corresponding to $W = L = 80 \xi_0$) and we employ a Dormand-Prince embedded method [47] for ordinary differential equations (an embedded Runge-Kutta integrator of order 8 with stepsize control) to find ψ . The electrostatic potential is obtained by the Fourier transform method [47]. When calculating the $E(J)$ [proportional to the $V(I)$] characteristics, we evaluated the electric field component E along current direction inside the superconducting sample at a distance $15 \xi_0$ from the current injection interface. In this way the contact resistance at the interface is not taken into account and our results simulate a four-probe measurement. Initial conditions were $|\psi| = 1$ and $\varphi = 0$. The behavior of the system is studied on a large time scale, so that time-averaged values are stationary.

In Fig. 3.5 we show a gray scale plot of the magnetic field $B_z(x, y)$ acting on the superconductor when the ferromagnet is in one of the two remanent states, as described by Eq.(3.5). For simplicity only one spatial period along y axis is represented. Bright (Dark) regions are for field pointing in positive (negative) z -direction. These stray field patterns mimic the ones of Fig. 3.4(a). Here a negative h_o parameter describes the state at $H_{x\downarrow} = 0$ and a positive h_o the state at $H_{x\uparrow} = 0$. In the micromagnetic simulations illustrated in Fig. 3.4, we found that the intensity of the stray fields is about 270 G at the center of the slab, rising to about ± 600 G at the edges. Noticing that in our Nb we estimate $H_{c1} \approx 300$ G at 4.2 K, the simulation parameters h_o and h_s are chosen so that the magnetic field is strong enough to nucleate vortices or antivortices at the edges of the film but not in the bulk of the film.

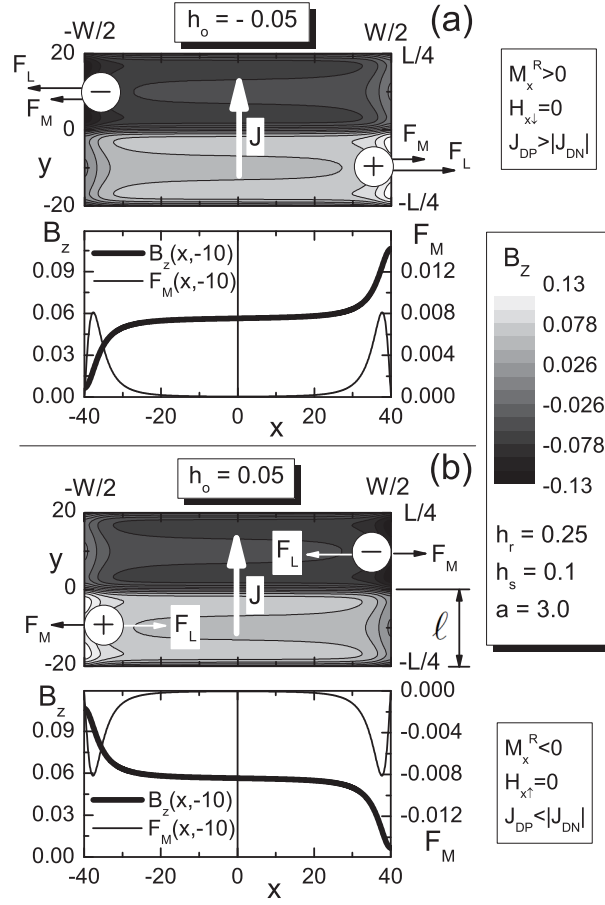


Figure 3.5: (a) Gray scale plot of the the stray magnetic fields $B_z(x, y)$ acting on the superconductor when the ferromagnet is in the remanent state at $H_{x\downarrow} = 0$. A sketch of the forces acting on the vortices and anti-vortices nucleating in the superconductor is also shown. In the bottom panel there are shown the magnetic field profile $B_z(x, -10)$ and the magnetic force $F_M(x, -10)$ experienced by a vortex along the channel centered at $y = -10$. (b) Same as in (a), but the ferromagnet is now in the remanent state at $H_{x\uparrow} = 0$.

In Fig. 3.5 we also show a sketch of the forces acting on the vortices and anti-vortices nucleating in the superconductor, as it helps to predict some results. Beside the Lorentz force associated to the transport current density, magnetic forces generated by the inhomogeneous magnetic field are present. Magnetic forces are proportional to the spatial gradient of the magnetic field $\mathbf{F}_M \propto \pm \nabla B_z(x, y)$, therefore in our patterns the vortices are attracted toward the brighter regions and the anti-vortices toward the darker regions. As an

example, in the bottom panels of Fig. 3.5(a) and Fig. 3.5(b) there are shown the magnetic field profile $B_z(x, -10)$ and the associated magnetic force $F_M(x, -10) \propto \partial B_z(x, -10)/\partial x$ experienced by a vortex along the channel centered at $y = -10$ when the ferromagnet is in one of the two remanent states. Before to proceed further, we would comment on the possibility of presence of the ratchet effect in our system. The ratchet effect [20, 24–28], that very often is at the origin of asymmetric response and rectifying effect, is characterized by a ratchet potential, i.e., a periodic potential that lacks spatial inversion symmetry. Beside the absence of a spatial periodicity along x , that should be a necessary condition for a "standard" ratchet, our potential $B_z(x, -10)$ exhibits an inversion symmetry along x . Precisely, but for an inessential additive constant, the $B_z(x, -10)$ is a simple odd function of x and it does not exhibit an asymmetric shape within the "spatial period" [24] $-W/2 < x < W/2$, that we could invoke to identify a ratchet. On the other hand, as can be seen Figs. 3.5(a) and 3.5(b), the magnetic force has ever same sign and same maximum intensity within a spatial period, differently from the forces originated from a standard ratchet potential [24], characterized by alternating sign and variable strength so that their spatial average is zero over a spatial period.

With reference to the top panel of Fig. 3.5(a), vortices and anti-vortices are generated at edges and stay channeled in the respective bright and dark regions by the magnetic forces acting in the y direction. When a transport current density J is applied along the y direction, the Lorentz force pushes the vortices and the anti-vortices along the channels. When $J > 0$, magnetic force along x -direction and Lorentz force cooperate to prevent that vortices and anti-vortices enter the strip. In this case a large positive depinning current should be expected. When the current is reversed, $J < 0$, the magnetic force at the strip edges points again outward but the Lorentz force points toward the interior of the strip, and, after the weak magnetic pinning force has been overcome, a stationary channeled flux motion regime can be established with associated onset of dissipation. This should account for the observed $I_{DP} > |I_{DN}|$ at $H_{\downarrow} = 0$ in Fig. 3.1(b). The lower panel illustrates the situation in the other stable state, $M_x^R < 0$, achieved at $H_{x\uparrow} = 0$. This time the Lorentz force associated to $J > 0$ moves the flux inward the strip and, after the weak magnetic force has been overcome, stationary flux motion is achieved with associated voltage generation. Instead, the Lorentz force associated to $J < 0$ adds to the magnetic force to prevent flux entry (and associated voltage generation), resulting in $I_{DP} < |I_{DN}|$ at $H_{\uparrow} = 0$, coherently with the experimental results reported in Fig. 3.1(b).

Numerical results substantially confirm the above predictions. In Fig. 3.6(a) we plot the calculated $E(J)$ [$V(I)$] curve of the superconductor while

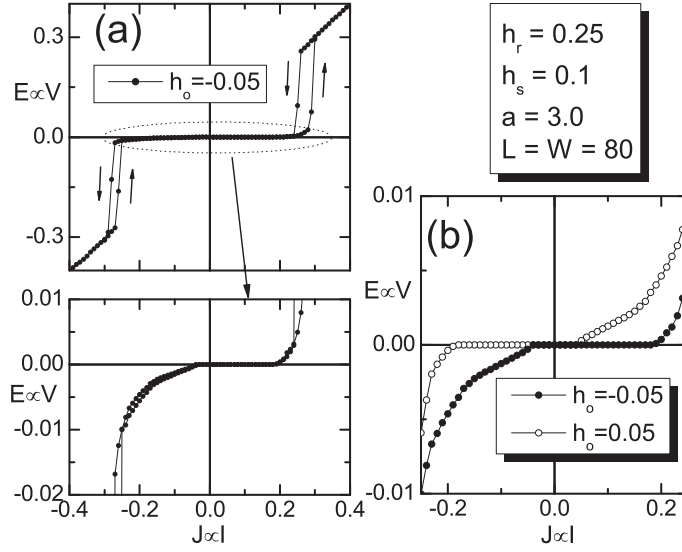


Figure 3.6: (a) Calculated $E(J)$ curve of the superconductor while the ferromagnet is in the remanent state at $H_{x\downarrow} = 0$. A blow up of the low voltage region is also shown. (b) Comparison of the $E(J)$ curves corresponding the two remanent states of the ferromagnet.

the ferromagnet is in the state at $H_{x\downarrow} = 0$ ($h_o < 0$). The positive and negative critical current densities differ only barely, in qualitative agreement with experimental results shown in Fig. 3.1(a). Notice that in our normalized units, the critical current density in the absence of perturbations (depairing current density) is $J_{depair} = 0.36$, and the resistivity of normal state is $\rho_n = 1$. The blow up of the low voltage region, plotted in the lower panel Fig. 3.6(a), confirms that a positive depinning current density substantially larger than the negative depinning current occurs. The calculated $E(J)$ curves corresponding the two remanent states are compared in Fig. 3.6(b). The curve in one stable state is mirrored with respect to the origin in the other state, as in the experimental results shown in Fig. 3.1(b).

In the lower panel of Fig. 3.7 we show contour plots of the squared order parameter when we are in the marked points of the $E(J)$ curve at $H_{x\downarrow} = 0$ shown above. Contour plots at left (right) correspond to negative (positive) current densities. The dark spots (local strong depression superconductivity) in these contour plots mark vortices or antivortices. In panel marked (3) is $J = 0.12$: vortices are nucleated at the right edge and antivortices at the left edge, but Lorentz force and magnetic pinning force point outward the strip and oppose flux entry, so that no electric field is generated. In panel (2) $J = -0.12$: now the Lorentz force points inward the strip and has overcome

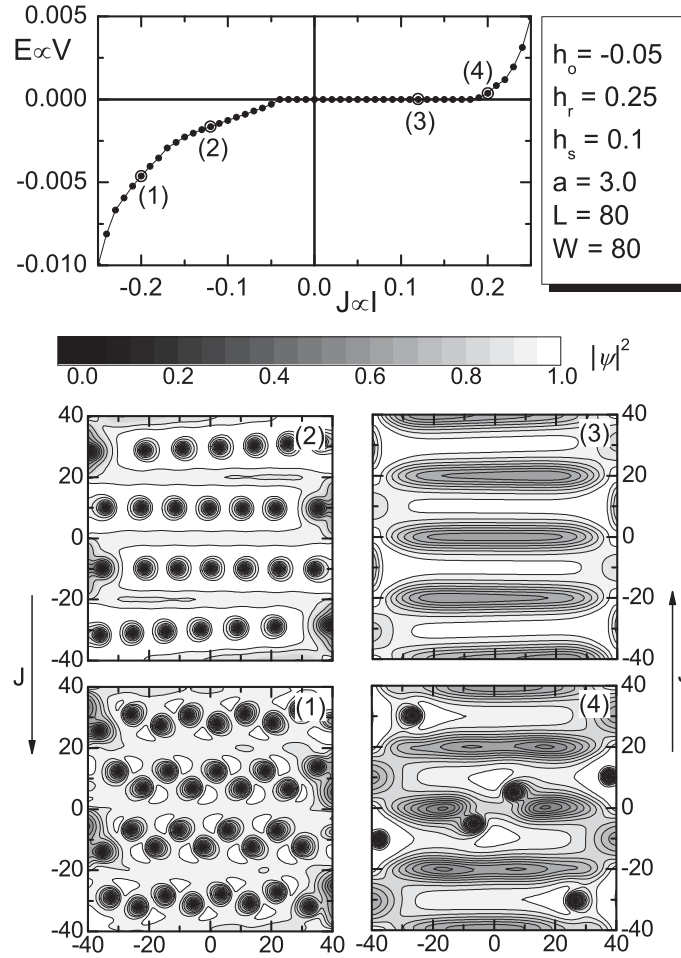


Figure 3.7: Contour plots of the squared order parameter when we are on the marked points of the calculated $E(J)$ curve at $H_{x\downarrow} = 0$ shown above.

the pinning magnetic force so that channeled flux motion is established and electric field is generated. Here vortex chains move from right to left and antivortex chains move from left to right. This is a nice example of a channeled flux flow regime with alternating vortex and antivortex chains moving in opposite directions in the strip. The flux flow regime [48] is characterized by an approximately linear $E(J)$ branch with slope proportional to flux density, as can be recognized in the calculated $E(J)$ curve and also in the experimental ones, to some extent. In panel (1) $J = -0.2$: we are again in a flux flow regime but now the flux density is doubled, as is doubled the slope of the corresponding branch in the $E(J)$ curve. The flux density increases despite the magnetic field is kept the same because when current density approaches the critical one the order parameter is depressed and the applied magnetic

field is large enough to nucleate more vortices or antivortices than for lower current densities. In other words, the growth of the transport current density produces effects qualitatively similar to the increasing temperature. Finally, in panel (4) is $J = 0.2$: as in panel (1) the order parameter is quite depressed and the field in the bulk is now strong enough to nucleate vortex-antivortex pairs that Lorentz force pushes outward the strip, with associated generation of electric field.

Experimentally, we observed a decrease of the asymmetry in samples with a 50 nm thick SiO_2 between Py and Nb, as shown in Fig. 3.2(b). This is consistent with the fact that the strength of stray fields from Py slab decreases with distance from the slab, as seen in also Fig. 3.4(c), and hence also the asymmetry they induce is decreased. We would notice that, as can be envisaged from Fig. 3.4(c), the perpendicular component of the stray fields at center of the strip diminishes in approximately the thickness of the SiO_2 spacer layer by less than 50%, that is, it remains quite high. Nevertheless, the diode-like behavior is significantly decreased. This is due to the fact that also the strength of stray field at edges of the Py strip diminishes proportionally from about 600 G to approximately 300 G, that is, to a value that is only slightly larger than the critical field of Nb, that at the working temperature of 4.72 K shown in Fig. 3.2(b) could be estimated to be around 250 G. So, the vortex generator effect of the stray fields at edges is significantly reduced and it is significantly reduced also the magnetic force at edges of the the strip which is another cause of asymmetry.

The asymmetry of the depinning currents was found to vanish at a temperature $T_v < T_c$, as shown in Fig. 1(c) of our previous work [29]. This can be explained noticing that when T_c is approached the lower critical field of Nb decreases and stray fields, that in the experimental temperature range can be considered constant, can be strong enough to nucleate vortices and antivortices in the bulk of the Nb strip. This should result in a decrease of depinning currents and asymmetry, because now the flux that can be affected by Lorentz force is already present in the Nb and the only cause of asymmetry comes from the weak magnetic pinning forces at ends of the channels. This effect is found also in the numerical simulations shown in Fig. 3.8(a). In the curve with open circles the magnetic field is, as in Fig. 3.7, such that vortices and antivortices are nucleated only at edges, while, to simulate an increased temperature, for the curve with solid circles the magnetic field is strong enough to nucleate vortices and antivortices also in the bulk of the strip.

We also observed strong suppression of asymmetry when the width of Py layer was made several micron larger than the Nb layer, as seen in Fig. 3.2(c). In this case the stray fields at the edges of the Py slab, that decay

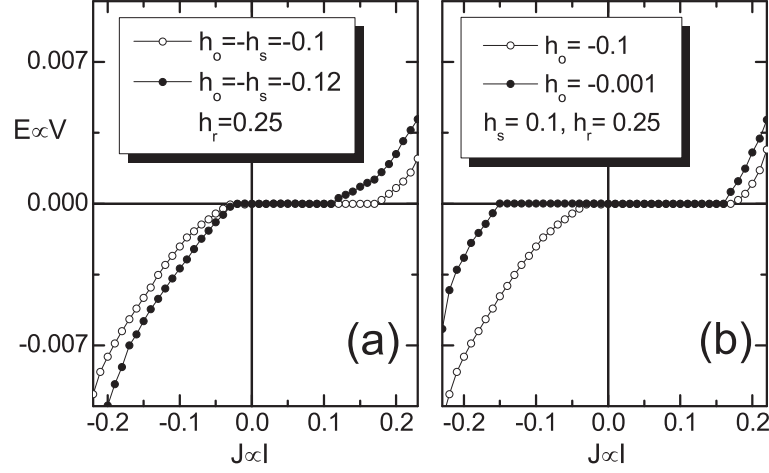


Figure 3.8: (a) Calculated $E(J)$ curves with different magnetic field strength. In the curve with solid circles the magnetic field is strong enough to nucleate vortices and antivortices also in the bulk of the strip. (b) The $E(J)$ curve with stray fields at edges (open circles) is compared with the one with strongly reduced stray fields at edges (solid circles).

inversely with distance from P_y , are not strong enough to generate vortices at the edges of the Nb strip. Numerical simulations shown in Fig. 3.8(b) confirm this kind of asymmetry suppression.

As shown in Fig. 3.2(a), we do not observe asymmetry when the preparing field is applied parallel to the current direction. This is consistent with the fact that in this case Lorentz force pushes vortices at edges where no stray field modulation is present, as suggested by contour plots in the right panels of Fig. 3.9. As in the experiments, the calculated $E(J)$ curve with current density parallel to the channels is found to be symmetric, as can be seen in the main panel of Fig. 3.9. We conclude noticing that for current parallel to the channels the dissipative regime is different from the one we have found in the case of current perpendicular to channels. As can be recognized from the sequence of contour plots shown in the bottom panels of Fig. 3.9, now the dissipation is due to nucleation of bound vortex-antivortex pairs in the channels ($t = t_0$). Lorentz force breaks the pairs and then moves the free vortices and antivortices from next neighbor pairs one toward the other causing them to annihilate in a collision ($t = t_1$). The whole process restarts with nucleation of new bound vortex-antivortex pairs ($t = t_2$).

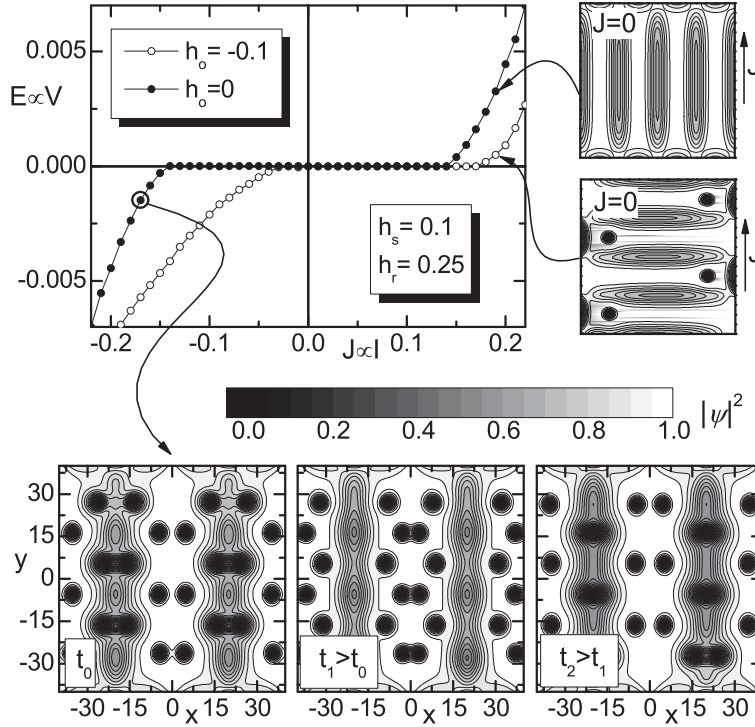


Figure 3.9: $E(J)$ curves with current density perpendicular (open circles) or parallel (solid circles) to the channels. The contour plots of the squared order parameter shown the lower panel correspond to the marked point of the above $E(J)$ curve with current density applied parallel to the channels .

3.4 Summary

Summarizing, we have further investigated the bistable vortex diode made of a ferromagnet-superconductor bilayer that we have recently demonstrated. With the help of numerical simulations, we analyzed in detail the main physical mechanism involved in the bistable diode. Micromagnetic simulations, performed using the Landau Lifshitz Gilbert model for the ferromagnet, and vortex dynamics of the superconductor, simulated using the two dimensional time dependent Ginzburg Landau equation, confirm that the observed bistable diode behavior can be accounted for by the stray fields from the ferromagnetic layer, that generate an asymmetric and bistable magnetic forces background for the Abrikosov vortices moving in the superconducting layer. In the dissipative branch of the bilayer, a peculiar channeled flux flow regime is achieved, with alternating vortex and antivortex chains moving in the opposite directions in the superconducting layer.

Bibliography

- [1] A. I. Buzdin, *Rev. Mod. Phys.* **77**, 935 (2005).
- [2] I. F. Lyuksyutov and V. L. Pokrovsky, *Adv. Phys.* **54**, 67 (2005).
- [3] A. Yu Aladyshkin, A. V. Silhanek, W. Gillijns, and V. V. Moshchalkov, *Supercond. Sci. Technol.* **22**, 053001 (2009).
- [4] J. Y. Gu, C. Y. You, J. S. Jiang, J. Pearson, Ya. B. Bazaliy, and S. D. Bader, *Phys. Rev. Lett.* **89**, 267001 (2002).
- [5] I. C. Moraru, W. P. Pratt, Jr., and N. O. Birge, *Phys. Rev. Lett.* **96**, 037004-1 (2006).
- [6] A. Singh, C. Sürgers, and H. v. Löhneysen, *Phys. Rev. B* **75**, 024513 (2007).
- [7] V. Peña, Z. Sefrioui, D. Arias, C. Leon, J. Santamaria, J. L. Martinez, S. G. E. te Velthuis, and A. Hoffmann, *Phys. Rev. Lett.* **94**, 057002 (2005).
- [8] N. M. Nemes, M. García-Hernández, S. G. E. te Velthuis, A. Hoffmann, C. Visani, J. Garcia-Barriocanal, V. Peña , D. Arias, Z. Sefrioui, C. Leon, and J. Santamaría, *Phys. Rev. B* **78**, 094515 (2008).
- [9] T. Hu, H. Xiao, C. Visani, Z. Sefrioui, J. Santamaria, and C.C. Almasan, *Physica B* **403**, 1167 (2008).
- [10] T. W. Clinton and M. Johnson, *Appl. Phys. Lett.* **70**, 1170 (1997).

-
- [11] C. Bell, S. Tursuku, J. Aarts, Phys. Rev. B. **74**, 214520 (2006).
 - [12] S. Steiner and P. Ziemann, Phys. Rev. B. **74**, 094504 (2006).
 - [13] D. Stamopoulos, E. Manios, and M. Pissas, Phys. Rev. B. **75**, 184504 (2007).
 - [14] G. Carapella, F. Russo, and G. Costabile, Phys. Rev. B. **78**, 104529 (2008).
 - [15] F. Russo, G. Carapella, and G. Costabile, Supercond. Sci. Technol. **22**, 055015 (2009).
 - [16] M. van Zalk, M. Veldhorst, A. Brinkman, J. Aarts, and H. Hilgenkamp, Phys. Rev. B. **79**, 134509 (2009).
 - [17] D. Y. Vodolazov, B. A. Gribkov, S. A. Gusev, A. Yu. Klimov, Yu. N. Nozdrin, V. V. Rogov, and S. N. Vdovichev, Phys. Rev. B. **72**, 064509 (2005).
 - [18] R. M. Ainbinder and I. L. Maksimov, Supercond. Sci. Technol. **20**, 441 (2007).
 - [19] N. Toitou, P. Bernstein, J. F. Hamet, Ch. Simon, L. Mechin, J. P. Contour, and E. Jacquet, Appl. Phys. Lett. **85**, 1742 (2004).
 - [20] G. Carneiro, Physica C **432**, 206 (2005).
 - [21] P. S. Swartz and H. R. Hart, Phys. Rev. **137**, 818 (1965).
 - [22] P. S. Swartz and H. R. Hart, Phys. Rev. **156**, 412 (1967).
 - [23] F. Raissi and J. E. Nordman, Appl. Phys. Lett. **65**, 1838 (1994).
 - [24] C.-S. Lee, B. Janko, I. Derenyi, and A.-L. Barabasi, Nature **400**, 337 (1999).
 - [25] G. Carapella and G. Costabile, Phys. Rev. Lett. **87**, 077002 (2001).
 - [26] J. E. Villegas, S. Savel'ev, F. Nori, E. M. Gonzalez, J. V. Anguita, R. Garcia, and J. L. Vicent, Science **302**, 1188 (2003).
 - [27] J. Van de Vondel, C. C. de Souza Silva, B. Y. Zhu, M. Morelle, and V. V. Moshchalkov, Phys. Rev. Lett. **94**, 057003 (2005).

-
- [28] C. C. de Souza Silva, A.V. Silhanek, J. Van de Vondel, W. Gillijns, V. Metlushko, B. Ilic, and V.V. Moshchalkov, *Phys. Rev. Lett.* **98**, 117005 (2007).
- [29] G. Carapella, V. Granata, F. Russo, and G. Costabile, *Appl. Phys. Lett.* **94**, 242504 (2009).
- [30] Z. Yang, M. Lange, A. Volodin, R. Szymczak, and V. V. Moshchalkov, *Nat. Mater.* **3**, 793 (2004).
- [31] W. Gillijns, A.Yu. Aladyshkin, M. Lange, M. J. Van Bael, and V.V. Moshchalkov, *Phys. Rev. Lett.* **95**, 227003 (2005).
- [32] L.Y. Zhu, T.Y. Chen, and C. L. Chien, *Phys. Rev. Lett.* **101**, 017004 (2008).
- [33] J. Ben Joussef, N. Vukadinovic, D. Billet, and M. Labrune, *Phys. Rev. B.* **69**, 174402 (2004).
- [34] A. Belkin, V. Novosad, M. Iavarone, J. Fedor, J. E. Pearson, A. Petrean-Troncalli, and G. Karapetrov, *Appl. Phys. Lett.* **93** 072510 (2008).
- [35] V. K. Vlasko-Vlasov, U. Welp, A. Imre, D. Rosenmann, J. Pearson, and W. K. Kwok, *Phys. Rev. B.* **78**, 214511 (2008).
- [36] V. V. Vlasko-Vlasov, U. Welp, G. Karapetrov, V. Novosad, D. Rosenmann, M. Iavarone, A. Belkin, and W.-K. Kwok, *Phys. Rev. B.* **77**, 134518 (2008).
- [37] A. V. Silhanek, J. Van de Vondel, A. Leo, G. W. Ataklti, W. Gillijns, and V. V. Moshchalkov, *Supercond. Sci. Technol.* **22**, 034002 (2009).
- [38] J. Van de Vondel, A. V. Silhanek, V. Metlushko, P. Vavassori, B. Ilic, and V. V. Moshchalkov, *Phys. Rev. B* **79**, 054527 (2009).
- [39] A. Nemoto, Y. Otani, S. G. Kim, K. Fukamichi, O. Kitakami, and Y. Shimada, *Appl. Phys. Lett.* **74**, 4026 (1999).
- [40] B. B. Pant, and K. N. Matsuyama, *Jpn. J. Appl. Phys.* **32**, 3817 (1993).
- [41] OOMMF, Object Oriented Micromagnetic Framework, <http://math.nist.gov/oommf>.
- [42] G. M. Maksimova, R. M. Ainbinder, and D. Yu. Vodolazov, *Phys. Rev. B.* **78**, 224505 (2008).

- [43] D. Y. Vodolazov, F. M. Peeters, S. V. Dubonos and A. K. Geim, *Phys. Rev. B.* **67**, 054506 (2003).
- [44] D. Y. Vodolazov, F. M. Peeters, I. V. Grigorieva and A. K. Geim, *Phys. Rev. B.* **72**, 024537 (2005).
- [45] L. Kramer and R. J. Watts-Tobin, *Phys. Rev. Lett.* **40**, 1041 (1978).
- [46] Q. Du and P. Gray, *SIAM J. Appl. Math.* **56**, 1060 (1996).
- [47] W. H. Press, S. A. Teukolsky, W. T. Vetterling, and B. P. Flannery, *Numerical recipes: the art of scientific computing* (Cambridge University Press, 2007), 3rd ed.
- [48] G. Blatter, M. V. Feigelman, V. B. Geshkenbein, A. I. Larkin, V. M. Vinokur, *Rev. Mod. Phys.* **66**, 1125 (1994).

High field vortex matching effects in superconducting Nb thin films with a nanometer-sized square array of antidots

4.1 Introduction

If a transport current is applied to a homogeneous ideal type-II superconductor vortices start to move at relatively small critical current density, j_c , with an associated onset of dissipation. This evidence, which represents one of the main factors restricting the field of possible applications of superconducting materials, imposes the need of a j_c enhancement which can be obtained, for example, by forcing and optimizing the vortex confinement in these systems [1]. Vortex pinning has been largely investigated and it has been shown that artificially produced periodic arrays of dots [2] and antidots (holes) [3–7] can drastically increase the j_c of superconductors. In particular, this happens when the vortex lattice (with intervortex distance a_0) is commensurate with the underlying periodic pinning array, *i.e.*, when the external magnetic field corresponds to integer multiples or fractions of the so-called first matching field H_1 . For a periodic square array, with distance among the pin sites d , $\mu_0 H_1 = \Phi_0/d^2$ where Φ_0 is the flux quantum. Nanolithographic techniques have been used to obtain submicrometer sized regular vortex pinning arrays giving $\mu_0 H_1$ of the order of millitesla. Moreover, in these systems matching effects detected by transport measurements have been observed only for temperatures very close to the superconducting transition temperature, T_c (at $t = T/T_c \approx 0.99$) [3, 8–11]. An increase of H_1 has been successfully realized using self-assembled templates as substrates for Nb thin films. Since typical interpore distances were in these cases less than 100 nm, matching effects have been observed for field values approaching 1 T [12–14].

Here we show high field vortex matching effects in perforated Nb thin films down to reduced temperature t as low as 0.33. Perforated Nb films, 25 nm thick, containing a square lattice of pores of diameter $a = 17$ nm and inter-pore distance $d = 50$ nm, have been obtained by electron beam lithography (EBL) and lift-off procedure. To allow transport measurements, by means of which matching phenomena have been observed in the $j_c(H)$ dependence, the samples were additionally patterned into bridges. The $j_c(H)$ curves exhibit pronounced maxima just above the $\mu_0 H_1 = 0.830$ T and $\mu_0 H_{1/2} = 0.415$ T matching fields expected for a square array of antidots with $d = 50$ nm. We have found a similar behavior in the $j_c(H)$ curves calculated using the time dependent Ginzburg-Landau model. An analysis of the calculated hysteresis loop $M(H)$ in the absence of transport current suggests that the complete occupation of the square array of antidots, assumed in the estimation $\mu_0 H_1 = \Phi_0/d^2$, is really present for a (small) finite range of magnetic field values that starts at $\mu_0 H_1$ in the increasing or decreasing branch of the $M(H)$ loop. So, in $j_c(H)$ curves measured by increasing the magnetic field, $\mu_0 H_1 = \Phi_0/d^2$ can fall just below the observed maximum, as it is in our case.

The Chapter is organized as follows. In Sec. 4.2, after a brief description on sample fabrication, the experimental results on the $j_c(H)$ curves at different temperatures are presented and discussed. In Sec. 4.3 the experimental $j_c(H)$ are further discussed with the help of numerical simulations. The $j_c(H)$ and $M(H)$ curves of a superconducting film with a square array of pinning centers at finite temperature are calculated in the framework of the time dependent Ginzburg-Landau model and an analysis of vortex configuration is given as well. A summary of the main results of the work is finally given in Sec. 4.4.

4.2 Experimental results and discussion

The samples have a bridge geometry consisting of two macroscopic continuous Nb banks contacting the [length(l) \times width(w) = $30 \times 20 \mu\text{m}^2$] nanoporous Nb film, as shown in the inset of Fig. 4.1(a). The banks were realized using standard optical lithography, while the nanoporous film was realized using EBL and a lift-off procedure. The EBL was performed in an FEI Inspect-F field emission scanning electron microscope (FE-SEM) equipped with a Raith Elphy Plus pattern generator. A 100-nm-thick positive tone resist consisting of 2% polymethylmethacrylate (PMMA) 950 000 molecular weight dissolved in anisole was spin-coated onto a Si/SiO₂ substrate and baked at 180 °C in a convection oven for 30 min. The writing was carried out using a beam current of 10.5 pA, an acceleration voltage of 30 KV, a write-field of $100 \times 100 \mu\text{m}^2$

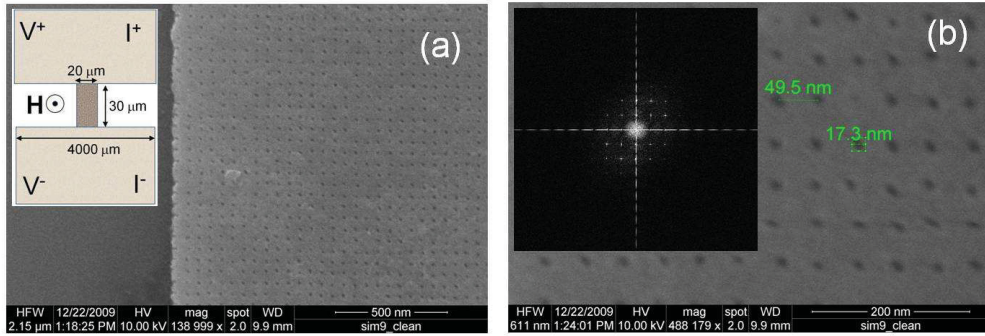


Figure 4.1: (a) *FE-SEM images of a portion of the nanoporous Nb film. A sketch (not on scale) of the sample geometry is shown in the inset.* (b) *Zooming-in on individual pores with indication of interpore distance and pore diameter. In the inset we show the Fourier transform determined on a $1 \times 1 \mu\text{m}^2$ area of the image in (a).*

and an area step size of 49.5 nm. After exposure, PMMA development was carried out in a methyl isobutyl ketone and isopropyl alcohol solution (1-MIBK:3-IPA) for 30 s, followed by rinsing in IPA and deionized water. With the above exposure parameters, the clearance dose of our PMMA was $300 \mu\text{C}/\text{cm}^2$. To achieve the square lattice of antidots shown in Fig. 4.1(a), we used an area dose of about $100 \mu\text{C}/\text{cm}^2$. Such a dose is enough to create, after development, a resist mask consisting of a square lattice of circularly shaped indentations (*i.e.*, regions where resist is thinned) with a diameter of about 50 nm and with a lattice constant equal to the used step size. A 3 min of light Ar sputter etching (corresponding to an etching rate of 2 nm/min), at 3.1×10^{-3} Torr and a self bias of 400 V, fully cleans the indentations down to the substrate, but the PMMA region complementary to the indentations is not cleaned. The resulting mask consists of a square lattice of resist dots of about 17 nm diameter and a separation again equal to the used step size. On this mask we deposit a 25 nm thick and 99.98% pure Nb film by rf magnetron sputtering in a high-vacuum system with a base pressure of 5.2×10^{-8} Torr in 99.999% pure Ar at 3.3×10^{-3} Torr with a rate of 2.2 nm/s. After lift-off in acetone, a Nb film with the square lattice of antidots shown in Fig. 4.1(a) is finally achieved. The square anti-dot lattice is quite regular, as more evident from the magnified FE-SEM image shown in Fig. 4.1(b) and from the Fourier transform determined on a $1 \times 1 \mu\text{m}^2$ area of the image in Fig.4.1(a) we show in the inset. The very small interpore distance of our porous Nb film, achieved here by means of a relatively simple sputter-etching-assisted EBL process, rivals the best results obtained using more complex techniques, such

as the block-copolymer-assisted lithography [15], or the technique based on Anodized Alumina Oxide templates [12, 16–20]. Also, our process allows to obtain a lattice of defects with a square symmetry, while using the other two processes lattices with (often only local) hexagonal symmetry are achieved.

The $V(I)$ characteristics have been measured using a four-probe technique at different temperatures with the magnetic field applied perpendicularly to the samples plane. During the measurement the temperature stabilization was around 1 mK. The values of j_c have been extracted using an electric field criterion of 1.67 V/m (corresponding to a voltage threshold of 50 μ V in the samples) for all the temperatures and fields. For the sample we report here (sample S1) the critical temperature $T_c = 6.9$ K was determined by transport measurements using a resistance criterion of 50% of the low-temperature normal state resistivity ρ_n , which in this sample was equal to 46 $\mu\Omega$ cm. The corresponding width of the resistive transition, estimated from the temperature difference at 10% and 90% of ρ_n , was $\Delta T_c \approx 100$ mK at zero field and with a bias current $I = 10$ μ A ($j = 2 \times 10^7$ A/m²). To determine the superconducting coherence length $\xi(0)$ we measured the (H, T) phase diagram. From the slope close to T_c of the $T_c(H)$ curve, shown in the inset of Fig. 4.2(a), and [21] $\mu_0 H_{c2}(T) = [\Phi_0/2\pi\xi(0)^2](1 - T/T_c)$ we estimate $\xi(0) = 8.2$ nm. This value is much smaller than the BCS coherence length of Nb, $\xi_0 = 39$ nm [22], so the sample is in the dirty limit regime with an electron mean free path $l = 1.38\xi(0)^2/\xi_0 = 2.4$ nm. The Ginzburg-Landau parameter $\kappa = \lambda/\xi$ (λ is the magnetic field penetration depth) can be estimated, in the dirty limit, using the expression $\kappa = 0.72\lambda_L/l \approx 12$, where $\lambda_L = 39$ nm is the London penetration depth of Nb [22]. This result implies that the investigated sample is a type-II superconductor. For the sake of comparison also a sample [S0 in Fig. 4.2(a)] with a 19 nm-thick continuous Nb film has been measured. For this sample $T_c = 5.86$ K, $\rho_n = 34$ $\mu\Omega$ cm, $\Delta T_c = 40$ mK, $\xi(0) = 8.6$ nm, $l = 2.6$ nm, and $\kappa = 11$. All these values are very similar to the corresponding ones of the porous sample indicating that the procedure of fabrication of the antidots does not significantly alter the superconducting properties of the Nb film. The reduced values for T_c measured in both samples are mainly related to their small thickness even though they are a bit lower with respect to those previously reported in the literature for high-quality rf sputtered thin films of Nb [23].

In Fig. 4.2(a) we show the magnetic field dependence of the critical current density for the porous sample $T = 4.2$ K and the reference Nb films taken at $T = 3.6$ K, which corresponds to the same reduced temperature $t = T/T_c = 0.61$. Comparing the two sets of data we see that, except at very low fields, the sample with holes has j_c values which are approximately two times larger than the corresponding values obtained on the virgin sample

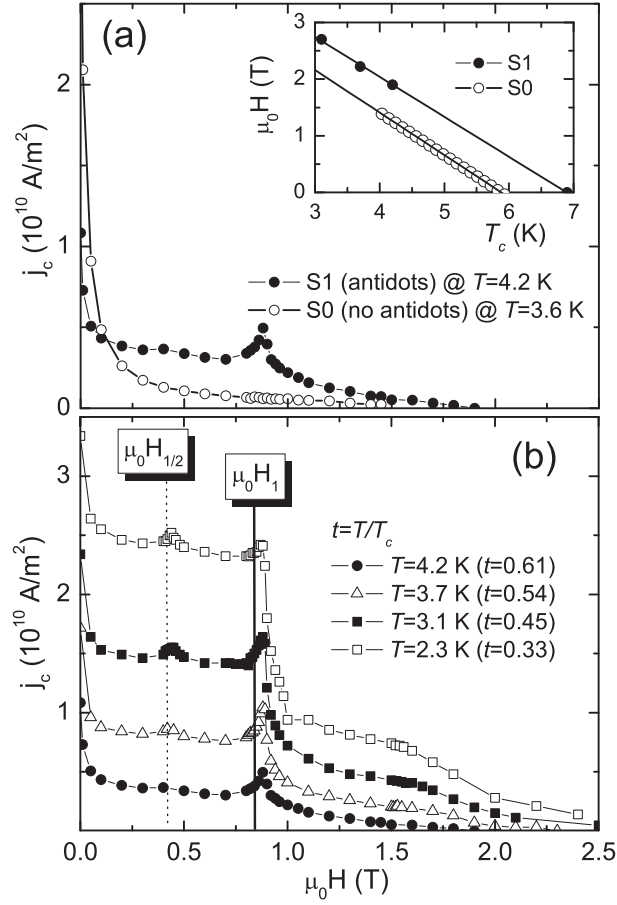


Figure 4.2: (a) *Magnetic field dependence of the critical current density for the Nb film with antidots (S1, solid circles) and for the reference sample (S0, open circles) at two temperatures corresponding to same reduced temperature $t = 0.61$. In the inset are shown the $T_c(H)$ curves of both samples.* (b) *Critical current density vs the magnetic field measured at four different temperatures for the Nb film with antidots. Thick (dashed) vertical lines indicate integer (rational) theoretically expected matching fields.*

indicating that a stronger confinement of the vortex lattice has been obtained in the porous sample. However, what is much more interesting is that the curve for the sample with holes exhibits a very pronounced maximum at 0.880 T. This value is very close to the expected first matching field $\mu_0 H_1 = 0.830$ T as estimated from the interpore spacing $d = 50$ nm.

Fig. 4.2(b) shows the $j_c(H)$ dependence for the porous Nb film taken at four different temperatures, corresponding to a range from 0.61 to 0.33 for t . At $t = 0.33$ and $H = 0$ the measured $j_c \approx 4 \times 10^{10}$ A/m² is

less than one order of magnitude smaller than the depairing current density j_{dp} whose expression [24] at zero magnetic field is given by $j_{dp}(t) = 7.84[(k_B T_c)^3 / e^2 \hbar v_F (\rho_n l) \rho_n]^{1/2} (1 - t)^{3/2}$. Using the above parameters for the Nb film with antidots, we estimate $j_{dp}(t = 0.33) \approx 2.1 \times 10^{11}$ A/m². All the curves show a clear peak just above the expected first matching field followed by a strong decrease which becomes more pronounced at lower temperatures. Also, in the $j_c(H)$ curves a maximum appears at $\mu_0 H = 0.440$ T, just above the expected half-harmonic matching field $\mu_0 H_{1/2} = 0.415$ T, which becomes clearer and clearer as the temperature is lowered. Apart from this peak which is related to the very well-known “checkerboard” vortex arrangement appearing in a square array of antidots [25], the form of the curves strongly resembles those obtained on Nb thin films with a triangular array of pinning centers [7]. Except for $T = 4.2$ K where matching fields $H_m = mH_1$ with $m > 1$ are larger than the upper critical field, the lack of observation of higher order matching phenomena can be easily explained considering the value of the saturation number n_s , *i.e.*, the maximum number of vortices which can fit into a pore of diameter a . If we consider its expression [26] $n_s = a/4\xi(T)$ where $\xi(T) = \xi(0)/\sqrt{1 - T/T_c}$ we obtain for our sample at $T = 2.3$ K that n_s is less than one and this still holds if the high-field expression [27] $n_s \sim [a/2\xi(T)]^2$ is considered. Another estimation has been given (but for a triangular array of cylindrical cavities) [28] according to which double occupancy of pinning sites is possible only if $a > 2[\xi(T)d^2]^{1/3}$. In our case $2[\xi(T)d^2]^{1/3} \approx 51$ nm and the above condition is not satisfied. So each hole can trap only one fluxon and multiquanta vortex lattice [6] is not allowed in our system.

4.3 Numerical simulations

As stated above, the observed peaks in the $j_c(H)$ curves, achieved here by direct transport measurements and not extrapolated from magnetic hysteresis loop, fall just above the integer or the rational matching field expected from $\mu_0 H_m = m\Phi_0/d^2$ with $m = 1, 1/2$. This peculiarity was envisaged [29] some years ago also in magnetization curves simulated in the framework of molecular dynamics approach and was explained as due to the flux gradient in the sample. In this sense, our experimental results seem to confirm predictions of Ref. [29]. However, in that work the addressed samples were superconducting slabs with a square array of columnar defects only in the central region of the slab, with no transport current and at zero temperature. Here we are concerned with a very thin film with a square array of holes (very strong pinning) that covers all the sample, so that the flux gradient in

the sample should be minimized. Nevertheless, we find again the peculiarity, also in the presence of a transport current and at finite temperature. To gain further insight on this fact and on the specific experimental system under study in general, we performed numerical simulations in the framework of the time dependent Ginzburg-Landau model, that, though more complex, is more accurate than the molecular dynamics approach.

As a model system we used the two-dimensional time-dependent Ginzburg-Landau equations (TDGLEs) at finite temperature [30]:

$$u \frac{\partial \psi}{\partial t} = (\nabla - i\mathbf{A})^2 \psi + [\rho(\mathbf{r}) - T - |\psi|^2] \psi \quad (4.1)$$

$$\frac{\partial \mathbf{A}}{\partial t} = \text{Re} [\psi^* (-i\nabla - \mathbf{A}) \psi] - k^2 \nabla \times \nabla \times \mathbf{A} \quad (4.2)$$

where $\psi = |\psi| e^{i\phi}$ is the complex order parameter, $\mathbf{A} = (A_x, A_y)$ is the vector potential, T is the temperature, k is the Ginzburg-Landau parameter and the coefficient $u = 5.79$ (Ref. [31]) governs the relaxation of the order parameter. The function $\rho(\mathbf{r})$, equal to 1 for an ideal superconductor, is used to simulate an array of antidots (pinning centers) as described below. All the physical quantities are measured in dimensionless units: the temperature T in units of the critical temperature T_c , the spatial coordinates are in units of the superconducting coherence length $\xi(0) = (8k_B T_c / \pi \hbar D)^{-1/2}$ (D is the diffusion constant) and time is scaled in units of the Ginzburg-Landau relaxation time $\tau_0 = 4\pi\sigma_n \lambda^2 / c^2$ ($\sigma_n = 1/\rho_n$ is the normal-state conductivity). The order parameter in units of $\Delta_0 = 4k_B T_c \sqrt{u} / \pi$ (the superconducting gap at $T = 0$ which follows from Gor'kov's derivation of the Ginzburg-Landau equations), the vector potential is scaled in units $\Phi_0 / 2\pi\xi(0)$ (Φ_0 is the quantum of magnetic flux). In these units the magnetic field is scaled with $H_{c2} = \Phi_0 / 2\pi\xi(0)^2$ and the current density with $j_0 = c\Phi_0 / 8\pi^2 \lambda^2 \xi(0)$.

To simulate a finite width and infinite length strip, we apply periodic boundary conditions in the y -direction, $\psi(y) = \psi(y + L)$, $\mathbf{A}(y) = \mathbf{A}(y + L)$ and the superconductor-vacuum boundary conditions in the x -direction, $(\nabla_x - iA_x)\psi|_{x=0,W} = 0$, where W is the width of the strip and L is the integration period. The transport current is introduced in the boundary condition for the vector potential in the x -direction, $(\nabla \times \mathbf{A})_z|_{x=0,W} = H \pm H_I$, where $H_I = 2\pi I / c$ is the magnetic field induced by the current I (per unit length in the z -direction) and H is the applied magnetic field in the z -direction. In all our calculations, we choose $k = 5$, $W = 50$, $L = 33$, to retain relevant information within capabilities of our computer.

Normal or ferromagnetic inclusions in superconductor can be modeled [32] by mean of a function $\rho(\mathbf{r}) < 1$ that accounts for a local suppression

of superconductivity. Holes in the superconductor are region with no superconductivity and this can be accounted for by $\rho(\mathbf{r}) = 0$ at hole locations. Thus, we introduce into Eq.(4.1) for ψ the function $\rho(\mathbf{r}) = 1 - b(x)b(y)$, where $b(x) = |h(x + a/2) - h(x - a/2)|$ is a Boxcar function and $h(x) = 1/\{\exp[b \sin(x\pi/d)] + 1\}$ is a sine modified Heaviside step function. This is a periodic distribution of square-shaped regions (with side a , center distance d , and sharpness b) where $\rho(\mathbf{r}) = 0$. We choose $b = 30$, to simulate abrupt suppression of superconductivity at the hole locations, while $a = 2.2$, and $d = 5.5$ are comparable to the experimental ones. A gray scale plot of the function $\rho(\mathbf{r})$ we used to model the square array of holes is shown in Fig. 4.3(a).

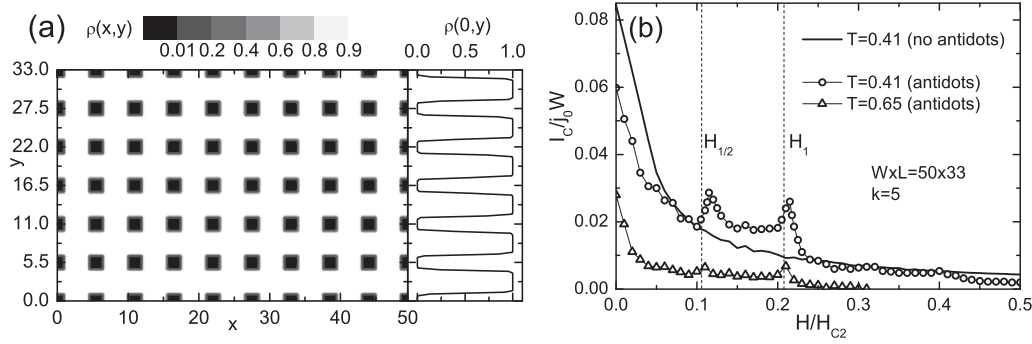


Figure 4.3: (a) Gray scale plot of the function $\rho(\mathbf{r})$ used into TDGLE to model a square array of antidots. A profile of $\rho(x,y)$ as a function of y at centerline of an antidot column is also shown. (b) Normalized critical current vs the applied magnetic field calculated for the strip with antidots (open symbols) and for the strip with no antidots (solid line). Dashed vertical lines indicate integer and rational theoretically expected matching fields.

To solve the system of Eqs.(4.1) and (4.2) we apply a finite-difference representation for the order parameter and vector potential on a uniform Cartesian space grid 100×66 and we use the link variable approach [33] and the simple Euler method [34] with time step $\Delta t = 0.002$ to find ψ . Initial conditions were $|\psi| = 1$ and $\mathbf{A} = 0$. The behavior of the system is studied on a large time scale when time-averaged values no longer depend on time.

In Fig. 4.3(b) we show the calculated magnetic field dependence of the critical current for the strip with antidots at reduced temperatures $T = 0.41$ and $T = 0.65$. As in the experiment [see Fig. 4.2(b)], we observe only two peaks, falling slightly above the expected H_1 and $H_{1/2}$ matching fields. At $T = 0.41$, the curve with antidots (open circles) is compared with the

curve without antidots (thick line). An enhancement of the critical current is achieved between the two matching fields, while at low fields the critical current results lower for the strip with pinning, again in qualitative agreement with experimental results in Fig. 4.2(a). We should notice that both in the experiment [see Fig. 4.1(a)] and in the simulations [see Fig. 4.3(a)] the left and right edges of the strip with pinning are rough on a mesoscopic scale. At low fields, such a roughness appreciably reduces [32,35] the surface barrier for flux entry or flux exit, resulting in a reduction of the critical current density of the perforated film with respect to the current density of the continuous film with ideally smooth edges.

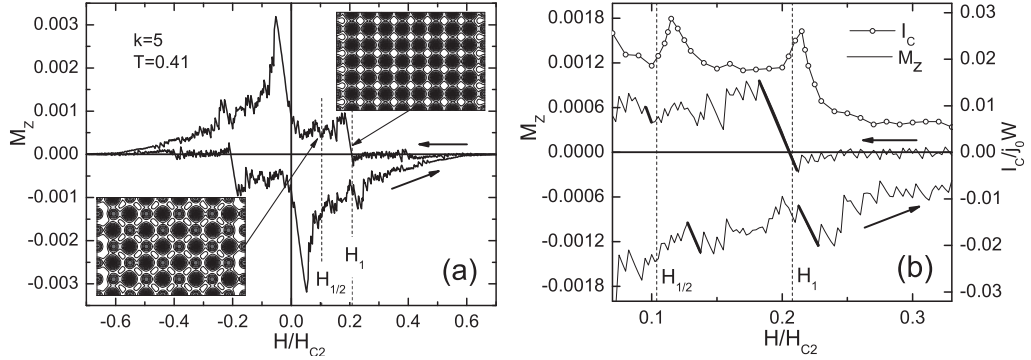


Figure 4.4: (a) *Calculated $M(H)$ loop of the strip with antidots. Dashed vertical lines indicate integer and rational theoretically expected matching fields. The two inset show contour plots of the squared order parameter at $H = 0.095$ and $H = 0.195$ where we have respectively half and full vortex filling of pinning centers.* (b) *$M(H)$ (solid line) is compared with critical current curve (open circles) at same temperature. Thicker lines in the $M(H)$ show magnetic field ranges where stable half and full vortex filling are achieved.*

In Fig. 4.4(a) we show the magnetization hysteresis loop calculated for the strip with holes at $T = 0.41$ and with no transport current. Beside the jagged shape, resulting from the threshold character of the vortex-entry process amplified [32,36] by the mesoscopic lateral dimension of our strip, the $M(H)$ exhibits local enhancement around the H_1 and $H_{1/2}$ fields where the full or half filling of pinning centers is expected. A snapshot of vortex arrangement at these relevant fields is shown in the inset of Fig. 4.4(a). In Fig. 4.4(b) both the increasing and decreasing branch of the $M(H)$ loop are compared with the increasing branch of the $I_c(H)$. The thick lines show magnetic field ranges where we have stable half and full vortex filling of pinning centers. With reference to the increasing H branch, full (half) vortex filling starts approximately at H_1 ($H_{1/2}$) and extends up to fields shortly after

the critical current peaks. This confirms that in $j_c(H)$ curves measured by increasing the magnetic field, $\mu_0 H_1 = \Phi_0/d^2$ can fall just below the observed maximum as, in fact, it has been observed in our experiment.

4.4 Summary

In conclusion, we obtained by a simple sputter-etching-assisted EBL process a regular square array of nanometer-sized pinning centers on Nb thin films. The $j_c(H)$ values, measured by transport measurements on patterned samples, are found to be considerably larger than those measured on a Nb film without antidots at the same reduced temperature and exhibit pronounced maxima just above the expected $\mu_0 H_1 = 0.830$ T and $\mu_0 H_{1/2} = 0.415$ T matching fields, down to $T = 2.3$ K ($t = 0.33$). Our experiment shows an increase of the critical current density at high fields and far from the superconducting transition temperature, a result promising in view of practical high-field applications of thin film superconductors. The behavior of $j_c(H)$ as well as the maxima locations have been found to be consistent with the ones calculated in the framework of time dependent Ginzburg-Landau model.

Bibliography

- [1] V. Misko, S. Savel'ev, and F. Nori, Phys. Rev. Lett. **95**, 177007 (2005).
- [2] A. Hoffmann, P. Prieto, and I. K. Schuller, Phys. Rev. B **61**, 6958 (2000).
- [3] A. T. Fiory, A. F. Hebard, and S. Somekh, Appl. Phys. Lett. **32**, 73 (1978).
- [4] A. N. Lykov, Solid State Commun. **86**, 531 (1993).
- [5] A. Castellanos, R. Wördenweber, G. Ockenfuss, A. v.d. Hart, and K. Keck, Appl. Phys. Lett. **71**, 962 (1997).
- [6] V. V. Moshchalkov, M. Baert, V. V. Metlushko, E. Rosseel, M. J. van Bael, K. Temst, Y. Bruynseraede, and R. Jonckheere, Phys. Rev. B **57**, 3615 (1998).
- [7] J. Eisenmenger, M. Oettinger, C. Pfahler, A. Plettl, P. Walther, and P. Ziemann, Phys. Rev. B **75**, 144514 (2007).
- [8] L. Horng, J. C. Wu, T. C. Wu, and S. F. Lee, J. Appl. Phys. **91**, 8510 (2002).
- [9] L. Van Look, B. Y. Zhu, R. Jonckheere, B. R. Zhao, Z. X. Zhao, and V. V. Moshchalkov, Phys. Rev. B **66**, 214511 (2002).
- [10] M. Kemmler, C. Gürlich, A. Sterk, H. Pöhler, M. Neuhaus, M. Siegel, R. Kleiner, and D. Koelle, Phys. Rev. Lett. **97**, 147003 (2006).

-
- [11] A. D. Thakur, S. Ooi, S. P. Chockalingam, J. Jesudasan, P. Raychaudhuri, and K. Hirata, *Appl. Phys. Lett.* **94**, 262501 (2007).
- [12] W. Vinckx, J. Vanacken, V. V. Moshchalkov, S. Mátéfi-Tempfli, M. Mátéfi-Tempfli, S. Michotte, L. Piraux, and X. Ye, *Physica C* **459**, 5 (2007).
- [13] M. Trezza, S. L. Prischepa, C. Cirillo, R. Fittipaldi, M. Sarno, D. Sannino, P. Ciambelli, M. B. S. Hesselberth, S. K. Lazarouk, A. V. Dolbik, V. E. Borisenko, and C. Attanasio, *J. Appl. Phys.* **104**, 083917 (2008).
- [14] M. Trezza, C. Cirillo, S. L. Prischepa, and C. Attanasio, *Europhys. Lett.* **88**, 57006 (2009).
- [15] A.-M. Popa, P. Niedermann, H. Heinzelmann, J. A. Hubbell, and R. Pugin, *Nanotechnology* **20**, 485303 (2009).
- [16] U. Welp, Z. L. Xiao, J. S. Jiang, V. K. Vlasko-Vlasov, S. D. Bader, G. W. Crabtree, J. Liang, H. Chik, and J. M. Xu, *Phys. Rev. B* **66**, 212507 (2002).
- [17] U. Welp, Z. L. Xiao, V. Novosad, and V. K. Vlasko-Vlasov, *Phys. Rev. B* **71**, 014505 (2005).
- [18] W.-K. Kwok, Z. L. Xiao, U. Welp, A. Rydh, V. Vlasko-Vlasov, and V. Novosad, *Physica C* **412–414**, 347 (2004).
- [19] X. Hallet, M. Mátéfi-Tempfli, S. Michotte, L. Piraux, J. Vanacken, V. V. Moshchalkov, and S. Mátéfi-Tempfli, *Appl. Phys. Lett.* **95**, 252503 (2009).
- [20] X. Hallet, M. Mátéfi-Tempfli, S. Michotte, L. Piraux, J. Vanacken, V. V. Moshchalkov, and S. Mátéfi-Tempfli, *Small* **5**, 2413 (2009).
- [21] M. Tinkham, *Introduction to Superconductivity* (McGraw-Hill, New York, 1996).
- [22] W. Buckel, *Supraleitung*, 3rd edition (Physik-Verlag, Weinheim, 1984).
- [23] S. A. Wolf, J. J. Kennedy, and M. Niesenoff, *J. Vac. Sci. Technol.* **13**, 145 (1976).
- [24] M. Yu. Kupriyanov and V. F. Lukichev, *Fiz. Nizk. Temp.* **6**, 445 (1980) [*Sov. J. Low Temp. Phys.* **6**, 210 (1980)].

-
- [25] A. N. Grigorenko, G. D. Howells, S. J. Bending, J. Bekaert, M. J. Van Bael, L. Van Look, V. V. Moshchalkov, Y. Bruynseraede, G. Borghs, I. I. Kaya, and R. A. Stradling, *Phys. Rev. B* **63**, 052504 (2001).
- [26] G. S. Mkrtchyan and V. V. Shmidt, *Zh. Eksp. Teor. Fiz.* **61**, 367 (1971) [*Sov. Phys. JETP* **34**, 195 (1972)].
- [27] M. M. Doria, S. C. B. de Andrade, and E. Sardella, *Physica C* **341**, 1199 (2000).
- [28] A. I. Buzdin, *Phys. Rev. B* **47**, 11416 (1993).
- [29] C. Reichhardt, J. Groth, C. J. Olson, Stuart B. Field, and Franco Nori, *Phys. Rev. B* **54**, 16108 (1997).
- [30] D. Y. Vodolazov and F. M. Peeters, *Phys. Rev. B.* **76**, 014521 (2007).
- [31] L. Kramer and R. J. Watts-Tobin, *Phys. Rev. Lett.* **40**, 1041 (1978).
- [32] D. Y. Vodolazov, I. L. Maksimov, and E. H. Brandt, *Physica C* **384**, 211 (2003).
- [33] R. Kato, Y. Enomoto, and S. Maekawa, *Phys. Rev. B* **47**, 8016 (1993).
- [34] W. H. Press, S. A. Teukolsky, W. T. Vetterling, and B. P. Flannery, *Numerical Recipes: The Art of Scientific Computing*, 3rd ed (Cambridge University Press, 2007).
- [35] D. Y. Vodolazov, and F. M. Peeters, *Phys. Rev. B* **72**, 172508 (2005).
- [36] C. Bolech, G. C. Buscaglia, and A. López, *Phys. Rev. B* **52**, R15719 (1995).

Magneto-transport properties of curved mesoscopic superconducting strips

5.1 Introduction

Thin mesoscopic superconductive strips, i.e., strips with lateral dimensions at sub-micrometer scale, have received a growing interest in the last years, mainly due to the remarkable advances in the nanotechnology and nanofabrication subfields achieved in the last two decades. Most of experimental and theoretical studies reported to date were focused on flat strips. Recently, curved strips conforming to cylindrical shells have been theoretically addressed with emphasis on self magnetic field distribution and dissipation [1], phase slip line nucleation in the presence of a magnetic field longitudinal to the cylinder axis [2], and thermal activation of phase slip lines in doubly connected superconducting cylinders [3]. Moreover, ultrathin doubly connected superconducting cylinders in the presence of a magnetic field longitudinal to the cylinder axis have been experimentally [4,5] addressed with emphasis on phase separation near a quantum phase transition [4] or destruction of the global phase coherence [5].

In this work we investigate numerically, in the framework of the time-dependent Ginzburg-Landau (TDGL) formalism, the transport properties and the vortex dynamics of strips conforming to cylindrical shells in the presence of a magnetic field transverse to the cylinder axis. As a homogeneous external magnetic field is experienced as inhomogeneous by curved strips, their behavior is quite different from the one observed in flat strips. Here we show that a simple curved strip can exhibit asymmetric transport properties, qualitatively similar to those observed in more complex systems as, e.g., the Ferromagnet/Superconductor bilayers [6–10]. The asymmetry in

the critical current densities could be exploited to realize superconducting current rectifiers at sub-micrometer scale using a single (curved) strip. The electric field-current density $[E(J)]$ curves of the full cylindrical surface exhibit well developed dissipative branches with dynamical resistivity larger than the normal state resistivity. We explain these branches as due to phase slip lines [11], similar to the phase slip lines of kinematic vortex-antivortex pairs recently reported [12, 13] in flat mesoscopic strips strongly driven by nonuniform bias current or perturbed by localized stray fields from ferromagnets. The presence of phase slip lines compels voltage oscillations in a relatively high frequency range. This makes the simple superconducting cylindrical shell potentially interesting as a mesoscopic voltage oscillator.

The Chapter is organized as follows. In section 5.2 we describe the TDGL model as specialized to the two geometries that we address in the present work. In section 5.3 we discuss the asymmetry of critical currents that can be exhibited by a section of a cylindrical shell as well as the vortex dynamics involved. The transport properties of a full cylindrical shell in the presence of magnetic field is the subject of section 5.4. Here the dynamical origin of highly resistive dissipative branches in the $E(J)$ curves is considered in detail. A summary of the main results of the work is given in section 5.5.

5.2 Theoretical model

The superconducting strips considered in this work are an (open) section of a cylindrical shell and a full (closed) cylindrical shell, as sketched in figure 5.1. With respect to the cylindrical reference frame (ρ, θ, y) shown in figure 5.1, the length of strips lies parallel to the y -axis (cylinder axis), a uniform transport current J is applied along the strip length, and the magnetic field is applied perpendicular to the y -axis, making an angle α with the ρ -axis at $\theta = 0$. Noticing that for the cylindrical surface the radial coordinate is constant, ($\rho = R$), we can use the curvilinear coordinate $x = R\theta$ (length of arc along the circumference, and directed as $\hat{\theta}$) instead of the coordinate θ . In this reference frame the strips can be described using only x and y coordinates with ranges $-L/2 < y < L/2$ and $-W/2 < x < W/2$. Moreover, all spatial derivatives reduce to the simple cartesian form.

For our numerical study we use the time-dependent Ginzburg-Landau (TDGL) equation supplemented with the equation for the electrostatic po-

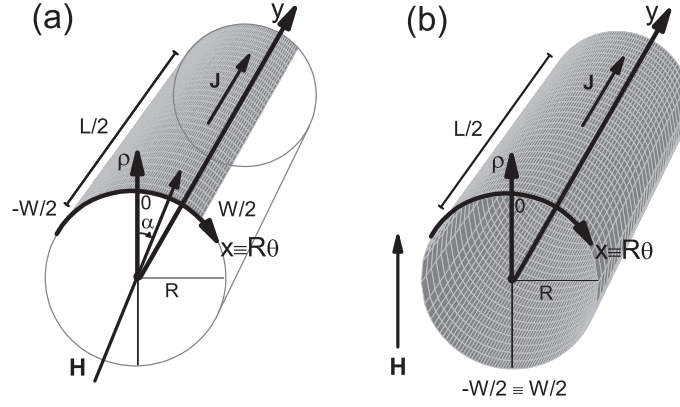


Figure 5.1: *Geometry of superconducting strips considered and direction of external magnetic field and bias current. (a) Section of a cylindrical shell. (b) Full cylindrical shell. The cylindrical coordinate frame (ρ, θ, y) can be mapped to an (x, y) coordinate frame, the x -coordinate being the length of the arc.*

tential [14–16]:

$$u \left(\frac{\partial}{\partial t} + i\varphi \right) \psi = (\nabla - i\mathbf{A})^2 \psi + (1 - |\psi|^2) \psi \quad (5.1)$$

$$\nabla^2 \varphi = \text{div} \{ \text{Im} [\psi^* (\nabla - i\mathbf{A}) \psi] \} \quad (5.2)$$

where $\psi = |\psi| e^{i\phi}$ is the complex order parameter, \mathbf{A} the vector potential, φ the electrostatic potential and the coefficient $u = 5.79$ [17] governs the relaxation of the order parameter. All physical quantities are measured in dimensionless units: the coordinates are in units of the coherence length $\xi_{GL}(T) = \xi_0 / \sqrt{1 - T/T_c}$, with $\xi_0 = \sqrt{\pi \hbar D / 8 k_B T_c}$, and T_c is the critical temperature, D is the diffusion constant. Time is measured in units of the relaxation time $\tau = \tau_0 / (1 - T/T_c)$ with $\tau_0 = 4\pi \sigma_n \lambda^2 / c^2 = \xi_0^2 / Du$ (σ_n is the normal-state conductivity, $\lambda = \kappa \xi_{GL}$ the magnetic field penetration depth, with κ the G-L parameter). The order parameter is in units of $\Delta(T) = \Delta_0 \sqrt{1 - T/T_c}$, where $\Delta_0 = 4k_B T_c \sqrt{u} / \pi$ is the superconducting gap at $T = 0$ which follows from Gor'kov's derivation of the Ginzburg-Landau equations. The vector potential is measured in units $\Phi_0 / 2\pi \xi_{GL}$ ($\Phi_0 = ch/2e$ is the quantum of magnetic flux) and the electrostatic potential is in units of $\varphi_0(T) = \hbar/2e\tau$. In these units the magnetic field is scaled with $H_{c2}(T) = \Phi_0 / 2\pi \xi_{GL}^2$ and the current density with $j_0(T) = c\Phi_0 / 8\pi^2 \lambda^2 \xi_{GL}$.

For the sake of simplicity, we neglect pinning effects that can be intrinsic in polycrystalline materials [18]. Self fields associated to the bias current and the screening effects are also neglected, otherwise an equation [19] for the

vector potential \mathbf{A} should be integrated in the above model. This simplification is justified in the high κ limit [20] (definitely type-II superconductors) and in the mesoscopic limit we are dealing with, i.e., very thin ($d \leq \xi_{GL} \ll \lambda$) and sufficiently narrow ($W \leq 2\lambda$) strips. Large κ values are typical for very thin films achieved by sputtering. As an example, thin Nb films can exhibit $\kappa \sim 11$ already when the thickness is about 25 nm [21, 22] rising to $\kappa \sim 20$ at 10 nm. [21]. Typical estimated values of effective [23] coherence length and penetration depth at very low temperatures for 10 nm-thick Nb films [21] can be as low as $\xi_{GL} \simeq 10$ nm and as large as $\lambda \sim 200$ nm, corresponding to $\kappa = 20$. In the following we will assume to work in a temperature range so close to T_c , that the phenomenological TDGL model is supposedly adequate, and we shall put $W = L = 40\xi_{GL}$, $d \leq \xi_{GL}$, and $\kappa \gg 1$.

Being in the limit of very thin strips of type II superconductors, in the following we shall presume that the strips are affected by the magnetic field component that is normal to the surface (i.e., H_ρ) much more than by the component tangent to the surface (i.e., H_θ). This is justified by the fact [23] that the upper parallel critical field of a very thin strip is larger than the upper perpendicular critical field. This is even more true for the lower parallel critical fields (first flux penetration), because $H_{c1}^\parallel/H_{c1}^\perp \approx \lambda/d \gg 1$. Moreover, as we assumed $d \leq \xi_{GL}$, the tangent component cannot nucleate vortices parallel to the superconducting surface and its role is only reduced to a monotonic suppression [23] of the order parameter, $|\psi(x)| = \sqrt{1 - (H_\theta(x)/H_{c2}^\parallel)^2}$. Therefore, for the sake of simplicity, in the following we will neglect the component H_θ when assigning the vector potential to equations (5.1) and (5.2) because qualitatively not so influent, but we should remember that, due to this approximation, the magnetic field axis should suffer for a correction that becomes more and more relevant as the field values approach the H_{c2}^\parallel that, however, is expected [23] to be larger than the H_{c2}^\perp .

Finally, we refer to the realistic experimental situation where the mesoscopic samples are electrically connected by superconductive banks which have better superconductive properties than the thin strip itself, which occurs when, e.g., the banks are much thicker than the strip. To account for the presence of these banks, in our calculations we make use of the "bridge" condition in the y -direction: in a region of length $2.5\xi_{GL}$ at the ends of the strip the equations (5.1) and (5.2) are reduced to $(\partial_t + i\varphi)\psi = 0$, $\nabla^2\varphi = 0$ with boundary conditions $\partial_y\psi = 0$ and $\partial_y\varphi = -J$, where J is the uniformly injected bias current density.

The boundary condition in the x -direction depends on the geometry of superconducting strips. For the section of a cylindrical shell [see figure 5.1(a)], an insulator-superconductor boundary condition $(i\partial_x + A_x)\psi = 0$ is used

for the order parameter and the Neumann boundary condition $\partial_x \varphi = 0$ is applied for the electrostatic potential. For the full cylindrical shell [see figure 5.1(b)] we take periodic boundary conditions $\psi(-W/2, y) = \psi(W/2, y)$, $\varphi(-W/2, y) = \varphi(W/2, y)$. The initial conditions are $|\psi| = 1$ and $\varphi = 0$.

We apply a finite-difference representation for the order parameter ψ and the electrostatic potential φ on a uniform Cartesian space grid 129×129 and follow the link variable approach [19]. To solve the equation (5.1) we adopt a Dormand-Prince embedded method [24] for Ordinary Differential Equations (an embedded Runge-Kutta integrator of order 8(5,3) with stepsize control), whereas for the equation (5.2) we adopt a Fourier transform method [24]. When calculating the spatially and time averaged electric field E to build up the $E(J)$ curves, we take the electrostatic potential difference inside the superconducting sample, a distance $10\xi_{GL}$ away from the boundary. In this way our results correspond to a four-probe measurement. The behavior of the system is studied on a large time scale when time-averaged values no longer depend on time.

5.3 Section of a cylindrical shell: asymmetry

For this geometry we assume $R = 1.6W \gg W/2\pi$. The width of the strip is $W = 40\xi_{GL}$. The relevant component of the magnetic field applied as in figure 5.1(a) is $H_\rho(x) = H \cos(x/R - \alpha)$ with the vector potential $A_y(x) = HR \sin(x/R - \alpha) + \text{const}$. As it is seen in figure 5.2(a), the spatial distribution of $H_\rho(x)$ can be tuned by varying the value of the angle α . At $\alpha = 0$ the distribution is almost homogeneous and symmetric around the middle of the strip, but at $\alpha = \pi/2$ the distribution is quite inhomogeneous, antisymmetric and, most important, the sign is reversed at the edges of the strip. This is a peculiarity of a curved geometry, where a field applied homogeneously (e.g., using a coil) is experienced as inhomogeneous by the curved strip. Due to this, the transport properties of the cylindrical section should depend on the magnetic field direction, namely on the angle α . In fact, we found from the $E(J)$ curves that the critical current densities (the current values J_C corresponding to the transition $E = 0 \rightarrow E \neq 0$) can be asymmetric, and the asymmetry is determined by the angle α . In the absence of magnetic field, or when the magnetic field is applied with an angle $\alpha = 0$, no asymmetry occurs, as shown in figure 5.2(b). When $0 < \alpha \leq \pi/2$, the positive critical current density J_{CP} is larger than the negative J_{CN} and the asymmetry ratio $J_{CP}/|J_{CN}|$ depends on α . For $\alpha = \pi/2$, the magnetic field is tangent to the middle point of the curved strip, as shown in the inset of figure 5.2(c). In this case, the positive and the negative critical current densities begin

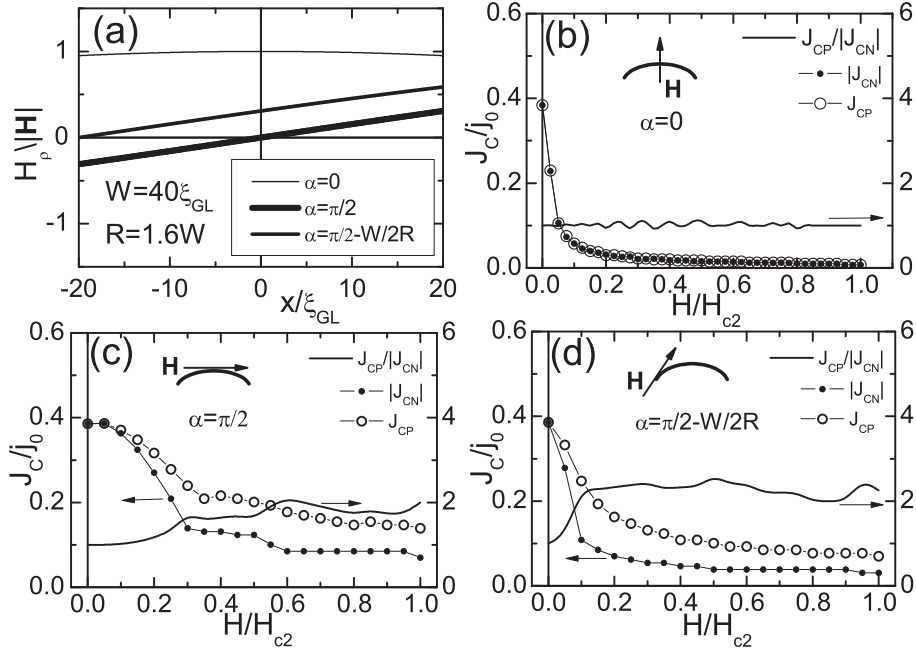


Figure 5.2: (a) Spatial distribution of the normalized radial component of the magnetic field for three values of the angle α . The calculated positive and negative critical currents, and the asymmetry ratio as a function of magnetic field are shown in (b) $\alpha = 0$, (c) $\alpha = \pi/2$ and (d) $\alpha = \pi/2 - W/2R$.

to differ when $H > 0.1H_{c2}$ and, for magnetic fields larger than $0.6H_{c2}$, the asymmetry ratio increases up to about two. On the other hand, if \mathbf{H} is tangent to the left edge of the curved strip, as shown in figure 5.2(d), the positive current density is equal to the negative only when H is close to zero, while as $H > 0$ the asymmetry ratio quickly becomes larger than two and stays almost constant in the investigated field range. Simulations in progress (to be reported in future work) show that when $0 < \alpha < \pi/2$ and a suitable R is chosen, the asymmetry ratio can increase up to four.

In figure 5.3 we plot the $E(J)$ curve in the low electric field range when the magnetic field is tangent to the middle of the curved strip. The value $H = 0.6H_{c2}$ falls in the range of magnetic field where marked asymmetry of the critical current densities takes place [see figure 5.2(c)]. The lower right inset shows the full range $E(J)$. The numbered insets are contour plots of the squared order parameter (snapshots) corresponding to the marked points of the $E(J)$ curve. The dark spots (local strong depression of superconductivity) in these contour plots identify vortices (labeled with +) or anti-vortices (labeled with -). The contour plot labeled (1) shows the squared

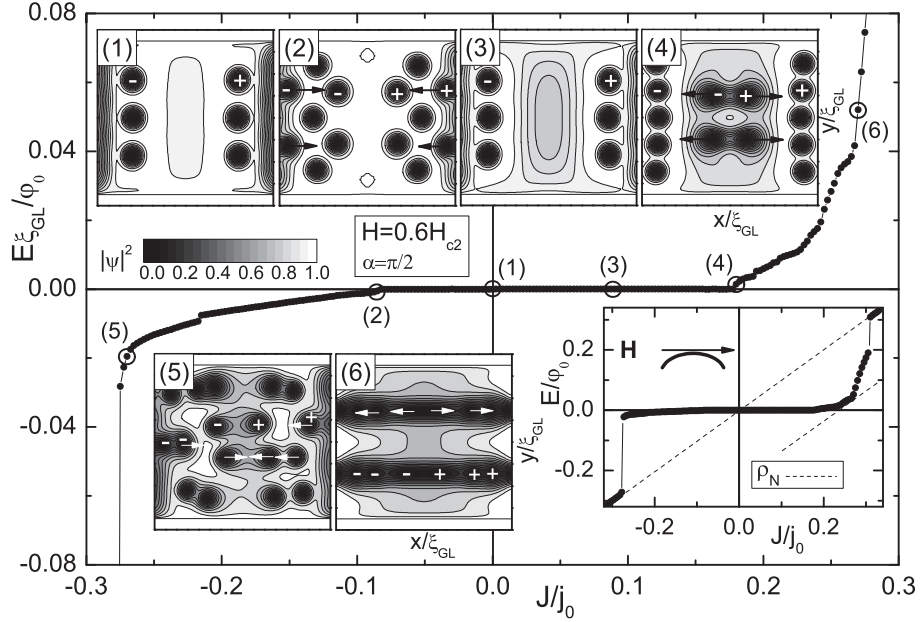


Figure 5.3: $E(J)$ curve in the low electric field range for $H = 0.6H_{c2}$ and $\alpha = \pi/2$. The lower right inset is the full range $E(J)$. The numbered insets show the contour plots of the squared order parameter at the marked points of the $E(J)$ curve.

order parameter at $J = 0$. The magnetic field, whose spatial distribution is antisymmetric [see figure 5.2(a), curve for $\alpha = \pi/2$], generates vortices at the right edge and antivortices at the left edge. Due to the spatial dependence of the field, there exists a magnetic force $F_M \propto \pm \partial_x H_\rho(x)$ that opposes the flux entry. When a negative J is fed into the strip, the Lorentz force F_L points inward the strip both for vortices and antivortices. In snapshot (2) $J = -0.085j_0$, that is, the critical value $J = J_{CN}$ at which the F_L overcomes the F_M . Now flux can enter the strip, with vortices moving from right to the middle and antivortices moving from left to the middle, where they annihilate giving the onset of dissipation ($E \neq 0$). After annihilation, new vortices and antivortices are created again at the strip edges, continuing the ever dynamic process. This periodic nucleation and motion leads, for increasing negative J , to a linear $E(J)$ branch with slope proportional to the flux density. The snapshot (3) shows the state for the same current value of snapshot (2) but positive, i.e., $J = -J_{CN}$. Now Lorentz force and magnetic force point both outward the strip and cooperate to oppose the flux entry, so that no electric field is generated at $J = -J_{CN}$. Therefore, the asymmetry of the critical current densities comes from the net force, depending on current polarity,

acting against flux entry. When J is positive the two forces sum up, hence the only way to generate dissipation is to nucleate vortex-antivortex (V-Av) pairs in the middle of the strip, at some critical current $J_{CP} > -J_{CN}$. This can be seen in snapshot (4), corresponding to $J = J_{CP} = 0.18j_0$. The V-Av pairs so nucleated are driven to opposite directions by Lorentz force and expelled at the edges of the strip. Subsequently, new V-Av pairs are created again in the middle of the sample and the whole kinematic process restarts. When the applied current is increased, the rate of the nucleation/annihilation process increases, as well as the flux density and the slope of the corresponding branch in the $E(J)$ curve. For negative current densities, the periodic nucleation, motion and annihilation is gradually destroyed by the increasing flux density, producing a more complex dynamic as shown in snapshot (5) where $J = -0.27j_0$. Increasing further the current, the system makes a transition to the normal state (superconductivity is destroyed). Turning back to the dissipative branch with positive J , we notice the abrupt switching (at $J = 0.27j_0$) into a state of larger electric resistivity. The differential resistivity $\rho_d(J) = \partial E/\partial J$ of this branch is larger than resistivity of normal state ρ_N , as can be appreciated from the full scale $E(J)$ curve plotted in the inset. As shown in the snapshot (6), this corresponds to a dissipative phase-slip state with two “vortex streets” (VSs) [11, 25] characterized by the motion of V-Av pairs propagating in opposite directions. The nucleation of V-Av pairs is always in the middle and their expulsion at the edges, but the motion is channeled on two phase slip lines arising by increasing the applied current in the sample. The observed dynamics is similar to that of the kinematic V-Av pairs recently reported [12, 13] in mesoscopic strips with localized current injection [12] or subjected to spatially localized magnetic fields from ferromagnets [13]. In our curved strips, as discussed above, we are in the presence of a geometry-induced inhomogeneous magnetic field that enhances nucleation of V-Av pairs, so, we should expect to observe these peculiar high resistivity branches also for the full cylindrical surface, as we will discuss in the *next section*.

We should notice that the asymmetry exhibited by the curved strip is qualitatively not influenced by the tangential component of magnetic field $H_\theta(x)$ that we neglected in our analysis, though for some angle its strength can be larger than the normal component $H_\rho(x)$. For example, with the parameters used in the simulations is, for $\alpha = \pi/2$, $H_\rho(x)/H = \sin x/R \approx x/R$ reaching a maximum value of about ± 0.31 at the edges of the strip, and the tangent component is always larger than the normal component, being $H_\theta(x)/H = \cos x/R \approx 1$. However, as we discussed above, the tangent component only accounts for a monotonic, and in this case also almost homogeneous, reduction of the order parameter, while the normal component

generates the vortex dynamics explaining the asymmetry. As said above, if also the tangent component is used in the simulations, results qualitatively similar to the ones shown in figure 5.2(c) are expected, but, quantitatively, the field axis values should span a smaller range, due to the monotonic suppression of order parameter (compelling a monotonic reduction of the critical currents independent of their sign) associated to the tangent component of magnetic field we have neglected. As said above, we also neglected self fields associated to the bias current, because we have supposed to be in the high κ limit [20] (definitely type-II superconductors) and we have considered sufficiently narrow ($W \leq 2\lambda$, that means $W \leq 2\kappa$ in normalized units) strips. For the chosen width $W = 40\xi_{GL}$, the condition of sufficiently narrow strips strictly holds if a material with $\kappa \geq 20$ were used. To give an example, the 10 nm thick dirty Nb we discussed above with $\kappa \cong 20$ and $W = 400$ nm would be adequately described by the above simplified analysis. If the sample is not strictly mesoscopic, one can expect that self field could play some role, at least at low applied magnetic fields. In fact, the self field depends on the polarity of the bias current and exhibits a spatial dependence that qualitatively resembles the spatial dependence of the normal component of the applied magnetic field. Simulations in progress (to be reported in a future work) on the non mesoscopic limit and performed in the framework of full TDGL model [19] accounting both for screening and self-field confirm that, in fact, in the vortex free regime (Meissner regime), a compensation of self field of positive currents is possible, compelling a moderate enhancement of the positive critical current with respect to the zero field value before its subsequent reduction. However, also in the non mesoscopic limit we noticed that the most robust asymmetry is reached in the vortex regime (mixed regime) achieved at relatively large fields and with the same mechanism we have described here, pertinent to the strictly mesoscopic limit we are interested in the present work.

We conclude this section noticing that the mechanism of asymmetry in the critical currents discussed here is similar to the one we recently reported [7,8] for a Nb/Py bilayer diode. However, in the bilayer the inhomogeneous field was generated by the stray fields at the edges of the ferromagnetic strip, while here the inhomogeneous field is more easily achieved exploiting the curvature of a mesoscopic thin strip. The physical system we have discussed above is very similar to the asymmetric field rectifier [26] experimentally demonstrated many years ago using curved tapes of macroscopic type II superconductors, and explained within the classical critical state model of superconductors. The present analysis performed within the TDGL model for type II superconductors, suggests that the original geometry [26] used to realize the asymmetric field rectifier might work also at mesoscopic scale.

5.4 Cylindrical shell: high dynamical resistivity branches

For this geometry we put $R = W/2\pi$, with $W = 40\xi_{GL}$, and $L = 40\xi_{GL}$. The external magnetic field is applied as shown in figure 5.4(a), giving $H_\rho(x) = H \cos(x/R)$, and vector potential $A_y(x) = HR \sin(x/R)$. As the external field applied homogeneously and perpendicularly to the axis of the full cylindrical shell [see inset of figure 5.4(a) and figure 5.1(b)] produces a zero total magnetic flux through the surface, there will be the same number of vortices and antivortices. Moreover, due to the closed and symmetric geometry, the spatial dependence of radial component of magnetic field is characterized by periodicity, $H_\rho(x + W) = H_\rho(x)$, and symmetry. This implies that, differently from the curved open strip of *previous section*, for this geometry asymmetric response cannot be achieved for any choice of angle α [see figure 5.1] between the direction of external field and the $x = 0$ axis.

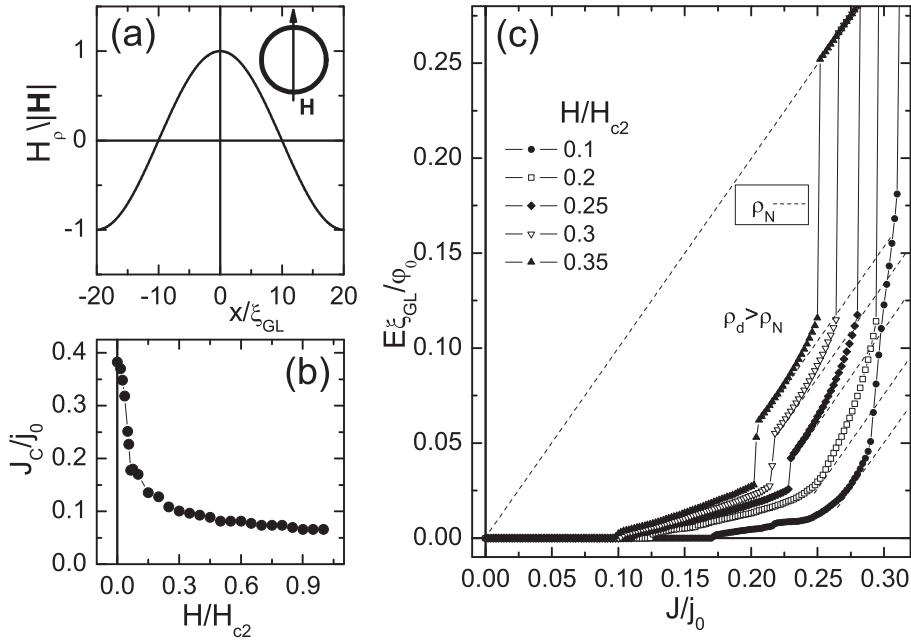


Figure 5.4: (a) *Spatial distribution of the normalized radial component of magnetic field applied as shown in the sketch.* (b) *Calculated positive critical current as a function of magnetic field.* (c) *$E(J)$ curves for several values of magnetic.*

The $E(J)$ curves as well as the critical current densities were all found to be symmetric in the simulations, as expected. The calculated critical current

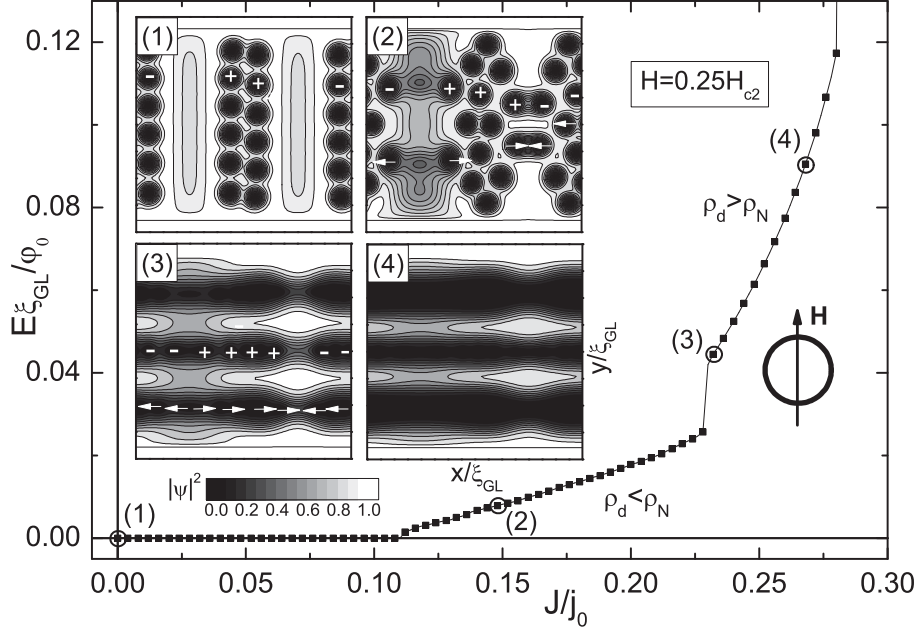


Figure 5.5: $E(J)$ curve at $H = 0.25H_{c2}$. The numbered insets show the contour plots of the squared order parameter corresponding the marked points of the $E(J)$ curve.

density $J_{CP} = -J_{CN}$ as a function of magnetic field is shown in figure 5.4(b). Several $E(J)$ curves at different magnetic field values are shown in figure 5.4(c). For negative currents the curves are simply mirrored with respect to the origin, so that we show only the $E(J)$ curves in the first quadrant. The curves are all characterized by two species of dissipative branches. At a fixed magnetic field value H , the first dissipative branch, starting at $J = J_c(H)$, is roughly linear with a slope lower than ρ_N , the normal state resistivity, like an ordinary flux flow branch. By further increasing the current, E switches to another relatively extended branch having high dynamical resistivity $\rho_d > \rho_N$, then makes the transition to the normal state. The high resistivity branches, are present in a broad magnetic field range, spanning a wider electric field range at low magnetic fields, and are absent at zero applied magnetic field. This is evident in figure 5.4(c), where we also plotted the $\rho = \rho_N$ curve (dashed line) as a guide to the eye.

Vortex dynamics involved in these two species of dissipative branches is described in in figure 5.5, where we plot the $E(J)$ curve at $H = 0.25H_{c2}$ together with some order parameter snapshots relative to the labeled points of the $E(J)$ curve. Snapshot (1) shows the V-Av configuration in the steady-state after we have applied the magnetic field at zero current. As said above,

the total applied magnetic flux is zero and consequently an equal number of vortices and antivortices is induced. Snapshot (2) shows the state for $J = 0.148j_0$, located on the approximately linear, low resistivity branch of the $E(J)$ curve. The V-Av pairs nucleated in the middle of the left side of strip are driven to opposite directions by Lorentz force and move toward the center of the right side of the strip, where they annihilate (in the snapshot the arrows help locating the motion direction). After the annihilation, new V-Av pairs are created again, continuing the whole periodic process. Though complicated by the presence of vortices of opposite charges, this dynamical process is similar to the ordinary flux flow [27], normally associated to almost linear branches with resistivity lower than ρ_N and approaching ρ_N only for magnetic field values approaching the upper critical field. By increasing the applied current the speed of the nucleation/annihilation process increases and at point (3), where $J = 0.23j_0$, there is a sharp transition to a dissipative branch with differential resistivity $\rho_d > \rho_N$. As shown in the snapshot (3), this branch is explained by a dynamical regime qualitatively different from the ordinary flux flow process. Here the motion of V-Av pairs, that takes place in the same way described in snapshot (2), is channeled within three “vortex streets” generated by increasing the applied current. In other words, a dynamical regime takes place that is a mixing between the phase slip line and the flux flow regime [11, 25], similar to the regime accounting for the high resistivity branches discussed in Section 5.3. Snapshot (4) shows that a further increase of the bias current compels the degeneration of phase slip lines in wide normal channels while the motion of the V-Av pairs is progressively suppressed, until the transition to the full normal state is accomplished. This transition to the normal state characterized by the conversion of phase slip lines in elementary resistive domains strongly reminds the mechanisms proposed [28] some years ago to explain experimental results on resistive transition of flat superconducting strips.

As remarked in [12], the oscillations of the order parameter may not be uniform along the phase slip lines: these oscillations may occur in the form of propagating waves carrying the order parameter singularities across the sample. Such waves are named kinematic vortices because are characterized by a velocity larger than the one associated to the ordinary Abrikosov vortex, though lower than that of the Josephson vortex. Moreover, the phase slip lines should behave as localized Josephson weak links, as experimentally proved in [11]. Further insight into this point and into the dynamical regime aimed to explain the high dynamical resistivity branches is presented in figure 5.6. Here we plot the curve at low magnetic field values, where the generation of only two phase slip lines allows to simplify the analysis. Moreover, making use of a logarithmic scale for the contour plots of the squared

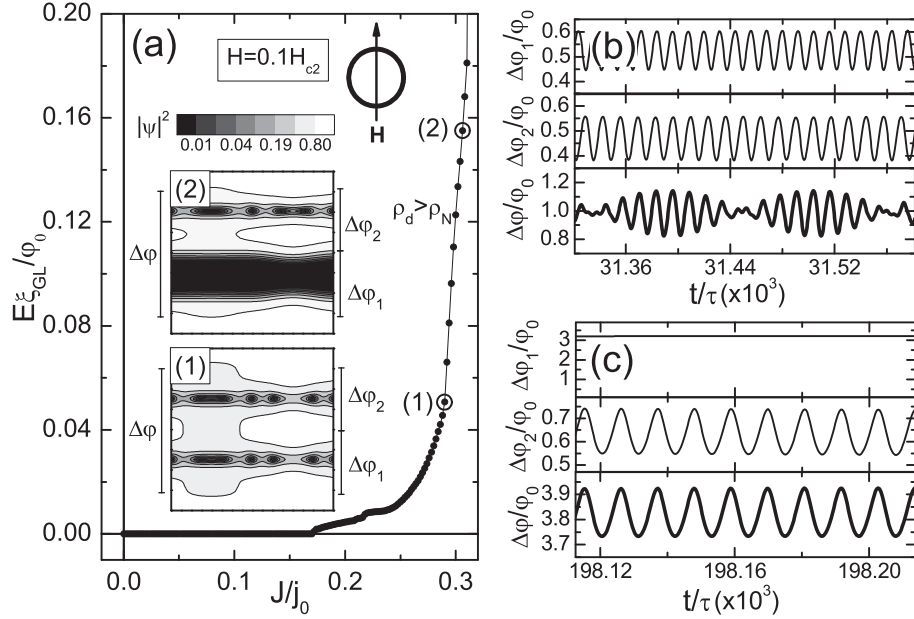


Figure 5.6: (a) $E(J)$ curve at $H = 0.1H_{c2}$. The numbered insets show the contour plots of the squared order parameter when we are on the marked points of the $E(J)$ curve. (b) Partial and total voltages vs time at point (1) of (a). (c) Voltages vs time for point (2) of (a).

order parameter, the V-Av pairs in the channels are better resolved. Figure 5.6 shows the configuration of the two V-Av phase slip lines occurring at the very beginning of the high resistivity branch [snapshot (1)] and at higher current [snapshot (2)], and the voltage across the lines. In the first case each phase slip line generates almost sinusoidal voltage oscillations [figure 5.6(b)] with comparable oscillation frequencies, similar to that expected for (spatially localized) Josephson weak links. The period of the voltage oscillations ($T_{PSL} \approx 7\tau$) is found to be much shorter than the one ($T_{FF} \approx 200\tau$) associated to the impulsive voltage oscillations generated by the flux flow motion in the low resistivity branch, in agreement with the fact that kinematic V-Av pairs move faster than ordinary V-Av pairs. This behavior is observed in a relatively large current range. In the second case [snapshot (2)], one of the phase slip lines has evolved into a wide normal channel, while the other still generates voltage oscillations [figure 5.6(c)]. Further increase of the bias current turns the remaining phase slip line into a normal channel, followed by an avalanche transition to the fully normal state.

The evolution of phase slip lines in wide normal channels with avalanche transition to the normal state provides a qualitative physical explanation

for the somewhat anti-intuitive fact that the extent of the high resistivity branches reduces as the magnetic field is increased. As can be appreciated from comparison of snapshots in figure 5.6(a) and 5.5, the separation between phase slip lines decreases as the magnetic field increases. The phase slip lines evolves in wide normal channels when current is increased and, intuitively, if the normal channels are less dense (low magnetic fields) the avalanche transition to the normal state (that determines the extent in current of the high resistive branch) is delayed in current with respect to the case of more dense normal channels (large magnetic fields).

We conclude this section noting that the voltage oscillations associated to the high resistivity branches can fall in a frequency range that can be of interest for operation of the superconducting cylindrical strip as a magnetic field and bias current tuned high frequency mesoscopic oscillator. As an example, using Nb, a $\tau \approx 10$ ps is typical [12], giving $T_{PSL} \approx 100$ ps, i.e., a frequency of the voltage oscillations falling in the 10 GHz range.

5.5 Summary

Summarizing, we have investigated numerically the vortex dynamics in curved mesoscopic superconducting strips conforming to cylindrical shells. The cylindrical section exhibits asymmetric transport properties for a suitable choice of the orientation of the external magnetic field, while the full cylindrical surface features a very rich vortex-antivortex dynamics, ranging from the familiar V-Av flux flow regime to kinematic V-Av pairs phase slip lines regime as the bias current is increased. The kinematic V-Av pairs account for dissipative branches in the $E(J)$ curves exhibiting a dynamical resistivity larger than the normal state resistivity.

Bibliography

- [1] Mawatari Y 2009 *Phys. Rev. B* **80** 184508
- [2] Lu-Dac Mathieu and Kabanov V V 2009 *Phys. Rev. Lett.* **105** 157005
- [3] Qiu C and Qian T 2009 *Phys. Rev. B* **79** 054513
- [4] Wang H, Rosario M M, Kurz N A, Rock B Y, Tian M, Carrigan P T and Liu Y 2005 *Phys. Rev. Lett.* **95** 197003
- [5] Liu Y, Zadorozhny Yu, Rosario M M, Rock B Y, Carrigan P T, Wang H 2001 *Science* **294** 2332
- [6] Aladyshkin A Yu, Vodolazov D Yu, Fritzsche J, Kramer R B G and Moshchalkov V V 2010 *Appl. Phys. Lett.* **97** 052501
- [7] Carapella G, Granata V, Russo F and Costabile G 2009 *Appl. Phys. Lett.* **94** 242504
- [8] Carapella G, Sabatino P and Costabile G 2010 *Phys. Rev. B* **81** 054503
- [9] Vodolazov D Y, Gribkov B A, Klimov A Yu, Rogov V V and Vdovichev S N 2009 *Appl. Phys. Lett.* **94** 012508
- [10] Papon A, Senapati K and Barber Z H 2008 *Appl. Phys. Lett.* **93** 172507
- [11] Sivakov A G, Glukhov A M, Omelyanchouk A N, Koval Y, Muller P and Ustinov A V 2003 *Phys. Rev. Lett.* **91** 267001
- [12] Berdiyrov G R, Milosevic M V and Peeters F M 2009 *Phys. Rev. B* **79** 184506

-
- [13] Berdiyrov G R, Milosevic M V and Peeters F M 2009 *Phys. Rev. B* **80** 214509
- [14] Vodolazov D Y, Peeters F M, Dubonos S V and Geim A K 2003 *Phys. Rev. B* **67** 054506
- [15] Vodolazov D Y, Peeters F M, Grigorieva I V and Geim A K 2005 *Phys. Rev. B* **72** 024537
- [16] Kramer L and Baratoff A 1977 *Phys. Rev. Lett.* **39** 518
- [17] Kramer L and Watts-Tobin R J 1978 *Phys. Rev. Lett.* **40** 1041
- [18] Carty G J and Hampshire D P 2008 *Phys. Rev. B* **77** 172501
- [19] Winiecki T and Adams C S 2002 *Phys. Rev. B* **65** 104517
- [20] Du Q and Gray P 1996 *SIAM J. Appl. Math.* **56** 1060
- [21] Gubin I, Ilin K S, Vitusevich S A, Siegel M and Klein N 2005 *Phys. Rev. B* **72** 064503
- [22] Sabatino P, Cirillo C, Carapella G, Trezza M and Attanasio C 2010 *J. Appl. Phys.* **108** 053906
- [23] Tinkham M 1996 *Introduction to Superconductivity* (Singapore: McGraw-Hill)
- [24] Press W H, Teukolsky S A, Vetterling W T and Flannery B P 2007 *Numerical recipes: the art of scientific computing* (Cambridge University Press)
- [25] Vodolazov D Y and Peeters F M 2007 *Phys. Rev. B* **76** 014521
- [26] Swartz P S and Hart H R 1967 *Phys. Rev.* **156** 412
- [27] Blatter G, Feigelman M V, Geshkenbein V B, Larkin A I and Vinokur V M 1994 *Rev. Mod. Phys.* **66** 1125
- [28] Il'ichev E V, Kuznetsov V I and Tulin V A 1992 *JETP Letters* **56** 295 (arXiv:cond-mat/0305584)

Single Abrikosov vortex trapped in a mesoscopic superconducting cylindrical surface

6.1 Introduction

Due to the remarkable advances in the nanotechnology and nanofabrication subfields achieved in the last two decades thin mesoscopic superconductive strips, i.e., strips with lateral dimensions at sub-micrometer scale, have received a growing interest in the last years. Most of experimental and theoretical studies reported to date were focused on flat strips. Recently, curved strips conforming to cylindrical shells have been theoretically addressed with emphasis on self magnetic field distribution and dissipation [1], phase slip line nucleation in the presence of a magnetic field longitudinal to the cylinder axis [2], and thermal activation of phase slip lines in doubly connected superconducting cylinders [3] (toroidal shells).

In this work we investigate numerically, in the framework of the time-dependent Ginzburg-Landau (TDGL) formalism, the transport properties of a sub-micrometer scale superconducting cylindrical surface with a single Abrikosov vortex trapped in the surface. In contrast to the flat strips case, in the system that we propose here the ideal conditions for the study of the dynamics of a single Abrikosov vortex are easily achieved, and also experimentally. In fact, the edge effects that dominate and complicate the dynamics in the flat strips here are suppressed and, instead, intrinsically periodic boundary conditions are realized. Moreover, here an external spatially periodic potential of controlled strength can be easily applied by means of a homogeneous magnetic field. Finally, in the proposed system the dynamics of the single vortex can be addressed also in the absence of a magnetic field. This is achieved by means of the fluxoid conservation that holds in our cylin-

dricial shell, but it is not applicable for open geometries such as the common flat strip with no holes.

In annular Josephson tunnel junctions [4], a single Josephson vortex can be trapped in the junction in several ways. For example, cooling the sample below the critical temperature T_c [5] while a small magnetic field or a small bias current are applied can result, due to the fluxoid quantization [4, 6], in the trapping of a flux quantum linked to a current vortex. Below T_c , due to the fluxoid conservation [4, 6], this vortex will be stable also in the absence of an externally applied field. Here we discuss a similar picture in the mesoscopic cylindrical superconducting shell. The shell is assumed to be contacted by hollow superconductive leads (i.e., the leads have a hole), so that flux lines can close, to much thicker than the shell itself, so to confine the vortex along the length of the shell. A magnetic field applied transverse to the axis of the cylindrical surface is a simple way to bind the Abrikosov vortex trapped in the surface to a spatially periodic potential that can be tilted by the transport current. Here we show that the vortex behaves nicely as an overdamped quasi-particle in a tilted washboard potential, provided the transport current and the magnetic field are not large. In this solid state system, mechanical quantities are proportional to electrical quantities. The vortex velocity is proportional to the measured electric field E and the external force acting on the vortex is proportional to applied transport current density J . The cylindrical thin strip with the trapped vortex exhibits $E(J)$ curves and time-dependent electric fields $E(t)$ very similar to the ones exhibited by a resistively shunted Josephson weak link.

The Chapter is organized as follows. In section 6.2 we describe the TDGL model as specialized to the physical system that we address in the present work. The dynamics of the single Abrikosov vortex trapped in the shell is approached in section 6.3 both by a simple quasi-particle approximation model and by full integration of the TDGL model. A brief summary of the results of the work is given in section 6.4.

6.2 The theoretical model

The superconducting strip considered in this Chapter is sketched in figure 6.1(a). With respect to the cylindrical reference frame (ρ, θ, y) shown in figure 6.1, the length of the strip lies parallel to the y -axis (cylinder axis), a uniform transport current J is applied along the strip length, and the magnetic field is applied perpendicular to the y -axis. Noticing that for the cylindrical surface the radial coordinate is constant, ($\rho = R$), we can use the curvilinear coordinate $x = R\theta$ (length of arc along the circumference, and

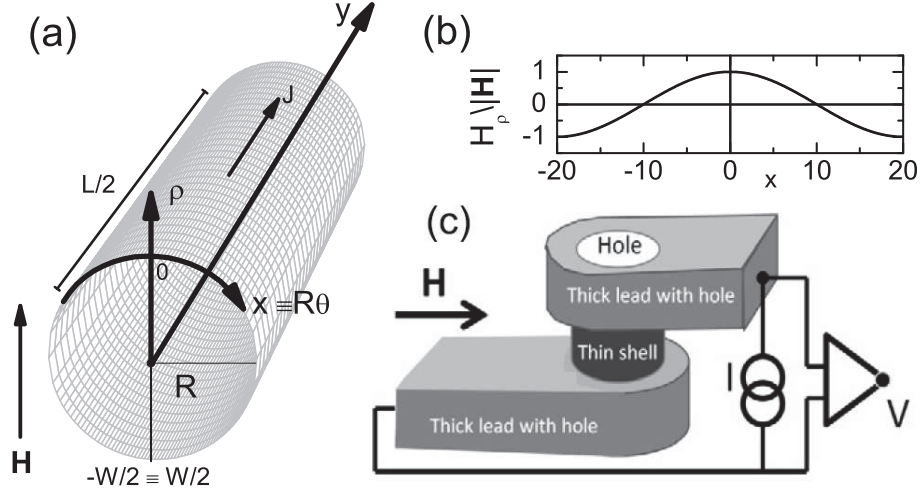


Figure 6.1: (a) Superconducting cylindrical shell and direction of external magnetic field and bias current. The cylindrical coordinate frame (ρ, θ, y) can be mapped to an (x, y) coordinate frame, the x coordinate being the length of the arc. (b) Spatial distribution of the radial component of magnetic field applied as in (a). (c) The thin shell is electrically contacted with thick leads with a hole at the center.

directed as $\hat{\theta}$) instead of the coordinate θ . In this reference frame the strip can be described using only x and y coordinates with ranges $-L/2 < y < L/2$ and $-W/2 < x < W/2$. Moreover, all spatial derivatives reduce to the simple cartesian form. For our numerical study we use the time-dependent Ginzburg-Landau (TDGL) equation supplemented with the equation for the electrostatic potential [7–9]:

$$u \left(\frac{\partial}{\partial t} + i\varphi \right) \psi = (\nabla - i\mathbf{A})^2 \psi + (1 - |\psi|^2) \psi \quad (6.1)$$

$$\nabla^2 \varphi = \text{div} \{ \text{Im} [\psi^* (\nabla - i\mathbf{A}) \psi] \} \quad (6.2)$$

where $\psi = |\psi| e^{i\phi}$ is the complex order parameter, \mathbf{A} the vector potential, φ the electrostatic potential and the coefficient $u = 5.79$ [10] governs the relaxation of the order parameter. All physical quantities are measured in dimensionless units: the coordinates are in units of the coherence length $\xi_{GL}(T) = \xi_0 / \sqrt{1 - T/T_c}$, with $\xi_0 = \sqrt{\pi \hbar D / 8 k_B T_c}$, and T_c is the critical temperature, D is the diffusion constant. Time is measured in units of the relaxation time $\tau = \tau_0 / (1 - T/T_c)$ with $\tau_0 = 4\pi \sigma_n \lambda^2 / c^2 = \xi_0^2 / Du$ (σ_n is the normal-state conductivity, $\lambda = \kappa \xi_{GL}$ the magnetic field penetration depth, with κ the GL parameter). The order parameter is in units of $\Delta(T) = \Delta_0 \sqrt{1 - T/T_c}$, where $\Delta_0 = 4k_B T_c \sqrt{u} / \pi$ is the superconducting gap at $T = 0$ which follows

from Gor'kov's derivation of the Ginzburg-Landau equations. The vector potential is measured in units $\Phi_0/2\pi\xi_{GL}$ ($\Phi_0 = ch/2e$ is the quantum of magnetic flux) and the electrostatic potential is in units of $\varphi_0(T) = \hbar/2e\tau$. In these units the magnetic field is scaled with $H_{c2}(T) = \Phi_0/2\pi\xi_{GL}^2$ and the current density with $j_0(T) = c\Phi_0/8\pi^2\lambda^2\xi_{GL}$.

For the sake of simplicity, we neglect intrinsic pinning effects. Self-fields associated with the bias current and the screening effects are also neglected, otherwise an equation [11] for the vector potential \mathbf{A} should be integrated in the above model. This simplification is justified in the high κ limit [12] (definitely type-II superconductors) and in the mesoscopic limit we are dealing with, i.e., very thin ($d \leq \xi_{GL} \ll \lambda$) and sufficiently narrow ($W \leq 2\lambda$) strips. In the following we will assume to work in a temperature range so close to T_c , that the phenomenological TDGL model is supposedly adequate, and we shall put $W = L = 40\xi_{GL}$, $d \leq \xi_{GL}$, and $\kappa \gg 1$.

Being in the limit of very thin strips of type II superconductors, in the following we shall presume that the strips are affected by the magnetic field component that is normal to the surface (i.e., H_ρ) much more than by the component tangent to the surface (i.e., H_θ). This is justified by the fact [6] that the upper parallel critical field of a very thin strip is larger than the upper perpendicular critical field. This is even more true for the lower parallel critical fields (first flux penetration), because $H_{c1}^{\parallel}/H_{c1}^{\perp} \approx \lambda/d \gg 1$. Therefore, for the sake of simplicity, in the following we will neglect the component H_θ when assigning the vector potential to equations (6.1) and (6.2). The external magnetic field, applied as shown in figure 6.1(a), produces the $H_\rho(x) = H \cos(x/R)$ shown in figure 6.1(b). To describe this field we use the vector potential $A_y(x) = HR \sin(x/R)$. Notice that, due to the closed and symmetric geometry, the spatial dependence of radial component of magnetic field is characterized by intrinsic periodicity, $H_\rho(x+W) = H_\rho(x)$, and symmetry.

Finally, we refer to the realistic experimental situation where the mesoscopic samples are electrically connected by superconductive banks (leads) which have better superconductive properties than the thin strip itself, which occurs when, e.g., the banks are much thicker than the strip, as sketched in figure 6.1(c). The banks have a hole at the center. This allows a single Abrikosov vortex to be trapped as described above, because its magnetic field lines can exit from the hole in the cylinder (along the y -axis), similarly [5] to the magnetic field line of a Josephson vortex in a long annular Josephson junction. Moreover, if the banks are much thicker than the shell, they also confine, or pin, the trapped vortex along the y -direction. This can be easily understood if one remembers [13] that the vortex-line energy is proportional to its length. In our case this means that the vortex will

be pinned to the region where the thickness is lower, i.e., will stay in the shell. Moreover, another confining mechanism can work if the hollow banks are much thicker than the shell. In fact, also assuming the leads made of the same material as the shell, the effective penetration depth [6] of the shell $\Lambda_S = \lambda^2/d$ will be much larger than the effective penetration depth of the leads $\Lambda_L \approx \lambda$, because we assumed $d \ll \lambda$. As recently reported [14], the walls of the region with shorter penetration depth (the leads) will repel the vortex towards the region with larger penetration depth (the thin shell), so realizing a confinement, or channelling, along the y -direction. To account for the presence of these leads, in our calculations we make use of the “bridge” condition in the y -direction: in a region of length $2.5\xi_{GL}$ at the ends of the strip, equations (6.1) and (6.2) are reduced to $(\partial_t + i\varphi)\psi = 0$, $\nabla^2\varphi = 0$ with boundary conditions $\partial_y\psi = 0$ and $\partial_y\varphi = -J$, where J is the uniformly injected bias current density.

The boundary condition in the x -direction for the scalar potential is $\varphi(-W/2, y) = \varphi(W/2, y)$. To describe the single vortex trapped in the cylindrical shell we use for the order parameter the boundary conditions [15] $\psi(W/2, y) = \psi(-W/2, y) \exp(i\pi)$, $\psi(-W/2, y) = \psi(W/2, y) \exp(-i\pi)$ in the model Eqs. (6.1) and (6.2). This constraint on phase ϕ of order parameter is similar to the one used to describe a trapped fluxon in annular Josephson junctions [5, 16] and here accounts for a flux $\Phi = \Phi_0$ (2π in our units) threading the surface [15]. The initial condition is chosen as [17] $\psi(x, y, 0) = (x + iy)/\sqrt{x^2 + y^2}$, describing a “seed” solution with behaviour [17] of phase ϕ consistent with the constraint imposed by the boundary conditions. After a small transient this initial condition evolves in the standard Abrikosov vortex solution achieved in presence of external magnetic field.

We apply a finite-difference representation for the order parameter ψ and the electrostatic potential φ on a uniform Cartesian space grid 129×129 and follow the link variable approach [11]. To solve the equation (6.1) we adopt a Dormand-Prince embedded method [18] for Ordinary Differential Equations (an embedded Runge-Kutta integrator of order 8(5,3) with stepsize control), whereas for the equation (6.2) we adopt a Fourier transform method [18]. When calculating the space- and time-averaged electric field E to build up the $E(J)$ curves, we take the electrostatic potential difference inside the superconducting sample, a distance $10\xi_{GL}$ away from the boundary. In this way our results correspond to a four-probe measurement. The behaviour of the system is studied on a large time scale when time-averaged values no longer depend on time.

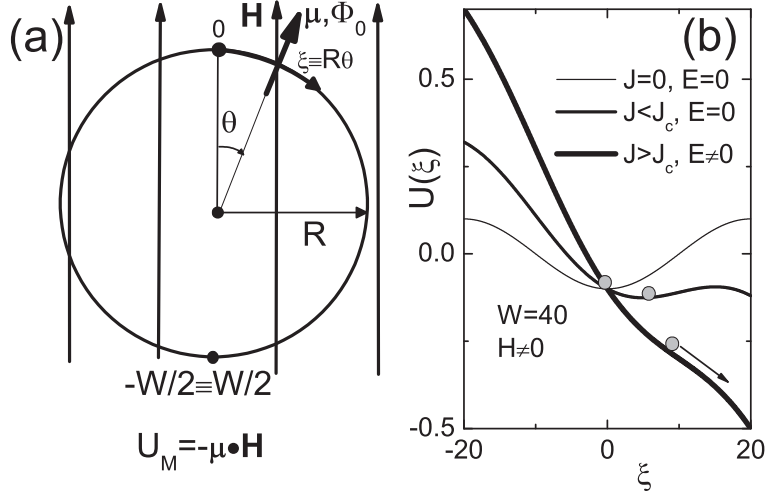


Figure 6.2: (a) A single vortex as a quasi-particle with magnetic moment $\boldsymbol{\mu}$ and position $\xi(t)$ along the circumference of a cylindrical surface at $y = 0$. The homogeneous magnetic field \mathbf{H} induces a sinusoidal potential on the vortex. (b) The washboard potential experienced by the vortex at different values of current density J . When $J > J_c$ the vortex starts a revolution and an electric field E is established.

6.3 Numerical results and discussion

First, we think it is worth discussing the physics of a single Abrikosov vortex trapped in the cylindrical shell on an intuitive grounds, as for the “quasi-particle” description of a Josephson flux quantum trapped in an annular Josephson junction [5, 16, 19–21]. Like the Josephson vortex, the Abrikosov vortex is a current vortex linked to a quantum of a magnetic flux Φ_0 having a magnetic moment $\boldsymbol{\mu}$, directed as $\hat{\rho}$ [see figure 6.2(a)]. If the external forces acting on the vortex vary on a spatial scale larger than the vortex extension (diameter of the order of $2\sqrt{2}\xi_{GL}$) we can describe the vortex as a quasi-particle with a magnetic moment $\boldsymbol{\mu}$ and a spatial position $\xi(t)$, the time-dependent position of the normal core. When an external magnetic field is homogeneously applied as in figure 6.2(a), and it is so weak that no other vortices are induced, the vortex experiences a sinusoidal magnetic potential $U_M = -\boldsymbol{\mu} \cdot \mathbf{H} \propto -H \cos(\theta) = -H \cos(2\pi\xi/W)$, which gives a magnetic force $F_M \propto -H \sin(2\pi\xi/W)$. This field-induced potential can be tilted by the potential $U_L \propto -J\xi$ due to the Lorentz force $F_L \propto J$ associated to a bias current density J . Since the motion of the normal core results in a strong damping, the vortex can be described as a massless particle [22], i.e., its velocity is proportional to the applied force. Therefore, the single vortex

trapped in the cylindrical shell should exhibit the dynamics of an overdamped particle in a washboard potential $U(\xi) = U_M + U_L$

$$\eta \dot{\xi}(t) \propto E(t) = -\frac{\partial U(\xi)}{\partial \xi} = F_M + F_L, \quad (6.3)$$

where η is a damping coefficient and we take into account that with a flux motion there is associated an electric field, $\dot{\xi}(t) \propto E(t)$. As sketched in figure 6.2(b), when $J = 0$ the vortex is at rest ($\dot{\xi}=0$) in the potential minimum; hence, $E = 0$. When J is increased, the washboard is tilted, and the vortex will be at rest ($E = 0$) as long as a small barrier potential is still present. At some critical current density J_c , the potential barrier will vanish and for $J > J_c$ the vortex will be in motion with $E \neq 0$. The critical value J_c is the value at which the Lorentz force ($\propto J$) overcomes the maximum of the magnetic force ($\propto H$), as can be deduced from equation (6.3). This means that we should expect a dependence $J_c \propto H$ for the critical current density as a function of magnetic field. When no magnetic field is applied, the only external force that acts on the vortex is the Lorentz force. From equation (6.3), a linear relation $E = \rho_F J$ between electric field (velocity) and current density (force) should be expected. When a magnetic field is turned on, a non linear $E(J)$ relation is expected, with $E = 0$ for $J \leq J_c$ (the vortex at rest) and $E \neq 0$ for $J > J_c$ (the vortex revolving along the circumference). The functional form of $E(J)$, as well as some information on the $E(t)$, can be found analytically if we recast equation (6.3) in the form of the overdamped pendulum equation. Identifying the position of the vortex core by the angle $\theta = 2\pi\xi/W$ [see figure 6.2(a)] and making use of the $J_c \propto H$ and ρ_F discussed above, equation (6.3) can be rewritten in the familiar form

$$\alpha = \beta \dot{\theta} + \sin(\theta), \quad (6.4)$$

where $\alpha = J/J_c$, and $\beta = \rho_F/J_c$, and, in these units, $E(t) = \dot{\theta}(t)$. This equation is analytically solvable. For $\alpha > 1$ the $\theta(t)$ is periodic with period $[4] T_v = 2\pi\beta(\alpha^2 - 1)^{-\frac{1}{2}}$, and the time-averaged electric field is $E = \langle \dot{\theta} \rangle = 2\pi/T_v$. This allows us to write the $E(J)$ curve of the single vortex trapped in the cylindrical surface as

$$E/(J_c\rho_F) = \sqrt{(J/J_c)^2 - 1}, \quad (6.5)$$

and the instantaneous electric field as

$$\frac{E(t)}{\rho_F J_c} = \frac{(\alpha^2 - 1)/\alpha}{\cos^2 \frac{\pi t}{T_v} + \frac{1}{\alpha^2} \left(\sqrt{\alpha^2 - 1} \sin \frac{\pi t}{T_v} - \cos \frac{\pi t}{T_v} \right)^2}. \quad (6.6)$$

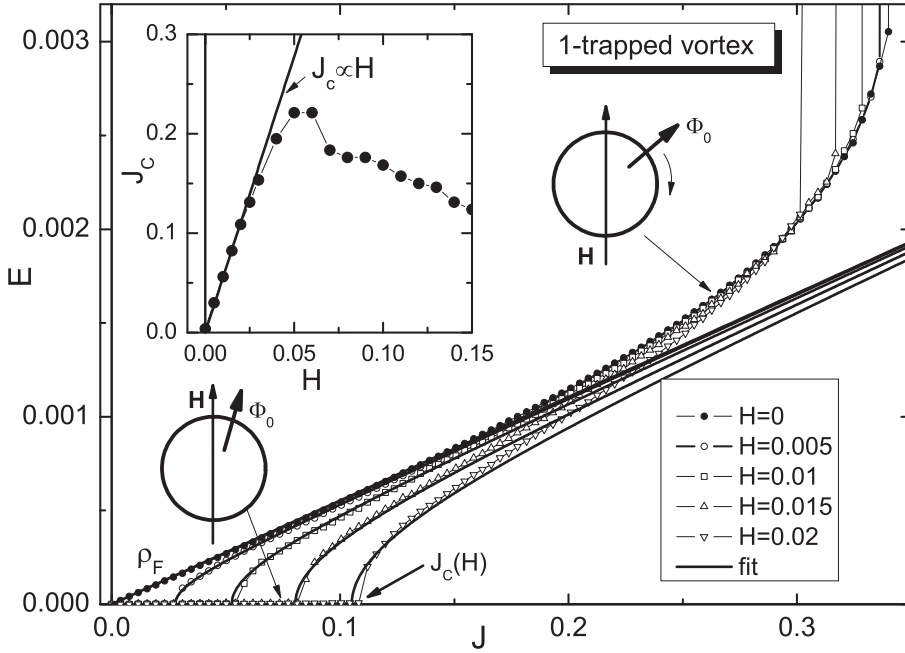


Figure 6.3: $E(J)$ curves when a single vortex is trapped, calculated for several values of the magnetic field applied as shown in the sketches, fitted with Eq. (6.5) (solid lines). The inset shows the critical currents as a function of magnetic field.

The main results of the analysis carried on in the quasi-particle approximation are substantially confirmed by the numerical simulation of the TDLG model. In figure 6.3 we show the calculated $E(J)$ curves for a single vortex trapped in the cylindrical surface at several magnetic fields. As predicted by equation (6.5), when $H = 0$ we find a linear dependence $E(J) = \rho_F J$, while when $H \neq 0$ we find a critical current density $J_c(H)$. The vortex is at rest for $J < J_c(H)$, and revolves for $J > J_c(H)$, as sketched in figure 6.3. The calculated $J_c(H)$ increases proportionally to the magnetic field strength H (see the inset of figure 6.3), provided H is low enough. As anticipated above, the departure from linearity of $J_c(H)$ approximately occurs at magnetic field values that induce the creation of vortex-antivortex pairs.

In figure 6.3 we also show the calculated $E(J)$ compared with functional form equation (6.5), where the $J_c(H)$ are the ones shown in the inset and ρ_F is the flow resistivity at $H = 0$. The fit is satisfactory, provided the magnetic field is weak and the bias current density is safely lower than the depairing current density $J_D \simeq 0.39$; in other words, the simple description given by Eq.(6.5) is valid only up to $J/J_D \simeq 0.4$. The main reason for this departure

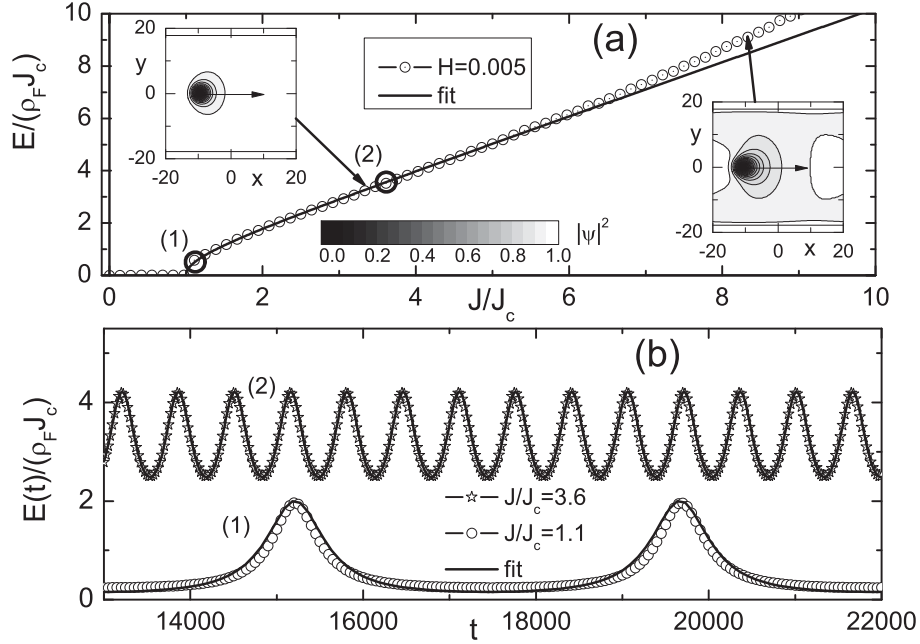


Figure 6.4: (a) Calculated $E(J)$ curve for a single vortex trapped in magnetic field (open circle) compared to the theoretical fit (line). The insets show the contour plots of the squared order parameter at the points highlighted by the arrows. (b) Voltages vs time response (symbols) on the two marked point in (a) compared to the theoretical fit (solid line).

from an ideal behaviour is the progressive reduction of order the parameter caused by an increasing transport current J , because $|\psi|^2 = 0$ when $J = J_D$. In figure 6.4(a) we compare the $E(J)$ curve at $H = 0.005$ with the ideal behaviour equation (6.5) together with the contour plots of the squared order parameter for two representative J . When the current density is low, and the calculated $E(J)$ strictly follows the ideal behaviour, the single vortex moves over a fully superconductive background ($|\psi|^2 = 1$), while for large current densities the departure from the ideal behaviour becomes evident because the vortex solution is perturbed as it moves over a weaker superconducting background ($|\psi|^2 < 1$). In figure 6.4(b) we show the electric field $E(t)$ for the two bias current densities (1) and (2) in figure 6.4(a). Here we are in the ideal regime, and, as expected, the calculated $E(t)$ (open symbols) can be nicely fitted with equation (6.6) (solid lines). For the curve (1) in figure 6.4(b), J is only slightly larger than J_c and $E(t)$ appears as a set of periodic pulses. The time lapse T_v between the pulses decreases when J is increased and $E(t)$ tends to oscillate sinusoidally [curve (2) shown in figure 6.4(b)].

We conclude by pointing out that the dynamics of a single Abrikosov vor-

tex trapped in the cylindrical shell shows many similarity with the dynamics of the phase difference of an overdamped Josephson weak link [4]. In fact, equation (6.5) also describes the form of voltage-current curve and equation (6.6) the voltage oscillation of a resistively shunted Josephson junction [4]. To some extent, there are similarities also with the dynamics of a single Josephson flux quantum trapped in an annular Josephson tunnel junction in the presence of a field-induced potential [5, 16, 20, 21]. However, due to the normal core, dynamics of Abrikosov vortex is intrinsically strongly overdamped and non relativistic. Therefore, the Josephson vortex will behave as the Abrikosov vortex only in the limit of vortex velocity quite low compared to the Swihart velocity [4] or in the presence of very strong damping, that can be achieved [21, 23], e.g., working near to T_c , or adding an external resistive shunt to the Josephson tunnel junction.

6.4 Summary

Summarizing, we have investigated numerically the dynamics of an Abrikosov vortex trapped in a mesoscopic superconducting cylindrical shell embedded in a magnetic field applied transverse to its axis. Provided the transport current and the magnetic field are not large, we have found that the vortex behaves as an overdamped quasi-particle in a tilted washboard potential and that the cylindrical shell with the trapped vortex exhibits $E(J)$ curves and time-dependent electric fields very similar to the ones exhibited by a resistively shunted Josephson weak link.

Bibliography

- [1] Mawatari Y 2009 *Phys. Rev. B* **80** 184508
- [2] Lu-Dac Mathieu and Kabanov V V 2009 *Phys. Rev. Lett.* **105** 157005
- [3] Qiu C and Qian T 2009 *Phys. Rev. B* **79** 054513
- [4] Barone A and Paterno G 1982 *Physics and Applications of the Josephson Effect* (New York: Wiley)
- [5] Wallraff A, Lukashenko A, Lisenfeld J, Kemp A, Fistul M, Koval Y and Ustinov A V 2003 *Nature (London)* **425** 155
- [6] Tinkham M 1996 *Introduction to Superconductivity* (Singapore: McGraw-Hill)
- [7] Vodolazov D Y, Peeters F M, Dubonos S V and Geim A K 2003 *Phys. Rev. B* **67** 054506
- [8] Vodolazov D Y, Peeters F M, Grigorieva I V and Geim A K 2005 *Phys. Rev. B* **72** 024537
- [9] Kramer L and Baratoff A 1977 *Phys. Rev. Lett.* **39** 518
- [10] Kramer L and Watts-Tobin R J 1978 *Phys. Rev. Lett.* **40** 1041
- [11] Winiecki T and Adams C S 2002 *Phys. Rev. B* **65** 104517
- [12] Du Q and Gray P 1996 *SIAM J. Appl. Math.* **56** 1060

-
- [13] Daldini O, Marinoli P, Olsen J L and Berner G 1973 *Phys. Rev. Lett.* **32** 218
 - [14] Yu K, Heitmann T W, Song C, DeFeo M P, Plourde B L T, Hesselberth M B S and Kes P H 2007 *Phys. Rev. B* **76** 220507(R)
 - [15] Du Q, Gunzburger M D and Peterson J S 1992 *SIAM Review* **34** 54
 - [16] Groenbech-Jensen N, Lomdahl P S and Samuelsen M R 1991 *Phys. Rev. B* **43** 12799
 - [17] Liao H Y, Zhou S P and Shi X Y 2004 *Chin. Phys.* **13** 737
 - [18] Press W H, Teukolsky S A, Vetterling W T and Flannery B P 2007 *Numerical Recipes: The Art of Scientific Computing* (Cambridge: Cambridge University Press)
 - [19] McLaughlin D W and Scott A C 1978 *Phys. Rev. A* **18** 1652
 - [20] Ustinov A V and Thyssen N 1997 *J. Low Temp. Phys.* **106** 193
 - [21] Carapella G 2001 *Phys. Rev. B* **63** 054515
 - [22] Blatter G, Feigelman M V, Geshkenbein V B, Larkin A I and Vinokur V M 1994 *Rev. Mod. Phys.* **66** 1125
 - [23] Carapella G and Costabile G 2001 *Phys. Rev. Lett.* **87** 077002

Considerable asymmetry of the critical current in a Niobium thin strip of plano-convex section due to double kink formation

7.1 Introduction

Asymmetric voltage-current [$V(I)$] curves exhibited by superconducting devices are at the base of superconducting rectifiers, or superconducting diodes, [1–12]. A superconducting diode is the dual of a semiconducting diode, as the role of current and voltage are interchanged. It exhibits zero or finite resistance depending on the sign of the bias current. Compared to a semiconducting diode, this kind of diode is a rather low impedance device that can support and rectify very high current densities even near the absolute zero. Recently, asymmetric $V(I)$ curves have been reported [6–12] in Ferromagnet-Superconductor hybrids on the micron scale. The asymmetry in the critical [13] currents in these hybrids has often been attributed [6–12] to the inhomogeneous stray magnetic fields generated by the ferromagnet.

Here we demonstrate experimentally that a marked asymmetry in the critical currents can be also exhibited by a single thin superconducting strip having plano-convex cross section when subjected to a homogeneous magnetic field applied parallel to the substrate. Unlike the Ferromagnet-Superconductor hybrids, this kind of rectifier does not undergo hysteresis or the bistability phenomena normally associated to a ferromagnetic film, that, though desirable for some applications (e.g., memory elements), could be unwanted in some other applications. Our strip is made of a type II superconductor [13], Niobium, in the dirty limit regime. Here we report measurements on $V(I)$ curves and asymmetry ratios as function of the applied magnetic field and temperature, besides an example of rectification of an AC current.

From the physical point of view, here we are concerned with the the magneto-transport properties of a a superconducting thin strip with curved and asymmetric cross section, a subject relatively unexplored until now. We will show, with the help of numerical simulations performed in the framework of the full three-dimensional (3D) time dependent Ginzburg Landau (TDGL) model, that the asymmetry can be mainly accounted for by the magnetic field component normal to the convex top surface. Such a component is inhomogeneous, being antisymmetric with respect to the the middle of the strip, and affects the flux entry and flux exit. Here the flux consists of 3D vortices that have sections locally perpendicular to the top convex surface, though the bulk section, when present, is parallel to the applied magnetic field and to the bottom flat surface. These sections, that from the point of view of the top curved surface can be seen as two-dimensional (2D) vortex-antivortex pairs (double kinks), surprisingly play the most significant role in the generation of the observed asymmetry. This allows us to idealize the real 3D strip with a more simple geometry, consisting of a curved 2D strip conformal to a cylindrical surface subjected to a magnetic field applied tangent to its middle point. 2D TDGL model used here to describe this idealized 2D geometry can be applied to the more general problem of a flat strip subjected to a magnetic field applied perpendicular to the surface, but that is antisymmetric with respect the middle point of the strip. We anticipate that the result of the analysis can be summarized as follows. At low magnetic fields (Meissner state) the asymmetry comes from the balance of the normal component of the magnetic field and the polarity dependent self-field of the transport current. At larger magnetic fields (mixed state) the asymmetry comes from the balance of the magnetic force due to the inhomogeneous normal component of field and the polarity dependent Lorentz force associated to the transport current.

Chapter is organized as follows. In Sec. 7.2, after a brief description on how the Nb strip with plano-convex section is fabricated, we report the main experimental results on asymmetry of critical currents as well as an example of rectification of an AC current. In Sec. 7.3 the observed asymmetry in magneto-transport properties of the superconducting strip is explained with the help of numerical simulations performed in the framework of time-dependent Ginzburg Landau equations [13], that are reliably used [14–19] whenever direct computation of voltage-current curves of a type II superconductor in the presence of magnetic field is needed. Numerical simulations are performed both in the 3D Cartesian reference frame and in the 2D cylindrical reference frame. A brief summary of main results is given in Sec. 7.4.

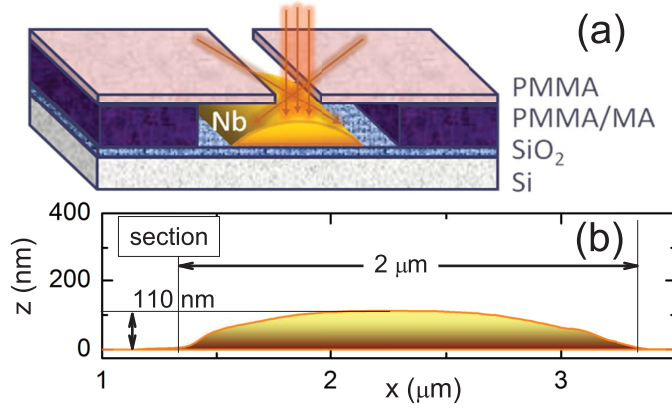


Figure 7.1: (a) A sketch (not on scale) of the bilayer resist mask used to sputter Nb. (b) AFM profile of the Nb strip along its width.

7.2 Experimental results

We fabricated a Nb thin strip with convex upper surface by means of rf-sputter deposition through a bilayer resist shadow mask [20] [see Fig.7.1(a)] made by Electron Beam Lithography (EBL). The resist bilayer consisted of a $0.2 \mu\text{m}$ thick layer of polymethylmethacrylate (PMMA) and a $0.7 \mu\text{m}$ thick layer of PMMA-Copolymer (PMMA/MA). A $1 \mu\text{m}$ wide strip is patterned on the bilayer with an area dose of $100 \mu\text{C}/\text{cm}^2$. Due to the remarkable difference in sensitivity between the two resist layers, a large undercut in the PMMA/MA layer below the PMMA layer is obtained after development, so that the bilayer can work as a shadow mask [see Fig.7.1(a)]. To enhance resistance to plasma, after development the mask is further baked at $130 \text{ }^\circ\text{C}$ for 30 min in a convection oven. Moreover, to minimize resist contamination [20], prior to the deposition of the strip a 10 nm thick Nb passivation layer is first sputtered and allowed to relax to passivate the resist surface. Due to the isotropy of the sputter process, the Nb is smeared under the window formed by the top layer of resist, resulting in a smoothly graded profile for the Nb deposited on the Si/SiO₂ substrate, as sketched in Fig.7.1(a). The profile of the Nb strip recorded with an Atomic Force Microscope (AFM) confirms the expected plano-convex (bottom surface is flat and top surface is convex) shape, as shown in Fig. 7.1(b). The sample has a four contact geometry, with voltage pads $10 \mu\text{m}$ apart. The Nb strip is $2 \mu\text{m}$ wide and is 100 nm thick in the middle [see Fig. 7.1(b)]. We acknowledge the cooperation of Dr. A. Scarfato and Dr. F. Bobba for recording the AFM images at Dipartimento di Fisica “E. R. Caianiello”.

In Fig. 7.2(a) we show the $V(I)$ curve of the strip recorded at $T = 4.2 \text{ K}$ ($T_c = 6.0 \text{ K}$) with a magnetic field $\mu_0 H = 0.2 \text{ T}$ applied parallel to the substrate and perpendicular to the transport current, as sketched in the inset. In the reference frame shown in the inset, the magnetic field is directed as the

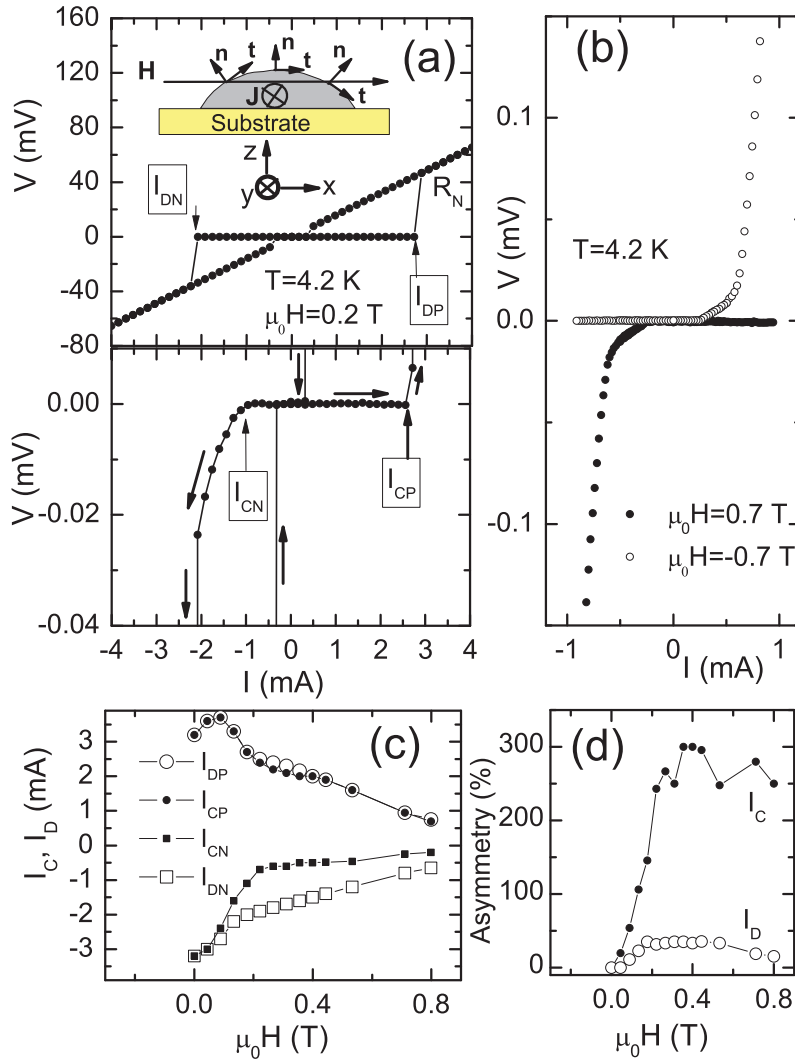


Figure 7.2: (a) $V(I)$ curve of the strip with the identification of the depairing currents. The magnetic field is applied as sketched in the inset. In the bottom panel the magnification of the low voltage region emphasizes the difference between the critical currents. The arrows indicate the history of the voltage-current loop. (b) $V(I)$ curves at magnetic fields of opposite polarities. Positive and negative depairing and critical currents (c) and asymmetry ratio (d) as a function of magnetic field.

x -axis, $\mathbf{H} = (H, 0, 0)$, and the current density as the y -axis, $\mathbf{J} = (0, J, 0)$. The positive and the negative depairing currents [13] [I_{DP} and I_{DN} , the current values at which the transition to the fully normal state takes place, see arrows in Fig. 7.2(a)] are found to be moderately different and the positive and

negative critical currents [13] [I_{CP} and I_{CN} , the current values corresponding to the transition $V = 0 \rightarrow V \neq 0$, see arrows in the bottom panel of Fig. 7.2(a)] are found to be remarkably different, as emphasized in the bottom panel of Fig. 7.2(a). The $V(I)$ curves are mirrored with respect to the origin when the magnetic field polarity is reversed [Fig. 7.2(b)], therefore, in the following we will show data concerning only the positive magnetic fields. The critical currents, estimated using a $0.2 \mu\text{V}$ criterion, and the depairing currents as a function of magnetic field are shown in Fig. 7.2(c). The maximum asymmetry ratio [Fig. 7.2(d)] for the depairing currents is $100 \times (I_{DP} - |I_{DN}|)/|I_{DN}| = 40\%$ and is $100 \times (I_{CP} - |I_{CN}|)/|I_{CN}| = 300\%$ for the critical currents.

From Fig. 7.2(c) we notice that, at the chosen polarity of magnetic field, the positive critical current I_{CP} is always larger than the negative critical current I_{CN} . Moreover, though at large magnetic field values the positive critical current is depressed as the magnetic field is increased, at low magnetic fields an opposite behavior is observed, i.e., the critical current is enhanced with respect to the zero magnetic field value. The enhancement, that at 4.2 K is of about 30% reaches 60% at lower temperatures as can be appreciated in Fig. 7.3(a), where we compare the $V(I)$ curve at zero field with the one at $\mu_0 H = 0.18 \text{ T}$, both recorded at 0.3 K. The critical currents and their asymmetry ratio as a function of magnetic field at this temperature are plotted in Fig. 7.3(b). The asymmetry ratios in 7.2(d) and 7.3(b) indicate that maximum asymmetry is always achieved at relatively high magnetic field values, where both critical currents are depressed with respect to the zero field value. Nevertheless, the qualitative difference in the positive critical current trend at low fields with respect to the large fields values suggests that there can be two different mechanisms at the origin of the asymmetry, depending on the field range. In Fig. 7.3(c) we show some $V(I)$ curves recorded near the critical temperature $T_c = 6.0 \text{ K}$ at a fixed value of the applied magnetic field. A considerable asymmetry is observed in a large temperature range, reaching vanishingly small values only at $T/T_c \approx 0.98$, as can be better appreciated in Fig. 7.3(d), where we plotted the critical currents as function of reduced temperature T/T_c at a fixed field.

Finally, the asymmetry is practically absent if the magnetic field is applied perpendicular to the substrate, as shown in the Fig. 7.4(a), where we report some $V(I)$ curves recorded at different magnetic fields at 4.2 K. For this field orientation, besides some vanishingly small asymmetry of the voltages probably accounted for by the not perfect symmetry of the strip profile around its middle point [see Fig. 7.1(b)], the critical currents are found to be reasonably symmetric within 10% accuracy, as can be appreciated in Fig. 7.4(b).

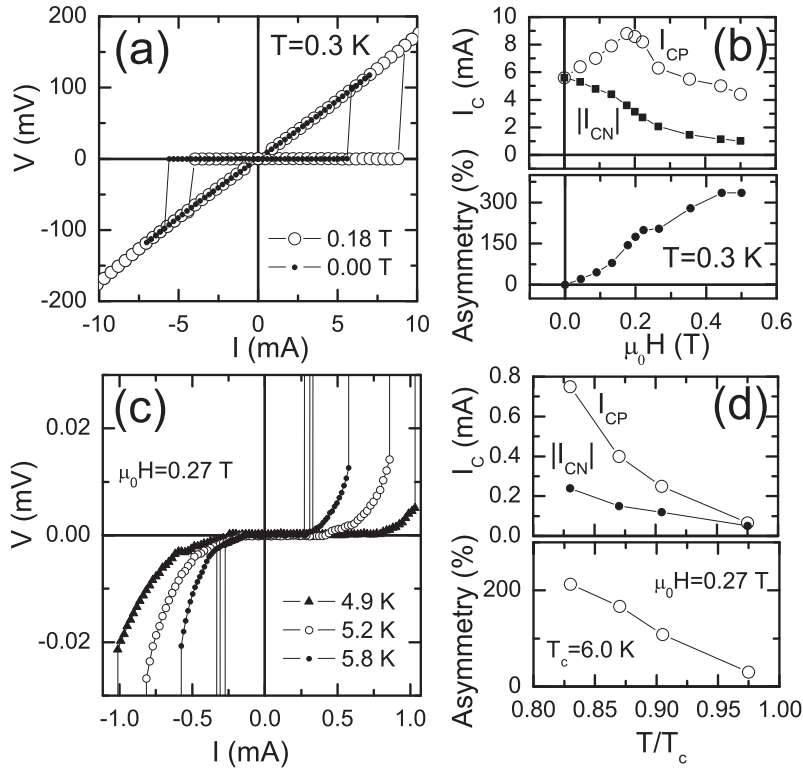


Figure 7.3: (a) $V(I)$ curve of the strip in zero magnetic field compared with the curve at $\mu_0 H = 0.18$ T, emphasizing enhancement of positive critical current (almost coincident with the positive depairing current). The temperature is 0.3 K. (b) Positive and negative critical currents (top panel), and asymmetry ratio (bottom panel) as a function of magnetic field, at $T = 0.3$ K. (c) $V(I)$ curves recorded near the critical temperature T_c at a fixed magnetic field. (d) Positive and negative critical currents (top panel), and asymmetry ratio (bottom panel) as a function of temperature, at fixed field $\mu_0 H = 0.27$ T.

Due to the asymmetry of depairing or critical currents, our strip in parallel magnetic field can exhibit a zero or finite resistance depending on the direction of the bias current. This behavior is evidenced in Fig. 7.5(a), where we plot the $V(I)$ curve of the strip recorded at $\mu_0 H = 0.5$ T: at $I = 1$ mA the resistance is zero, while at $I = -1$ mA the resistance is finite (though quite low, few percent of $R_N \simeq 17 \Omega$). The curve in Fig. 7.5(a) was recorded at $T = 4.2$ K driving the strip with a low frequency triangular current $I(t)$ with amplitude $-I_{CN} < I_{AC} < I_{CP}$ [see top panel of Fig. 7.5(b)], measuring the voltage $V(t)$ [see bottom panel of Fig. 7.5(b)], then eliminating the time. The time average of the current is $\langle I(t) \rangle = 0$ but the time average of the

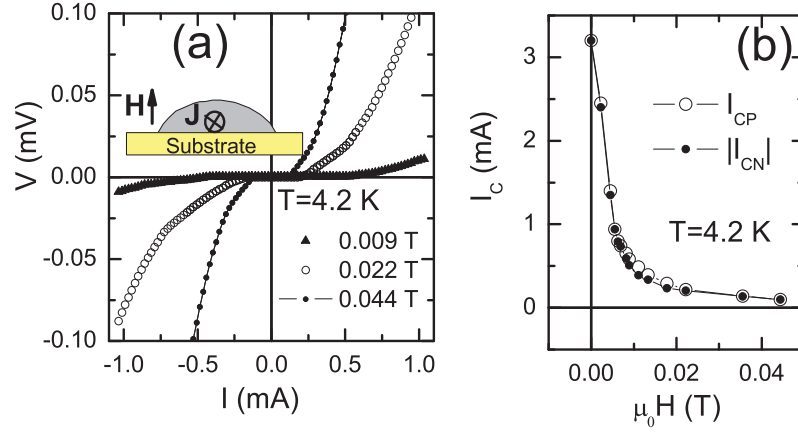


Figure 7.4: (a) $V(I)$ curves at $T = 4.2$ K at different magnetic fields applied perpendicular to the substrate, as shown in the inset. (b) Critical currents as a function of magnetic field applied as in (a), at 4.2 K.

output voltage is $\langle V(t) \rangle \neq 0$, i.e., our strip behaves as a current rectifier. It is worth noticing that the current density here is rather large, of the order of 10 GA/m², as should be expected for a superconducting device. A way to characterize the rectification capability [3, 5] of the strip is to plot the time average of the output voltage $\langle V(t) \rangle \equiv V_{DC}$ as a function of the amplitude I_{AC} of AC driving current. An example of such a $V_{DC}(I_{AC})$ curve at $\mu_0 H = 0.5$ T is shown Fig. 7.5(c). This curve is recorded driving the device with a sinusoidal signal at 1 kHz with amplitude I_{AC} while stepping to progressively larger values of I_{AC} and measuring the voltage at each amplitude with a DC nano-voltmeter. In this case, the V_{DC} is in the μ V range and it is achieved for $|I_{CN}| < I_{AC} < I_{CP}$, due to the difference in the critical currents. In Fig. 7.5(d) the field is $\mu_0 H = 0.3$ T and the AC current amplitude is in a wider range. Here rectification when V_{DC} increased up to the mV range occurs for $|I_{DN}| < I_{AC} < I_{DP}$, because now the finite resistance involved is the normal state resistance R_N . Notice that, though the normal state is approached with high current density, dissipative heating is minimized, because the sample is immersed in liquid helium and is in the resistive state only during a small fraction of the signal cycle.

The results of Fig. 7.5(d) suggest that to achieve high output DC voltage in a large current range it is more convenient to have strongly different depairing currents rather than strongly different critical currents. A way to convert the strong asymmetry of critical currents in a strong asymmetry of depairing currents can be the inclusion of impurities acting as pinning centers. We pursued such a goal with another sample, for which we intentionally

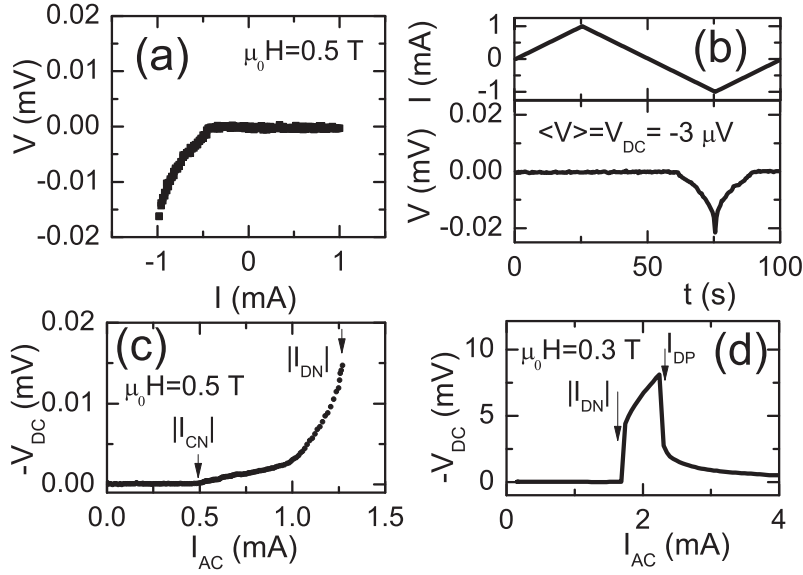


Figure 7.5: (a) $V(I)$ curve of the strip at 4.2 K subjected to an in-plane magnetic field of $\mu_0 H = 0.5$ T. (b) Time traces of forcing current and output voltage corresponding to $V(I)$ curve in (a). (c) DC voltage output as a function of the amplitude of a sinusoidal driving current of 1 kHz. (d) Same as in (c), but the range of the AC current amplitude is larger and the field is $\mu_0 H = 0.3$ T.

avoided the passivation layer and, to further enhance contamination of Nb with resist impurities [20], we sputtered Nb with substrate tilted at 90° with respect to the cathode. The tilted deposition produces a rather asymmetric, though again convex, profile for the strip, as shown in the inset of Fig. 7.6(a). The presence of impurities (contaminations from resist) in the Nb of sample was confirmed by the appreciable increase of the room temperature resistivity. Consistently with the intentional addition of impurities, the critical temperature ($T_c = 1.5$ K) is found much lower and the normal resistance ($R_N \simeq 1$ k Ω) at cryogenic temperatures is found rather larger than the previous device. In Fig. 7.6(a), we show the $V(I)$ curve of the device recorded at $T=0.3$ K for a magnetic field $\mu_0 H = 0.27$ T, applied again parallel to the substrate, compared with the curve in the absence of field. We successfully enhanced pinning, because now critical and depairing current are found almost coincident and a maximum asymmetry ratio of 200% occurs in both critical and depairing currents [see Fig. 7.6(b)]. This can be considered a promising result in view of the operation of the device as a rectifier with a DC voltage output up to 50 mV [as it can be inferred from inspection of Fig.

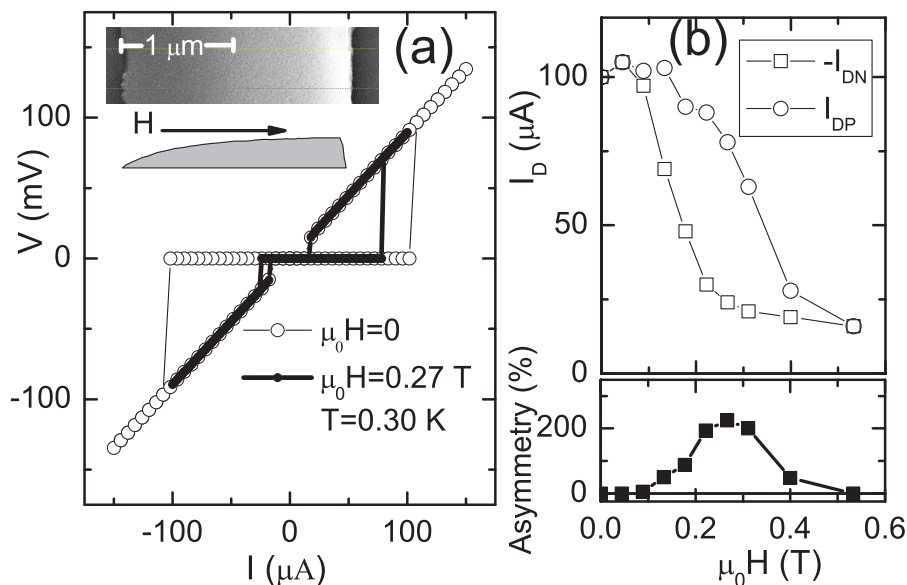


Figure 7.6: (a) $V(I)$ curve of device recorded at $T = 0.3$ K when no magnetic field or a magnetic field $\mu_0 H = 0.27$ T is applied parallel to the substrate. In the inset we show a FE-SEM micrograph of the strip together with a sketch of the inferred curved profile. (b) Positive and negative depairing currents (top panel) and asymmetry ratio (bottom panel) as a function of magnetic field.

7.6(b)], in a reasonably large current range.

7.3 Numerical results and discussion

From the profile shown in Fig. 7.1(b) we notice that the top surface of the strip can be approximated by a cylindrical surface having a curvature radius $R \simeq 4 \mu\text{m}$. In the experiment the magnetic field is applied parallel to the cord of the arc, as shown in the inset of Fig. 7.2(a). Though the applied magnetic field \mathbf{H} is homogeneous, both the component H_n normal and the component H_t tangent to the top surface are inhomogeneous, but the H_n is qualitatively different, because it changes sign in the middle of the strip and can probably explain the asymmetry. In fact, the analysis we present below substantially confirms this hypothesis.

From the slope close to T_c of the upper critical field $\mu_0 H_{c2}(T)$ we estimate [21] for our sputtered Nb thin film a coherence length $\xi(0) \simeq 9$ nm. This value is much smaller than the BCS coherence length of Nb, $\xi_0 = 39$ nm, so the sample is in the dirty limit regime with an electron mean free path

$l = 1.38\xi(0)^2/\xi_0 \simeq 2.8$ nm. In the dirty limit regime the Ginzburg-Landau parameter can be estimated by $\kappa = 0.72\lambda_L/l \simeq 10$, with $\lambda_L = 40$ nm the London penetration depth of Nb. This result implies that the investigated sample is a type-II superconductor. The Ginzburg-Landau London penetration depth is $\lambda(0) = \kappa\xi(0) = 90$ nm, that is of the order of the thickness d of our strip at its middle. Normalized relevant physical dimensions of the strip are $W \simeq 222\xi(0)$, $d \simeq 11\xi(0)$, $L = 5W$ and $R \simeq 2W$.

To gain insight in the origin of asymmetric magneto-transport properties of our superconducting strip with plano-convex section, we performed numerical simulations in the framework of the time-dependent Ginzburg-Landau (TDGL) model [14–19], both in the full three-dimensional version (3D model) and in a simplified two-dimensional version (2D model). The full 3D model with realistic parameters is computationally very expensive. Hence, we have used this model only as a guide to individuate the main mechanism for the asymmetry that could be retained in a simplified 2D model. Full 3D simulations suggest that the magneto-transport properties of our three dimensional strip can be reasonably accounted for by just only the top convex surface. Hence, in the 2D model, we approximate the real strip with plano-convex section with a much more simple geometry: a curved two-dimensional strip of constant thickness. The 2D model is computationally more affordable and allowed us to make more extensive simulations, including the computation of asymmetric $V(I)$ curves and the computation of critical currents as a function of magnetic field. Finally, the simplified 2D model admits some approximated analytical results, making possible the description of involved physics in a more simple and intuitive way as it is the energetic approach we describe at the end of this section.

7.3.1 Full 3D model: exploration

The celebrated three-dimensional time-dependent Ginzburg-Landau (TDGL) model [14–19] reads:

$$u \frac{\partial \psi}{\partial t} = (\nabla - i\mathbf{A})^2 \psi + (1 - T - |\psi|^2) \psi, \quad (7.1)$$

$$\frac{\partial \mathbf{A}}{\partial t} = \frac{1}{2i} (\psi^* \nabla \psi - \psi \nabla \psi^*) - |\psi|^2 \mathbf{A} - \kappa^2 \nabla \times (\nabla \times \mathbf{A} - \mathbf{H}). \quad (7.2)$$

Here $\psi = \psi(x, y, z)$ is the complex order parameter, $\mathbf{A} = (A_x, A_y, A_z)$ is the vector potential, \mathbf{H} is the applied magnetic field, T is the temperature, κ is the Ginzburg-Landau parameter and the coefficient $u = 5.79$ controls the relaxation of ψ . All physical quantities are measured in dimensionless units: the coordinates are in units of the coherence length $\xi(0) = \sqrt{\pi\hbar D/8k_B T_c}$,

with T_c the critical temperature, and D is the diffusion constant. Temperature is in units of T_c . Time is measured in units of the relaxation time $\tau(0) = 4\pi\sigma_n\lambda(0)^2/c^2$ (σ_n is the normal-state conductivity, $\lambda(0) = \kappa\xi(0)$ the magnetic field penetration depth, with κ the G-L parameter). The order parameter is in units of $\Delta(0) = 4k_B T_c \sqrt{u}/\pi$, i.e., the superconducting gap at $T = 0$ which follows from Gor'kov's derivation of the Ginzburg-Landau equations. The vector potential is measured in units $\Phi_0/2\pi\xi(0)$ ($\Phi_0 = ch/2e$ is the quantum of magnetic flux). In these units the magnetic field is scaled with $H_{c2}(0) = \Phi_0/2\pi\xi(0)^2$ and the current density with $j_0(0) = c\Phi_0/8\pi^2\lambda(0)^2\xi(0)$. We use the model as stated in Ref. [15], but our normalization is relative to the variables at $T = 0$. This results in the explicit inclusion of normalized temperature T in the first equation, as found, e.g., in Refs. [18,19]. The first equation governs the relaxation of the superconducting order parameter ψ and the second equation is the Maxwell equation for magnetic induction field $\mathbf{B} = \nabla \times \mathbf{A}$.

Equations (7.1) and (7.2) are integrated in the three-dimensional rectangular domain shown in Fig. 7.7(a), with external boundary $\partial\bar{\Omega}$. The superconducting material occupies the plano-convex cylindrical region Ω and it is surrounded by vacuum. The boundary $\partial\Omega$ of Ω is the interface between the superconductor and the vacuum. As in the experiment, in the Cartesian reference frame shown in Fig. 7.7(a) the applied magnetic field is directed as the x -axis, $\mathbf{H} = (H, 0, 0)$, and the transport current density as the y -axis, $\mathbf{J} = (0, J, 0)$. Notice that in this reference frame, $\nabla \times \mathbf{H} = 0$ and the applied magnetic field only appears in the boundary condition of the vector potential. This condition is chosen such that magnetic induction field $\mathbf{B} = \nabla \times \mathbf{A}$ on the outer boundary goes to the applied field \mathbf{H} when the outer boundary is chosen reasonably far from the superconductor, meaning that screening current does not modify sensibly the applied field at large distances from the superconductor. Mathematically, the condition reads [16, 22]: $(\nabla \times \mathbf{A})|_{\partial\bar{\Omega}} = \mathbf{H}$. When a transport current is present, we add [16] to the applied magnetic field \mathbf{H} also the field \mathbf{H}_J induced by the bias density current \mathbf{J} , calculated using the Biot–Savart law. For the order parameter, we use the superconductor-insulator boundary conditions, i.e., we set the normal component of the supercurrent across the boundary $\partial\Omega$ to zero [13]: $(\nabla - i\mathbf{A})\psi \cdot \mathbf{n}|_{\partial\Omega} = 0$, where \mathbf{n} is the outward normal unit to the surface $\partial\Omega$. Finally, to simulate an infinite length strip, we apply periodic boundary conditions in the y -direction: $\psi(x, y - \Lambda/2, z) = \psi(x, y + \Lambda/2, z)$ and $\mathbf{A}(x, y - \Lambda/2, z) = \mathbf{A}(x, y + \Lambda/2, z)$, where Λ is the spatial period along y -direction.

To numerically solve the system of Eqs.(7.1) and (7.2) we apply a finite-difference representation for the order parameter and vector potential on a

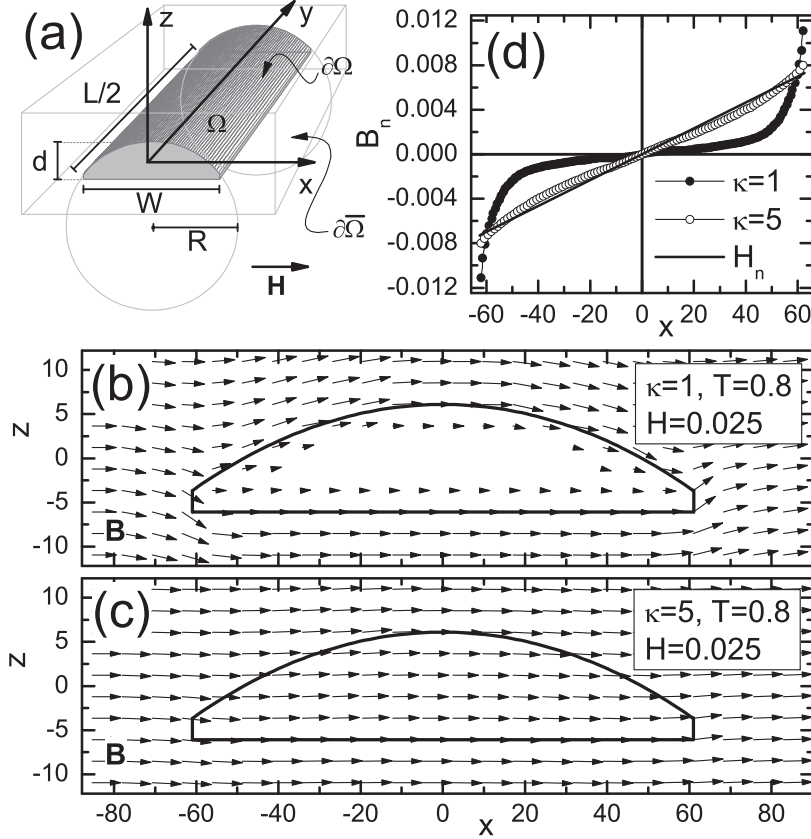


Figure 7.7: (a) Sketch the superconducting strip placed in an insulating (vacuum) rectangular box. (b) and (c) show the vector plots of the magnetic induction field for two values of κ , when a weak magnetic field is applied parallel to the bottom surface. (d) Component of the magnetic induction field along the outer normal of the convex surface (B_n) compared the same component of applied magnetic field (H_n).

uniform Cartesian space grid with step size 0.5 and we use the link variable approach [15, 16] and the simple Euler method [23] with time step $\Delta t = 0.002$ to find ψ and \mathbf{A} . Initial conditions are $|\psi| = 1$ in the region Ω , $|\psi| = 0$ outside, and $\mathbf{A} = 0$ everywhere. The behavior of the system is studied on a large time scale when time-averaged values no longer depend on time. In our calculations we choose parameters $\kappa = 5$, $T = 0.8$, $W = 122$, $R = 1.6W$, thickness at middle $d = 12$, and the spatial period along y -direction $\Lambda = 20$. These parameters, comparable though not the same as in the experiment, were chosen to take into account the efficiency of our computing tools while saving the relevant features. Here we are only interested on main physical

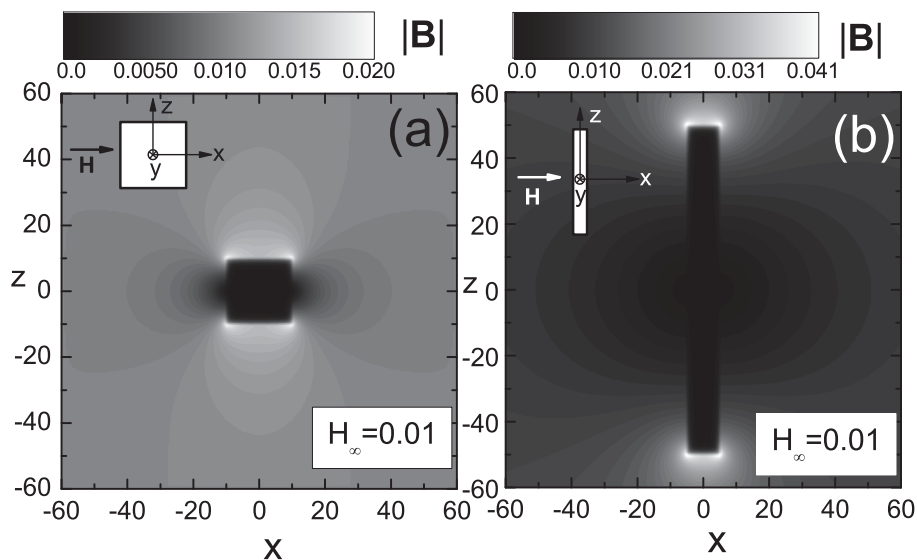


Figure 7.8: Contour plots of the intensity of magnetic field for a superconducting strip infinitely extended in the y -direction with square (a) and rectangular (b) cross section, in an homogeneous applied parallel magnetic field.

mechanism accounting for the observed asymmetry and we are not interested in quantitative fitting of experimental data with numerical data. Moreover, we remark that reduced temperature $T/T_c = 0.8$, chosen to qualitatively account for most significant experimental results summarized in Fig. 7.2, though relatively far from T_c , is not beyond the range of validity of Ginzburg-Landau theory, because [18] we are concerned with a type II superconductor in the dirty limit, compelling a large κ parameter.

As a check of our numerical algorithms we have calculated the intensity of magnetic field for a superconducting strip infinitely extended in the y -direction with square and rectangular cross section, subjected to a weak homogeneous parallel magnetic field. As seen from Fig. 7.8, in both cases the magnetic field reaches its maximum at the corners of the superconductor (in order $B \approx 2H_\infty$ and $B \approx 4.1H_\infty$). At the middle of top and bottom side, the magnetic field is less intensive than the field at the corners, but appreciably larger than the applied magnetic field ($B \approx 1.45H_\infty$ and $B \approx 2.9H_\infty$). These results, for $\kappa = 1$ and $T = 0$, are in agreement to those in Ref. [22].

In Fig. 7.7(b) and 7.7(c) we show the vector plots of the calculated magnetic induction field \mathbf{B} for two type-II superconductors of same dimensions but with different κ subjected to a magnetic field applied parallel to the bottom surface. In both cases we are in the Meissner state. When κ is small [see

Fig. 7.7(b), $\kappa = 1$] the magnetic field is completely expelled from the bulk of the superconductor (full Meissner screening), and the field lines near the external surface of the strip follow the profile of the strip. Increasing κ , the magnetic field almost completely penetrates the superconductor (very weak screening) and the field lines are almost aligned with the applied magnetic field [see Fig. 7.7(c), $\kappa = 5$]. This is not surprising if we remember that the strips have different thickness in units of magnetic penetration length λ . At the used temperature $T = 0.8$ the thickness of the strip with $\kappa = 1$ is $d \approx 6\lambda$, allowing a substantial screening of the external magnetic field. Conversely, for the strip with $\kappa = 5$ is $d \approx 1\lambda$ (our experimental strip at this temperature is also more thin, $d \approx 0.5\lambda$), and screening of applied magnetic field is very weak. In Fig. 7.7(d) the component of magnetic induction normal to the the convex top surface, B_n , is compared with the normal component of the applied magnetic field, H_n . Consistently, the screening of this component is rather evident when $\kappa = 1$ and very weak when $\kappa = 5$. Moreover, the modification of the induction field (here an enhancement at the edges of the strip) with respect to the applied field, commonly described with a geometry-dependent demagnetizing factor, is quite noticeable in the strip with low κ but almost absent in the other strip. In the following we always use $\kappa = 5$, more comparable with the experimental one, i.e., $\kappa = 10$.

In Fig. 7.9 (a) there is shown the contour plot of the squared order parameter at $H = 0.11$. For this critical magnetic field value the strip is at onset of the the mixed state. Flux enters the strip as 3D vortices that have the bulk section parallel to the applied field, but the lateral sections are perpendicular to the convex top surface, in qualitative agreement with reported numerical results [16] on flux penetration in cylindrical superconductors with field applied perpendicular to the cylinder axis. Moreover, there is also a qualitative agreement with the analytic results on a problem dual with respect to the one we are addressing here, i.e., flux penetration in the case of flat strips with magnetic field tilted with respect to the surface. Also in that case, the vortex was found [24] to penetrate perpendicular to the surface despite of tilting, as it happens in our top convex surface, that is locally tilted with respect to the applied field. In Fig. 7.9 (a) only the 3D vortex at section $y = 0$ it is shown, for the sake of simplicity. By feeding a transport current density J in the strip, the 3D vortex can be moved by the Lorentz force F_L . In panel (b) we show the effect of a negative transport current density corresponding to the onset of stationary flux motion with associated dissipation, i.e., we are at the negative critical current density $J = J_{CN}$. At this current value, vortex shown in panel (a) is ejected upwards because of the F_L and flux enters again as an antivortex (Av) at the left edge and a vortex (V) at the right edge of the strip as shown in panel (b). This time the bulk section is not present and

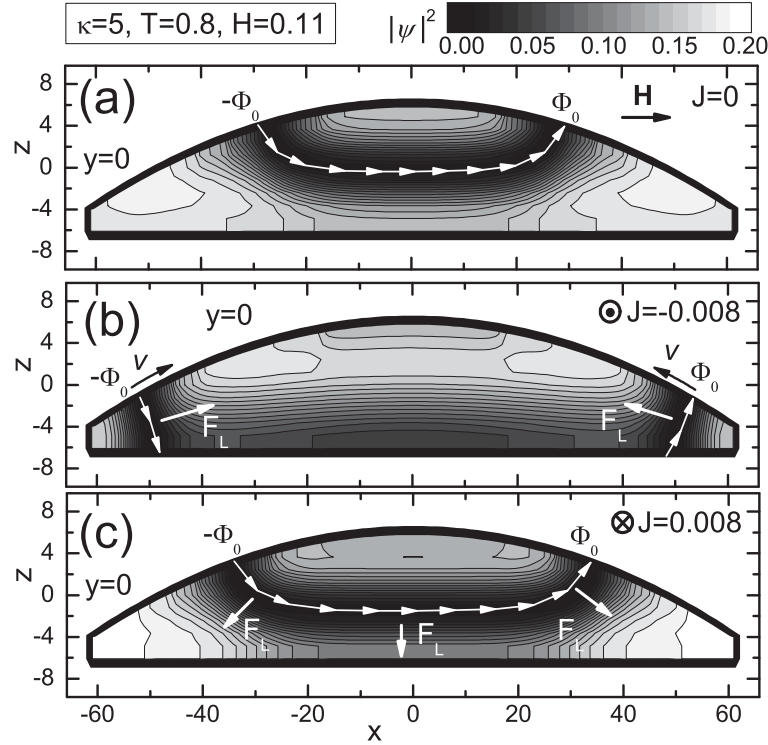


Figure 7.9: *Contour plots of the squared order parameter at a magnetic field value allowing the first entrance of vortices. Here the section at $y = 0$ is shown. In (a) there is no bias current. In (b) is $J = J_{CN}$. In (c) is $J = |J_{CN}| < J_{CP}$. The white arrows indicate direction of the magnetic flux line at the core of the vortex.*

the 3D V and 3D Av are perpendicular to both top curved surface and bottom flat surface. Under the action of F_L , the V and Av move inwards until they joint together to form again a vortex as the one in the panel (a). Again, this vortex is expelled from the top surface, continuing the ever dynamic process. In panel (c) we show the effect of application of a positive current density of same modulus as the negative critical current density, $J = |J_{CN}|$. This time the Lorentz force merely shift down and slightly deforms the 3D vortex of panel (a), but no stationary flux motion is established, meaning no dissipation. To establish dissipation we must feed a positive current larger than the negative critical current. In other words is $J_{CP} > |J_{CN}|$, as in the experiments. However, stationary flux motion is achieved at large enough positive current, $J = J_{CP}$, and consists of expulsion of the 3D vortex shown in panel (c) from the bottom of the strip followed by entrance of a new vortex from the top the strip and so on. We notice that as seen from the top convex

surface, the 3D vortex shown in Fig. 7.9 (a) would be equivalent to a 2D antivortex -2D vortex pair, with flux entering at the left ($-\Phi_0$, 2D antivortex) and exiting at the right (Φ_0 , 2D vortex). In the same view, the dynamical process accounting for dissipation at $J = J_{CN}$, would consist of a continuous nucleation of a 2D Av-V pair at the edges of the strip [see panel (b)] followed by its annihilation at the middle of the strip, while dissipation at $J = J_{CP}$ would correspond to nucleation of a 2D Av-V pair at middle of the strip (3D vortex entering from the top) followed by their expulsion at the edges of the strip.

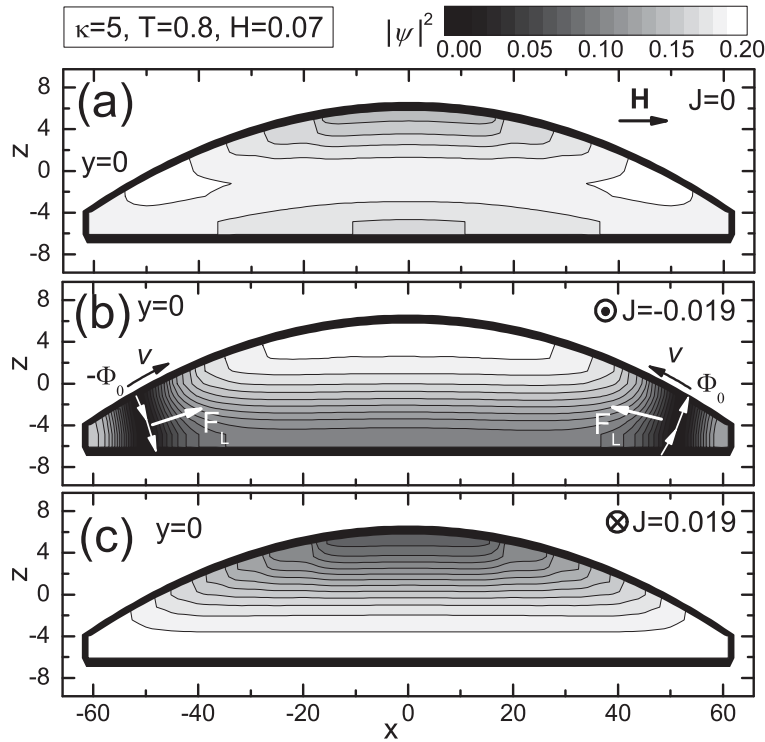


Figure 7.10: *Contour plots of the squared order parameter in the Meissner state. (a) $J = 0$. (b) Bias current corresponding to negative critical current, $J = J_{CN}$. (c) $J = |J_{CN}| < J_{CP}$.*

In Fig. 7.10 we analyze the situation at a low magnetic field, $H = 0.07$, for which we are again in the Meissner state. In panel (a) is $J = 0$. In panel (b) we are at the negative critical current density, $J = J_{CN}$. The dynamical process accounting for dissipation is very similar to the one we discussed above, but for the initial stage. Here flux was not pre-existing, and it enters the strip as a 3D antivortex at the left and a 3D vortex at the right. Under the action of F_L , the 3D V and 3D Av move inwards until they joint to form

again a vortex as the one in the Fig. 7.9 (a). This vortex is expelled from the top surface, continuing the ever dynamic process. Again, as seen from the top convex surface, this process would be equivalent a continuous nucleation of 2D Av-V pairs at the edges of the strip followed by their annihilation at the middle of the strip. In Fig. 7.10(c) is $J = |J_{CN}|$. As it is seen, no flux is present and no dissipation is established. Hence, also starting with the strip in the Meissner state we again observe $J_{CP} > |J_{CN}|$, as in the experiment. At positive critical current, a 3D vortex enters from the top of the strip and the same dynamical process as the one we described above when the strip is in the mixed state and $J = J_{CP}$ is again established.

7.3.2 Simplified 2D model: numerical results

Full 3D simulations suggest that the asymmetry in the magneto-transport properties of our three dimensional strip could be reasonably accounted for by just only the top convex surface. As noticed above, the flux enters or exits the strip as 3D vortices that are parallel to the magnetic field only in the very bulk of the strip. The portion of the 3D vortex near the top curved surface is, however, always perpendicular to the surface, though the field is applied parallel to the bottom surface. Differently from the bulk portion, these pieces of the total 3D vortex experiences the component of magnetic induction field that is normal to the curved surface. This component is inhomogeneous, as shown in Fig. 7.7(d), and, hence, generates a magnetic force that rivals the current polarity dependent Lorentz force and hence can accounts for the observed asymmetry. If we concentrate on these vortex pieces, the dynamics of 3D vortices can be mapped in the dynamics of 2D vortices and 2D antivortex pairs, as we anticipated in the discussion of Fig. 7.9 and Fig. 7.10 above. In this framework the real 3D strip with plano-convex section can be idealized, for what concerns the main mechanism of asymmetry, in a much more simple 2D geometry: a curved two-dimensional strip conformal to the top convex surface.

For this simplified model we adopt a curvilinear cylindrical reference frame, that is more suitable than the Cartesian frame for the description of the top convex surface. With respect to the cylindrical reference frame (ρ, θ, y) shown in the sketch of Fig. 7.11, the length of the 3D strip lies parallel to the y -axis (cylinder axis), the uniform transport current J is applied along the strip length, and the magnetic field is applied perpendicular to the y -axis, making an angle $\pi/2$ with the ρ -axis at $\theta = 0$. Noticing that for the top cylindrical surface the radial coordinate is constant, ($\rho = R$), we can use the curvilinear coordinate $x = R\theta$ (length of arc along the circumference, and directed as $\hat{\theta}$) instead of the coordinate θ . In this reference

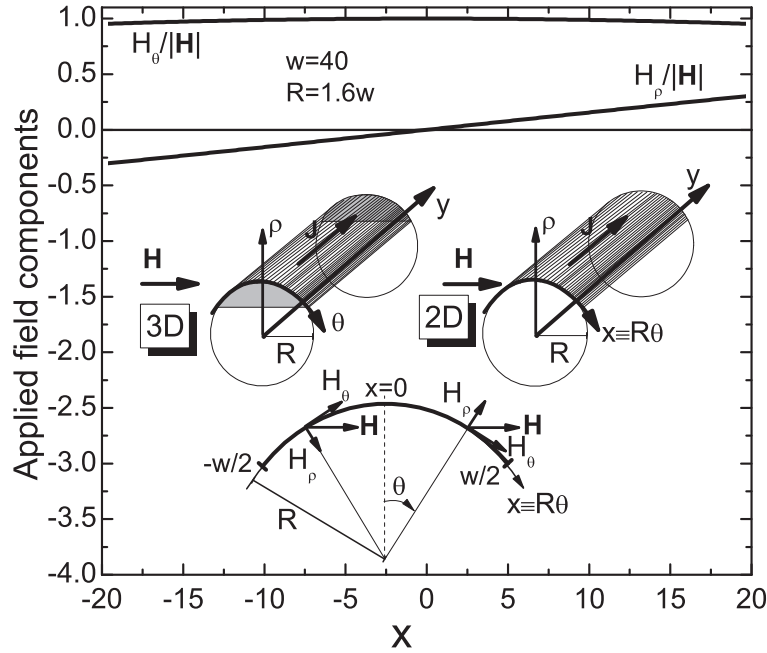


Figure 7.11: In the top there are plotted the spatial distribution of the normal component H_ρ (coincident with the radial component) and the tangent component H_θ of the applied magnetic field \mathbf{H} in the curvilinear reference frame. In the bottom is sketched the change from the three-dimensional cylindrical reference frame (ρ, θ, y) to the two-dimensional curvilinear reference frame $(x \equiv R\theta, y)$ we have adopted.

frame, shown in the sketch labeled "2D" of Fig. 7.11, the strip can be described using only x and y coordinates with ranges $-L/2 < y < L/2$ and $-w/2 < x < w/2$, where w is the length of the arc. Moreover, all spatial derivatives reduce to the simple Cartesian form. In the curvilinear reference frame, sketched in the bottom of Fig. 7.12, the normal component (coincident with the radial component) of the applied field is $H_\rho = H \sin(x/R)$ and the tangent component is $H_\theta = H \cos(x/R)$. These components are plotted in the top of Fig. 7.11. Following a related pioneering work [1] on rectifiers based on macroscopic curled ribbons of type II superconductors, we assume the normal component as the most relevant with respect to the asymmetry in the response of our strip to magnetic field. The larger sensitivity to the normal component with respect to the tangent component is, on the other hand, suggested also by comparison of the experimental data shown in Fig. 7.2(c) with the ones shown in Fig. 7.4(b). In Fig. 7.4(b) the field is practically completely accounted by the almost homogeneous normal

component (in this case $H_\rho = H \cos(x/R) \approx H$, because $|x|/R < 0.25$) and, as it is seen, the critical current is considerably reduced with respect to the zero field value already at field values as low as $\mu_0 H = 0.01$ T. Thus, in the following we neglect the effect of the tangent component [25] and we model the strip as two-dimensional, with an applied magnetic field described by $H_\rho = H \sin(x/R)$. For the sake of simplicity, we neglect also the thickness variation [26], as for this particular magnetic field configuration we found in preliminary simulations to produce a higher order effect.

Hence, for the 2D simplified version of the general model Eq. 7.1 and Eq. 7.2 we use:

$$u \frac{\partial \psi}{\partial t} = (\nabla_{2D} - i\mathbf{A})^2 \psi + (1 - T - |\psi|^2) \psi, \quad (7.3)$$

$$\frac{\partial A_y}{\partial t} = J_{sy} + \kappa^2 \frac{\partial^2 A_y}{\partial x^2} + \kappa^2 \frac{\partial^2 A_y}{\partial y^2} - \kappa^2 \frac{\partial H_\rho}{\partial x}, \quad (7.4)$$

where $\nabla_{2D} \equiv (\frac{\partial}{\partial x}, \frac{\partial}{\partial y})$ is the two-dimensional gradient operator and $J_{sy} = \frac{1}{2i}(\psi^* \nabla_y \psi - \psi \nabla_y \psi^*) - |\psi|^2 A_y$ is the y-component of the supercurrent density \mathbf{J}_s . Notice that in the used curvilinear reference frame the external field described by $H_\rho = H \sin(x/R)$ explicitly appears both in the bulk of the Eq. 7.4 and in the boundary conditions for the vector potential \mathbf{A} . As for the 3D model, to simulate a sample length much larger than the sample width, we apply periodic boundary conditions in the y -direction, both for the vector potential and the order parameter: $A_y(x, y + \Lambda/2) = A_y(x, y - \Lambda/2)$ and $\psi(x, y + \Lambda/2) = \psi(x, y - \Lambda/2)$, where Λ is the spatial period along y -direction. The superconductor-vacuum boundary [13] conditions for the order parameter are instead applied in the x -direction. These conditions, stating that the normal component of the supercurrent is zero at the boundary Γ of the superconductor (supercurrent cannot exit from the superconductor) are mathematically expressed [13] as $(\nabla_{2D} - i\mathbf{A})\psi \cdot \mathbf{n}|_\Gamma = 0$. Here, noticing that $A_x = A_\rho = 0$ and that our 2D approximation implies $\partial\psi/\partial\rho = 0$, these conditions simplify in $\nabla_x \psi|_{x=\pm w/2} = 0$, meaning $J_{sx}|_{x=\pm w/2} = 0$. The bias current is introduced through the boundary condition for \mathbf{A} in the x -direction. As in the 3D case discussed above, this condition should be such that the radial component of induction field $B_\rho = (\nabla \times \mathbf{A})_\rho$ goes to the radial component of the applied field quite far from the edges of the strip. However, for the applied field orientation and the large κ involved here, the demagnetizing factor is found to be very small, as can be appreciated in Fig. 7.7(d) (for $\kappa = 5$ is $B_\rho \simeq H_\rho$ at the edges of the strip). So, in the simplified 2D model we simplify the boundary condition in $(\nabla \times \mathbf{A})_\rho|_{x=\pm w/2} = H_\rho(x = \pm w/2) \mp H_J$, where $H_\rho(x = \pm w/2)$ is the radial component of the applied magnetic field

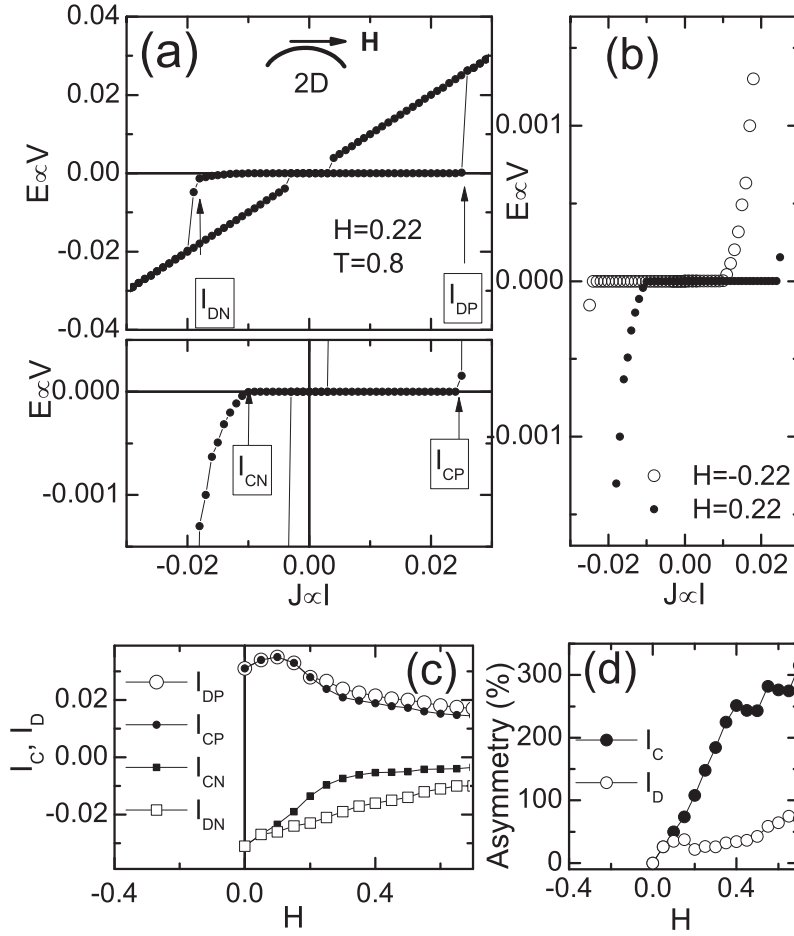


Figure 7.12: (a) Calculated $V(I)$ curve in magnetic field $H = 0.22$. The low-voltage range is magnified in the bottom panel. In the inset we show a sketch of the strip with curvilinear reference frame used to model the device. (b) The $V(I)$ curve is mirrored with respect to the origin when magnetic field direction is inverted. (c) Positive and negative depairing and critical currents as a function of magnetic field. (d) Asymmetry ratio as a function of magnetic field.

and $H_J = Jw/2\kappa^2$ is the radial component of magnetic field generated by the bias current density J (self-field of transport current) at the edges of the strip. We choose parameters $\kappa = 5$, $T = 0.8$, $w = 40$, $R = 1.6w$, and the spatial period along y -direction $\Lambda = 20$. We notice that a numerical analysis of the problem of magneto-transport of mesoscopic 2D strips conforming to cylindrical shells in the framework of simplified TDGL where both screening and self field are neglected has been recently reported [25, 27] by our group.

In Fig. 7.12(a) we show the calculated $V(I)$ curve of the strip for a normalized magnetic field $H = 0.22$, together with the amplification of the low voltage region. In Fig. 7.12(b) the $V(I)$ curve at $H = 0.22$ is compared with the one at $H = -0.22$, while the calculated critical and depairing currents, and the corresponding asymmetry ratios as a function of magnetic field are shown in Fig. 7.12(c) and 7.12(d), respectively. As it is seen, all the significant qualitative experimental features shown in Fig. 7.2 are reproduced by our 2D simplified model.

As in the experiments [Fig. 7.2(c) and Fig. 7.3(b)], the calculated [Fig. 7.12(c)] positive critical current I_{CP} is found to be always larger than the negative critical current I_{CN} , and at low fields the I_{CP} is enhanced with respect to the zero magnetic field value. As anticipated in the experimental section, depending on the field range, we could expect two different mechanisms that can originate the asymmetry. In the low field range the polarity dependent self-fields associated to the transport current can play a relevant role. However, at large fields, the intensity of self-fields is expected to be dominated by the external field and some new mechanism should play a relevant role in the generation of asymmetry. This intuitive picture is confirmed by the numerical results shown in Fig. 7.13 and 7.14. In Fig. 7.13 the field is $H = 0.1$, falling in the low field region where the positive critical current is enhanced [see Fig. 7.13(c)] with respect to its zero field value. In Fig. 7.14 the field is $H = 0.4$, falling in the large field region where also positive critical current is depressed [see Fig. 7.12(c)] and the asymmetry ratio becomes rather large.

In Fig. 7.13(a) there are shown the the calculated magnetic fields when the bias current takes the values $I = 0, \pm |I_{CN}|$. The magnetic field \mathbf{H} , applied parallel to the substrate, gives the applied field $H_\rho(x)$, as discussed above. The local magnetic induction field is calculated as $B_\rho(x) = \partial A_y / \partial x$, where A_y is numerically calculated in the 2D model Eqs. (7.3) and (7.4). The generalized (i.e., accounting also for self field of transport current) local magnetization is $M_\rho(x, H, J) = B_\rho(x, H, J) - H_\rho(x)$. In the top panel of Fig. 7.13(a) is $J = 0$. As in the 3D model [see Fig.7.7(d)], the distribution of the normal component of the magnetic induction $B_\rho(x)$ is almost the same as the applied field $H_\rho(x)$, but for a small correction due to the screening current, as evidenced from diamagnetic character of the $M_\rho(x)$. When the bias current is negative [as in the middle panel of Fig. 7.13(a)] the self field $H_I(x)$ cooperates with the applied field $H_\rho(x)$, so that the magnetic induction field $B_\rho(x)$ is larger than what the applied field $H_\rho(x)$ would generate by itself. In other words, when a negative current is present, the magnetization exhibits a paramagnetic behavior (i.e., the paramagnetic contribution of the self field dominates the diamagnetic contribution of the screening currents),

as can be appreciated again in the middle panel. This causes the negative critical current to be lower than the positive critical current. The negative critical current dynamically corresponds, as in 3D model [see discussion of Fig. 7.10(b)], to a nucleation of vortices and antivortices at the edges of the strip that annihilate at the center because of Lorentz force with associated onset of dissipation, as can be appreciated in the order parameter snapshot (2) shown in Fig. 7.7(b). When the bias current is positive [as in the bottom panel of Fig. 7.13(a), $I = |I_{CN}|$], the self-field $H_I(x)$ opposes to the external field $H_\rho(x)$, i.e., adds a diamagnetic contribution to the magnetization that enforces the diamagnetic contribution of the screening current, producing a $B_\rho(x)$ lower than what $H_\rho(x)$ would generate. This allows a positive bias current $I > |I_{CN}|$ to be fed into the strip before order parameter is destroyed at the center of the strip [snapshot (4) of Fig. 7.13(b)] at the positive critical current $I = I_{CP}$, with associated onset of dissipation. As evident from snapshot (1) of Fig. 7.13(b), for the chosen low magnetic field value there are no vortices in the strip at $I = 0$, i.e., we are again in the Meissner state. From the above analysis we conclude that in the Meissner state the asymmetry is due to the balance of polarity dependent self fields and the inhomogeneous normal component of external magnetic field. The compensation of self field for positive currents also implies a more uniform distribution of the superconducting current density $J_{sy}(x)$, with associated enhancement of positive critical current. In Fig. 7.13(c) we plot the y component of current density distribution $\langle J_{sy}(x) \rangle$ averaged along the length of the strip while we are on the marked points of $V(I)$ curve shown in 7.13(b). As it is seen, the distribution is more uniform at positive currents than at negative currents, reaching an almost flat distribution at $I \simeq I_{CP}$. This explains the enhancement of the I_{CP} in the presence of field with respect to the I_{CP} in the absence of field, where, as it is known, the $J_{sy}(x)$ is nonuniform, being peaked at the edges of the strip.

In Fig. 7.14(a) we plot the calculated relevant magnetic field distributions for applied field $H = 0.4$. As anticipated above, at this large field the self fields cannot sensibly modify the applied field distribution and the magnetic induction field is now almost equal to the applied field. The applied magnetic field, whose spatial distribution is antisymmetric with respect to the middle of the strip [see Fig. 7.14(a)], is now large enough to generate vortices at the right edge and antivortices at the left edge of the strip also at $I = 0$, as shown in snapshot (1) of Fig. 7.14(b). Hence, for this field value we are in the mixed state. Due to the spatial dependence of the field, there exists a magnetic force $F_M \propto \pm \partial_x M_\rho(x, H, 0)$ that opposes the entry of the flux in the bulk of the strip, as will be more clear below. When a negative current is fed into the strip, the Lorentz force F_L associated to the transport current points inward

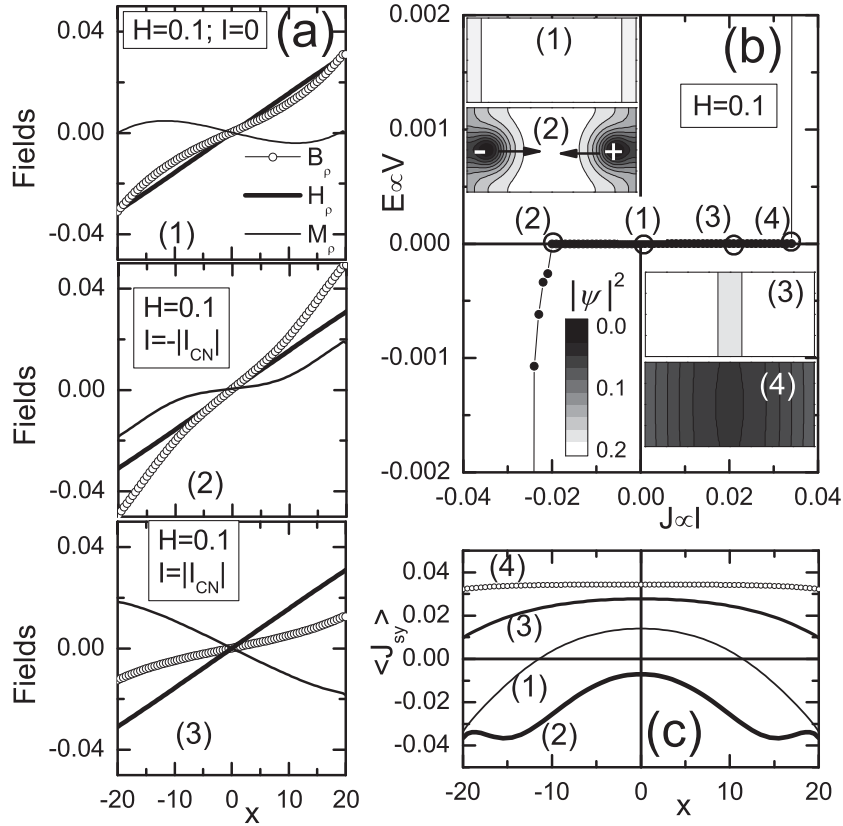


Figure 7.13: (a) Calculated field distributions for applied magnetic field $H = 0.1$: without bias current (top panel), at $I = I_{CN}$ (middle) and at $I = |I_{CN}|$ (bottom). (b) $V(I)$ curve calculated at $H = 0.1$ and snapshots of the order parameter corresponding to the points marked by circles on the $V(I)$ curve. (c) Superconducting current density distributions when we are on the points marked by circles in (b).

the strip both for vortices and antivortices. In snapshot (2) is $I = I_{CN}$ at which the F_L overcomes the F_M and the V and Av annihilate in the middle of the strip. Now new flux can enter the strip, consisting of vortices moving from right to the middle and antivortices moving from left to the middle, where they annihilate giving the onset of dissipation. Again, we remark a strong similarity with the 3D case when dynamics is seen from the top convex surface [see discussion of Fig. 7.9(b)]. The snapshot (3) shows the state for the same current value of snapshot (2) but positive, i.e., $I = |I_{CN}|$. Now Lorentz force and magnetic force point both outward the strip and cooperate to oppose the flux entry in the bulk, so that no electric field is generated at $I = |I_{CN}|$. Therefore, in the mixed state the asymmetry of the critical

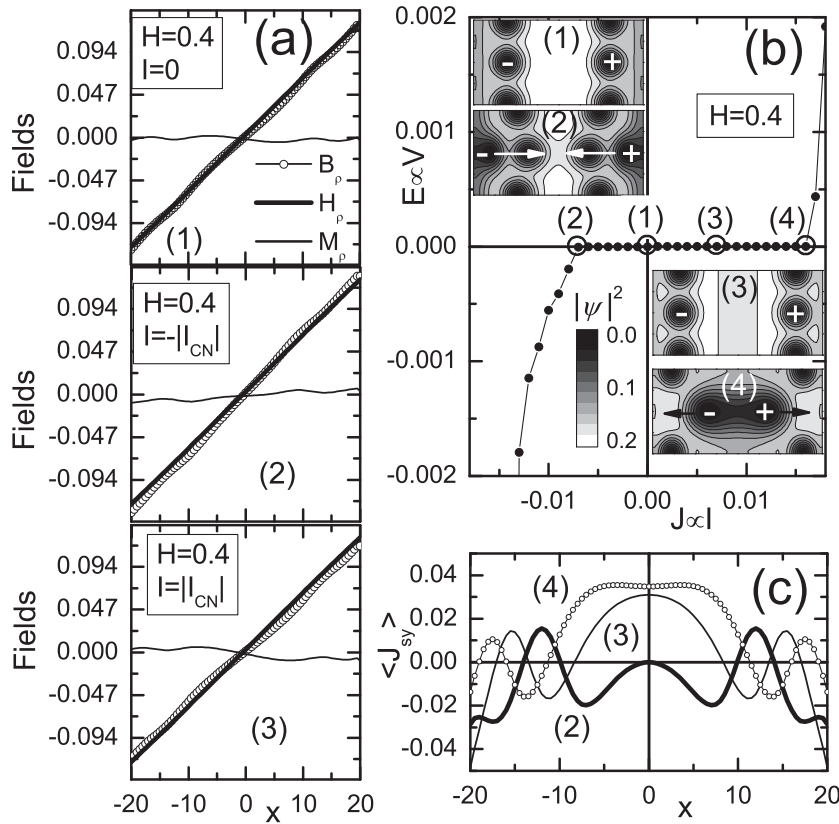


Figure 7.14: Same as in Fig. 7.13, but now is $H = 0.4$.

current densities comes from the net force, depending on current polarity, acting against entry of flux in the bulk. When I is positive the two forces sum up, hence the only way to generate dissipation is to nucleate vortex-antivortex (V-Av) pairs in the middle of the strip, at some critical current $I_{CP} > |I_{CN}|$. This can be seen in snapshot (4), corresponding to $I = I_{CP}$. The V-Av pairs so nucleated are driven to opposite directions by Lorentz force and expelled at the edges of the strip, similarly to the 3D case [see discussion of Fig. 7.9(c)]. Finally, the superconducting current density distributions shown in Fig. 7.14(c) suggest that, at some extent, the distributions are again more uniform for positive currents than for negative currents, that alternatively explains the observed positive critical currents always larger than the negative ones also at large field values. Alternatively, we can say that at positive currents the Lorentz force cooperates with magnetic force to confine the vortices and antivortices at the edges of the strip, leaving a vortex-free channel inside the strip [see snapshot (3) in Fig. 7.14(b)] which increases the total current flowing without dissipation. However, now the enhancement

of positive critical current we discussed in the low field region is not possible, because the spatial extent of the region in which the superconducting current density can be made homogeneous is considerably reduced by the presence of vortices and antivortices that pile up at the edges of the strip.

7.4 Summary

Summarizing, we have reported the experimental and numerical investigation of magneto-transport properties of a Nb thin strip with plano-convex section. The strip exhibits a considerable asymmetry in the critical currents when the magnetic field is applied parallel to the substrate. An asymmetry ratio of critical currents as large as 300% has been observed at 4.2 K, that makes the single superconducting thin strip with tailored section possibly interesting for applications as a superconducting current rectifier at micron scale. The observed asymmetry has been ascribed to the inhomogeneous (antisymmetric) magnetic field component normal to the convex top surface of the strip that affects, in the idealized 2D description of the real 3D strip, the double kinks present in the strip. At low applied fields, the normal component can enhance or weaken the polarity dependent self-field of the bias current. At larger magnetic fields the asymmetry comes from the balance of the magnetic force and the polarity dependent Lorentz force associated to the transport current.

Bibliography

- [1] P. S. Swartz and H. R. Hart, *Phys. Rev.* **156**, 412 (1967).
- [2] F. Raissi and J. E. Nordman, *Appl. Phys. Lett.* **65**, 1838 (1994).
- [3] G. Carapella and G. Costabile, *Phys. Rev. Lett.* **87**, 077002 (2001).
- [4] J. E. Villegas, S. Savelaev, F. Nori, E. M. Gonzalez, J. V. Anguita, R. Garcia, and J. L. Vicent, *Science* **302** 1188 (2003).
- [5] K. Yu, T. W. Heitmann, C. Song, M. P. DeFeo, B. L. T. Plourde, M. B. S. Hesselberth, and P. H. Kes, *Phys. Rev. B* **76**, 220507(R) (2007).
- [6] A. Yu. Aladyshkin, D. Yu. Vodolazov, J. Fritzsche, R. B. G. Kramer, and V. V. Moshchalkov, *Appl. Phys. Lett.* **97**, 052501 (2010).
- [7] G. Carapella, P. Sabatino, and G. Costabile, *Phys. Rev. B* **81**, 054503 (2010).
- [8] G. Carapella, V. Granata, F. Russo, and G. Costabile, *Appl. Phys. Lett.* **94**, 242504 (2009).
- [9] D. Y. Vodolazov, B. A. Gribkov, A. Yu. Klimov, V. V. Rogov, and S. N. Vdovichev, *Appl. Phys. Lett.* **94**, 012508 (2009).
- [10] D. Y. Vodolazov, B. A. Gribkov, S. A. Gusev, A. Yu. Klimov, Yu. N. Nozdrin, V. V. Rogov, and S. N. Vdovichev, *Phys. Rev. B* **72**, 064509 (2005).

-
- [11] A. Papon, K. Senapati, and Z. H. Barber, *Appl. Phys. Lett.* **93**, 172507 (2008).
 - [12] M. Morelle and V. V. Moshchalkov, *Appl. Phys. Lett.* **88**, 172507 (2006).
 - [13] M. Tinkham, *Introduction to Superconductivity* (McGraw-Hill, Singapore, 1996).
 - [14] M. Machida and H. Kaburaki, *Phys. Rev. Lett.* **71**, 3206 (1993).
 - [15] T. Winiecki and C. S. Adams, *Phys. Rev. B* **65**, 104517 (2002).
 - [16] T. Winiecki and C. S. Adams, *J. Comput. Phys.* **179**, 127 (2002).
 - [17] D. Y. Vodolazov and F. M. Peeters, *Phys. Rev. B* **76**, 014521 (2007).
 - [18] D. Y. Vodolazov, F. M. Peeters, M. Morelle and V. V. Moshchalkov, *Phys. Rev. B* **71**, 184502 (2005).
 - [19] L. P. Gorkov, *Soviet Physics JETP* **36**, 1364 (1959).
 - [20] K. Ohnishi, T. Kimura, and Y. Otani, *Appl. Phys. Exp.* **1**, 021701 (2008).
 - [21] P. Sabatino, C. Cirillo, G. Carapella, M. Trezza, and C. Attanasio, *J. Appl. Phys.* **108**, 053906 (2010).
 - [22] D. Y. Vodolazov and I. L. Maksimov, *Physica C* **349**, 125 (2001).
 - [23] W. H. Press, S. A. Teukolsky, W. T. Vetterling, and B. P. Flannery, *Numerical recipes: the art of scientific computing* (Cambridge University Press, 2007), 3rd ed.
 - [24] E. H. Brandt, *Phys. Rev. B* **48**, 6699 (1993).
 - [25] P. Sabatino, G. Carapella, and G. Costabile, *Supercond. Sci. Technol.* **24**, 125007 (2011).
 - [26] M. V. Milosevic and F. M. Peeters, *Appl. Phys. Lett.* **96**, 192501 (2010).
 - [27] G. Carapella, P. Sabatino, and G. Costabile, *J. Phys.: Condens. Matter* **23**, 435701 (2011).

Preferentially directed flux motion in a very thin superconducting strip with nanostructured trapezoidal profile

8.1 Introduction

Vortex matter manipulation in thin superconducting strips is a very active research field from many decades also due to the technologically important problem to oppose, or to pin, the vortex motion that generates unwanted dissipation in type II superconductors [1]. In a pioneer research on the subject, Martinoli and coworkers [2–4] proposed long time ago a very elegant pinning mechanism for vortices based on the spatial modulation of the thickness of a superconducting strip. The subject has been further theoretically addressed in the following years both in the framework of London approximation [5] and in the framework of Ginzburg Landau model [6–9] for superconductivity. Recently, variable thickness models have been used to account for the intrinsic roughness often present in thin films [10], and to study the vortex matter in thin strips with blind holes [11, 12], a system proposed [13, 14] also as a possible realization of fluxonic cellular automata. Also, the asymmetric thickness modulation of a thin superconducting strip was theoretically proposed [15] as a way to achieve flux cleaning in thin superconducting strips by classical ratchet effect, and, very recently, arrays of asymmetric blind antidots (local thickness reduction) have been used to realize [16] guided vortex motion by means of collective ratchet pinning potentials.

In this Chapter we address both experimentally and numerically the geometrical force expected [2–5] to act on vortices when the thickness of a type II superconductor is made variable. Differently from most of previous works, here we focus on the role that such a force can have on the moving vortex

matter present in the dissipative regime of a moderately wide but very thin type II superconducting strip, with thickness profile asymmetrically variable on a few tens of nanometers. As a type II superconductor we use a sputtered Niobium thin film in the dirty limit regime. The asymmetric profile of the strip generates a geometrical force landscape that promotes the motion of vortices in one direction (achieved at positive current) and opposes the motion in the opposite direction (achieved at negative current), so setting a preferential direction for vortex motion. This results, for a certain range of applied magnetic field, in an uncommon voltage-current $[V(I)]$ curve of the strip, characterized by vanishingly small asymmetry in the positive and negative critical currents but appreciably large asymmetry in the voltages. Both the peculiar behavior of the $V(I)$ curve of the strip and the more general problem of the geometrical force experienced by the vortices are addressed here in the framework of time dependent Ginzburg-Landau model for superconductors.

The Chapter is organized as follows. In Sec. 8.2, after a brief description on how the Nb thin strip with variable thickness is fabricated, we report the main experimental results on asymmetry of voltages observed in the presence of a magnetic field. In Sec. 8.3 the observed asymmetry and its relation with geometrical force is explained with the help of numerical simulations performed in the framework of time-dependent Ginzburg Landau equations specialized to the case of very thin superconducting films with variable thickness. A brief summary of main results is given in Sec. 8.4.

8.2 Experimental results

We fabricated Nb thin strips with variable thickness by means of rf-sputter deposition through a bilayer resist shadow mask [17] [see Fig. 8.1(a)] made by Electron Beam Lithography (EBL). The resist bilayer consisted of two 200 nm thick layers of 2% polymethylmethacrylate (PMMA) 950K MW dissolved in anisole. The bilayer is fabricated first spinning and curing the first layer, labeled (1)PMMA in Fig. 8.1(a), and then spinning and curing the second layer, labeled (2)PMMA in Fig. 8.1(a). We noticed that this double step deposition produced an appreciably different sensitivity in the two resist layers. For an accelerating voltage of 10 kV, the clearance dose of top (2)PMMA is $100 \mu\text{C}/\text{cm}^2$, while for the bottom (1)PMMA is $50 \mu\text{C}/\text{cm}^2$. The shadow mask sketched in Fig.8.1(a) was achieved writing a $3 \mu\text{m}$ wide area with an area dose of $100 \mu\text{C}/\text{cm}^2$ and the two lateral areas, $2 \mu\text{m}$ wide at right and only $0.2 \mu\text{m}$ wide at the left, with the area dose of $50 \mu\text{C}/\text{cm}^2$. After development in a methyl isobutyl ketone and isopropyl alcohol solution

(1-MIBK:3-IPA) for 30 s, followed by rinsing in IPA and deionized water, the bilayer is expected to work as the shadow mask sketched in Fig. 8.1(a). To enhance resistance to plasma, after development the mask is further baked at 130 °C for 30 min in a convection oven. Due to the isotropy of the sputter process, the Nb is smeared under the window formed by the top layer of resist, (2) PMMA, resulting in a smooth trapezoidal profile for the Nb deposited on the Si/SiO₂ substrate, as sketched in Fig.8.1(a). A FE-SEM image of a typical Nb strip after lift-off in acetone is shown in Fig. 8.1(b) and confirms the expected shape for the section of the film.

The sample has a bridge geometry consisting of two macroscopic continuous Nb banks contacting the Nb thin strip, realized using standard optical lithography, with the current and voltage contacts 30 μm apart. The Nb strip of Fig. 8.1(b) has a width $W \simeq 5.2 \mu\text{m}$, and a maximum thickness $d_M \simeq 30 \text{ nm}$. Such a thickness gradually reduces to zero in the two lateral wedges, that were intentionally chosen to have quite different widths. The width of left wedge is only 0.2 μm while the right wedge is approximately 2 μm wide [see Fig. 8.1(c)], resulting in a thickness profile of the strip quite asymmetrically nanostructured.

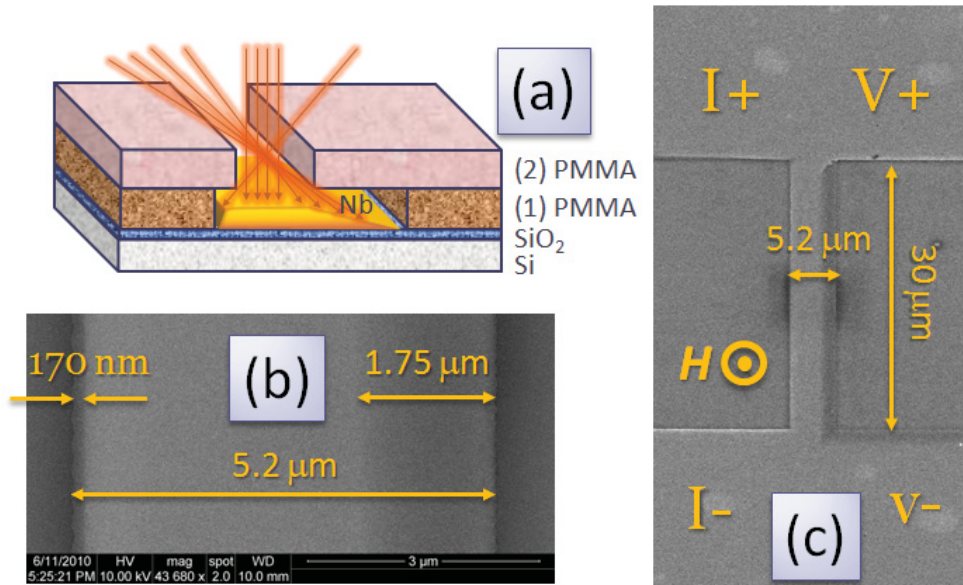


Figure 8.1: (a) A sketch (not on scale) of the bilayer resist mask used to sputter Nb. (b) and (c) FE-SEM micrograph of the deposited Nb strip.

In Fig. 8.2 we show the $V(I)$ curves of the sample, recorded at $T = 4.2 \text{ K}$ (the critical temperature is $T_c \simeq 6 \text{ K}$), at several magnetic field values. The magnetic field is applied perpendicular to the substrate and perpendicular

to the transport current. We observe that, for relatively low magnetic field, the $V(I)$ curves have a positive and negative dissipative branches with a meaningfully different dynamical resistivity, instead at zero or high magnetic fields this asymmetry is not present. Conversely, the critical currents (I_{CP} and I_{CN} , the current values corresponding to the transition $V = 0 \rightarrow V \neq 0$), estimated using a $0.2 \mu\text{V}$ criterion, are found to be basically symmetric, as better appreciated in the inset of Fig. 8.2. The magnetic pattern shows that the critical currents are weakly asymmetric only in a narrow range at low magnetic field, instead when $H = 0$ or $H > 15$ Oe this asymmetry is almost absent though an appreciable asymmetry in the voltages is again present.

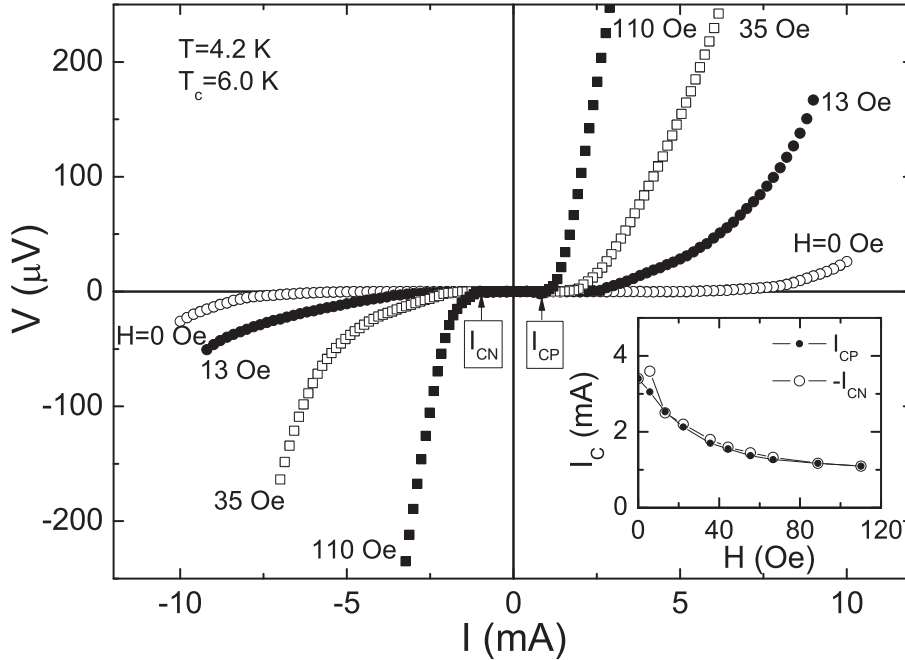


Figure 8.2: $V(I)$ curves of the sample recorded at $T = 4.2$ K for several magnetic fields applied perpendicular to substrate. The magnetic field dependence of the positive and negative critical currents is shown in the inset.

In the top panel of Fig. 8.3(a) we compare the positive and negative branch of $V(I)$ curve of the strip in the low voltage range, recorded at $T = 4.2$ K and when a weak magnetic field $H = 22$ Oe is applied. The voltage difference can be quantified by the asymmetry ratio $|V(I)/V(-I)|$ as a function of current amplitude I . Such a curve is shown in the bottom panel of Fig. 8.3(a). As it is seen, the asymmetry ratio assumes an average value of about three, except at the onset of the resistive branches where its value reaches about four. When magnetic field is reversed, the $V(I)$ curves

are mirrored with respect to the origin, so the inversion of magnetic field is equivalent to inversion of bias current. In Fig. 8.3(b) we show the comparison of the voltages under opposite applied magnetic field (top panel) and their asymmetry ratio (bottom panel) as a function of magnetic field, when the sample is supplied by a bias current $I = 3$ mA. The results suggest that there is a magnetic field range where we have strongly different positive and negative voltages, but increasing the magnetic field, this difference gradually tends to zero.

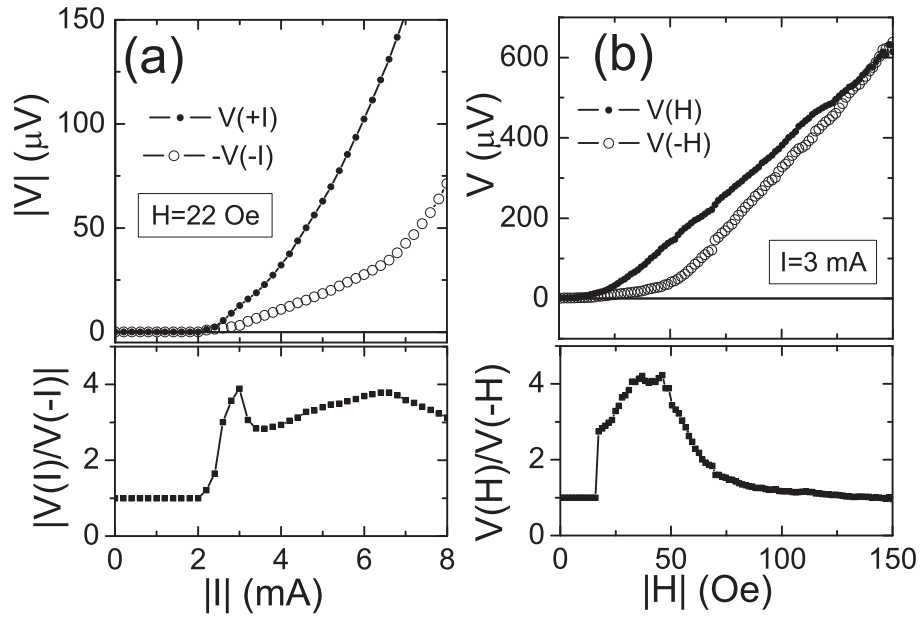


Figure 8.3: (a) Comparison of the positive and negative branch of $V(I)$ curve of the strip in the low voltage range (top panel) and asymmetry ratio (bottom panel) recorded at $T = 4.2$ K when a weak magnetic field $H = 22$ Oe is applied. (b) Comparison of the voltages under opposite applied magnetic field (top panel) and asymmetry ratio (bottom panel) as a function of magnetic field when the sample is biased with a current $I = 3$ mA.

8.3 Discussion

By assuming that the voltage in the resistive branches of the moderately wide thin strip is generated by flux motion [1], experimental results shown in Fig. 8.3(a) suggest that motion in one direction, achieved at positive bias current, is enhanced with respect to the motion in the opposite direction, achieved at negative bias current. This asymmetry in the motion could be intuitively

explained by the asymmetric thickness profile of the strip [see Fig. 8.1(b)]. The variable thickness, in fact, is expected to induce a geometrical force [2–5] pointing toward the thinnest region of the strip. This force acts on the core of the single vortices, and it is expected [5] to be relevant only in the low vortex density regime, i.e., only at low magnetic fields. With reference to the Fig. 8.1(b), by neglecting the very narrow region of variable thickness at left edge, there is a force on the right side of the strip, that extends for about 2/5 of the strip width, that can set the motion from the left to the right as the preferred flux motion direction, as results of Fig. 8.3(a) seem to suggest. For stronger applied magnetic fields, or for vortices closer together, the effects of varying thickness will become more and more negligible, because the force generated by neighboring vortices starts to dominate the geometrical force. This is consistent with results shown in Fig. 8.3(b), which show that at high magnetic field, meaning high vortex density present in the strip, the effect that the asymmetric thickness of the strip can exert on the vortex motion is progressively washed out.

In this section we give further theoretical insight both in the observed asymmetry of voltages suggesting a preferential directed flux motion and in the geometrical force generated by the variable thickness that sets such a preferential direction. To the purpose we use the time dependent Ginzburg-Landau model specialized to superconducting films with variable thickness.

8.3.1 Model

To account for a length much larger than the width of the strip, we model our superconducting strip as infinite in the y -direction, but finite in the x - and z -directions. We assume that the variable extent of the film is in the z -direction, $d_0 < z < d(x)$, as sketched in Fig. 8.4. After averaging across the thickness of the film [6–8], i.e., in the z -direction, the steady-state three-dimensional Ginzburg-Landau (GL) model for superconductivity in homogeneous and isotropic materials is reduced to the well-known two-dimensional GL equations, except that the variations in the thickness of the film appear into the coefficients of the differential equations. An extension to the time dependent case was reported in Ref. [8, 9]. Therefore, we performed numerical simulations in the framework of the time dependent Ginzburg-Landau (TDGL) model at finite temperature for thin films of variable thickness [6–9]:

$$\begin{aligned} u \frac{\partial \psi}{\partial t} &= (\nabla - i\mathbf{A}) \cdot d(\nabla - i\mathbf{A}) \psi + d(1 - T - |\psi|^2) \psi \\ \frac{\partial \mathbf{A}}{\partial t} &= d \operatorname{Re} [\psi^* (-i\nabla - \mathbf{A}) \psi] - \kappa^2 \nabla \times d(\nabla \times \mathbf{A} - \mathbf{H}) \end{aligned}$$

where $\psi = |\psi| e^{i\phi}$ is the complex order parameter, \mathbf{A} the vector potential, $\mathbf{H} = (0, 0, H)$ the applied magnetic field along the z -direction, T the temperature, κ the Ginzburg-Landau parameter, the coefficient u [18] governs the relaxation of the order parameter, and $d = d(x)$ with $0 < d_0 < d(x) < d_M$ is the smooth function that represents variations in the thickness of the film. All physical quantities are measured in dimensionless units: the coordinates are in units of the coherence length $\xi(0) = \sqrt{\pi\hbar D/8k_B T_c}$ and T_c is the critical temperature, D is the diffusion constant. The temperature T is in units of critical temperature T_c . The time is scaled in units of the Ginzburg-Landau relaxation time $\tau_0 = 4\pi\sigma_n\lambda(0)^2/c^2 = \xi(0)^2/Du$ (σ_n is the normal-state conductivity, $\lambda(0) = \kappa\xi(0)$ the magnetic field penetration depth). The order parameter is in units of $\Delta(0) = 4k_B T_c \sqrt{u}/\pi$, i.e., the superconducting gap at $T = 0$ which follows from Gor'kov's derivation of the Ginzburg-Landau equations. The vector potential is scaled in units $\Phi_0/2\pi\xi(0)$ ($\Phi_0 = ch/2e$ is the quantum of magnetic flux). In these units the magnetic field is scaled with $H_{c2} = \Phi_0/2\pi\xi(0)^2$ and the current density with $j_0 = c\Phi_0/8\pi^2\lambda(0)^2\xi(0)$. Our normalization is relative to the variables at $T = 0$. This results in the explicit inclusion of normalized temperature T in the first equation, as found, e.g., in Ref. [19, 20].

To simulate a finite width and infinite length strip, we apply periodic boundary conditions in the y -direction, $\psi(x, y) = \psi(x, y + \Lambda)$, $\mathbf{A}(x, y) = \mathbf{A}(x, y + \Lambda)$, where Λ is the spatial period. The superconductor-normal metal boundary conditions [1] are instead used in the x -direction, i.e., the conditions $(\nabla_x - iA_x)\psi|_{x=\pm W/2} = -b^{-1}\psi$ with the extrapolation length $b > 0$, where W is the width of the strip. We used these conditions instead of the superconductor-insulator boundary condition [1] because, realistically, our strip is expected to become normal at the edges. In fact, here the thickness is vanishingly small and superconductivity is expected to be destroyed below some critical thickness d_0 at finite working temperatures. The transport current density $\mathbf{J} = (0, J, 0)$ is introduced in the boundary condition for the vector potential in the x -direction, $(\nabla \times \mathbf{A})_z|_{x=\pm W/2} = H \mp H_J$, where $H_J = JW/2k^2 d_0$, with $d_0 = d(\pm W/2)$, is the magnetic field induced by the bias current density J along the y -direction and H is the applied magnetic field in the z -direction. The initial conditions are $|\psi| = 1$ and $\mathbf{A} = 0$. We apply a finite-difference representation for the order parameter ψ and the vector potential \mathbf{A} on a uniform Cartesian space grid, and use the link variable approach [21, 22] and the standard Euler integration method [23] to find ψ and \mathbf{A} . The behavior of the system is studied on a large time scale when time-averaged values no longer depend on time.

From the slope close to T_c of the upper critical field $\mu_0 H_{c2}(T)$ we es-

timate [24] for our sputtered Nb thin film a coherence length $\xi(0) \simeq 9$ nm. This value is much smaller than the BCS coherence length of Nb, $\xi_0 = 39$ nm, so the sample is in the dirty limit regime with an electron mean free path $l = 1.38\xi(0)^2/\xi_0 \simeq 2.8$ nm. In the dirty limit regime the Ginzburg-Landau parameter can be estimated by $\kappa = 0.72\lambda_L/l \simeq 10$, with $\lambda_L = 40$ nm the London penetration depth of Nb. This result implies that the investigated sample is a type-II superconductor. The Ginzburg-Landau penetration depth is $\lambda(0) = \kappa\xi(0) = 90$ nm, so our strip is quite thinner than $\lambda(0)$. In normalized units, the experimental strip has a width $W \simeq 500\xi(0)$, a maximum thickness $d_M \simeq 3\xi(0)$, and a length $L \simeq 6W$. Experimental data are recorded at reduced temperature $T/T_c = 0.7$. In all our calculations, we choose $\kappa = 5$, $u = 5.79$, $T = 0.8$, $b = 1$, width along x -direction $W = 80\xi(0)$, spatial period along y -direction $\Lambda = 20\xi(0)$. The variable thickness regions at the edges of the strip are modeled as lateral wedges, as sketched in Fig. 8.4, where the thickness of the strip linearly decreases from the maximum thickness $d_M = 1\xi(0)$ to the minimum thickness $d_0 = 0.1\xi(0)$. The left wedge is $7\xi(0)$ wide and the right wedge is $30\xi(0)$ wide. These parameters, comparable though not the same as in the experiment, allow us to retain relevant information within capabilities of our personal computer.

8.3.2 Preferentially directed flux motion

In Fig. 8.4 we show the calculated $E(J)$ curves at $T = 0.8$ of the strip for three values of normalized magnetic field H . In the bottom inset there are shown the calculated positive and negative critical current densities (J_{CP} and J_{CN} , corresponding to the transition $E = 0 \rightarrow E \neq 0$) as a function of magnetic field. As in the experiment (see Fig. 8.2), we observe that the critical current densities are weakly asymmetric only in a narrow range at low magnetic fields, instead when $H = 0$ or $H \geq 0.01$ this asymmetry in the critical current density disappears. However, at small but finite magnetic fields, an appreciable asymmetry in the electrical fields is apparent (see curve at $H = 0.02$) though the critical current densities are almost symmetric, again in qualitative agreement with experimental results shown in Fig. 8.2.

Vortex dynamics involved in these dissipative branches is described in Fig. 8.5. In the top panel we compare both negative and positive branches of the $E(J)$ curve at $H = 0.01$. In the bottom panel we show some order parameter snapshots relative to the labeled points of the negative and positive branches of the $E(J)$ curve. We observe that the asymmetry in the critical currents is already absent at this magnetic field value, instead it is clearly evident that the positive branch has a dynamical resistivity much larger than the negative one, as evidenced by a asymmetry ratio (thick line in top panel)

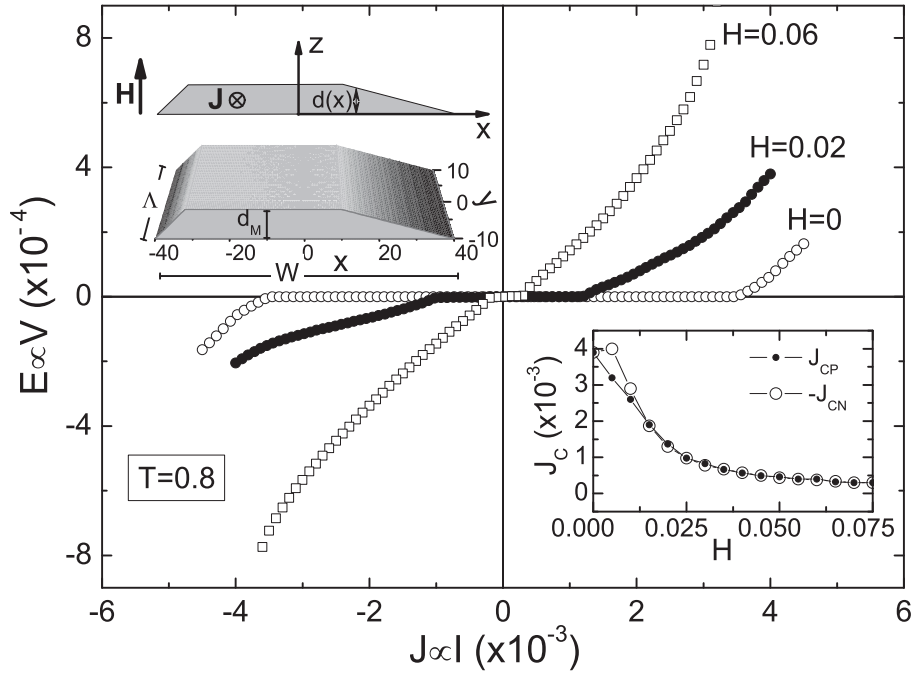


Figure 8.4: Calculated $E(J)$ curves at $T = 0.8$ for some H values. The bottom inset shows the calculated positive and negative critical current densities as a function of magnetic field. In the top inset there is sketched (not on scale) the geometry of the thin superconductive strip with variable thickness.

of about three for the current range shown, in qualitative agreement with experimental results in Fig. 8.3(a).

The snapshots (1) and (2) in the bottom panel of Fig. 8.5 show the contour plot of squared order parameter for increasing positive J values along the first approximately linear piece of the positive branch of the $E(J)$ curve. The vortices are driven by the Lorentz force associated to the transport current density from the left edge toward the right edge of the strip, where they are expelled and the whole periodic process restarts. We observe that on this almost linear piece there is a single row of moving vortices. By increasing the applied bias current the speed of the nucleation process grows and a piece with larger slope is developed in the branch, accounted for by vortices making an alternating double row (vortex density is doubled), as shown in the snapshot (3). The snapshots (4), (5) and (6) show the vortex dynamics at the same previous current values but with opposite polarity, so that now the Lorentz force drives the vortices from the right to the left edge of the strip. We immediately realize that though the dynamical regime is again an unidirectional flux motion (flux flow), this time such a motion is

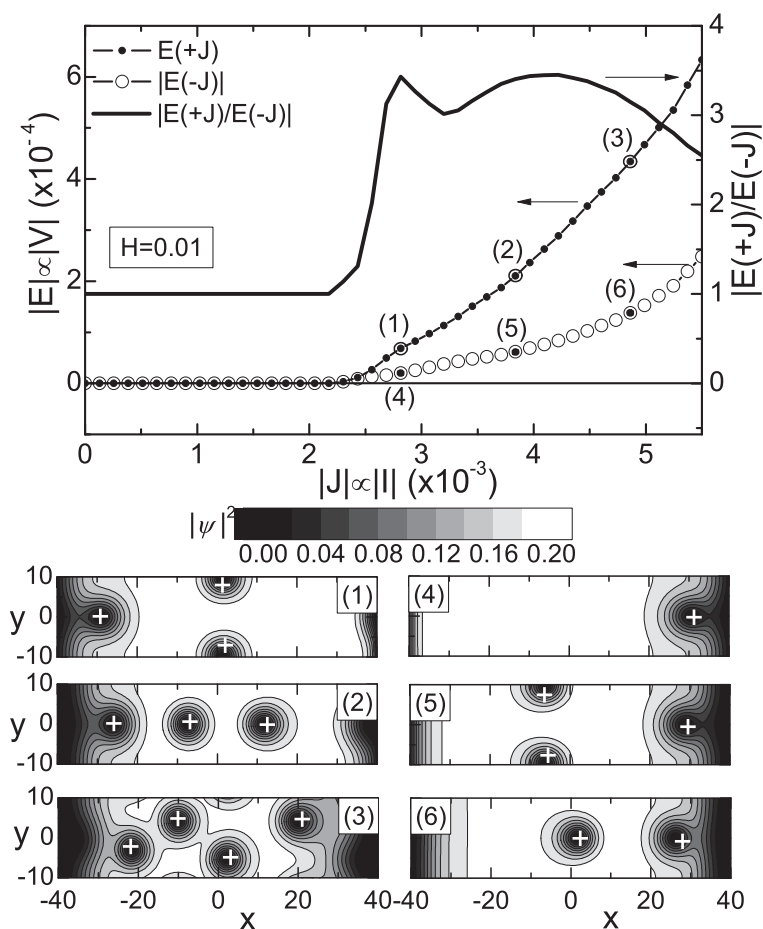


Figure 8.5: Comparison of the calculated positive and negative branches of $E(J)$ curve and the asymmetry ratio, in the low electric field range, for $H = 0.01$ (top panel). The numbered contour plots (lower panel) correspond to the squared order parameter when we are on the marked points of the $E(J)$ curves.

sensibly slowed by some force opposing the Lorentz force directed from the left to the right edge of the strip. In other words, the asymmetric profile of the strip promotes the motion of vortices in one direction (left to the right) and opposes motion in the opposite direction (right to the left), so setting a preferential direction for vortex motion.

The origin of the asymmetry in the electric field shown in Fig. 8.5 can be better appreciated if we focus our attention on the single vortex dynamics. In Fig. 8.6 we have again $H = 0.01$ as in Fig. 8.5, but now we apply a lower positive or negative current density with same modulus $|J| = 2.4 \cdot 10^{-3}$ cor-

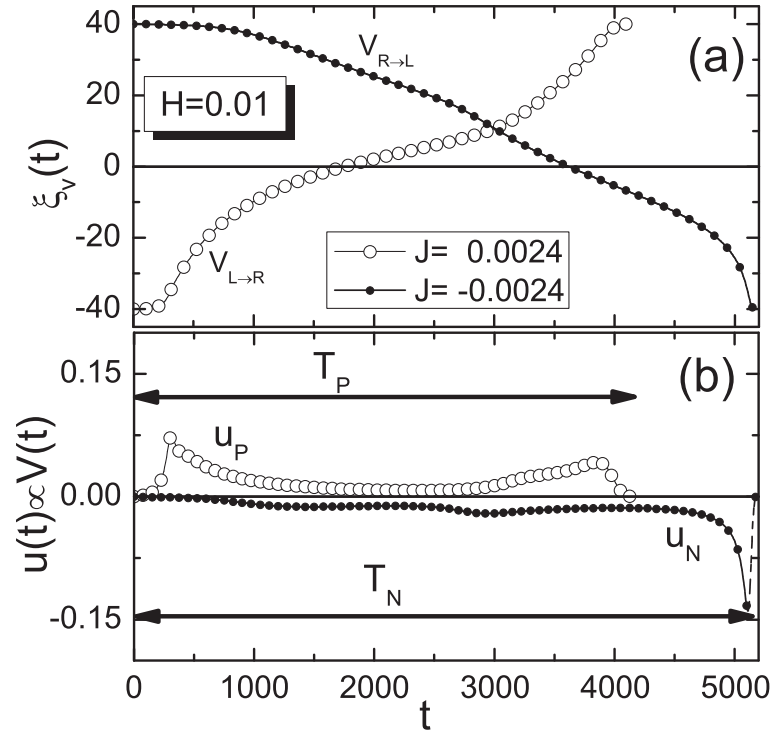


Figure 8.6: (a) Comparison of the core position vs time for a single vortex traveling from left to the right ($V_{L\rightarrow R}$) of the strip with the one of a vortex traveling in the opposite direction ($V_{R\rightarrow L}$). The applied field is $H = 0.01$ and the current density has same intensity in both cases, but it is positive for $V_{L\rightarrow R}$ and negative for $V_{R\rightarrow L}$. (b) Velocity vs time for the vortex in the two cases shown in (a).

responding to the onset of the dissipative positive and negative branches (see Fig. 8.5). For these current density values the dissipation is accounted for only a single vortex in the spatial period along y -direction, moving from left to the right ($V_{L\rightarrow R}$) at positive current density and in the opposite direction ($V_{R\rightarrow L}$) for negative current density, as shown Fig. 8.6(a), where the core position of the vortex ξ_V versus time is plotted for the two relevant current densities. The instantaneous vortex velocity curves $u_P(t)$ and $u_N(t)$ for the two cases in (a) are plotted in the panel (b). All these temporal curves are for a single period of the motion. As it is seen, the time to travel the strip from left to the right ($V_{L\rightarrow R}$, period T_P) is lower than the time to travel the strip in the opposite direction ($V_{R\rightarrow L}$, period T_N), in agreement with above discussion on the asymmetric thickness profile of the strip that speed up motion in one direction and slows motion in the opposite direction. The difference

in the two periods, in particular $T_N > T_P$, is directly related to the observed asymmetry in the electric field. In fact, with only a single vortex involved, the measured electric field is simply $E \equiv \langle E(t) \rangle_T \propto \langle u(t) \rangle_T = W/T$, where $\langle .. \rangle_T$ indicates the time average on a period of motion and W is the width of the strip. This results in the measured electric field asymmetry ratio $|E(J)/E(-J)| = T_N/T_P > 1$, observed for the $E(J)$ branches reported in Fig. 8.5(a), at least in the first linear region, where dissipation is accounted for by single vortex dynamics.

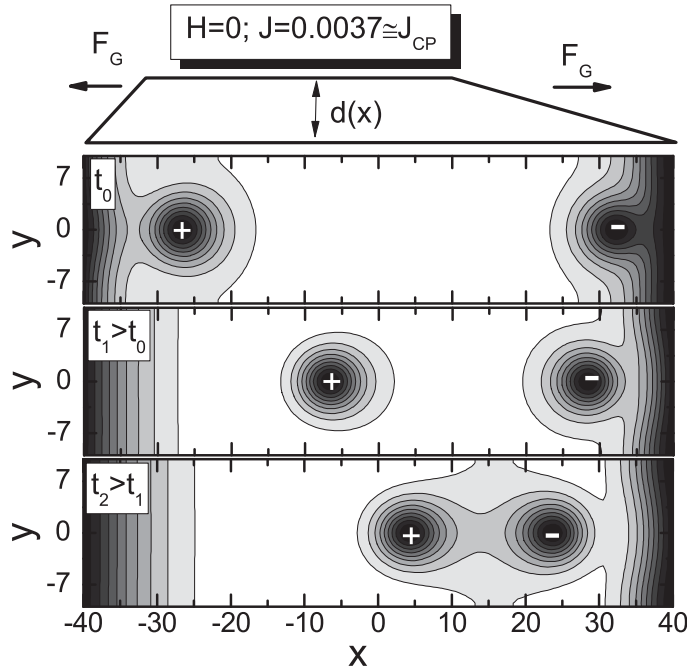


Figure 8.7: Sketch of geometrical force experienced by the vortices and antivortices in the lateral wedges of the strip (top panel). Time evolution of the squared order parameter on the onset of the dissipative branch at $H = 0$ and $J \simeq J_{CP}$ (bottom panel).

Further insight into preferentially directed flux motion is presented in Fig. 8.7. This time we set $H = 0$ and we study the onset of dissipation due to the motion of vortices and antivortices nucleated at edges of the strip by the self field associated to the transport current. As discussed above, the variable thickness wedges result in a geometrical force that points toward the thinnest sides of the strip independently of vortex polarity, as sketched in the top panel of Fig.8.7. In our case the geometrical force F_G points always outward of the strip, but it is strong and acts over a small extent in the left wedge, while it is weak but acts over a large extent in the right wedge. At

positive critical current density J_{CP} , the Lorentz force, that points inward the strip both for vortices and antivortices, overcomes the geometrical force so that flux motion is established and electric field is generated. However, due to the small extent of the left wedge and to the finite spatial extension of the vortex that also results in an impairment of the geometrical force acting in the narrow left wedge, after a while the vortex nucleated at left edge essentially moves freely inward the strip in the constant thickness region (where $F_G = 0$), differently from the the antivortex that is braked by F_G in the appreciably wider right wedge and its motion is slowed compared to the motion of the vortex. So, also in the absence of applied magnetic field, the asymmetric thickness profile sets the left to the right direction as the preferential direction for flux motion. This can be better appreciated in the bottom panel of Fig. 8.7, where we plot the temporal sequence of the squared order parameter on the onset of the dissipative branch at $H = 0$ and $J \simeq J_{CP}$. At negative critical current $J \simeq J_{CN}$ same dynamics shown in the Fig. 8.7 is observed, but for the inversion of role of vortices with antivortices, resulting in symmetry both in the electric fields and in the critical current, as can be appreciated in the calculated $E(J)$ curve at $H = 0$ shown in Fig.8.4 and in the corresponding experimental $V(I)$ curve shown in Fig.8.2. We would remark that, differently from the well known wide strip with constant thickness where dissipation due to the self field consists of nucleation of vortex and antivortex at the edges followed by their annihilation at the middle of the strip [1, 25], here the motion is made spatially unbalanced and mainly accounted for by flux of one polarity (vortices) at positive bias current and opposite polarity (antivortices) at negative bias current.

8.3.3 Geometrical force

An approximated functional form for the geometrical force acting on the vortex core can be derived from the spatial derivative of the self-energy of a single vortex. When, as it is our case, the strip thickness $d(x)$ is lower than the penetration depth, $d(x) < \lambda$, such energy should be approximately described by [4] $U_V \propto \lambda_E^{-1} \log(2\lambda_E/\xi)$, where $\lambda_E = \lambda^2/d(x)$ is the Pearl penetration depth. Hence, in our normalized units, the geometrical force is expected to be approximately described by

$$F_G(\xi_V) \propto - \frac{\partial}{\partial x} \left(d(x) \log \frac{2\kappa\lambda(T)}{d(x)} \right) \Big|_{x=\xi_V}, \quad (8.1)$$

where ξ_V is the core position of a vortex and $\lambda(T) = \lambda(0)/\sqrt{1-T}$ is the temperature dependent Ginzburg-Landau penetration depth.

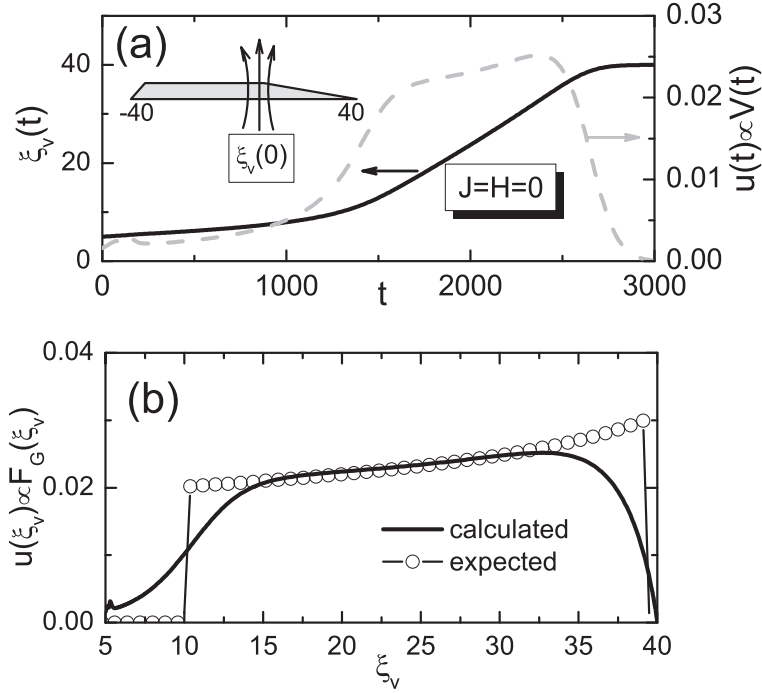


Figure 8.8: (a) Core position and velocity vs time for a single vortex in the right wedge without external forces ($J = H = 0$). The initial vortex core position is sketched in the inset. (b) Velocity (Force) versus core position for the vortex in (a). The open circles are a fit with Eq. (8.1).

In Fig. 8.8 we focus on such a geometrical force acting over a single vortex in the absence of other applied forces. To account for the presence of a single vortex in the strip, the initial condition for order parameter is chosen as [26, 27] $\psi(x, y, 0) = (x - \xi_V + iy) / \sqrt{(x - \xi_V)^2 + y^2}$, describing a seed solution for a single vortex with core position at $(x = \xi_V, y = 0)$. After a small transient this initial condition evolves in the standard Abrikosov vortex solution achieved in presence of external magnetic field. As shown in the sketch of Fig. 8.8(a), we choose the initial position of the vortex core as $\xi_V(0) = 5$. Due to its finite spatial extension (the radius at half-height of a vortex [1] is $r_v \approx \sqrt{2}\xi(T)$, and its total half-width is of the order of $2r_v \cong 6.1$ at our $T = 0.8$) the vortex partially extends in the right wedge [see sketch in panel (a)] and so can experience a fraction of the geometrical force F_G . In panel (a) we plot the core position (center of vortex) versus time for the said vortex. After the time needed to enter the right wedge region (starting at $\xi_V = 10$) under the action of a fraction of the geometrical force, the core position evolves in time almost linearly ($1500 < t < 2500$)

when it is in the wedge, up to the vortex expulsion at right edge of the strip. We also plotted in panel (a) the core velocity (i.e., the time derivative of the core position) $u(t) \propto V(t)$. Removing the time coordinate from the previous curves, the core velocity as a function of core position, $u(\xi_V)$, shown in panel (b) is found. Noticing that for the Abrikosov vortex the inertial effects can be neglected [1], the position dependent velocity of the vortex is proportional to the local force experienced by the vortex. In our case this means $u(\xi_V) \propto F_G(\xi_V)$ that allows us to extract the functional form of the geometrical force plotted in Fig. 8.8(b). We notice that in bulk of the wedge ($15 < \xi_V < 35$), where the finite spatial extension of the vortex makes only small corrections on the effective force experienced by the vortex core, the extracted $F_G(\xi_V)$ (solid line) is in qualitative agreement with the functional form Eq. (8.1) (open circles) we anticipated above that can be predicted from vortex self-energy [4] in the framework of London approximation (near core analysis) neglecting finite size effects related to the finite spatial extension of the vortex that in the Ginzburg Landau model we are using are instead fully accounted.

We conclude noticing that the geometrical force acting on the core of a vortex addressed here shows qualitative similarities with the one observed to act on vortices in variable width channels realized on the top of superconducting strips [28] and also with the one acting on Josephson vortices in variable width long Josephson junctions [29].

8.4 Summary

Summarizing, we have reported magneto-transport measurements performed on a moderately wide but very thin Nb strip, with thickness profile asymmetrically variable on a few tens of nanometers. In a certain range of applied magnetic field, the $V(I)$ curve of the strip is characterized by vanishingly small asymmetry in the positive and negative critical currents but appreciably large asymmetry in the voltages. This behavior has been explained by the asymmetric profile of the strip that generates a geometrical force landscape that sets a preferential direction for vortex motion. Both experimental data and the more general problem of the geometrical force experienced by the vortices have been addressed here in the framework of the time dependent Ginzburg-Landau model specialized to superconducting films with variable thickness.

Bibliography

- [1] M. Tinkham, *Introduction to Superconductivity*. (McGraw-Hill, Singapore, 1996).
- [2] O. Daldini, P. Martinoli, J. L. Olsen, and G. Berner, Phys. Rev. Lett. **32**, 218 (1974).
- [3] P. Martinoli, O. Daldini, C. Leemann, and B. Van den Brandt, Phys. Rev. Lett. **36**, 382 (1976).
- [4] P. Martinoli, Phys. Rev. B **17**, 1175 (1978).
- [5] S.J. Chapman and D.H. Heron, SIAM J. Appl. Math. **58**, 1808 (1998).
- [6] Q. Du and M.D. Gunzburger, Physica D **69**, 215 (1993).
- [7] Q. Du, M.D. Gunzburger, and J. S. Peterson, Phys. Rev. B **51**, 16194 (1995).
- [8] S. J. Chapman, Q. Du, and M. D. Gunzburger, ZAMP **47**, 410 (1996).
- [9] E. Coskun, Appl. Math. Comput. **106**, 31 (1999).
- [10] E. Sardella and E. H. Brandt, Supercond. Sci. Technol. **23**, 025015 (2010).
- [11] G. R. Berdiyrov, M. V. Milošević, B. J. Baelus, and F. M. Peeters, Phys. Rev. B **70**, 024508 (2004).
- [12] G. R. Berdiyrov, M. V. Milošević, and F. M. Peeters, New J. Phys. **11**, 013025 (2009).

-
- [13] M. V. Milošević, G. R. Berdiyorov, and F. M. Peeters, *Appl. Phys. Lett.* **91**, 212501 (2007).
- [14] M. V. Milošević and F. M. Peeters, *Appl. Phys. Lett.* **96**, 192501 (2010).
- [15] C. S. Lee, B. Janko, I. Derenyi, and A. L. Barabasi, *Nature (London)* **400**, 337 (1999).
- [16] A. Palau, C. Monton, V. Rouco, X. Obradors, and T. Puig, *Phys. Rev. B* **85**, 012502 (2012).
- [17] K. Ohnishi, T. Kimura, and Y. Otani, *Appl. Phys. Exp.* **1**, 021701 (2008).
- [18] L. Kramer and R. J. Watts-Tobin, *Phys. Rev. Lett.* **40**, 1041 (1978).
- [19] L. P. Gor'kov, *Soviet Phys.—JETP* **9**, 1364 (1959).
- [20] D. Y. Vodolazov, F. M. Peeters, M. Morelle, and V. V. Moshchalkov, *Phys. Rev. B* **71**, 184502 (2005).
- [21] T. Winiecki and C. S. Adams, *J. Comput. Phys.* **179**, 127 (2002).
- [22] T. Winiecki and C. S. Adams, *Phys. Rev. B* **65**, 104517 (2002).
- [23] W. H. Press, S. A. Teukolsky, W. T. Vetterling, and B. P. Flannery, *Numerical Recipes: The Art of Scientific Computing*. (Cambridge University Press, 3rd ed., 2007).
- [24] P. Sabatino, C. Cirillo, G. Carapella, M. Trezza, and C. Attanasio, *J. Appl. Phys.* **108**, 053906 (2010).
- [25] M. Machida and H. Kaburaki, *Phys. Rev. Lett.* **71** 3206 (1993).
- [26] H. Y. Liao, S. P. Zhou, and X. Y. Shi, *Chin. Phys.* **13**, 737 (2004).
- [27] G. Carapella, P. Sabatino, and G. Costabile, *J. Phys.: Condens. Matter* **23**, 435701 (2011).
- [28] K. Yu, T. W. Heitmann, C. Song, M. P. DeFeo, B. L. T. Plourde, M. B. S. Hesselberth, and P. H. Kes, *Phys. Rev. B* **76**, 220507(R) (2007).
- [29] G. Carapella, N. Martucciello, and G. Costabile, *Phys. Rev. B* **66**, 134531 (2002).

Conclusions

In this thesis novel mesoscopic superconducting devices have been fabricated and characterized, with both magneto-transport measurements and with numerical simulations. In summary, the work has been focused on the realization of superconducting nanostructures on silicon, using the Electron Beam Lithography and metal lift-off. Such a technology offers a powerful solution for nanofabrication able to conjugate spatial resolution, operation flexibility, and costs. The interest for these devices is stimulated by the unexplored fascinating fundamental physics at the nanoscale as well as by the perspective of future technological applications. However, one of the major challenges associated with the realization of these devices is that any physical defects within the patterned films can perturb the magneto-transport properties and thus the behavior of the device is also determined by the fabrication quality. Therefore, during the course of this PhD project, an extensive patterning trials and optimization of the fabrication procedure were carried out in order to obtain good results on particular sample geometries.

The interpretation of the experimental results are been supported by numerical simulations based on the Time-Dependent Ginzburg-Landau theory, how we have explained in details in Chapter 1. We have introduced the equations of the TDGL model using both phenomenological and microscopic approaches. Then, the TDGL equations are been written in their dimensionless form, making them easier for analysis and computations. The TDGL model has been also examined in the high- κ , high magnetic field limit which simplifies the complexity of the general model. Moreover, we have analyzed in detail how to employ a transport current both in the general and in the simplified model, and how to derive from both the interest physical quantities. Some numerical methods for solving TDGL equations have been discussed

and implemented in this thesis work. We have introduced two methods to discretize the TDGL equations with the help of link variables and we describe how to impose the boundary conditions for finite geometries. Finally, we have reported a short description of the hardware and software platform used for simulating both models.

Chapter 2 contains a general description of the equipments used, the pattern transfer process (including electron beam lithography and photolithography techniques), metal deposition and lift-off processes and electrical characterization of the patterned device. The main instrumental aspects of EBL are described in this Chapter. Finally, we briefly presented the best devices obtained using the above fabrication techniques and some preliminary results of electrical transport measurement successfully performed for two fabricated samples that not been discussed in detail in this thesis work. Moreover, we describe the measurement system setup (cryostats and measurement electronics) used for the acquisition of the I-V characteristics in magnetic field of fabricated devices.

The main results that have been achieved are next summarized and embrace the backbone information that has been exposed within Chapters 3, 4, 5, 6, 7 and 8.

Chapter 3 contains the further investigation on the bistable vortex diode made of a ferromagnet-superconductor bilayer that we have recently demonstrated.

In Chapter 4 we showed how a regular square array of nanometer-sized pinning centers on Nb thin films has been obtained by a simple sputter-etching-assisted EBL process. The critical current $j_c(H)$ values, measured by transport measurements on patterned samples, are found to be considerably larger than those measured on a Nb film without antidots at the same reduced temperature and exhibit pronounced maxima just above the expected matching fields, down to $T = 2.3$ K ($T/T_c = 0.33$). The behavior of $j_c(H)$ as well as the maxima locations have been found to be consistent with the ones calculated in the framework of time dependent Ginzburg-Landau model.

Chapter 5 summarizes the numerical simulations performed on the vortex dynamics in curved mesoscopic superconducting strips conforming to cylindrical shells. The cylindrical section exhibits asymmetric transport properties for a suitable choice of the orientation of the external magnetic field, while the full cylindrical surface features a very rich vortex-antivortex dynamics, ranging from the familiar V-Av flux flow regime to kinematic V-Av pairs phase slip lines regime as the bias current is increased. The kinematic V-Av pairs account for dissipative branches in the $E(J)$ curves exhibiting a dynamical resistivity larger than the normal state resistivity.

In Chapter 6 we have investigated numerically the dynamics of an Abrikosov vortex trapped in a mesoscopic superconducting cylindrical shell embedded in a magnetic field applied transverse to its axis. Provided the transport current and the magnetic field are not large, we have found that the vortex behaves as an overdamped quasi-particle in a tilted washboard potential and that the cylindrical shell with the trapped vortex exhibits $E(J)$ curves and time-dependent electric fields very similar to the ones exhibited by a resistively shunted Josephson weak link.

In Chapter 7 we have reported the experimental and numerical investigation of magneto-transport properties of a Nb thin strip with plano-convex section. The strip exhibits a considerable asymmetry in the critical currents when the magnetic field is applied parallel to the substrate. An asymmetry ratio of critical currents as large as 300% has been observed at 4.2 K, that makes the single superconducting thin strip with tailored section possibly interesting for applications as a superconducting current rectifier at micron scale. The observed asymmetry has been ascribed to the inhomogeneous (antisymmetric) magnetic field component normal to the convex top surface of the strip that affects, in the idealized 2D description of the real 3D strip, the double kinks present in the strip. At low applied fields, the normal component can enhance or weaken the polarity dependent self-field of the bias current. At larger magnetic fields the asymmetry comes from the balance of the magnetic force due to the inhomogeneous magnetic field and the polarity dependent Lorentz force associated to the transport current.

Finally, Chapter 8 we reported the magneto-transport measurements performed in a moderately wide but very thin Nb strip, with thickness profile asymmetrically variable on a few tens of nanometers. In a certain range of applied magnetic field, the $V(I)$ curve of the strip is characterized by vanishingly small asymmetry in the positive and negative critical currents but appreciably large asymmetry in the voltages. This behavior has been explained by the asymmetric profile of the strip that generates a geometrical force landscape that sets a preferential direction for vortex motion. Both experimental data and the more general problem of the geometrical force experienced by the vortices have been addressed here in the framework of the time dependent Ginzburg-Landau model specialized to superconducting films with variable thickness.

To conclude this thesis, we identify some open goals as well as future directions. The first pending work is to perform transport measurements on the sideward comb-shaped structure more detailed than preliminary results presented in Chapter 2. Furthermore, this geometric structure also deserves a numerical analysis with the TDGL model described above, taking into account the problem of an irregular profile in our calculation algorithms.

A further improvement to the general TDGL model could be to consider the random thermal fluctuations or the intrinsic pinning of superconducting materials. Moreover, in this thesis work we have mainly addressed magneto-transport properties in quasi-static or DC regimes. However, we are confident that with the already acquired numerical and experimental skills the study of AC regime (losses, AC susceptibility, microwave response) could also be addressed in the next future without particular effort. We are also considering to work on bigger integration domains which contain many more grid points to enhance our computations in 3D. In both cases, a new workstation with hardware accelerators (read GPUs) is needed and other parallel computation methods must be integrated into our simulation software.